

Calibration of a Laser-Raman-System using gas samples of all hydrogen isotopologues for KATRIN

Zur Erlangung des akademischen Grades eines
Doktors der Naturwissenschaften (Dr. rer. nat)
von der KIT-Fakultät für Physik
des Karlsruher Instituts für Technologie (KIT)
angenommene
Dissertation
von
Dipl.-Phys.

Simon Niemes

aus Mannheim

Referent: Prof. Dr. Guido Drexlin
Institut für Astroteilchenphysik
Karlsruhe Institut für Technologie

Korreferent: Prof. Dr. Helmut Telle
Departamento de Química Física Aplicada
Universidad Autónoma de Madrid

Tag der mündlichen Prüfung: 15.01.2021



This document is licensed under a Creative Commons Attribution 4.0 International License (CC BY 4.0): <https://creativecommons.org/licenses/by/4.0/deed.en>

Abstract

Neutrinos are the most abundant particles with non-zero mass in the universe known today and play a key role in cosmology and particle physics. At the time the Standard Model was developed, it was assumed that neutrinos have exactly zero mass; however, observations of neutrino flavour oscillations showed that neutrinos must have a finite, non-zero mass. Thus, an accurate constraint, or even better an exact experimental determination would go a long way to help discriminate between several proposed theories that extend the Standard Model. A diverse range of experimental efforts are currently pursued; amongst these the Karlsruhe Tritium Neutrino experiment (KATRIN) has just provided the most recent and lowest experimental upper limit of $m(\nu_e) < 1.1$ eV (90 % C. L.).

This limit was derived via high-resolution spectroscopy of the kinematic β -endpoint of the tritium decay spectrum. As a source, molecular tritium with an isotopic purity of >95 % T_2 is injected into the Windowless Gaseous Tritium Source (WGTS). The tritium gas is prepared in the facilities of the Tritium Laboratory Karlsruhe (TLK); however due to the separation process for tritium gas at TLK, traces of HT and DT in addition to the dominant T_2 are unavoidable, resulting in fluctuations of compositions between gas batches. The presence of these additional tritiated molecules affects the shape of the measured β -spectrum and thus must be continuously and accurately monitored.

A custom-developed Laser-Raman (LARA) spectroscopic system is used to identify and quantify all six hydrogen isotopologues. However, for quantitative analysis, a system- and isotopologue calibration factor is necessary. In the current calibration strategy, these factors are derived from the measured spectral sensitivity of the setup, and theoretical Raman intensities based on *ab initio* calculations. This approach was validated for the stable isotopologues H_2 , HD and D_2 , but is pending for the KATRIN-relevant tritiated isotopologues T_2 , DT and HT.

The aim of this work was to design, construct and commission a system capable of providing well-defined gas samples of all six hydrogen isotopologues in chemical equilibrium and to determine the experimental, isotopologue specific calibration factors for gas monitoring using LARA.

This new facility, conveniently named TRItium HYdrogen DEuterium experiment (TRIHUDE), is able to prepare samples with initial molar fractions known to within 1 % by accurately measuring pressure and gas volume of each component. In order to process the tritium gases and achieve this accuracy for tritiated isotopologues, several challenges had to be overcome:

Firstly, the whole setup had to be devised to meet all tritium-related safety requirement, including material selection and quality, process control, and containment. Based on the experiences and insights gained during the setup and operation of the predecessor experiment HYDE, the handling and processing was improved in addition to a general reduction in systemic uncertainty, e.g. volume determination. Furthermore, the system

had to be integrated into the closed tritium loop of the TLK infrastructure in order to receive high purity tritium as well as to recycle gas mixtures after use to the respective TLK facility.

Secondly, a successful commissioning with the stable isotopologues H_2 and D_2 showed a threefold reduction in calibration uncertainty, besides the general applicability of the applied sample preparation procedure.

Thirdly, commissioning with radioactive gases was necessary, in order to account for the radiochemistry introduced by the β -decay of tritium within gas samples. In contrast to gas samples comprised of only stable isotopologues, additional processes like impurity formation and self-equilibration induced by β -decay had to be studied.

It was shown that the inevitable formation of tritiated methane due to interactions with the stainless steel walls was detectable, but had no detrimental effect on sample quality during the measurement campaigns. The observed formation rates were very much as expected, similar to those deduced from outgassing data obtained in past experiments at TLK.

In contrast to hydrogen and deuterium, no high-purity tritium gas samples with a certified composition are available. In order to obtain a LARA-independent estimate of the initial composition, a modified method-of-standard-addition was developed, as no isotopic pure DT and HT samples are available. By stepwise adding a well defined amount of D_2 to the sample and using the self-equilibration process to form DT, any initial DT concentration can be derived with rather high accuracy.

Detailed studies of the self-equilibration process in tritiated mixtures allows one to utilise these reactions in sample production for the heteronuclear isotopologues by choosing suitable process parameters. This avoided the use of any previously deployed catalyst or permeator, which could potentially alter the isotopic composition of the sample; thus, highly accurately equilibrated samples can be obtained. Additional isotope exchange in gas-wall-interaction were observed, but this process exhibited a time constant of >600 h and therefore was negligible for sample production in TRIHYDE.

Based on these samples, the first direct experimental determination of the LARA-calibration factors for all hydrogen isotopologues, using both homonuclear samples as well as heteronuclear samples in chemical equilibrium. All obtained values agree with the theoretical predictions within the stated uncertainties. These complementary findings validate the currently deployed calibration procedure used at KATRIN. In the case of T_2 , a twofold uncertainty reduction was achieved, while for the heteronuclear isotopologues the uncertainties remained unchanged.

In conclusion, utilising the TRIHYDE facility it has been demonstrated that gas samples of all six hydrogen isotopologues -including those with tritium content- can be produced with unprecedented accuracy, on a technical scale. Their availability made it possible to fully validate the calibration approach used for source gas composition monitoring at KATRIN via Laser Raman spectroscopy, whilst also increasing calibration trueness.

Contents

List of Figures	vii
List of Tables	ix
1 Introduction	1
2 Introduction to neutrino physics	3
2.1 The role of neutrinos in the Standard Model	3
2.1.1 Discovery and properties of neutrinos	3
2.1.2 Theory of neutrino flavor oscillation	5
2.1.3 Overview and current state of neutrino oscillation experiments	10
2.2 Relevance of massive neutrinos in particle physics and cosmology	16
2.2.1 Theory of neutrino mass generation	16
2.2.2 Methods of neutrino mass measurement	17
3 Overview of the Karlsruhe TRitium Neutrino experiment (KATRIN)	23
3.1 Direct measurements of neutrino mass in KATRIN	23
3.1.1 Physical characteristics of the tritium beta-spectrum	24
3.1.2 Overview of the experimental setup of KATRIN	26
3.2 Description of major components in the KATRIN setup	27
3.2.1 Windowless Gaseous Tritium Source and Inner Loop	27
3.2.2 Calibration and monitoring section	30
3.2.3 Transport section	31
3.2.4 Spectrometer and detector section	32
3.3 Composition monitoring of source gas using Raman spectroscopy	35
4 Overview of the Laser-Raman-Systems (LARA) used for KATRIN	38
4.1 Introduction to quantitative Raman spectroscopy	38
4.1.1 Rotational and vibrational states in diatomic molecules	39
4.1.2 Basic principles of the Raman effect	42
4.1.3 Raman line intensity	44
4.1.4 Raman spectroscopy on hydrogen isotopologues	48
4.2 Experimental setup of the KATRIN LARA system	51
4.2.1 Overview of Components	51
4.2.2 Description of spectrum analysis	53

4.3	Calibration strategy for the KATRIN LARA system	53
4.3.1	Influence of spectral sensitivity	56
4.3.2	Influence of theoretical intensity	57
4.3.3	Status of the calibration for quantitative analysis and the need for a dedicated experimental calibration facility	57
4.4	Objectives of this work	58
5	Experimental setup of the calibration facility TRIHYDE for LARA-calibration	61
5.1	Experimental goals and working principle	61
5.2	Design considerations of TRIHYDE	64
5.2.1	General design considerations	64
5.2.2	Improvements over the predecessor experiment HYDE	65
5.2.3	Considerations for T ₂ handling	65
5.2.4	Evaluation of the uncertainty budget	67
5.3	Description of the TRIHYDE setup	71
5.3.1	The analysing loop (A-Loop) for gas sample production	71
5.3.2	The processing loop (P-Loop) for tritiated gas handling	73
5.4	Overview of selected components	75
5.4.1	Mixing vessels	75
5.4.2	LARA2-Setup	79
5.4.3	Additional analytical methods	84
5.5	Commissioning of TRIHYDE	88
6	LARA-calibration based on the stable hydrogen isotopologues H₂, D₂, and HD	90
6.1	Overview of measurements with H ₂ and D ₂	90
6.2	Experimental determination of the calibration factors	91
6.2.1	Description of experimental procedure and analysis strategy	91
6.2.2	Evaluation of the measurement uncertainty	97
6.2.3	Experimental results of the LARA calibration factors	101
6.2.4	Comparison of TRIHYDE results with predecessor experiment HYDE	105
6.3	Evaluation of the results with reference to the experimental procedures using tritiated gas mixtures	106
6.4	Conclusions	107
7	LARA-calibration including the radioactive hydrogen isotopologues T₂, HT and DT	109
7.1	General overview	109
7.1.1	Summary of procedures using tritiated gases	109
7.1.2	Commissioning of TRIHYDE using tritiated gases	112

Contents

7.2	Experimental determination of the initial tritium purity	112
7.2.1	Impurity build-up during sample preparation and measurements .	112
7.2.2	Evaluation of the initial sample purity using the method of standard addition	116
7.2.3	Implications of the initial T ₂ gas purity for LARA-calibration measurements	122
7.3	Influence of self-equilibration in tritiated gas mixtures	124
7.3.1	Introduction to self-equilibration processes	124
7.3.2	Determination of the pressure dependence	127
7.3.3	Determination of the time constants	129
7.3.4	Experimental study of self-equilibration of all six isotopologues . .	132
7.4	Experimental determination of the calibration factors for T ₂ , DT and HT .	135
7.4.1	Description of the experimental procedure and the analysis strategy	135
7.4.2	Calibration factors for mixtures of T ₂ + H ₂ + HT	139
7.4.3	Calibration factors for mixtures of T ₂ + D ₂ + DT	143
7.5	Comparison to literature values and implications for KATRIN	146
7.6	Conclusions	148
8	Summary and Outlook	151
	Bibliography	155

List of Figures

2.1	Overview of the elementary particles in the Standard Model	6
2.2	Overview of the oscillation length and the neutrino energy of current and future neutrino experiments	9
2.3	Overview of the neutrino mass hierarchy	14
3.1	Impact of neutrino mass on the tritium β -spectrum	25
3.2	Overview of the KATRIN beamline components	26
3.3	Simplified diagramm of WGTs central beamline and the Inner Loop	29
3.4	Working Principle of a MAC-E filter	32
3.5	Final states distribution of T_2 and DT	36
4.1	Vibrational energy levels of a diatomic molecule in an anharmonic Morse potential	40
4.2	Overview of Rayleigh and Raman photon scattering by molecules	43
4.3	Spectrum of generic photon scattering from a diatomic molecule	44
4.4	Scattering angles for Raman emission relative to the polarisation plane . .	45
4.5	Overview of a basic Raman system	49
4.6	Spectrum of the Q_1 -branches in an equi-concentrated sample of all six hydrogen isotopologues.	50
4.7	Overview of the LARA3 setup used at KATRIN	52
4.8	Calibration strategy for LARA-systems for KATRIN	55
4.9	Image of NIST traceable luminous spectrum 2242 and calibration cell holder	55
4.10	Certified spectrum of NIST SRM2242 luminous standard	56
5.1	Overview of a basic manometric-volumetric mixing setup	62
5.2	Overview of the A-Loop and the P-Loop tasks	63
5.3	Gas handling of TRIHYDE with TLK infrastructure	66
5.4	Image of the glovebox containing the P- and A-Loop	71
5.5	Simplified overview of the A-Loop	72
5.6	Simplified overview of the P-Loop	74
5.7	Volume determination setup of mixing vessels	77
5.8	Uncertainty of volume determination depending on reference body	78
5.9	Beam path of LARA2 setup	80
5.10	Setup of the BIXS experiment TRACE2.0	87
6.1	Overview of measurement steps in the H_2 campaign	91

List of Figures

6.2	Pressure, temperature, concentration and Raman signal profile of a typical calibration run with stable isotopologues.	94
6.3	Sample calibration curves of the binary and tertiary gas samples	95
6.4	Confidence interval of the NIST luminescence standard SRM 2242.	98
6.5	Q ₁ -line intervals of all hydrogen isotopologues used during calibration.	99
6.6	Calibration curve for H ₂ -D ₂ binary mixtures	101
6.7	Bootstrapping distribution for H ₂ -D ₂ binary calibration curve	102
6.8	Calibration curve for H ₂ -D ₂ -HD-tertiary mixtures.	103
7.1	Overview of the measurement goals in the T ₂ campaign	110
7.2	Pressure and concentration profiles during initial tritium circulation	114
7.3	Methane production during initial T ₂ circulation	115
7.4	Schematic overview of the method of standard addition (MSA).	117
7.5	Pressure and concentration profiles during MSA procedure	119
7.6	Standard addition method for estimating the initial DT-concentration before mixing.	120
7.7	Initial T ₂ -sample composition during the D ₂ -T ₂ campaign	123
7.8	Temperature dependence of the chemical equilibrium constant K_{eq}	126
7.9	Equilibration process in equiconcentrated gas samples at different pressure	128
7.10	Pressure dependence of self-equilibration time constants τ_x for 50:50 H ₂ :T ₂ calibration samples	128
7.11	Self-equilibration process of a D ₂ -T ₂ gas sample in a typical calibration run	130
7.12	Influence of the concentration gradient on the equilibration time constant τ_x	131
7.13	Equilibration process in the equiconcentrated gas sample at 300 mbar	133
7.14	Equilibration process of T ₂ in an equiconcentrated gas sample at 300 mbar on a logarithmic scale	134
7.15	Pressure and Raman signal profiles of a typical calibration run for a 60:40 T ₂ :D ₂ mixture	138
7.16	Calibration curve for H ₂ -T ₂ binary mixtures	140
7.17	Calibration curve for H ₂ -T ₂ -HT tertiary mixtures with applied spectral sensitivity correction	141
7.18	Calibration curve for D ₂ -T ₂ binary mixtures	143
7.19	Calibration curve for D ₂ -T ₂ -DT tertiary mixtures with applied spectral sensitivity correction	144
7.20	Comparison of TRIHYDE and literature values for the theoretical sensitivities of all hydrogen isotopologues	147

List of Tables

2.1	Overview of neutrino properties	5
2.2	Overview of the currently published oscillation parameter	11
4.1	Selection rules and nomenclature for Raman transitions	45
4.2	Nuclear properties of hydrogen molecules and their influence on rotational Raman line intensities	48
5.1	Uncertainty budget of an A-Loop gas sample	70
5.2	Selected specifications of used pumps	74
5.3	Overview of LARA2 components	81
5.4	Overview of selected Loop instrumentation parameter	84
5.5	Overview of general TRIHYDE components and capabilities	89
i	Experimental capabilities	89
ii	Overview of components	89
6.1	Overview of the measurement procedure for calibration-gas samples with stable isotopologues	92
6.2	Comparison of the H_2-D_2 factors derived in HYdrogen Deuterium Equilibrium experiment (HYDE) and TRIHYDE.	105
7.1	Overview of the measurements performed with the tritiated isotopologues	111
7.2	Equilibration time constants of T_2-H_2 mixtures in the range from (200 to 1000) mbar	129
7.3	Equilibration time constants of the equiconcentrated gas sample at 300 mbar	135
7.4	Overview of the sample preparation procedure for tritiated isotopologues .	136
7.5	LARA calibration factors R_x for H_2-HT-T_2	142
7.6	LARA calibration factors R_x for D_2-DT-T_2	145

1 Introduction

Neutrinos are the lightest, massive particle species in the universe known today. Despite being considered massless in the basic form of the Standard Model of particle physics, the observation of neutrino flavour oscillation implies that neutrinos must have a finite, non-zero mass [Fuk98b; McD02; Kam08]. This discovery was the first confirmed evidence of physics beyond the Standard Model and sparked progress in the fields of particle physics, cosmology and astrophysics. Nonetheless, it has not answered the question of the neutrino mass scale [Fae20; Par20].

A direct laboratory measurement of the absolute value of the neutrino mass is thus a crucial step towards answering fundamental questions in physics, as it helps to discriminate between several proposed theories that extend the Standard Model [Zub11]. A broad range of historic [Kra05; Ase11] and current [Gia17] experimental efforts, using different techniques [For12; CUO20], have not yet been able to pin down the effective neutrino mass, with the most stringent upper limit by a direct kinematic approach reported by [Ake19]

$$m(\nu_e) < 1.1 \text{ eV (90 \% C. L.)} \quad (1.1)$$

This limit was obtained by the Karlsruhe Tritium Neutrino experiment (KATRIN), by performing high-precision spectroscopy of the β -electrons from molecular tritium decay. The effective neutrino mass is imprinted in the shape of the β -electron energy spectrum and causes a small distortion close to the kinematic endpoint [Fer34].

In an effort to achieve the design sensitivity of $m(\nu_e) < 0.2 \text{ eV (90 \% C. L.)}$ [Ang04], KATRIN had to push several technical boundaries, most prominently by constructing (i) one of the largest ultra-high-vacuum vessels; (ii) a high voltage-system with ppm-stability; and (iii) a high-luminosity Windowless Gaseous Tritium Source (WGTS), which is activity and temperature stabilised on the part-per-mille level. In order to account for changes in the highly purified T_2 gas ($>95\%$) in the WGTS, which can alter the shape of the β -spectrum and therefore impact $m(\nu_e)$ -measurements [Kle19a], the source gas composition must be continuously and accurately monitored [Bab12].

Raman spectroscopy was identified as a suitable method for tritium source gas monitoring as it is capable of unambiguous identification of all six hydrogen isotopologues (H_2 , HD, D_2 , HT, DT and T_2) [Sch11]. Since the start of tritium operation of KATRIN [Ake20a], a Laser Raman Spectroscopy (LARA) system developed and built at the Tritium Laboratory Karlsruhe (TLK) [Stu10a; Sch12; Fis12; Fis14], which fulfilled all performance requirements and has become invaluable in reaching the ambiguous goals of KATRIN [Ake20b; Wel20].

Although LARA is able to detect general variations in the gas composition on a 0.1 %-level [Fis11], additional system and isotope-specific calibration factors are required for quantitative analysis [Sch13b]. Currently, these values are derived from theoretical calculations [Sch87] and indirectly verified by depolarisation measurements [Jam13a]. In the case of the stable isotopologues, the obtained calibration factors have been validated via accurate gas samples of hydrogen and deuterium mixtures. Due to the relative agreement in the order of 2 %, the remaining calibration factors were assumed to be correct [Sch14a].

However, a direct measurement and validation of the calibration factors for all tritiated isotopologues were still missing. As a means to obtain these factors, a dedicated experimental facility, able to provide tritiated calibration gas samples, is required. In addition to considering the general safety requirements for tritium handling, this facility needs to incorporate the following capabilities:

- (i) Provide both homonuclear and heteronuclear gas samples of all six hydrogen isotopologues in chemical equilibrium,
- (ii) Enable detailed studies on the radiochemical impact of tritium on calibration sample purity and stability,
- (iii) Enable in-situ calibration and characterisation of LARA-systems as well as additional methods used in tritium analytics.

All of these objectives are addressed with the construction and commissioning of the TRItium HYrogen DEuterium experiment (TRIHUDE) at the TLK, which is the main objective of this work. The thesis is structured as follows:

An introduction to neutrino properties, their oscillation and mass generation mechanisms as well as recent experimental efforts for neutrino mass measurements is given in Chapter 2.

In Chapter 3, the KATRIN experiment and the requirements of a Raman system for source gas monitoring are described.

The theoretical foundation of quantitative Raman spectroscopy, the implementation for tritiated hydrogen isotopologues and the calibration strategy are summarised in Chapter 4. At the end of Chapter 4, the objectives of this work are further refined.

An overview of the design, components and commissioning of TRIHUDE is given in Chapter 5.

In Chapter 6, the results of the measurement campaign with the stable isotopologues H₂, D₂ and HD are presented.

Chapter 7 presents the commissioning of TRIHUDE with tritium and describes the measurement results obtained using the radioactive isotopologues T₂, HT and DT. The chapter ends with a discussion of the calibration results in the context of the KATRIN-experiment.

A summary and outlook in Chapter 8 concludes this work.

2 Introduction to neutrino physics

Since the onset of β -decay studies in 1914 [Cha14], neutrino physics have been a vivid section in particle physics, with many links and connections to other areas of physics. Neutrinos are electrically neutral elementary particles that only take part in the weak interaction; thus, they are hard to detect and study. Although many initially puzzling features of neutrino properties have been explained, even after a century of neutrino and weak interaction physics, fundamental questions remain, including [Zub11]:

- Are neutrinos of Dirac or Majorana type, and what is their mass?
- Why is their mass so small compared to other elementary particles and are there additional neutrino generations?
- How did neutrinos influence the formation of large scale structures in the early universe?

This chapter opens with a historic overview of important neutrino experiments and the neutrinos properties in the Standard Model of particle physics (Section 2.1.1). This is followed by an introduction to the mechanism of neutrino oscillation and experimental efforts undertaken in order to establish the mixing parameters. The second part focuses on the theoretical foundation of neutrino mass generation, experimental methods for neutrino mass measurements and an overview of current neutrino mass limits (Section 2.2).

2.1 The role of neutrinos in the Standard Model

2.1.1 Discovery and properties of neutrinos

The first occurrence of neutrino physics can be traced back to 1914, when CHADWICK [Cha14] discovered the continuous electron energy spectrum of the β -decay of ^{214}Pb and ^{214}Bi . This was in contrast to the expected discrete spectrum, similar to the α - and γ -decay. Two other experiments confirmed the continuous energy spectrum, a blunt breach of the principle of energy conservation for the two observed reaction bodies [Ell27; Mei30]. In order to solve the puzzle, Pauli postulated a participating neutral, half-integer spin particle in his famous letter, making the β -decay a three-body process [Pau30]. The particle, nowadays known as *neutrino*, is part of the equation first published by Fermi [Fer34],

$${}^A_Z X \rightarrow {}^A_{Z+1} Y + e^- + \bar{\nu}_e, \quad (2.1)$$

describing the β -decay of the mother nuclei A to the daughter nuclei Y . This process is known today as a weak interaction with a cross section in the order of $\sigma < 10^{-44} \text{ cm}^{-2}$.

More than 20 years later, the first experimental detection of the so up to then theoretical particle was achieved by COWAN et al. [Cow56]. They placed a 200-l water target enriched with cadmium chloride in the vicinity of a nuclear fission reaction in order to use it as a neutrino source. The neutrinos react via the inverse β -decay reaction

$$\bar{\nu}_e + p \rightarrow n + e^+, \quad (2.2)$$

leaving the resulting neutron in an excited state. When the neutron, which is quickly captured by a cadmium nucleus, returns to the ground state, photons in the energy range of (3 to 11) MeV are emitted. These photons were detected using liquid-scintillator chambers placed around the target, each equipped with photomultiplier tubes. The positron was promptly annihilated by a surrounding electron and the two resulting photons, each of 511 keV, were detected by the aforementioned chambers. The neutrino event signals were discriminated from background signal by the photon delay of 17 μs between the neutron and positron reaction. The experimentally measured cross section was $(11.0 \pm 2.6) \cdot 10^{-44} \text{ cm}^{-2}$, well in agreement with the theoretical predictions [Bet34; Rei59] and worth the Nobel prize in physics in 1995 [Nob20c].

After the electron (anti-)neutrino, two additional neutrino flavour states, coupling to the μ and τ , were discovered in subsequent particle accelerator experiments: The muon neutrino ν_μ via pion decay at the AGS neutrino experiment [Dan62] in 1962 and the ν_τ via D-meson decay in 2000 at the DONUT experiment [Kod01]. During precision measurements at the e^-e^+ -collider LEP, no fourth neutrino flavour state with $m(\nu) \leq 104 \text{ GeV}/c^2$ was found. In the same experiment, the measured width of the Z_0 -resonance is consistent with the predicted lifetime, assuming only $N_\nu = 3$ generations [ALE06].

In the decades after the first discovery, more and more properties of the neutrino were investigated in various experiments. An overview of the neutrino properties is collated in Table 2.1. In the Standard Model of particle physics, the neutrinos belong the group of leptons and only participate in weak interactions (see Figure 2.1). Wu et al. [Wu57] was the first to experimentally show that parity was not conserved in weak interaction by measuring the emitted electron- and γ -distribution from cold, aligned cobalt atoms in

$$\text{Co} \rightarrow \text{Ni} + e^- + \bar{\nu}_e + 2\gamma \quad . \quad (2.3)$$

The detected anisotropy of the electron distribution led to the verification that the weak interaction is violating parity conservation, as proposed by T. Lee and C. Yang [Lee57] and later honoured with the Nobel prize in 1957 [Nob20b]. This was the first hint that only left-handed neutrinos and right-handed anti-neutrinos exist.

In 1958, Goldhaber measured the neutrino helicity

$$h = \frac{\vec{p} \cdot \vec{s}}{|\vec{p} \cdot \vec{s}|} \quad (2.4)$$

Table 2.1: Overview of neutrino properties This table lists all relevant properties in the Standard Model of particle physics. All values based are on Ref. [Zub11].

Attribute	Property
particle class	Lepton
generations	3 (ν_e, ν_μ, ν_τ)
interactions	only weak interactions
electric charge	0
spin	$1/2$ (Fermion)
weak isospin ^a	$1/2$ for left-handed neutrinos 0 for right-handed neutrinos
helicity	left-handed neutrinos right-handed anti-neutrinos
mass	0

^a inverted for anti-particles

with spin \vec{s} and momentum \vec{p} and observed a value of $h_\nu = 1.0 \pm 0.3$ [Gol58]. This confirmed that only left-handed neutrinos and right-handed anti-neutrinos participate in weak interactions. Since helicity is not Lorentz-invariant, both left- and right-handed neutrinos would be observed in case of a non-zero neutrino mass.

In the Standard Model, the particle mass is generated by Yukawa coupling to the Higgs-field [Zub11]. In order to produce the neutrino mass in a similar fashion, right-handed neutrinos and left-handed anti-neutrinos must also exist to obtain the necessary four-component Dirac spinors (see Section 2.2). Until today, there is no evidence of right-handed neutrinos or left-handed anti-neutrinos.

These and additional observations led to to the assumption that neutrinos are massless in the Standard Model (for a detailed overview, see Ref. [Kin08] and references therein). In subsequent experiments however, the discovery of neutrino flavor oscillations indicates that neutrinos have a non-vanishing mass. This hints that the neutrino mass and its properties are key to physics beyond the Standard Model, which will be explored in more detail in the following sections.

2.1.2 Theory of neutrino flavor oscillation

This introduction is based on Ref. [Coo97; Kin08; Zub11], if not noted otherwise. Throughout this text $\hbar = c = 1$ is used for better readability, i. e. $[m] = \text{eV}$.

mass - charge - spin -	$\simeq 2.2 \text{ MeV}/c^2$ $2/3$ $1/2$ u up	$\simeq 1.28 \text{ GeV}/c^2$ $2/3$ $1/2$ c charm	$\simeq 173 \text{ GeV}/c^2$ $2/3$ $1/2$ t top	0 0 1 g gluon
	$\simeq 4.7 \text{ MeV}/c^2$ $-1/3$ $1/2$ b down	$\simeq 96 \text{ GeV}/c^2$ $-1/3$ $1/2$ s strange	$\simeq 4.18 \text{ GeV}/c^2$ $-1/3$ $1/2$ b bottom	0 0 1 γ photon
	$\simeq 0.511 \text{ MeV}/c^2$ -1 $1/2$ e electron	$\simeq 105.7 \text{ MeV}/c^2$ -1 $1/2$ μ muon	$\simeq 1.77 \text{ GeV}/c^2$ -1 $1/2$ τ tau	$\simeq 91.2 \text{ GeV}/c^2$ 0 0 1 Z Z boson
	$< 1.0 \text{ eV}/c^2$ 0 $1/2$ ν_e electron neutrino	$< 0.17 \text{ MeV}/c^2$ 0 $1/2$ ν_μ muon neutrino	$< 18.2 \text{ MeV}/c^2$ 0 $1/2$ ν_τ tau neutrino	$\simeq 80.4 \text{ GeV}/c^2$ ± 1 1 W W boson
				$\simeq 125 \text{ GeV}/c^2$ 0 0 H Higgs

Figure 2.1: Overview of the elementary particles in the Standard Model. This chart shows the masses, symbols, names, and electric charges of all known particles in the Standard Model. The quark sector is marked in lila and the lepton sector in green. All particles in both sectors are fermions. The vector bosons with spin 1, colored in light blue, mediate the strong, the weak and the electromagnetic interaction. The Higgs boson with spin 0 is marked dark blue. All masses and charges are taken from Ref. [Par20].

Solar neutrino problem

The observed discrepancy of the expected and the measured solar neutrino flux in early neutrino experiments lead to the formulation of the so-called *solar neutrino problem*, which triggered the investigation of neutrino oscillations [Bah90]. Based on the solar model, the nuclear fusion reaction in the sun propagates via two chains:

1. The pp-cycle,
2. The CNO-cycle.

In the pp-cycle, hydrogen fuses to ^4He in multiple reaction steps, which possibly include intermediate ^7Be , ^8B and ^8Be stages. This represents the main reaction, with the alternative CNO-cycle only contributing about 1.6 % to the energy production of the sun. Here the presence of C, N, and O act as a catalyst for the hydrogen fusion [Wur17].

In both chains neutrinos are generated with characteristic energies and reaction rates, which range from $E_{\nu,pp} < 0.42 \text{ MeV}$ up to $E_{\nu,^8\text{B}} < 15 \text{ MeV}$ [Bah05]. Hence, the solar neutrino spectrum can give insight in the reaction kinematics occurring inside the sun.

The first experimental observation of solar neutrinos was achieved in the chlorine experiments performed by Davis [Dav64; Dav94] at the Homestake mine, based on the

reaction



with an energy threshold of 814 keV [Zub11]. In over 20 years of acquisition time, the observed flux rate was only a third of the flux rate predicted by the solar model[Cle98]. In subsequent years, additional experiments like Kamiokande [Fuk98b], GALLEX/GNO [GAL99a; GNO05] and SAGE [SAG02], with detection limits able to detect ν_{pp} , confirmed the discrepancy.

The puzzle was eventually solved by the experimental observation of flavour oscillation, which explains the missing flux because. Although the electron neutrino flux is reduced, the observed total flux of all flavours is in accordance to source production rates.

Neutrino oscillations

Parallel to the aforementioned experiments, Pontecorvo and Gribov proposed a ‘transition’ between the neutrino flavours [Pon68; Gri69]. Based on this assumption, a fraction of the electron neutrinos produced in the sun change their flavour state while travelling towards the earth.

This introduction to the description of these transitions is based on Ref. [Coo97; Kin08; Zub11], if not noted otherwise. Although some simplified arguments are used, the results are still representative.

The neutrino flavour eigenstates ($\alpha = e, \mu, \tau$) produced by the weak interaction can therefore be described as weak eigenstates $|\nu_\alpha\rangle$. For neutrinos with non-zero mass, the corresponding mass eigenstates do not necessarily have to coincide with their flavour eigenstates. This feature is also known in the quark sector, where the mixing between the different states is described by the unitary 3x3 Cabbibo-Kobayashi-Maskawa matrix (CKM matrix) [Kob73]. In a similar fashion, the flavour and mass eigenstates can be connected using

$$|\nu_\alpha\rangle = \sum_i U_{\alpha,i} |\nu_i\rangle \quad \text{and} \quad |\nu_i\rangle = \sum_\alpha U_{i,\alpha}^* |\nu_\alpha\rangle \quad (2.6)$$

with a unitary mixing matrix $U_{\alpha,i}$ given by

$$U_{\alpha,i} = \begin{pmatrix} U_{e1} & U_{e2} & U_{e3} \\ U_{\mu1} & U_{\mu2} & U_{\mu3} \\ U_{\tau1} & U_{\tau2} & U_{\tau3} \end{pmatrix}. \quad (2.7)$$

This matrix is established as the Pontecorvo-Maki-Nakagawa-Sakata matrix (PMNS matrix) [Mak62] and often parametrised in the form

$$U = \begin{pmatrix} 1 & 0 & 0 \\ 0 & \cos \theta_{23} & \sin \theta_{23} \\ 0 & -\sin \theta_{23} & \cos \theta_{23} \end{pmatrix} \cdot \begin{pmatrix} \cos \theta_{13} & 0 & \sin \theta_{13} e^{i\delta} \\ 0 & 1 & 0 \\ -\sin \theta_{13} e^{i\delta} & 0 & \cos \theta_{13} \end{pmatrix} \cdot \begin{pmatrix} \cos \theta_{12} & \sin \theta_{12} & 0 \\ -\sin \theta_{12} & \cos \theta_{12} & 0 \\ 0 & 0 & 1 \end{pmatrix} \quad (2.8)$$

Here the θ_{ij} describe the mixing angles between different flavour and mass base and δ is the CP violating Dirac phase [Par20]. If neutrinos are Majorana particles, i. e. they are their own anti-particle, two additional Majorana-phases have to be added to the PMNS-matrix (see Section 2.2.1).

Neutrinos are produced and detected in weak interactions as flavour eigenstates, which themselves are a mixture of mass eigenstates according to Equation (2.6). Since the flavour eigenstates oscillate due to this mixture on the way to the detector, the transition probability P is an important parameter to gain access to the mixing angles of the PMNS matrix.

The time dependence of a neutrino with flavour eigenstate α created at $t = 0$ is given by

$$|\mathbf{v}_\alpha(t, x)\rangle = \sum_i U_{\alpha i} \exp(-i(E_i t - p_i x)) |\mathbf{v}_i\rangle. \quad (2.9)$$

In case of relativistic neutrinos, the energy E_i of the mass eigenstates can be written as

$$E_i = \sqrt{p^2 + m_i^2} \simeq E + \frac{m_i^2}{2E}. \quad (2.10)$$

In order to obtain the time-dependent transition amplitude between to flavour eigenstates, the aforementioned equations can be combined to

$$\langle \mathbf{v}_\beta | \mathbf{v}_\alpha(t, x) \rangle = \sum_i U_{\beta i}^* U_{\alpha i} \exp\left(-i \frac{m_i^2 L}{2E}\right) \quad (2.11)$$

with the oscillation length $L = x = c \cdot t$, given by the distance between neutrino source and detector in vacuum.

Introducing $\Delta m_{ij}^2 = m_i^2 - m_j^2$, the transition probability from one flavour to another is expressed by the squared transition amplitude:

$$\mathcal{P}(\mathbf{v}_\alpha \mapsto \mathbf{v}_\beta) = |\langle \mathbf{v}_\beta | \mathbf{v}_\alpha(t, x) \rangle|^2 = \sum_i \sum_j U_{\alpha i} U_{\alpha j}^* U_{\beta j}^* U_{\beta i} \exp\left(-i \frac{\Delta m_{ij}^2 L}{2E}\right). \quad (2.12)$$

In today's experiments, the three flavour form of the mixing matrix U must be considered in data analysis (when neglecting potential sterile neutrinos, see Section 2.2). Given that the observed oscillation scales of solar and atmospheric neutrinos are separated by more than one order of magnitude, one can limit the discussion to two mass and flavour eigenstates for simplicity [Par20]. Assuming no CP violation, the mixing matrix reduces to

$$U = \begin{pmatrix} \cos \theta & \sin \theta \\ -\sin \theta & \cos \theta \end{pmatrix} \quad (2.13)$$

with a single mixing angle θ . The transition probability from flavour α to β is then expressed by the *appearance probability*

$$\mathcal{P}(\mathbf{v}_\alpha \mapsto \mathbf{v}_\beta)(L, E) = \sin^2 2\theta \sin^2\left(\frac{\Delta m^2 L}{4E}\right) \geq 0, \quad (2.14)$$

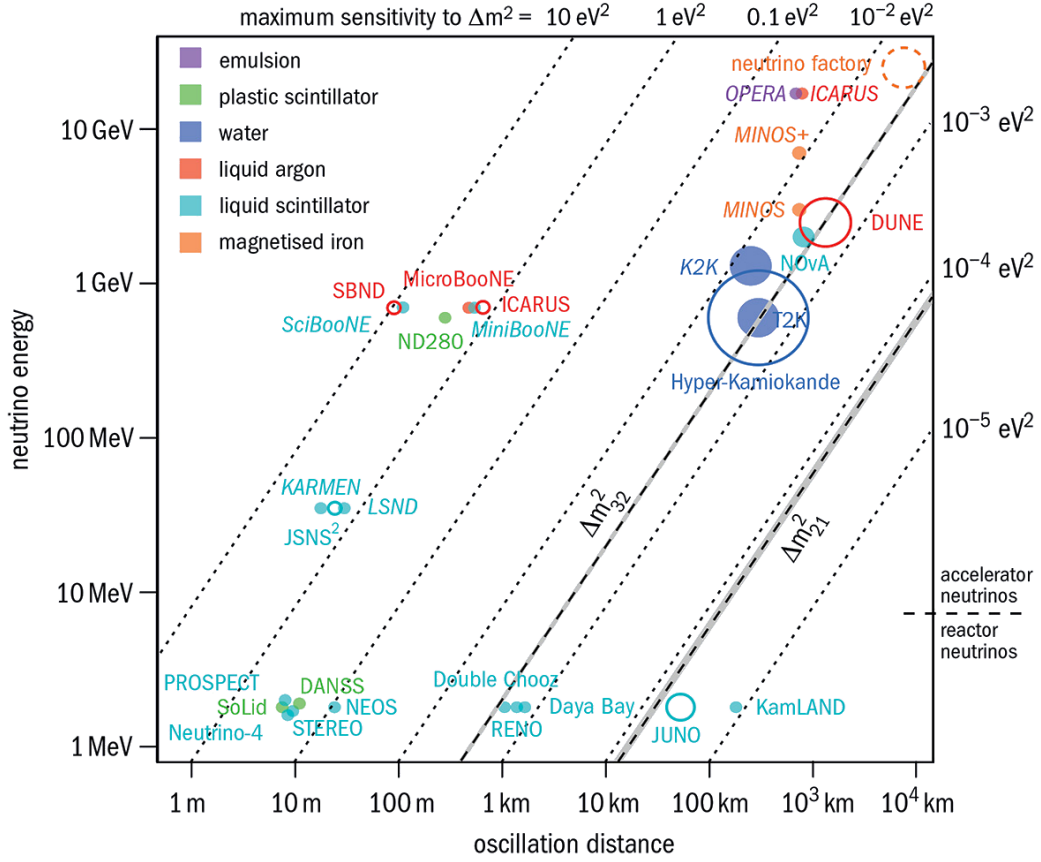


Figure 2.2: Overview of the oscillation length and the neutrino energy of current and future neutrino experiments. The theoretical ‘neutrino factory’ marked at $L \sim (7000 \text{ to } 7300) \text{ km}$ would allow a clean measurement of Θ_{13} with almost no parameter degeneracies [Hub03]. Credit: M Rayner. Reused with permission from “Tuning in to neutrinos” CERN Courier July/August 2020 p.32 (<https://cerncourier.com/a/tuning-in-to-neutrinos/>).

while the *survival probability* is accordingly given by

$$\mathcal{P}(v_\alpha \mapsto v_\alpha) = 1 - \sum_{\beta \neq \alpha} \mathcal{P}(v_\alpha \mapsto v_\beta) \leq 1. \quad (2.15)$$

The maximum value of the transition probability is fixed by the mixing angle θ , while the difference of the mas squares defines the oscillation frequency.

Oscillation experiments can be classified in two categories, depending on the observed process:

1. Experiments searching for a new flavor not present in the initial source are called *appearance experiments*,
2. Experiments measuring a reduction in the initial neutrino flavour flux due to oscillation into another flavour are called *disappearance experiments*.

An overview of recent and planned neutrino oscillation experiments based on their oscillation length and sensitivity is given in Figure 2.2, with a more detailed description in Section 2.1.3.

In general, both types of experiments detect a variation in the observed neutrino flux relative to the initial flux rate at the position of the neutrino production. The characteristic oscillation length, which depends on the neutrino energy, the mass square difference, and the source volume, gives the position of maximum flavour transition and thus best detection sensitivity

$$L_{\text{osc}} = \frac{4E}{\Delta m_{ij}^2}. \quad (2.16)$$

For $\Delta m^2 = 2.5 \cdot 10^{-3} \text{ eV}^2$, the oscillation length for reactor neutrinos with energies between (1 to 8) MeV is about $L_0 = (1 \text{ to } 10) \text{ km}$ [Par20]. As a consequence, the detector should be placed in the near vicinity of the source reactor. For accelerator neutrinos with energies in the 1 GeV region, this distance increases significantly to $L_0 \sim 10^3 \text{ km}$, posing some limitations on optimal placement. In case of solar neutrinos, both source volume and detector distance are well beyond experimental control.

2.1.3 Overview and current state of neutrino oscillation experiments

In the past years, various experiments have investigated the components of the PMNS-matrix, with an overview of the current experimental values collated in Table 2.2. Each experiment is sensitive to different energies, type and baseline, probing the different components mostly independent of the initial neutrino flux. Due to the large difference in the scale of the two known Δm^2 by about two orders of magnitude, the determination of the PMNS matrix splits into two regimes. The first regime applies to solar ν_e and reactor $\bar{\nu}_e$ and is driven by $(\Delta m_{21}^2, \theta_{12})$ mixing parameters. The second regime describes the appearance and disappearance of ν_μ and $\bar{\nu}_\mu$ characterised by $(\Delta m_{32}^2, \theta_{23})$. [San11]

In order to form a general understanding of neutrino properties, these efforts need to be combined in a global combination of the three-flavour results from different experiments. Here, a brief overview of selected setups and results is given.

Solar neutrinos

As discussed in Section 2.1.2, studies on solar neutrino detection already started in 1970 in the Homestake experiment, which eventually led to the formulation of the solar neutrino problem [Dav68; Cle98]. In order to achieve lower energy sensitivities, similar experiments using gallium instead of chlorine were subsequently built, making (p,p)-neutrino detection possible. The three experiments SAGE, GALLEX and GNO also confirmed a measured neutrino flux deficit [SAG99; GAL99b].

Table 2.2: Overview of the currently published oscillation parameter. Most values are derived from multiple experiments in a global three-flavour framework, with their dominant experimental neutrino sources listed. Since only the Δ mass squares, but not their signs, are known, both possible hierarchies are listed. All numbers are taken from Ref. [Par20].

Parameter	Normal hierarchy	Inverted hierarchy	Dominant experiments
$\sin^2\theta_{12}$	$0.307^{+0.013}_{-0.012}$	-	solar, reactor
Δm_{21}^2	$(7.53 \pm 0.18) \cdot 10^{-5} \text{ eV}^2$	-	reactor, solar
$\sin^2\theta_{23}$	0.545 ± 0.021	0.547 ± 0.021	accelerator, atmospheric
Δm_{32}^2	$(2.453 \pm 0.034) \cdot 10^{-3} \text{ eV}^2$	$-2.456^{+0.034}_{-0.040} \text{ eV}^2$	reactor, atmospheric
$\sin^2\theta_{13}$	2.18 ± 0.07	-	reactor, atmospheric
δ	1.36 ± 0.17	-	accelerator, atmospheric

In order to allow real-time detection, the water Cherenkov detectors Kamiokande and later Super-Kamikande were built [Fuk03]. These detectors were able to resolve the direction of the incident neutrino by electron-neutrino-scattering (ES)

$$\nu_\alpha + e^- \rightarrow e^- + \nu_\alpha. \quad (2.17)$$

The recoil electrons are mostly constrained to the direction of the incident neutrinos. In principle, this reaction is sensitive to all three flavours, but due the additional charged-current reactions the measured events were dominated by electron neutrinos. [Zub11] Using the angle between the recoil electrons and the sun's position as discriminator, both experiments confirmed a deficit of the measured flux compared to the predicted flux of the ^8B -neutrinos by about a factor of two [Bah01].

The solar neutrino problem was finally solved and neutrino oscillation confirmed by the Sudbury Neutrino Observatory (SNO), a 1 kt heavy water (D_2O) Cherenkov detector [Sin88]. The neutral-current reaction (NC)

$$\nu_\alpha + \text{D} \rightarrow \text{p} + \text{n} + \nu_\alpha \quad (2.18)$$

is sensitive to all neutrino flavour and was used to measure the total solar neutrino flux. The experimentally derived neutrino flux of $(5.44 \pm 0.99) \cdot 10^6 \text{ cm}^{-2} \text{ s}^{-1}$ is consistent with the flux predicted by the solar model [McD03]. Based on the charged-current reaction (CC)

$$\nu_e + \text{D} \rightarrow \text{p} + \text{p} + e^- \quad (2.19)$$

the survival rate of only electron neutrinos was measured by observing the Cherenkov radiation cone of the fast moving electrons. The NC neutrons were detected in three different phases:

1. In a pure D_2O detector configuration, the Cherenkov light from the conversion γ produced by the free neutron capture on deuterium.

2. By adding NaCl in a second phase, the free neutrons were mainly captured by the chlorine which resulted in isotropic γ cascades. These could be separated from the oriented CC Cherenkov cones on a statistical basis.
3. Last, the neutrons were detected by an array of ^3He -filled neutron counters.

The neutrino flux rate in the NC channel was consistent with the results from Super-Kamiokande and the flux rate observed in the CC channel (solely sensitive to ν_e) was one third of the total flux.[SNO01] This enabled first measurements of the oscillation parameters Δm_{21} and θ_{21} , with the recent values collated in Table 2.2.

In order to study solar neutrinos with sub-MeV energy, the ongoing BoreXino experiment uses a organic, liquid scintillator shielded by a water tank, doubling as a muon veto. Besides the first wideband spectrum of solar neutrino activity, including ^7Be , pep and pp neutrinos [Ago19], BoreXino was essential in demonstrating the Mikheyev-Smirnov-Wolfenstein (MSW) [Wol78; Mik86] effect on survival probability [Bel13a]. Up to this point, only neutrino oscillation in vacuum has been considered. When passing through an area with large electron density, an additional potential affects the transition probability of the electron neutrino given by

$$V = \sqrt{2} G_F n_e \quad (2.20)$$

with the Fermi constant G_F and electron density n_e [Zub11]. In contrast to the other flavours, the electron neutrinos can participate in a CC coherent forward scattering process, leading to a reduction in survival probability for high-energy electron neutrinos.

The envisaged SOX experiment [Bel13b], which planned to investigate short baseline oscillation by placing a neutrino- and anti-neutrino source below the BoreXino detector and search for deformation of the spatial and/or energy distribution of their interactions, was cancelled due to source production problems [Nat18]. Currently, BoreXino focuses on the detection of low intensity CNO neutrinos, with their first experimental evidence published in Ref. [Ago20].

Atmospheric neutrinos

When cosmic rays impinge on the upper atmosphere, mesons can be produced which subsequently decay into muons and neutrinos [Zub11]. As an example the pion decays via

$$\begin{aligned} \pi^+ &\rightarrow \mu^+ + \nu_\mu & \pi^- &\rightarrow \mu^- + \bar{\nu}_\mu \\ &\hookrightarrow e^+ + \nu_e + \bar{\nu}_\mu, & &\hookrightarrow e^- + \bar{\nu}_e + \nu_\mu, \end{aligned} \quad (2.21)$$

which leads to an expected flavour ratio $R = (\nu_\mu + \bar{\nu}_\mu / \nu_e + \bar{\nu}_e)$ between the flux rates of $R = 2$ [Hir88]. The resulting neutrinos have energies in the GeV-range and the propagation baseline depends on their point of production. If the neutrino is produced directly above the detector, the baseline is $L \sim 10$ km, while a neutrino produced at the opposite side of the earth the baseline is enlarged to $L \sim 10^4$ km. This enables to probe the oscillation probability

as a function $P(L/E)$ by measuring the flavour ratio R in dependence of the zenith angle of neutrino direction.

First investigations were reported by Kamiokande, a 3 kt water Cherenkov detector originally build to search for proton decay events [Ari85]. The neutrino signals were flavour distinguished by their Cherenkov cone shape. In contrast to electron neutrinos, the ring pattern of the muon neutrinos is much sharper. First results revealed an observable muon neutrino flux much less than expected ($\sim 60\%$), while the electron neutrino flux agreed well with predictions [Hir88]. The detector was upgraded in the late 1990 to Super-Kamiokande, a 50 kt detector with a much larger number of PMTs, and was able to confirm the earlier hints of $\nu_\mu \rightarrow \nu_\tau$ oscillations [Fuk98a].

Today, Super-Kamiokande is part of the T2K experiment, an long-baseline experiment sending a muon neutrino beam 295 km from the J-PARC facility to the detector [Suz10].

Accelerator neutrinos

In accelerator experiments, the neutrino beams are produced by irradiating a target, like graphite [Nak08] or aluminium [Ahn06], with a proton beam. The produced meson, e.g. pions, can be charge selected for π^+ or π^- and collimated, and subsequently decay into muon (anti-) neutrinos according to Equation (2.21) with energies up to a few hundred GeV [Zub11]. Experimental challenges include directing and focusing the beam as well as controlling the neutrino energy spectrum, considering that neutrinos are neutral. The initial beam of pions is usually focused using one or more magnetic horns with the resulting neutrino beam equally focused [Ich12]. In order to obtain a monoenergetic energy spectrum, recent neutrino experiments like T2K and NOvA place the far detector with an offset from the beam axis [Ayr07]. Although the off-center neutrino flux is reduced based on the beam's angular distribution, the energy distribution is compressed as well [Bea95]. This allows optimising the placement for maximum flavour oscillation and reduced neutrino energy systematics. Typically a near and far detector with baselines from 1 km to up to 810 km are realised [Fel13].

Accelerator neutrinos allow precision studies on neutrino interactions and oscillations due to the high-intensity neutrino sources, whose beam characteristics can be controlled and their kinematics include fewer uncertainties compared to other sources. These experiments can be divided into:

- muon neutrino disappearance experiments like Minos[MIN06], Nova[Ayr07], and T2K [Suz10] and
- tau neutrino appearance experiments, like OPERA [Kod98].

In 2014, OPERA reported the first direct detection of oscillation $\nu_\mu \rightarrow \nu_\tau$ oscillation, confirming the three-flavour property of the PMNS-matrix [OPE14].

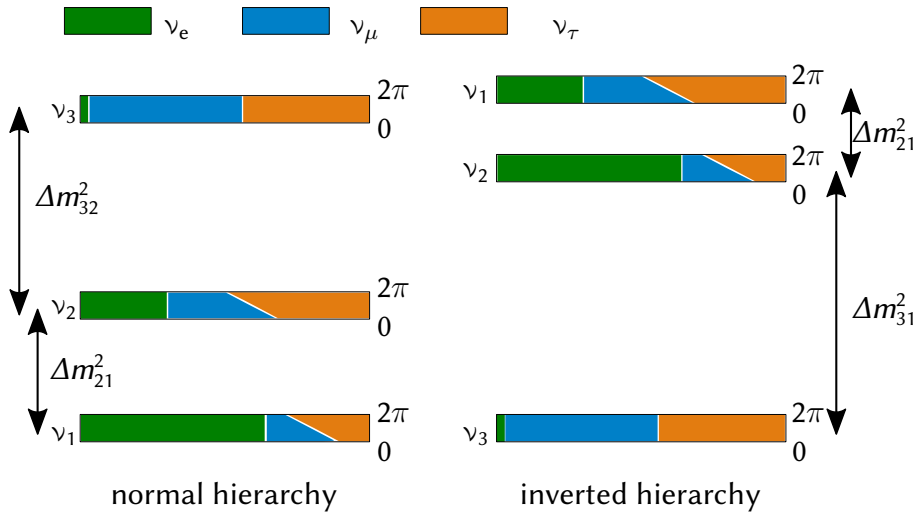


Figure 2.3: Overview of the neutrino mass hierarchy. Based on recent published values on oscillation parameters, two possible mass orders remain: A normal hierarchy and the so-called inverted hierarchy (see Table 2.2). Figure is based on Ref. [Sal18].

Reactor neutrinos

Since the beginning of neutrino physics experiments, reactors are used as intense neutrino sources [Cow56]. The neutrinos are produced by cascades of β -decay chains from the typical fission products of ^{238}U , ^{239}U , ^{239}Pu , and ^{241}Pu [Zub11]. Since all unstable fission products are neutron-rich nuclei, all β -decays are of β^- type, resulting in a pure anti-electron neutrino neutrino flux [Kim13].

Neutrino oscillation experiments using reactor neutrinos are always based on disappearance measurements, comparing the measured neutrino flux with the expected output based on the reactor's operating parameters. Notable experiments include Double Chooz [Dou12], Daya Bay [An16a], RENO [Ahn12] and KamLAND [Fog03]. At present time, the best limit of θ_{13} is derived from direct measurement by these experiments [Par20]. New precision measurements of θ_{13} will be performed at the upcoming experiment JUNO, which is expected to start taking data in 2021 [An16b].

Summary and neutrino mass hierarchy

In conclusion, our knowledge of neutrino oscillation today stems from a global analysis of various experiments and neutrino sources in the three neutrino flavour framework. The recent values for θ_{12} and Δm_{21}^2 are derived from KamLAND reactor neutrinos experiments combined with solar neutrino experiments. Values for θ_{23} and Δm_{32}^2 are a combination of results of atmospheric, reactor and accelerator neutrino experiments; while θ_{13} is based on reactor neutrino experiments. [Par20]

Although today's experiments have well established the parameter space of neutrino oscillations, three major questions remain:

(i) CP violating phase:

In order to explain the asymmetry of matter and anti-matter in the universe, CP violation is one of Sakharov conditions [Sak91]. CP-violation was observed in the quark sector, but not confirmed in the non-quark sector. Hence, many efforts are put into the experimental determination of the CP-violating phase in the neutrino sector (see Equation (2.8)). Recent observations of neutrino oscillation experiments hint to a non-zero value of $\delta = 1.36 \pm 0.17$, but are limited to a $3\text{-}\sigma$ confidence level [Par20].

(ii) Fourth neutrino generation (sterile neutrino):

So far only left-handed neutrinos and right-handed anti-neutrinos have been observed, which is a motivation for the zero neutrino mass in the Standard Model. Based on neutrino oscillations, neutrinos must have a non-vanishing mass, in principle allowing a Lorentz-transformation to flip the helicity of the particle. This allows the possibility of a fourth generation of neutrinos, not participating in any other interaction; thus, it is named *sterile neutrino*. Anomalies in the count rates of reactor neutrino experiments [Den17] and accelerator experiments [Agu10] hint towards a sterile neutrino, but could also be attributed to uncertainties in the source kinematics. A variety of experimental efforts, including future experiments like DUNE [Acc16], as well as existing setups, also within KATRIN [Mer15], are ongoing to either validate or disprove this hypothesis.

(iii) Neutrino mass hierarchy:

In principle, all conceivable orderings are possible for the three neutrino mass eigenstates. Based on observations of the MSW resonance on solar neutrinos, the ordering of $m_1 < m_2$ is fixed [Zub11]. This leaves two possible hierarchy scenarios, as illustrated in Figure 2.3:

- a) normal hierarchy: $m_1 < m_2 \ll m_3$,
- b) inverted hierarchy: $m_3 \ll m_1 < m_2$.

In order to solve this question, precision measurements of the mixing parameter in the disappearance channel and matter effects are planned by many collaborations in either upgrades [Aar17] or new experiments like JUNO and DUNE [An16b; Acc16].

An additional missing link to neutrino properties is the knowledge of the absolute neutrino mass scale, which is discussed in the next section.

2.2 Relevance of massive neutrinos in particle physics and cosmology

As discussed in the previous section, neutrino oscillation experiments are sensitive to the difference in squared mass eigenstates, but not the absolute squared mass scale. However, the observation of neutrino oscillation show that neutrinos must have a non-zero mass. In this section the framework of neutrino mass generation, its importance in different research topics in particle and astroparticle physics, and experimental efforts in neutrino mass determination are given.

2.2.1 Theory of neutrino mass generation

This following brief introduction is based on Ref. [Zub11; Moh02], if not noted otherwise. In the Standard Model of particle physics, Dirac particles obtain their mass from the term m_D in their Lagrangian

$$\mathcal{L} = m_D \bar{\Psi} \Psi \quad (2.22)$$

for their given Dirac Spinor Ψ . These can be rewritten using individual Weyl-spinors for left- and right-handed currents in the fermion field to

$$\mathcal{L} = m_D (\bar{\Psi}_L \Psi_R + \bar{\Psi}_R \Psi_L) \quad (2.23)$$

As already introduced in Section 2.1.1, only left-handed neutrinos have been observed; thus, without extension, the Standard Model neutrino is massless.

One possibility to generate the neutrino mass is to just add the right-handed neutrino singlet. In this case the Dirac mass m_D of the neutrino is interpreted, like for all other particles, as the Yukawa coupling to the Higgs field Φ_0 :

$$\Phi_0 = \begin{pmatrix} 0 \\ v \end{pmatrix} \quad (2.24)$$

with the vacuum expectation value v of the Higgs-field [Hig64]. The neutrino mass is then given by

$$\begin{aligned} \mathcal{L} &= -c_\nu \bar{\nu}_R \Phi_0^\dagger \begin{pmatrix} \nu_{eL} \\ e_L \end{pmatrix} + \text{h.c.} \\ &= -c_\nu v \bar{\nu} \nu \\ &\rightarrow m_{D,\nu} = c_\nu v \end{aligned} \quad (2.25)$$

with *h.c.* standing for the *hermetic conjugate*. The mass depends on the coupling constant c_ν , which is not predicted by theory; thus, it must be measured experimentally. In case of Dirac neutrinos, this constant must be many orders of magnitude smaller compared to other particles, a scenario often described as ‘unnatural’.

A second possibility to add massive neutrinos to the Standard Model is the assumption that neutrinos are Majorana particles. Then, neutrinos and anti-neutrinos are the same particle, but the discrimination in handedness remains. The resulting Lagrangian for the complex Majorana mass is

$$L = \frac{1}{2} (m_M \bar{\Psi} \Psi^C + m_M^* \bar{\Psi}^C \Psi) = \frac{1}{2} (m_M \bar{\Psi} \Psi^C) + \text{h.c.} \quad (2.26)$$

The complex Majorana mass can be split into real masses for left- and right-handed states:

$$L^L = \frac{1}{2} m_L \Psi_L \bar{\Psi}_R^C \quad (2.27)$$

$$L^R = \frac{1}{2} m_R \Psi_L \bar{\Psi}_R^C \quad (2.28)$$

A third possibility is a combination of Dirac and Majorana particles, which results in the most general term for neutrinos

$$L = \frac{1}{2} m_D (\bar{\nu}_L \nu_R + \bar{\nu}_L^C \nu_R^C) + \frac{1}{2} m_L \nu_L \bar{\nu}_R^C + \frac{1}{2} m_R \nu_L \bar{\nu}_R^C + \text{h.c.} \quad (2.29)$$

$$= (\bar{\nu}_L, \bar{\nu}_L^C) \begin{pmatrix} m_L & m_D \\ m_D & m_R \end{pmatrix} \begin{pmatrix} \nu_R^C \\ \nu_R^C \end{pmatrix} + \text{h.c.} \quad (2.30)$$

One possible explanation for the small observable neutrino mass is the so-called see-saw-mechanism [M G79; Yan80]. If $m_L \approx 0$ and $m_R \gg m_D$, two distinct mass eigenstates can be found:

$$m_1 = \frac{m_D^2}{m_R} \quad (2.31)$$

$$m_2 = m_R \left(1 + \frac{m_D^2}{m_R} \right) \sim m_R \quad (2.32)$$

This would leave m_1 in the (sub-)eV-range, while m_2 could possibly be in the range of MeV to GeV, similar to other Dirac particles [Zub11]. Furthermore, m_2 can be interpreted as the sterile neutrino mentioned in Section 2.1.2.

It should be noted that a lot of other theories for neutrino mass generation exist, like an extended Higgs sector with more than just one Higgs particle [Ant02]. In order to progress in this field, an experimental determination of the light neutrino mass scale is essential to reduce the number of unknown parameters.

2.2.2 Methods of neutrino mass measurement

As already described in Section 2.1.3, neutrino oscillation experiments are only sensitive to the squared mass difference, but not the absolute neutrino mass scale. Therefore, additional experimental efforts are needed to gain insight, which can be grouped into two methods:

- (i) Indirect or model-dependent measurements,
- (ii) Direct measurements.

Here, a brief overview of current experiments and derived upper mass limits is given.

Indirect methods

Cosmology: In order to describe the cosmological evolution, neutrinos must be considered through their contribution to the expansion history of the universe via their energy density as well as alteration of matter perturbation evolution. Based on different mechanisms, e.g. CMB lensing [Les06], galaxy clustering [Teg04] and Lyman- α forest [Pal15], the imprint of massive neutrinos in the cosmologic evolution can be probed [Dvo19]. First, a cosmological model has to be chosen to describe the early universe. The minimal cosmological model Λ CDM, currently providing a good fit to most cosmological data sets, assumes that the only massless or light (sub-keV) relic particles since the Big Bang Nucleosynthesis (BBN) epoch are photons and active neutrinos [Par20]. After the BBN, the neutrinos decouple from the thermal plasma and form the relic neutrino background CvB [Irv83]. Although it has not been observed directly, the CvB has been indirectly confirmed by the accurate agreements of predictions and observations in the power spectrum of the Cosmic Microwave Background (CMB) and the large scale clustering of cosmological structures [Par20]. Depending on the model and considered effects, a range of upper limits m_{tot} for the total sum of all neutrino masses are reported [Pla18]:

$$m_{\text{tot}} = \sum_i m_i \leq (0.11 \text{ to } 0.54) \text{ eV} \quad i = 1, 2, 3. \quad (2.33)$$

Although cosmological observations currently give the strongest bound on neutrino mass, the results are highly tentative on the model chosen. In case of the minimal Λ CMB, at least eight free parameters have to be simultaneously fitted; thus, this emphasises the importance of model-independent measurements.

Supernova neutrinos: In core-collapse supernovae, about 99 % of the released energy is isotropically emitted within the first 10 s [Sig16]. Supernova neutrinos have typical energies in the MeV-range and are produced in these processes:



The sensitivity to neutrino mass is based on the energy versus time-of-arrival pattern Δt of the neutrinos given by [Abb88]

$$\Delta t = t_1 - t_2 = \Delta t_0 + \frac{Lc^3m^2}{2} \left(\frac{1}{E_2^2} - \frac{1}{E_1^2} \right). \quad (2.35)$$

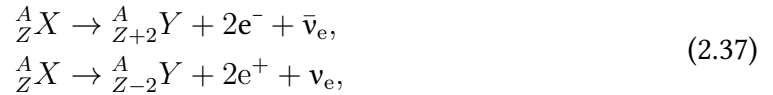
The neutrino energies E_1, E_2 can be observed by a neutrino detector and the travel distance L determined by other methods, e.g. gamma rays [Pan05]. The large uncertainty in neutrino mass limits arises from the model used to determine Δt_0 , which describes the supernova process. SN1987A was the first supernova that occurred while neutrino experiments with sufficient sensitivity were running [Hir87]. Based on the 20 observed events, an upper limit of

$$m_\nu \leq 5.7 \text{ eV} \quad (95 \% \text{ (C. L.)}) \quad (2.36)$$

was published [Lor02].

On account that neutrinos only participate in weak interactions, they can escape the star before the photons and the pressure shockwaves reach the surface (see Ref. [Jan17] for details on transport reaction details). As a result, the neutrinos arrive at Earth before the emitted photons; thus, they are a suitable indicator for galactic supernova events. Today's neutrino observatories are therefore combined to form an early-warning system for optical observatories [Abe16]. The determination of the neutrino mass in independent measurements would not only improve in distance-of-travel determination, but also allow deeper insights in the dynamics of supernovae [Zub11].

Neutrinoless double beta decay: In 1935, GOEPPERT-MAYER [Goe35] was the first to describe the rare process of double β -decay. In general, a decay of a nucleus X only happens if the binding energy of the daughter nucleus Y is larger, based on the Bethe-Weizsäcker equation [Wei35]. In case a single β -decay is forbidden, a double β -decay is possible as a second order process. The two possible processes are described by



and are based on the weak interaction, resulting in a very long lifetime ($\sim 10^{20}$ yr) of the nucleus X [Zub11]. If lepton number conservation is violated, an additional process without neutrino emission is possible, leading to



This is only possible if neutrinos are Majorana-particles, i.e. are their own anti-particle. Assuming the double beta-decay proceeds via a virtual intermediate state, the neutrino produced in the initial β -decay must flip its helicity to be absorbed in the second decay. In order to change its helicity, a particle must have a non-zero mass and since lepton number is violated, an experimental observation of $0\nu\beta\beta$ -decay would lead to physics beyond the Standard Model.

Several experiments are currently trying to establish limits of the half-lifetime $t_{1/2}^{0\nu}$ of this process [Dol19]. In contrast to the continuous β -spectrum of the nominal $2\nu\beta\beta$ -decay, the

$0\nu\beta\beta$ -decay is distinguished by a mono-energetic spectrum at the Q -value. The majorana-mass is derived by

$$\langle m_{\beta\beta} \rangle^2 = \left| \sum_{i=1}^3 U_i m_i \right|^2 = \frac{m_e^2}{G^{0\nu\beta\beta} \cdot |M^{0\nu\beta\beta}|^2 \cdot t_{1/2}^{0\nu}} \quad (2.39)$$

with the phase space factor $G^{0\nu\beta\beta}$ and nuclear matrix element $M^{0\nu\beta\beta}$. Since $\langle m_{\beta\beta} \rangle^2$ is derived by the coherent sum of the mixing matrix elements U_i multiplied by m_i , individual contributions can possibly cancel each other out. One of the major experimental challenges is background reduction due to the long-lifetime of $0\nu\beta\beta$ -decay. The most recent published results by CUORE therefore have rather large uncertainty and report a value of [CUO20]

$$m_{\beta\beta} \leq (75 \text{ to } 350) \text{ meV} \quad . \quad (2.40)$$

Care must be taken when interpreting and comparing these results to other measurements because:

- (i) The Majorana phases are unknown and can lead to cancelled out mass contributions;
- (ii) The calculation of the transition matrix elements necessary for analysis include large theoretical uncertainties [Eng17];
- (iii) In principle, if lepton number is violated, many other processes can explain or contribute to $0\nu\beta\beta$ -decay, e.g. supersymmetric particles [Päs15].

Direct methods

By investigating weak decays, it is possible to deduce the neutrino mass in a direct, model-independent way. In general, three types of weak decays exist:

$${}^A_Z X \rightarrow {}^A_{Z+1} Y + e^- + \bar{\nu}_e, \quad (2.41)$$

$${}^A_Z X \rightarrow {}^A_{Z-1} Y + e^+ + \nu_e, \quad (2.42)$$

$$e^- + {}^A_Z X \rightarrow {}^A_{Z-1} Y + \nu_e. \quad (2.43)$$

In all cases, the neutrino mass is imprinted in the shape of the β -spectrum, with details given in Chapter 3.

In contrast to the neutrinoless beta decay, the observable

$$m^2(\nu_e) = \sum_i |U_i|^2 m_i^2 \quad (2.44)$$

is the incoherent sum of the electron neutrino mass square, with no possible cancellation of contribution. The decay-energy Q of the β -decay is determined by the mass difference of

the neutral mother and daughter atoms. In the case of the β^- -decay, the Q -value is given by

$$Q = (m({}_Z^A X) - m({}_{Z+1}^A Y)) c^2 \quad (2.45)$$

For a massless neutrino and no excitation of the daughter nucleus, the so-called endpoint energy E_0 can be expressed as

$$E_0 = Q - E_{\text{rec}} \quad (2.46)$$

for a nucleus recoil energy E_{rec} . In case of a non-zero neutrino mass, the shape of the β -spectrum close to E_0 is affected.

There is a long history in using the hydrogen isotope tritium ${}^3\text{H}$ (in the following denoted as T) as the β -emitter in neutrino mass experiments, for reasons like [Ott08; Bor08; Zub11; Dre13]:

- (i) Tritium has a low Q -value of about 18.6 keV, one of the smallest of known β -emitters. This makes the effect of the neutrino mass on the endpoint region of the spectrum comparatively large.
- (ii) The half-life of tritium is only 12.3 yr, offering a highly luminous source with a small amount of material.
- (iii) Tritium has an atomic number of $Z = 1$ and therefore a simple electronic shell. This minimises Coulomb interaction between emitted electrons and the nucleus, allowing a detailed theoretical calculation of the process.
- (iv) A typical high-purity tritium source usually contains the molecular form T_2 , whose simple structure allows for the quantitative calculation of the excited final states distribution of the daughter molecule $({}^3\text{HeT})^+$.

Several neutrino mass limits from tritium β -decay have been reported by past experiments, e.g. Troitsk [Ase11] and Mainz [Kra05]. Since first experiments in 1947 [Kon47], significant improvements were achieved by using gaseous tritium sources and electrostatic spectrometers of the MAC-E-type (see Section 3.2). The latest iteration of this experimental type is KATRIN, which recently published the current value of [Ake19]:

$$m(\nu_e) < 1.1 \text{ eV (90 \% C. L.)} \quad (2.47)$$

An alternative concept to determine the shape of the β -spectrum is using Cyclotron Radiation Emission Spectroscopy (CRES), which is currently investigated by the Project8 collaboration [For12]. Strong magnetic fields around the source are used to generate synchrotron radiation from the β -electrons in the radio-frequency range, which can be used to determine the energy spectrum. At the time of writing, Project8 successfully measured β -electrons from both ${}^{83\text{m}}\text{Kr}$ and tritium and currently aims to implement an atomic tritium source [Gui20].

Another technique of direct neutrino mass measurements is based on the β -emitter ${}^{187}\text{Re}$, which has the lowest endpoint energy of $Q = 2.47$ keV [Sis04]. Although this makes it a

suitable candidate, the relatively long half-life of $4.32 \cdot 10^{10}$ yr results in a huge required source amount. In current ^{187}Re -experiments like MARE [Fer15], the decay energy including nucleus recoil is detected via cryogenic bolometers.

In another approach, the electron capture of ^{163}Ho with a Q -value of 2.83 keV [Eli15] is used. Similar to β -decay experiments, the neutrino mass affects the endpoint region of the observed spectrum. The HOLMES-experiment [Gia17] and ECHO [Gas17] use cryogenic micro-calorimeters based on transition edge sensors and metallic-magnetic calorimeters to reach a design sensitivity of <2 eV. Both experiments are currently being commissioned and aim to start data taking soon.

At present, the most sensitive and advanced direct neutrino mass experiment is KATRIN. As this work is performed within the context of KATRIN, the experiment and setup are described in detail in the following Chapter 3.

3 Overview of the Karlsruhe TRItium Neutrino experiment (KATRIN)

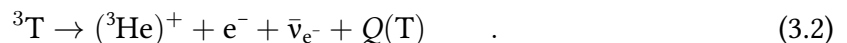
In order to fill a missing gap in neutrino physics, a model-independent experimental measurement of the neutrino mass is essential. This chapter gives an overview of KATRIN, whose aim it is to determine the effective (anti-) neutrino mass with a unprecedented sensitivity of 0.2 eV [Ang04]. In the first half an introduction of the working principle is given, followed by a description of the beamline setup and major components. The chapter concludes with a more detailed look at uncertainties introduced by source gas composition and how these are addressed to provide the context of the work performed in this thesis.

3.1 Direct measurements of neutrino mass in KATRIN

As mentioned in the previous Chapter 2, the neutrino mass is a missing but important link in the Standard Model. Based on the experience and insights gained in the neutrino mass experiments performed in Troitsk [Ase11], Mainz [Kra05], and Los Alamos [Wil91], KATRIN was set up to improve the previous sensitivity of $m(\nu_e) = 2$ eV by an order of magnitude. The current value published in Ref. [Ake19] by the KATRIN-collaboration is

$$m(\nu_e) < 1.1 \text{ eV (90 \% C.L.)} \quad (3.1)$$

The neutrino mass is obtained via high-accuracy spectroscopy in the endpoint-region of the tritium β -decay described by [Fer34]:



On account that not the neutrino mass, but the neutrino mass square is the observable in the β -spectrum of tritium (see Equation (3.3) below), KATRIN needs an improvement in the end point measurement by a factor of order 100 to reach the ambitious design sensitivity of $m(\nu_e) = 0.2$ eV.

To achieve this goal, the KATRIN experiment consists of a highly complex setup featuring the following key components:

1. A tritium source with a high luminosity of 10^{11} Bq stable on a 0.1 %-level to acquire the required statistics [Bab12].

2. A spectrometer with excellent energy resolution of 0.93 eV around the endpoint energy of 18.6 keV and ultra-high-vacuum of 10^{-11} mbar in a volume of 1240 m³ [Val06], respectively.
3. A total of 24 superconducting magnets ranging from (3.6 to 6) T to provide the magnetic flux tube of 191 T cm² to adiabatically guide the electrons from the source to the detector [Are18b].

The initial letter of intend was published in 2001 [KAT01], followed by the KATRIN design report in 2005 [Ang04]. Karlsruhe was chosen as a location due to the existence of the TLK [Dör08], one of the two civil laboratories worldwide handling tritium on a technical scale, offering a closed tritium cycle and an inventory permission of up to 40 g T₂ [Dör05]. First components like the pre-spectrometer and main spectrometer arrived on site in 2003 [Frä10] and 2006 [Val06]. Preparations for the integration of the KATRIN systems with the TLK-infrastructure started in parallel [Kaz08b; Stu10a; Fis11]. Construction of the beamline cryostats finished in 2015 with the delivery of the WGTs and Cryogenic Pump Section (CPS) [Are16]. Two major commissioning milestones were achieved with the First Light campaign in 2016 [Are18c] and a ^{83m}Kr-measurement program in 2017 [Are18a]. Based on these results KATRIN started tritium operation in 2018 and has since accomplished several successful measurement campaigns [Ake19; Pri20].

In the following sections, the experimental basics and principles are introduced, followed by the technical details of the main components.

3.1.1 Physical characteristics of the tritium beta-spectrum

The energy distribution Γ of the β -electron from tritium decay can be calculated using Fermi's golden formula given by [Fer34; Kle19a]

$$\begin{aligned} \frac{d\Gamma}{dE} = & \frac{G_F^2 \cdot |V_{ud}|^2}{2\pi^3} \cdot |M_{\text{nucl}}|^2 \cdot F(E, Z + 1) \cdot p_e \cdot (E + m_e) \\ & \cdot \sum_i |U_{ei}|^2 \cdot \epsilon \cdot \sqrt{\epsilon^2 - m_i^2} \cdot \Theta(\epsilon - m_i) \end{aligned} \quad (3.3)$$

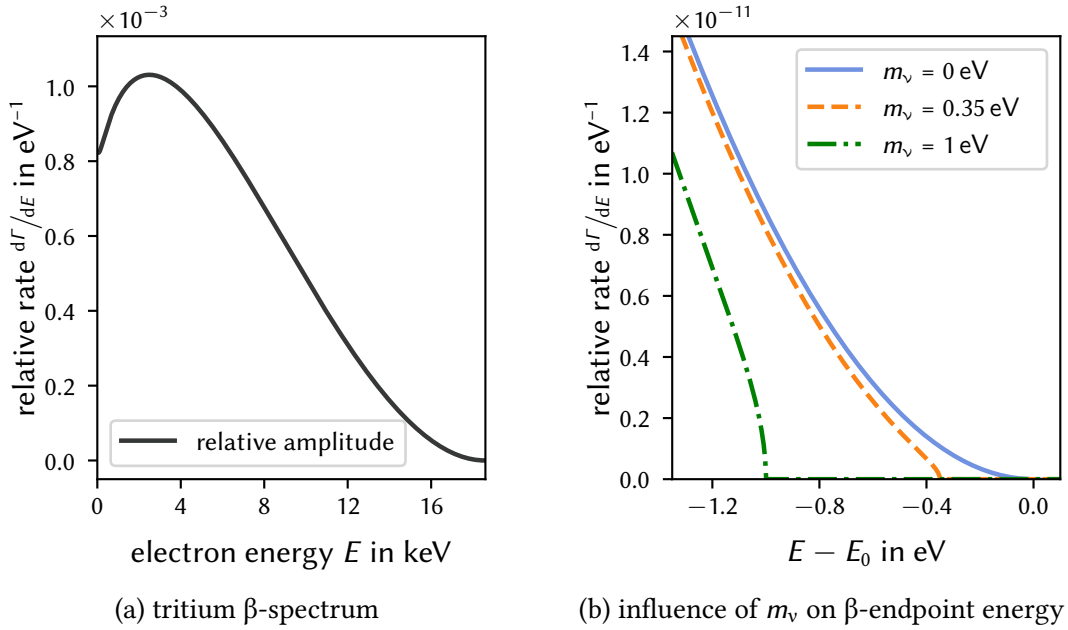


Figure 3.1: Impact of neutrino mass on the tritium β -spectrum. The area of the overall rate given via Fermi's golden rule (see Equation (3.3)) is normalised to 1. Depending on the neutrino mass m_ν the shape and endpoint of the spectrum is shifted. Figure based on Ref. [Kle19a].

with the factors:

- G_F : Fermi coupling constant,
- V_{ud} : CKM matrix element given by the Cabibbo angle $\cos(\theta_C)$,
- M_{nucl} : nuclear transition matrix element,
- $F(E, Z + 1)$: Fermi function to account for the interaction with the nuclear Coulomb field,
- $p_e \cdot (E + m_e)$: phase space factor with electron momentum p_e ,
- ϵ : neutrino energy $E_0 - E$,
- m_i : neutrino mass eigenstates m_i with $i = 1, 2, 3$,
- $\Theta(\epsilon - m_i)$: Heaviside function to ensure energy conservation.

For better readability, natural units ($\hbar = c = 1$) are used throughout the text.

In Figure 3.1 the overall distribution and the impact of the neutrino mass on the spectrum endpoint is shown. The neutrino mass not only dictates the endpoint energy, but also manifests itself in the general shape of the spectrum. Hence the β -energy spectrum from $E_0 - 40$ eV up to $E_0 + 50$ eV needs to be measured in the spectrometer [Ake19].

In KATRIN, the integrated β -spectrum is measured [Kle19a], i.e.

$$\dot{N}(t) = \frac{1}{2} N_T \cdot \int_{qU}^{E_0} \frac{d\Gamma}{dE} \cdot R(E, U) dE \quad (3.4)$$

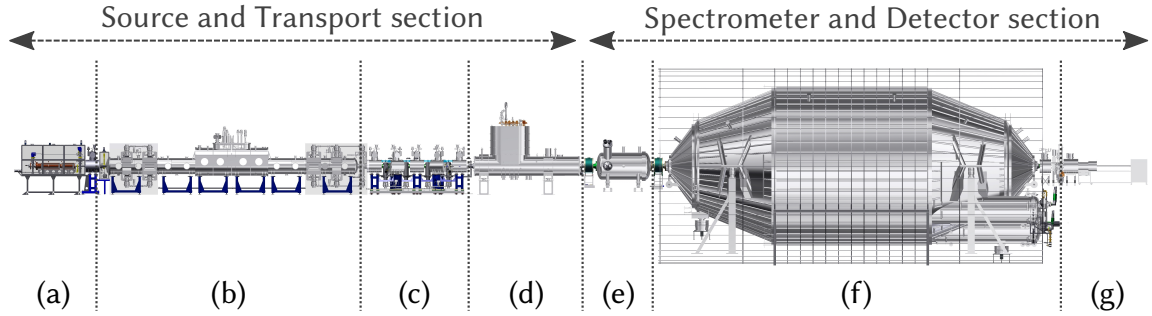


Figure 3.2: Overview of the KATRIN beamline components. Tritium is injected into the WGTS (b) and continuously pumped out at the ends. About half of the β -electrons are guided through the transport-section comprised of the DPS (c) and CPS(d) towards the detector; in this section also the tritium molecules are retained. The other half is used at the RS (a) for source activity monitoring and calibration purposes. The energy of the β -electrons is analysed with the pre-spectrometer(e) and main-spectrometer (f) and the electrons are counted afterwards by the focal plane detector (g). Figure based on Ref. [Ake20b].

depending on the total number of tritium atoms N_T inside the source and the response function R of the main spectrometer. The latter is influenced by the electrostatic potential U . As a result of Equation (3.4), any fluctuations in either N_T or U translate into a systematic uncertainty impacting the observed rate and thus the measured neutrino mass. This places strict stability requirements on all components which are described in Section 3.2.

3.1.2 Overview of the experimental setup of KATRIN

Basically, the KATRIN-experiment setup comprises the 70-m long beamline divided into two sections:

1. The Source and Transport Section (STS),
2. The Spectrometers and Detector Section (SDS).

Based on the configuration shown in Figure 3.2, the electrons start within the tritium processing STS and pass the following components:

(a) Rear Section (RS):

The RS performs both the calibration of the overall system (E-gun) as well as activity monitoring of the source. It also provides the rear wall unit, which influences the source plasma potential [Bab12].

(b) Windowless Gaseous Tritium Source (WGTS):

Tritium is injected in the middle of the WGTS and continuously pumped out at both ends, while the electrons are guided to either the RS or towards the detector. The tritium source gas is supplied by the Loop system [Kaz08b; Stu10a; Pri15].

(c) Differential Pumping Section (DPS):

In order to contain tritium molecules within the STS, the first step in tritium flux

reduction is a differentially pumped section of the beamline. The Differential Pumping Section (DPS) consists of two major elements:

- turbopumps within the WGTS-cryostat,
- a Ω -shaped section of the beamtube surrounded by superconducting magnets.

While the much lighter electrons can navigate the chicane guided by the magnetic fields, the neutral molecules collide with the wall and are evacuated [Luk12].

(d) Cryogenic Pump Section (CPS):

For further tritium flux reduction, the CPS beam tube is placed inside a cryostat. The beam tube is shaped similar to the DPS-section and internally covered with in Ar-frost layer, acting as a cold trap for the remaining molecules [Gil10].

Since of all these components are in contact with tritium, they are placed within the monitoring area of the TLK.

The energy of the transmitted electrons is then analysed via the following components

(e) Pre-Spectrometer:

The Pre-spectrometers filters out low energy electrons to reduce the flux into the main spectrometer[Frä10].

(f) Main spectrometer:

An electric retardation potential is used as a high-pass filter to determine the β -energy [Val06].

(g) Focal plane detector:

All electrons with sufficient energy to pass the retardation potential are registered via the focal plane detector [Dun08].

Not shown in the overview is the monitor-spectrometer, tasked with surveillance of the high-voltage stability. The individual components are described in more detail in the following sections.

3.2 Description of major components in the KATRIN setup

3.2.1 Windowless Gaseous Tritium Source and Inner Loop

The WGTS provides the necessary β -electrons, starting in the 10 m long central beam tube with a diameter of 90 mm. Molecular tritium is injected in the middle via an injection chamber with 415 orifices [Bab12]. At both ends of the beam tube, the gas is continuously pumped via four turbomolecular pumps to achieve a quasilinear decrease in column density

along the central beam tube according to the pressure profile shown in Figure 3.3a. The column density is given by

$$\mathcal{N} = \int_{-5\text{m}}^{5\text{m}} n(\vec{r}, p_{\text{in}}, p_{\text{out}}) T(\vec{r}) dz \quad (3.5)$$

with

- n : number density,
- \vec{r} : spatial coordinate,
- p_{in} : injection pressure,
- p_{out} : outlet pressure,
- $T(\vec{r})$: temperature profile.

The design specification of a total column density of $\mathcal{N} = 5 \cdot 10^{21}$ molecules/m² constitute a compromise, namely the balance between maximum count rate and increased scattering probability of the β -electrons [Ang04].

The beam tube is placed within a 16-m-long cryostat capable of temperatures down to 27 K and can be operated in two modes:

1. Tritium operation:
In normal operation the beam tube is cooled to 30 K as a trade-off between Doppler-broadening of the β -spectrum and cluster formation of tritium molecules.
2. ^{83m}Kr mode:
In a second mode, gaseous ^{83m}Kr is mixed to the tritium. This enables quantification of various source parameters otherwise not accessible, e.g. plasma density and e-loss function [Alt20]. In order to avoid freezing out the Kr, the beam tube is operated at (80 to 100) K.

In order to control the temperature, a novel two-phase Ne-cooling system made from two 16 mm tubes along the central beam tube is used [Gro08]. In normal operation the tubes are half filled with liquid neon and kept at a pressure of 2 bar, which corresponds to the vapour pressure of neon at 30 K. Heat transfer from the beam tube evaporates neon without temperature increase and the helium vapour is re-condensed via a heat exchanger along a gaseous helium loop at about 25 K. In order to adjust the amount of neon evaporation, four heating wires with a capacity of 2 W each are installed along each tube. The system has the advantage that no mechanical pumping is necessary and is described in detail in Ref. [Gro08; Gro09]. Temperature monitoring is done via 24 Pt500-sensors, ensuring the required temperature stability of 0.1 % along the beam tube.

In order to provide the magnetic flux of 191 T cm⁻², three superconducting magnets with a field up to 3.6 T are placed within the cryostat in a liquid helium bath at 4.2 K. An inner shield, supplied by the aforementioned neon heat exchanger, separates the magnets and inner beam tube to keep both temperatures stable. Around the whole system an outer

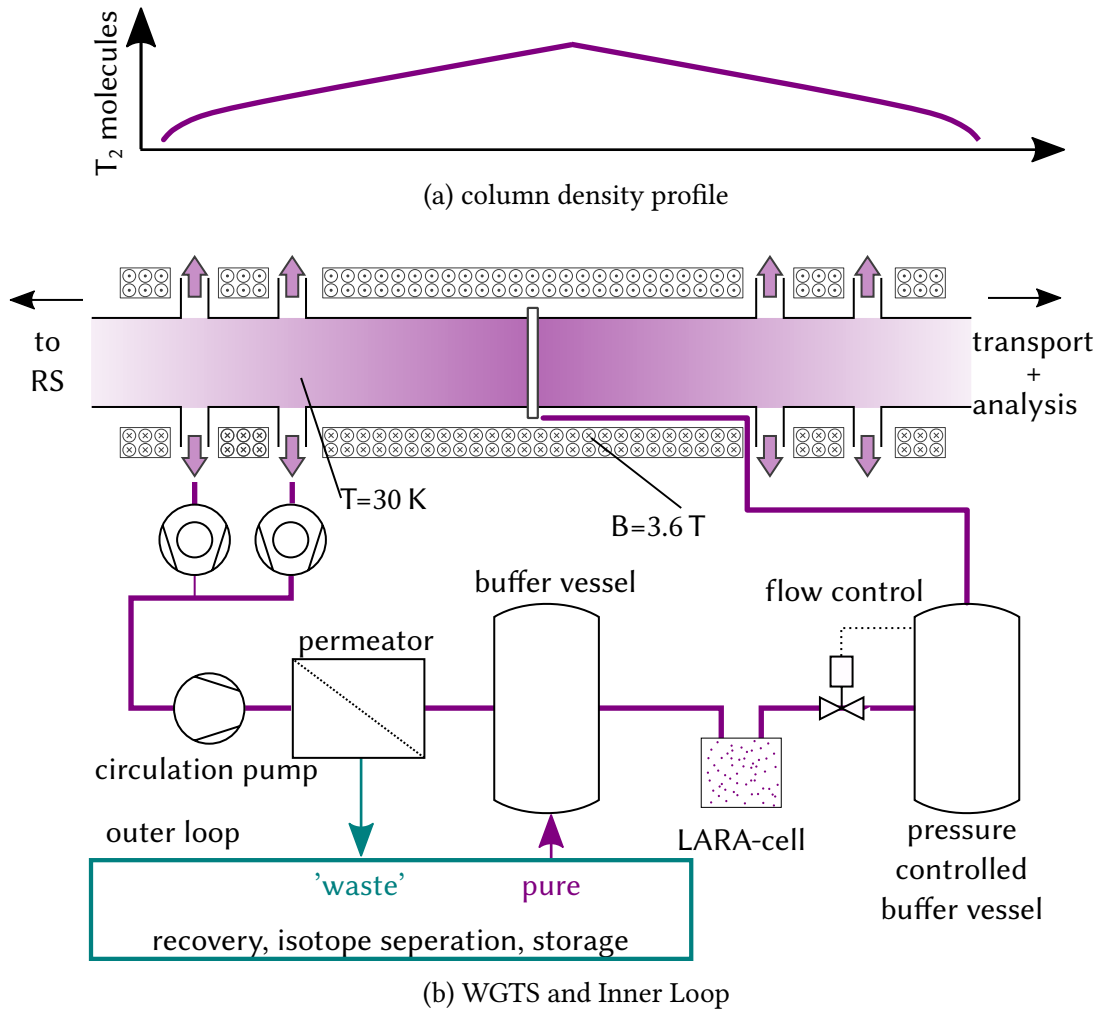


Figure 3.3: Simplified diagram of the WGTS central beamline and the Inner Loop. Tritium is injected into the middle of the WGTS via the pressure controlled buffer vessel and a capillary system. In order to achieve the pressure profile (a), the gas is pumped on both ends via turbomolecular pumps (here only two are shown for clarity). Decay-helium and impurities are removed by a Pd-permeator and the gas composition is subsequently monitored via a LARA-system. The impurities are processed in the Outer Loop and the recycled gas is re-injected into the buffer vessel. Figure based on Ref. [Ake20b].

shield at 77 K, operated with liquid nitrogen, reduces the heat load from the cryostat wall, which is at room temperature.

The tritium gas is provided via the *Inner Loop*: the general flow chart of the Loop system is given in Figure 3.3 [Kaz08b; Stu10a; Pri15]. In order to achieve the stable injection rate on a 0.1 % level, the tritium is transferred from a pressure controlled buffer vessel. For the purpose of avoiding thermal load inside the cryostat the injection capillary is thermally coupled to the two-phase neon cooling system. The tritium pumped out of the WGTS passes through a Pd-permeator to remove decay helium and impurities like methane from wall interaction [Kaz08b]. These contaminants are transferred to the *Outer Loop*, where the gases are separated and the remaining tritium content recouped [Wel17]. Processed gas together with stored tritium gas from the TLK infrastructure is re-injected into the Inner Loop via a buffer vessel.

In order to verify a tritium content of at least

$$\epsilon_T > 95 \%, \quad (3.6)$$

the gas is pumped through the LARA-cell and constantly monitored via the optical LARA system before transferred to the pressure controlled buffer vessel [Ake20b]. Since composition fluctuations are a major uncertainty in neutrino mass measurements, the gas composition needs to be monitored with 0.1 % precision. The operation and calibration of LARA systems is part of this thesis and will be discussed in detail in the next chapter (see Chapter 4). The whole loop system is capable of a throughput of up to 40 g tritium per day in normal operation [Wel17].

3.2.2 Calibration and monitoring section

Upstream of the WGTS is the RS, which contains several calibration and monitoring devices for the WGTS column density and the overall beam line performance.

The beamline is terminated by the rear wall, a Au-plated stainless steel disc with 14.5 cm diameter. A superconducting magnet of up to 4.7 T is mounted behind the rear wall to ensure that the rear wall is hit by the whole magnetic flux tube originating from the WGTS; thereby the plasma potential should be defined via the rear wall potential [Ang04; Röl15b; Kuc18]. Hence the work function of the rear wall has to be homogeneous with temporal and spatial fluctuations of less than 20 mV [Sch16]. In order to remove built-up space charges in the plasma, the rear wall can be illuminated by UV light to create low-energy electrons via the photoelectric effect.

The source activity is monitored via two Beta Induced Xray Spectrometry (Bixs) sensors [Röl15b]. The incoming β -electrons are stopped within the Au-surfaces and emit the corresponding bremsstrahlung. These X-rays are transmitted via two Be-windows, which are translucent for this energy region and detected via a Silicon Drift Detector (SDD) detector. The acquired bremsstrahlung spectrum intensity is proportional to the source

activity and allows monitoring with a sensitivity of 10^{-3} in less than 1000 s [Röl15b]. An additional design for a Bixs inline monitoring cell, which was used within this work, is given in Section 5.4.3.

For measurements of the column density inside the WGTs and energy loss function throughout the beamline, a dedicated electron gun is installed on the far end of the RS [Bab14]. The e-gun produces monoenergetic electrons by UV illumination of a cathode and subsequent acceleration via electrodes. These electrons are magnetically guided into the beam tube via a 5 mm aperture in the rear wall. The beam offers an energy width of ~ 0.2 eV and a pitch angle of less than 4° [Bab14].

3.2.3 Transport section

The transport section has to fulfil three tasks:

- (i) Reduce the tritium flow rate towards the spectrometer in conjunction with the WGTs by 14 orders of magnitude,
- (ii) Adiabatically guide the electrons towards the SDS,
- (iii) Block and analyse ions travelling in the same direction.

These capabilities are provided by two system sections:

DPS2-F: The DPS2-F beam tube is made up from five segments each tilted by 20° to its neighbouring element, arranged in an ‘ Ω ’-shape. Each element is enclosed by a superconducting magnet with a field strength of up to 5.7 T [Are18b]. Between the elements, pump ports with a total of four turbomolecular pumps continuously transfer the gas to the Loop system for recycling.

Since the final state of the molecular tritium decay is a charged (^3HeT)⁺ ion, different ions like T_2^+ , T_3^+ , T_5^+ , ... can form via ionisation or chemical processes [Ubi09]. These ions are guided in the same way as the electrons and can reach the spectrometer, where their subsequent decay would cause an unacceptable background rate as well as contamination of the components [Ang04]. For ion blocking and removal, the Dps deploys two ion-removal aids:

- Two ring electrodes set on a positive blocking potential,
- Four dipole electrodes to deflect the reflected ions from the flux tube via the $\vec{E} \times \vec{B}$ drift towards the wall where they are neutralised.

During the First Light and tritium campaigns, this dual ion blocking procedure was successfully tested [Hac17; Kle19b; Are18c].

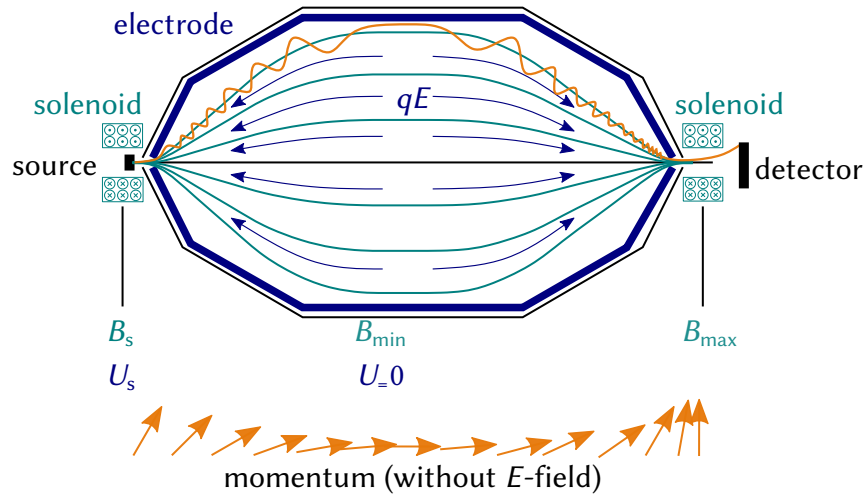


Figure 3.4: Working Principle of a MAC-E filter. The minimum of the magnetic field coincides with the maximum of the retarding electric potential, the so-called analysing plane. Figure based on Ref. [Ste13].

Cryogenic Pump Section (Cps): The second part consists of a similar Ω -shaped beam-line section made from five segments tilted by 15° . In contrast to the Dps the segments are placed inside a cryostat and cooled down to the level of 3 K via liquid helium. The electrons are again adiabatically guided via magnetic fields, and the elements are tilted to increase the probability that any neutral molecule hits the inner beam tube wall. The inner surface is Au-plated and covered with an Ar-frost layer, acting as a cold trap for the tritium molecules via cryosorption [Kaz08a; Gil10; Jan15]. After 60 d of KATRIN tritium operation, the Cps accumulates a maximum of $3.7 \cdot 10^{10}$ Bq and requires regeneration. The beam tube temperature is increased and the system purged with helium, removing the argon together with the tritium. Afterwards a new layer of Ar-frost is prepared with details found in Ref. [Jan15; Röt19]. During the first campaigns, measurements and simulations demonstrated that the effective reduction factor exceeded the totally required 14 orders of magnitude of tritium flow reduction [Röt19].

3.2.4 Spectrometer and detector section

Both spectrometers of KATRIN are operated as Magnetic Adiabatic Collimation combined with Electrostatic Filtering (MAC-E) filters to analyse the β -electron energy in order to achieve the required energy resolution. The detector principle was first proposed in 1980 [Bea80] and instrumentation based on this principle was already successfully deployed in previous neutrino mass experiments [Kra05; Ase11]. In general, the filter consists of a vacuum vessel combined with two strong magnets arranged as shown in Figure 3.4. The resulting filter displays the following properties, making it particularly suitable for the measurement principle of KATRIN:

(i) Adiabatic guidance of electrons:

The arriving electrons perform cyclotron motions around the magnetic field lines with their kinetic energy split between a transverse and longitudinal component according to

$$E_{\text{kin}} = \frac{|\vec{p}|^2}{2m} = E_{\parallel} + E_{\perp}. \quad (3.7)$$

This is the result of the isotropic character of the β -source in the WGTs with the angle θ between the magnetic field lines and decay direction. The transverse energy of a cyclotron motion for an electron with magnetic moment μ and constant Lorentz factor γ in a magnetic field B is given by

$$\mu = \frac{E_{\perp}}{B} = \text{const} \quad (3.8)$$

Hence, in order to minimise E_{\perp} , the magnetic field strength needs to be minimised as well. This is done by the strong magnetic field at the spectrometer entrance, which drops by several orders of magnitude towards the middle of the MAC-E filter unit. Since the magnetic moment is given by [Hak04]

$$\vec{\mu} = \frac{e}{2m_e} \vec{L}, \quad (3.9)$$

it is maintained based on the conservation of angular momentum \vec{L} . Due to energy conservation, all perpendicular energy is transformed into the parallel energy component at the middle of the spectrometer, the so-called *analysing plane*. As the perpendicular component should be close to zero at the analysing plane, this allows for the highest possible energy resolution.

In reality the magnetic field B_A does not vanish completely, limiting the energy resolution of the MAC-E filter depending on the residual magnetic field to

$$\frac{\Delta E}{E} = \frac{B_A}{B_{\text{max}}}. \quad (3.10)$$

For the Main Spectrometer this results in an energy resolution of $\Delta E = 0.93$ eV at 18.6 keV [Sei19].

(ii) Electrostatic filter:

The total electron energy is analysed by applying a negative high potential U_0 to the spectrometer parallel to the magnetic field lines, creating a high-pass filter. Only electrons with an energy of $E_{\parallel} > |qU_0|$ can pass the potential barrier and continue to the detector. As mentioned before, this method only allows to measure an integral energy spectrum since all electrons with sufficient energy can pass the filter. In order to acquire the shape of the β -spectrum, the voltage U needs to be scanned accordingly [Kra05; Ang04; Kle19a].

Additional effects like magnetic trapping, background reduction as well as the general response function need to be considered in the spectrum analysis. For a detailed description, see [Val10; Frä11; Gro15; Kra16; Sei19].

Pre-Spectrometer: The main purpose of the Pre-spectrometer is the reduction of the incoming β -electron flux by rejecting most of the lower-energy electrons outside the endpoint region. This is done by a blocking potential of ~ -10 kV. Using the expression for the energy resolution of a MAC-E filter and the maximum field strengths of up to 4.5 T of the used solenoids results in an energy window of $\Delta E = 70$ eV at 18.6 keV. A picoamperimeter connected to the inner electrode system allows *in-situ* monitoring of the residual ion flux into the spectrometer section [Kle19a].

The tandem setup of the spectrometers can lead to Penning traps filling with electrons, increasing the background rate [Val09]. In order to reduce this background, Penning wipers are installed between the two spectrometers [Pra11; Pra12].

In order to achieve the necessary ultra-high vacuum conditions, several turbomolecular pumps and non-evaporable Getter (NEG) sorption layers are deployed in both spectrometers [Are16].

Main-Spectrometer: Based on the constraints imposed by target sensitivity and required sensitivity, the main spectrometer is a vacuum vessel, with a length of 23 m and a diameter of 10 m, which has a total volume of 1240 m³. The whole vessel can be heated up to 200 °C to reduce the outgassing rate from the inner surface.

Inside the vessel a double layer of electrodes is installed in order to provide the necessary retarding potential as well as reduce the background rate originating from the vessel walls [Har15]. The spectrometer is surrounded by 15 air coils to adjust the magnetic field gradient along the main axis. An additional 26 current loops are installed to compensate the earth magnetic field and stray fields of the components in the vicinity of the spectrometer. These fields are constantly monitored via two mobile and 36 stationary Hall sensors [Erh18].

Focal Plane Detector: Before reaching the detector, the electron flux is bundled by a pinch magnet with 6 T and accelerated by a 10 keV electrode towards the sensor plane. The detector is a segmented silicon PIN diode with sensitive area with a diameter of 90 mm, divided into 12 rings of 12 pixel each, and a bullseye of 4 pixels [Sch14b]. This arrangement provides an energy resolution in the 1 keV-range [Ams15]. Not that, in order to achieve the required background rate, the acceleration electrode shifts the electron energy to a region with less detector background and

Monitor-Spectrometer: In order to ensure the stability requirements for the high-voltage are fulfilled (compare Section 3.1.1), an additional spectrometer analogous to the pre- and main spectrometer, is connected to the same high voltage system via a voltage divider [Erh14]. The monitor spectrometer is not used with a tritium source but connected to an implanted ⁸³Rb/^{83m}Kr source. The K-32 electrons emitted by ^{83m}Kr have a well-defined

energy of 17.83 keV, near the endpoint energy of tritium. By continuously sampling the position of this K-32 line with potential proportional to the beamline spectrometers potentials, any shift due to voltage fluctuations can be corrected [Are18a].

In summary, the KATRIN-setup consists of several complex components with stringent design and operational requirements in order to achieve the design sensitivity of $m(\nu_e) = 0.2$ eV [Ang04; Sei19]. The focus of this work is the provision of high purity tritium gas from the Inner Loop to the WGTs; therefore, some additional sensors and monitoring systems attached to the beamline as well as software tools are not described here, but can be found in the respective publications, e.g. [Chi10; Val11; Bau14; Ams15; Ake20b; Ake20a].

3.3 Composition monitoring of source gas using Raman spectroscopy

As described in the previous section, the stability requirements of the source gas in the WGTs is crucial to reach the target sensitivity of $m(\nu_e) = 0.2$ eV. Besides the already mentioned contributions from Doppler broadening and e^-T_2 -scattering, the absolute values of the molar fractions of other tritiated isotopologues introduce additional uncertainties:

(i) Recoil effect:

Not considered in Equation (3.3) is the recoil of the daughter molecule (${}^3\text{HeT}$)⁺ for T_2 and (${}^3\text{HeH}$)⁺/ $({}^3\text{HeD}$)⁺ for HT/DT due to the emission of the β -electrons. This manifests itself in a reduction of the electron endpoint energy and is given by

$$E_{\text{rec}} \sim E \cdot \frac{m_e}{m_{\text{mol}}}, \quad (3.11)$$

for energies close to the endpoint [Ang04]. Considering the large mass difference of the hydrogen isotopologues, the difference in endpoint energy is significant. In the presence of HT and DT, the measured β -spectrum is actually a superposition of several spectra with different endpoint energies, weighted by the molar fractions of the individual isotopologues.

(ii) Final states distribution:

Considering the energy of the final states of the daughter molecule V_f , Equation (3.3) needs to be modified to

$$\begin{aligned} \frac{d\Gamma}{dE} = & \frac{G_F^2 \cdot |V_{ud}|^2}{2\pi^3} \cdot |M_{\text{nucl}}|^2 \cdot F(E, Z+1) \cdot p_e \cdot (E + m_e) \\ & \cdot \sum_i |U_{ei}|^2 \sum_f P_f \cdot (\epsilon - V_f) \cdot \sqrt{(\epsilon - V_f)^2 - m_i^2} \cdot \Theta(\epsilon - m_i - V_f) \quad , \end{aligned} \quad (3.12)$$

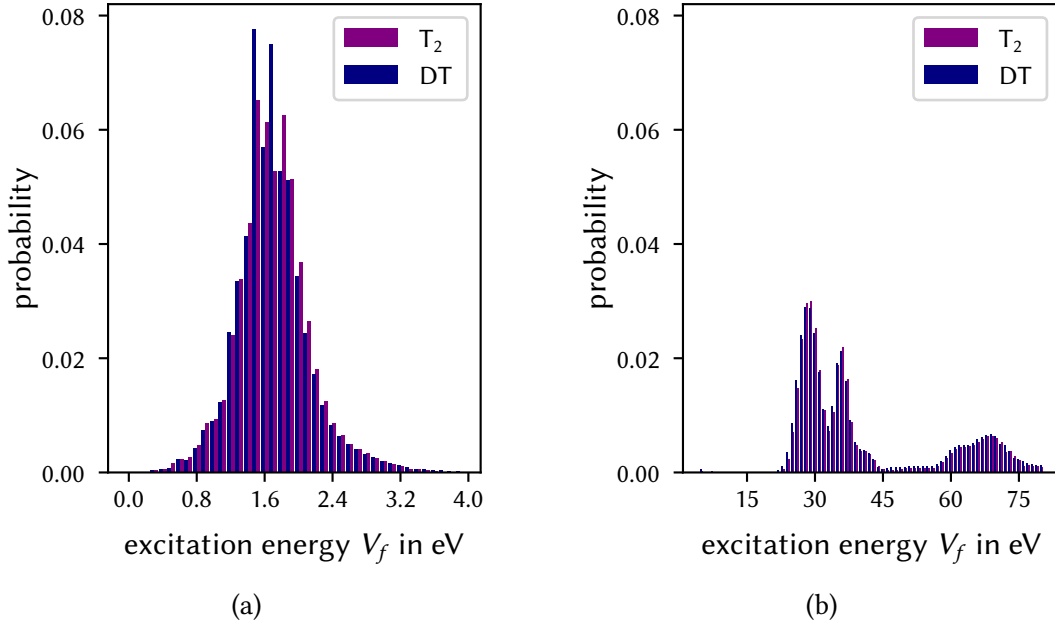


Figure 3.5: Final states distribution of T_2 and DT . The states are summed over the initial angular momentum states $0 < J < 2$ for the population at a temperature of 30 K. This figure is based on Ref. [Dos06] with data from Ref. [Dos06; Dos08].

including the individual transition probability P_f for each final state. As shown in Figure 3.5, the lowest rotational and vibrational excitation energies (see Chapter 4) are about 2 eV and can be excited by the nuclear recoil [Dos06]. Again, this distribution is specific for the individual isotopologue due to the large mass difference and thus the source composition affects the measured β -spectrum.

Due to gas processing in the Inner Loop as well as gas-wall interactions during transfers, HT and DT will be present in the source gas (see Chapter 5 and Ref. [Stu10a]). In order to consider and correct for these effects, both the overall tritium fraction ϵ_T as well as the ratio

$$\kappa = \frac{c_{DT}}{c_{HT}} \quad (3.13)$$

must be constantly monitored as an input parameter to the gas dynamical model of the WGTs [Käf12; Höt12]. More details on the necessary precision and trueness requirements of KATRIN and the current achievements are given in the next chapter (Chapter 4).

Raman Spectroscopy is an optical analysis method based on analysing the scattered light from a sample excited by a laser light source. Depending on the isotope specific energy level transitions, the shifts in the scattered light contains information for identification and quantification of the molar fraction. Due to the large mass difference, these shifts are prominent for the hydrogen isotopologues, making LARA a suitable tool for the source gas monitoring required by KATRIN:

1. All six hydrogen isotopologues can be identified simultaneously and unambiguously [Stu10b].
2. It offers contact-free and in-line gas sampling. This avoids taking a radioactive sample that need to be disposed of afterwards [Fis14].
3. Other than the sample cell, no components come in to contact with tritium, making the system easy to maintain and operate with tritium.
4. The system has no moving or mechanical parts, providing highly reliable monitoring during the KATRIN measurement campaigns [Ake20b].

In the next chapter, the basics of Raman spectroscopy of hydrogen isotopologues and the setup of the system used at KATRIN are described. Besides the already excellent performance of the system during the last campaigns [Wel17; Wel20; Ake20b], open questions related to calibration remained; the work described in this thesis is meant to fill these gaps and thus contribute to the overall goal of KATRIN to measure the neutrino mass.

4 Overview of the Laser-Raman-Systems (LARA) used for KATRIN

Raman spectroscopy proved to be a suitable tool for gas composition monitoring crucial for the WGTs operation in KATRIN, offering contact-less, in-line, non-destructive and near real-time sampling of all six hydrogen isotopologues [Ake20b]. In the first part of this chapter, the theoretical basics of molecular transitions and the resulting spectrum of Raman scattered light are discussed. Subsequently, the experimental setup of the system used for quantitative composition measurements at KATRIN is described and the applied calibration strategy to achieve quantification is outlined. The chapter closes with associated issues currently open and how this work helps to address the remaining questions for successful LARA-system deployment as well as reduction of calibration uncertainty.

4.1 Introduction to quantitative Raman spectroscopy

In this section, the scattering interactions between diatomic molecules and photons are covered. In 1923, the inelastic scattering of photons from molecules was predicted by Smekal [Sme23] and experimentally validated by C. V. Raman and K. S. Krishnan [Ram28]; for this work C. V. Raman was awarded the Nobel Prize in physics in 1930 [Nob20a].

On account of the inelastic scattering process, energy is transferred between the photon and molecule, the latter changing its excitation state. The energy difference between the initial state ‘i’ and final state ‘f’ is linked to the photon energies expressed in either wavenumber $\tilde{\nu}$ or wavelength $\lambda = 1/\tilde{\nu}$:

$$\begin{aligned}\Delta\tilde{\nu}_{if} &= |\tilde{\nu}_L - \tilde{\nu}_s| = \left| \frac{1}{\lambda_L} - \frac{1}{\lambda_s} \right| \\ &= \frac{1}{hc} (E_i - E_f).\end{aligned}\tag{4.1}$$

Here, the molecule is excited by a laser of wavelength λ_L , leading to a scattered wavelength λ_s . In order to compare the experimentally derived wavelength representation, which is usually conducted in air, to the wavenumber quantum representation in vacuum, the refraction index of air needs to be considered via:

$$\lambda_{\text{air}} = \frac{\lambda_{\text{vac}}}{n(\lambda_{\text{vac}})}\tag{4.2}$$

Due to the quantised nature of the molecular energy levels, only discrete changes in energy are possible. The resulting change in photon energy is called the Raman shift and gives insight into both abundance and structural properties of the molecule (see e. g. [Jon19]).

This section gives an overview of the different energy excitation levels relevant for calculating the Raman shifts of hydrogen molecules and the derived Raman spectrum observed when irradiated with a monochromatic light source. It concludes with a description of how the spectra can be evaluated quantitatively to use this method for gas composition monitoring.

4.1.1 Rotational and vibrational states in diatomic molecules

The following introduction to molecular excitation and the Raman effect uses a semi-classic approach and is based on the textbooks written by LONG [Lon02], ATKINS et al. [Atk06], TELLE et al. [Tel07] and HERMANN HAKEN [Her06] and HAKEN et al. [Hak13]. Although a full quantum mechanical description would account for energy levels that are more precise, these are not warranted by the experimental precision and resolution necessary for the work described here.

In order to understand the structure of the Raman spectrum obtained for the six hydrogen isotopologues (H_2 , HD, D_2 , HT, DT and D_2), a conceptual description of the energy levels of diatomic molecules is introduced.

In general, the possible modes of excitation include rotation, vibration and electronic states. Due to their respective energy scale necessary for excitation, only the former two are considered, while electronic excitation is outside the energy range and thus omitted (see [Sch87; Hub79]).

Rotational energy states: A generic model for the rotating, diatomic molecule is the rigid rotator, assuming the two nuclei are connected via a massless rod fixed at the equilibrium distance R_E rotating around the centre of mass. The quantised eigenenergy spectrum $\tilde{F}(J)$ for a given rotational quantum number J is given by

$$\tilde{F}(J) = B \cdot J \cdot (J + 1) \quad B = \frac{h}{(8\pi^2c) \cdot \Theta} \quad (4.3)$$

for $J = 0, 1, 2, \dots$ with the mass-dependent moment of inertia Θ . Equation (4.3) is derived from solving the Schroedinger equation for potential energy $V = 0$, and exploiting the transformation from energy Eigenvalues (in eV) to energy values (in cm^{-1} , i.e. $\tilde{F} = E/hc$)

This model is a suitable but coarse approximation, which is not sufficient to account for the centrifugally stretching of the internuclear distance R at higher J -values.

This can be corrected by replacing the rod with a spring, describing the stiffness of the connection via a spring constant k . As a consequence of this force constant, the system

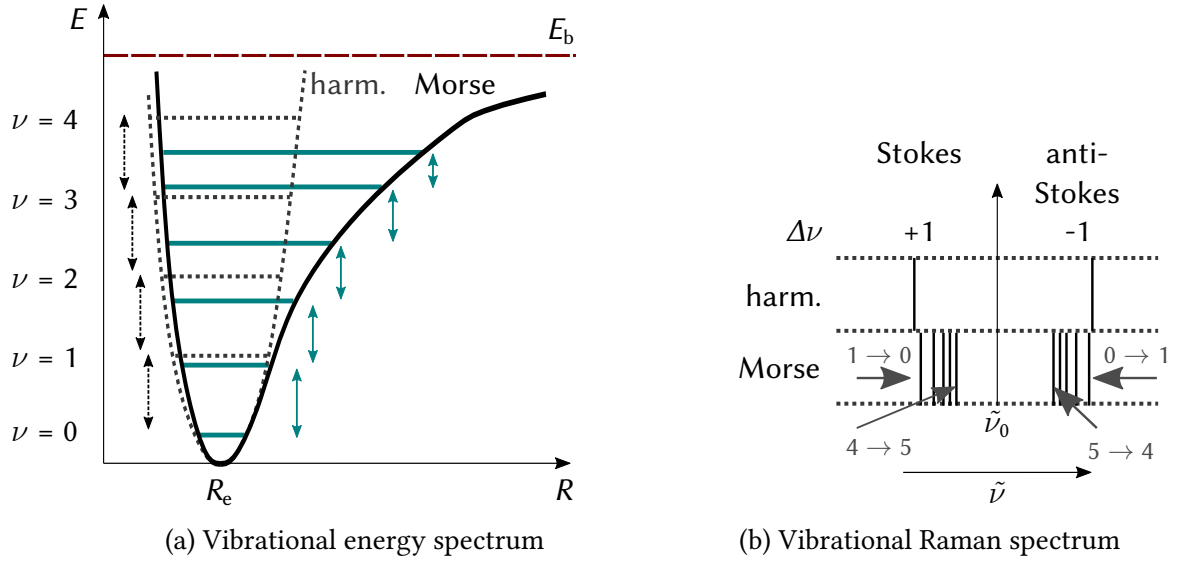


Figure 4.1: Vibrational energy levels of a diatomic molecule in an anharmonic Morse potential. In contrast to the equi-distant levels in the quadratic potential, the level distance compresses for the Morse potential for increased distance from the equilibrium distance R_e . The variable energy differences lead to multiple lines in Raman spectroscopy.

experiences (quadratic) potential energy $E_{\text{spring}} = 1/2k(|R|-R_e)^2$. Solving the Schrodinger equation including this potential energy, and applying a Taylor expansion of small displacements around the equilibrium distance R_e , in first-order approximation the modified term values are given by

$$\tilde{F}(J) = B \cdot J \cdot (J + 1) - D \cdot J^2 \cdot (J + 1)^2 \quad (4.4)$$

with the so-called centrifugal constant D . Even though higher order correction terms can be added, which results in better energy precision, these are not relevant within this work.

Vibrational energy states: The general approach to describe the vibrational states of a diatomic molecule is an approximation of the harmonic oscillator, assuming a linear restoring force between the nuclei. This results in an energy spectrum

$$\tilde{G}(v) = \omega_e(v + 1/2) \quad \omega_e = \frac{\sqrt{k/\mu}}{2\pi c} \quad , \quad (4.5)$$

characterised by the vibrational quantum number $v = 0, 1, 2, \dots$. The constant ω_e contains the reduced mass μ of the molecule as well as the aforementioned spring constant k . This results in an energy spectrum characterised by equi-distant energy levels and is shown in Figure 4.1a.

Similar to the approach to the rotational levels, additional correction terms can be introduced for improved accuracy.

The harmonic oscillator is only valid for small values of v and does not account for the dissociation of the molecules when reaching the finite binding energy E_B of the molecule.

In order to introduce anharmonic oscillations, the Morse potential based on the molecular specific constants E_B , R_E and potential width a can be used, as shown in Figure 4.1a. This results in a first-order correction term which modifies the energy spectrum to

$$\tilde{G}(v) = \omega_e(v + 1/2) - x_e\omega_e(v + 1/2)^2 \quad (4.6)$$

adding the anharmonicity constant x_e . As seen in Figure 4.1b this causes the former equidistant energy levels to compress at higher v which results in varying ΔE for each transition.

Ro-vibrational energy states: As already indicated by the common spring constant k , the rotational and vibrational excitations are not decoupled from each other, i.e. the influence of rotational excitations need to be considered in vibrational levels and vice versa. In general, this is necessary for Raman applications beyond pure rotational spectroscopy.

For accurate rotational-vibrational energy states, the increase in the mean internuclear distance $\langle R \rangle$ for higher v introduced by the Morse potential, leading to a shift in the rotational energy levels, needs to be considered.

Since the vibrational energy levels are commonly two to three orders of magnitude more energetic, the coupling is, in general, expressed as a functional dependence of the rotational constants B and D on the vibrational quantum number v . Assuming a Morse potential and only including first order corrections this substitutes

$$B \mapsto B_v = B - \frac{\alpha}{2}(v + 1/2) \quad (4.7)$$

$$D \mapsto D_v = D - \beta(v + 1/2) \quad (4.8)$$

with molecular specific constants α and β .

This results in the general expression for the energy levels \tilde{T} (in cm^{-1}) for coupled rotational-vibrational excitation of a diatomic molecule

$$\tilde{T}(v, J) = \tilde{G}(v) + \tilde{F}(v, J) \quad (4.9)$$

$$= \omega_e(v + 1/2) - x_e\omega_e(v + 1/2)^2 + B_v(J)(J + 1) - D_v J^2(J + 1)^2. \quad (4.10)$$

This equation is sufficient to calculate the energy levels for the transitions relevant in the studies performed in this work. Further correction details can be found in Ref. [Her89].

4.1.2 Basic principles of the Raman effect

Based on the term values established in the section above, light can interact with the molecule via absorption, emission or scattering. The Hamiltonian for general interactions between the electric dipole moment \vec{p} of the molecule and the electric component $\vec{\varepsilon}$ of the photon field is given by

$$H = -\vec{p} \cdot \vec{\varepsilon} \quad (4.11)$$

In case of a permanent dipole moment one photon can be absorbed or emitted in a first order process if the condition $\Delta E = h \cdot \nu$ is fulfilled.

For photon scattering neither a permanent dipole moment is necessary nor must the energy condition be fulfilled. In this case the incident photon field polarises the molecule and generates an induced linear dipole moment in addition to any permanent one, according to

$$\vec{p}_{\text{ind}} = \alpha \cdot \vec{\varepsilon} \quad (4.12)$$

which then interacts with the electric field according to Equation (4.11). The resulting second order process is characterised by the polarisability tensor α describing how strongly the specific molecule reacts to an external field.

Using a classical approach as outlined in Ref. [Lon02], it is assumed that the molecule is free to vibrations around the equilibrium position but does not rotate. In this case, a Taylor expansion of the components $\alpha_{p,\sigma}$ with respect to the normal coordinates Q_l, Q_k of a vibration yields

$$\alpha_{p,\sigma} = (\alpha_{p,\sigma})_0 + \sum_k \left(\frac{\partial \alpha_{p,\sigma}}{\partial Q_k} \right)_0 Q_k + \frac{1}{2} \sum_k \sum_l \left(\frac{\partial^2 \alpha_{p,\sigma}}{\partial Q_k \partial Q_l} \right)_0 Q_k Q_l + \dots \quad (4.13)$$

where the index '0' indicates the equilibrium state.

Again, neglecting higher than linear orders and assuming only a single vibration mode $k = i$ simplifies Equation (4.13) to

$$\alpha_i = \alpha_0 + \alpha'_i Q_i, \quad (4.14)$$

using the equilibrium and derived polarisability tensors α_0 and α_i .

Assuming a simple harmonic oscillation around the equilibrium state allows one to insert Equation (4.14) in Equation (4.12) which results in

$$Q_i = Q_{i,0} \cos \omega_i t + \delta_i \quad (4.15)$$

with oscillation frequency ω_i and arbitrary phase δ_i . For the irradiating field, one can assume an oscillation given by $\omega_{\text{ext}} \mapsto \vec{\varepsilon} = \vec{\varepsilon}_0 \omega_{\text{ext}}$ which extends Equation (4.12) to

$$\vec{p}_{\text{ind}} = \alpha_0 \vec{\varepsilon}_0 \cos(\omega_{\text{ext}} t) + \alpha'_i Q_{i,0} \vec{\varepsilon}_0 \cos(\omega_i t + \delta_i) \cos(\omega_{\text{ext}} t) \quad (4.16)$$

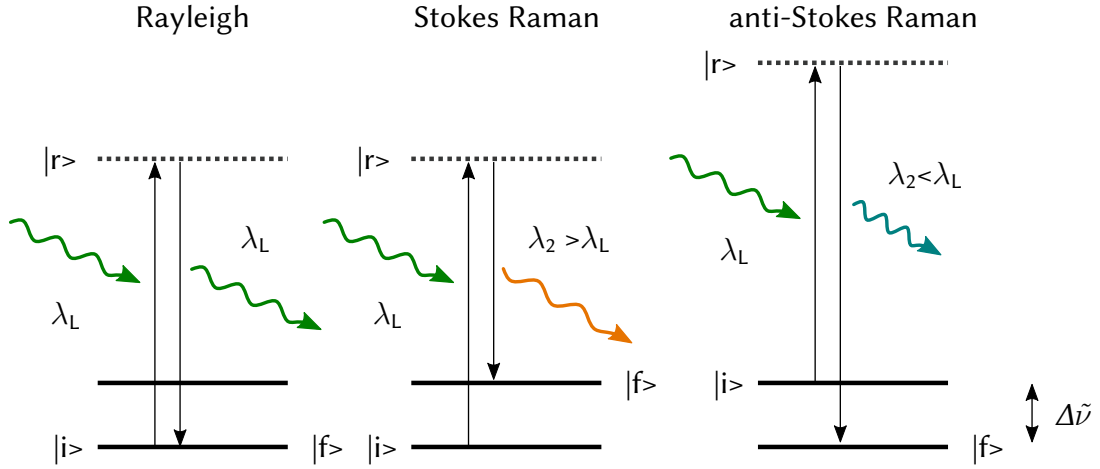


Figure 4.2: Overview of Rayleigh and Raman photon scattering by molecules. For a laser source with constant wavelength λ_L the laser photon connects with the initial state $|i\rangle$ to a transient ‘virtual’ state $|r\rangle$. Depending on the energy of the final state the molecule either loses, gains or keeps its energy. This energy difference corresponds to a wavelength shift of the scattered photon.

Using the trigonometric identity $\cos A \cos B = \frac{1}{2}(\cos(A+B) + \cos(A-B))$ this can be transformed to

$$\vec{p}_{\text{ind}} = \alpha_{\text{Ray}} \vec{\epsilon} \cos(\omega_{\text{ext}} t) + \alpha_{\text{Ram},i} \vec{\epsilon} \cos((\omega_{\text{ext}} \pm \omega_i) t \pm \delta_i) \quad (4.17)$$

$$\alpha_{\text{Ray}} = \alpha_0 \quad (4.18)$$

$$\alpha_{\text{Ram},i} = \frac{1}{2} \cdot \alpha'_i Q_{i0} \quad (4.19)$$

This expression describes the three possible dipole moments originating from the interaction with an external photon field as shown in Figure 4.2:

1. Rayleigh scattering without change of photon energy (ω_{ext})
2. Raman Scattering in which the molecule can
 - (a) gain energy via Stokes Raman ($\omega_{\text{ext}} + \omega_i$)
 - (b) loose energy via anti-Stokes Raman ($\omega_{\text{ext}} - \omega_i$)

It is important to mention that the Raman-related dipole moments only contribute if at least one of the components of the derived polarisability tensor α'_i is non-zero:

$$(\alpha'_{p,\sigma})_i = \left(\frac{\partial \alpha_{p,\sigma}}{\partial Q_i} \right)_0 \neq 0. \quad (4.20)$$

Although these statements are derived via classical approximations, it is in principle also valid using the quantum mechanical approach by replacing the polarisability tensors with their corresponding transition polarisability tensors (see Ref. [Lon02] for detailed derivations).

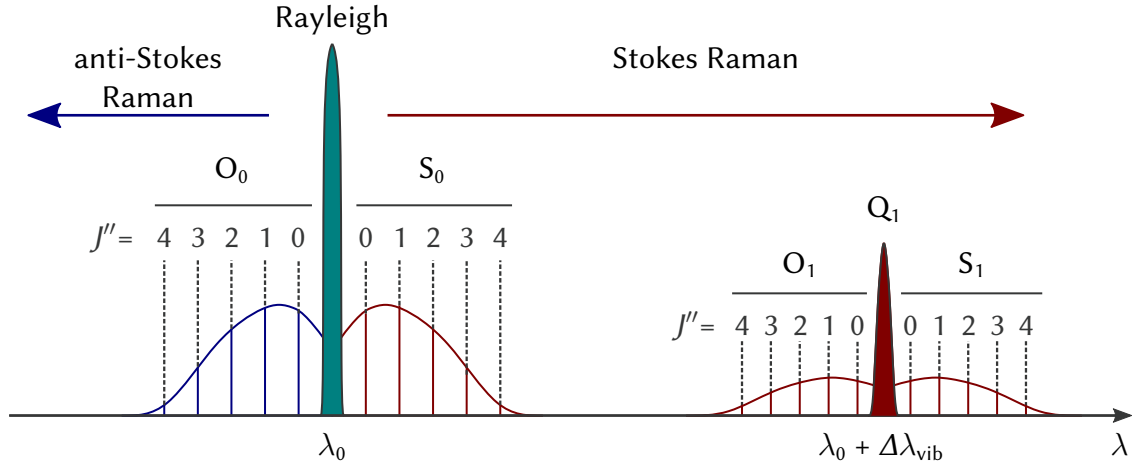


Figure 4.3: Spectrum of generic photon scattering on a diatomic molecule. The S_0 -, O_0 -, S_1 - and O_1 -branches exhibit (normally) resolved rotational substructure, annotated with the quantum number J'' of the initial energy level; the Q_1 -branch is much more compressed, and its structure is normally not resolved. Note that the red ‘envelop’ lines represent the (thermal) level-population probabilities.

Along with the general process description, certain selection rules need to be obeyed in order to calculate a scattering spectrum. In each process the photon carries a spin of $S = 1$, which leads to a rotational selection rule of $\Delta J = 0, \pm 2$ for the associated lower state J'' and excited state J' . For the vibrational transitions, in case of the harmonic oscillations, a selection rule of $\Delta v = 0, \pm 1$ is given. Although overtones with $\Delta v = \pm 2, \pm 3, \dots$ are in general possible, these are heavily suppressed [Dem10]. A summary of the selection rules and the associated nomenclature scheme are collated in Table 4.1, while a generic Raman spectrum for a diatomic molecule is shown in Figure 4.3.

4.1.3 Raman line intensity

Based on the selection and transition rules derived in the previous section, the parameters determining the Raman line intensities can be obtained. For quantitative composition monitoring on tritium-containing gases, these line strength functions are essential and have a significant impact on the calibration effort.

According to [Lon02], the intensity of Raman scattered light is expressed as

$$I(\varphi, \theta)_{p^s, p^i} = k_{\tilde{\nu}} \cdot \tilde{\nu}_s^4 \cdot n_i \cdot \Phi(\varphi, \theta, \alpha, \gamma)_{p^s, p^i} \cdot \mathcal{I} \quad (4.21)$$

with the individual factors described below. This general expression is only valid if the power of the scattered light is measured. In case the number of scattered photons is monitored, which is usually the case for most detector setups, the expression needs to be modified [McC06]. The signal intensity for a given molecule and transition is then given by

$$I(\varphi, \theta)_{p^s, p^i} = k_{\tilde{\nu}} \cdot \tilde{\nu}_0 \cdot \tilde{\nu}_s^3 \cdot N_i \cdot \Phi(\varphi, \theta, \alpha, \gamma)_{p^s, p^i} \cdot \mathcal{I} \quad (4.22)$$

Table 4.1: Selection rules and nomenclature for Raman transitions. Depending on the change in vibrational and rotational quantum number, the Raman spectrum shows different branches. The nomenclature within this work is based on Ref. [Lon02], which uses O, Q and S to denote ΔJ and the index of each letter indicates the $\Delta\nu$ value. Vibrational overtone branches with $\Delta\nu \geq 2$ are indexed with the relevant $\Delta\nu$ -value.

$\Delta\nu$	ΔJ	Branch	Raman shift $\Delta\tilde{\nu}$	scattering type
0	-2	O ₀	$-\Delta\tilde{\nu}_{\text{rot}}$	anti-Stokes
0	0	Q ₀	0	Rayleigh
0	2	S ₀	$\Delta\tilde{\nu}_{\text{rot}}$	Stokes
1	-2	O ₁	$\Delta\tilde{\nu}_{\text{vib}} - \Delta\tilde{\nu}_{\text{rot}}$	Stokes
1	0	Q ₁	$\Delta\tilde{\nu}_{\text{vib}}$	Stokes
1	2	S ₁	$\Delta\tilde{\nu}_{\text{vib}} + \Delta\tilde{\nu}_{\text{rot}}$	Stokes

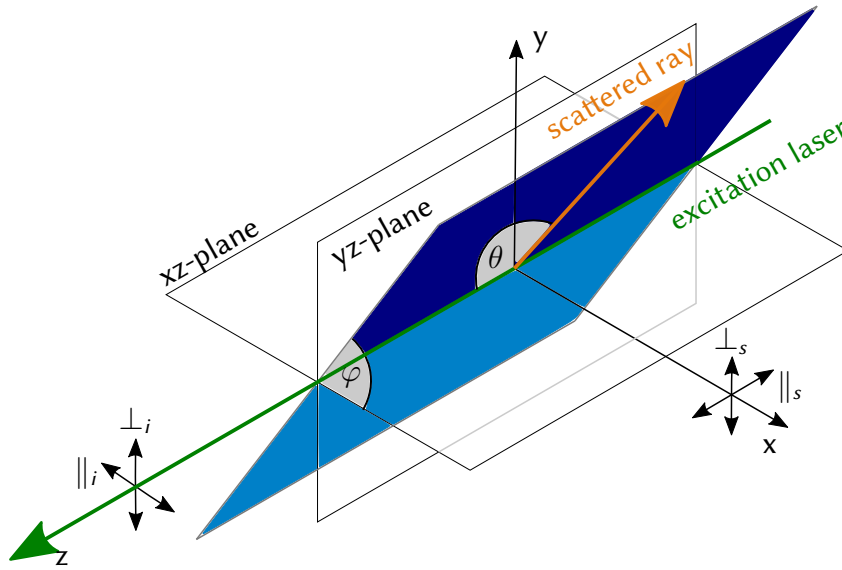


Figure 4.4: Scattering angles for Raman emission relative to the polarisation plane. In order to minimise the collection of non-Raman light, a 90° setup is chosen in this work. Figure adapted from Ref. [Sch13a] with permission from John Wiley & Sons, Inc.

using the following factors:

$(\varphi, \theta)_{p^s, p^i}$: These angles describe the angular distribution between the scattered beam (s) in relation to the scattering plane (i) for a given polarisation state $p = \perp, \parallel$. An visualisation of the angles and planes is given in Figure 4.4.

$k_{\tilde{\nu}}$: A constant given by

$$k_{\tilde{\nu}} = \frac{\pi^2}{\epsilon_0^2} \quad (4.23)$$

including the permittivity of vacuum ϵ_0 .

$\tilde{\nu}_0, \tilde{\nu}_s$: The wavenumbers of the irradiating beam (0) and scattered light (s), which is given by

$$\tilde{\nu}_s = \tilde{\nu}_0 - \Delta\tilde{\nu}_i \quad (4.24)$$

for a given Raman shift for the molecular state i .

N_i : The number of molecules (population) N in an initial state i given by

$$N_i = N \frac{g_i \cdot \exp(E_i/kT)}{Z} \quad (4.25)$$

with

- N : total number of irradiated molecules,
- kT : thermal energy,
- E_i : rotational and vibrational energy of the initial state,
- Z : molecular partition function,
- g_i : statistical weight.

Z is given by summation over all possible populated states j via

$$Z = \sum_j g_j \cdot \exp(-E_j/kT) \quad (4.26)$$

with the Boltzman factor $\exp(-E_j/kT)$ describing the thermal population of the ro-vibrational states. The partition function will become important again at a later stage to obtain the chemical equilibrium constant (see Chapter 6 and Ref. [McQ00] for details).

The statistical weight g_i depends on the individual weights of the vibrational and rotational states according to

$$g_i = g_v \cdot g_{J''} \quad (4.27)$$

In case of a diatomic molecule $g_v = 1$, on account of the non-degeneracy of the vibrational states.

The rotational statistical weight depends on the nuclear spin degeneracy and the quantum number J'' according to

$$g_{J''} = g_N \cdot (2J'' + 1) \quad (4.28)$$

For g_N , the symmetry of the molecule wave function needs to be considered, which takes the nuclear spin statistics of each nucleus into account. Based on the Born-Oppenheimer approximation, the total wave function is given by the product

$$\Psi_{\text{tot}} = \Psi_{\text{spin,nuc}} \cdot \Psi_{\text{el}} \cdot \Psi_{\text{vib}} \cdot \Psi_{\text{rot}} \quad (4.29)$$

of the nuclear spin, electronic, vibrational, and rotational wave functions. For the homonuclear molecules with fermionic nuclei (H_2 , T_2), the wavefunction needs to be anti-symmetric under inversion according to the Pauli principle. In contrast, the wavefunction of the homonuclear molecule with bosonic nuclei (D_2) has to be symmetric. In case of the heteronuclear isotopologues, no parity can be defined, thus $g_N = 1$. A summary of the spin statistics and properties of the hydrogen isotopologues is given in Table 4.2

$\Phi(\varphi, \theta, \alpha, \gamma)_{p^s, p^i}$: The line strength function depends on the polarisation angles on incident and scattered beam. According to [Lon02], the function is given by the isotropic squares of the transition polarisation tensor components. In case of a diatomic molecule, these can be expressed by the mean polarisability $a = 1/3(\alpha_{\parallel} + 2\alpha_{\perp})$ and the anisotropy $\gamma = \alpha_{\parallel} - \alpha_{\perp}$ [Lon02]. Assuming perpendicular polarised irradiating light $p^i = \perp^i$, the line strength functions for $p^s = \perp^s$ and $p^s = \parallel^i$ are described by

$$\Phi(\varphi, \theta, \alpha, \gamma)_{\perp^s, \perp^i} = a^2 \cos(\varphi)^2 + b_{J''}^{(2)} \frac{\gamma^2}{45} (4 - \sin(\varphi)^2) \quad (4.30)$$

$$\Phi(\varphi, \theta, \alpha, \gamma)_{\parallel^i, \perp^i} = a^2 \cos(\theta)^2 \sin(\varphi)^2 + b_{J''}^{(2)} \frac{\gamma^2}{45} (3 + \cos(\theta)^2 \sin(\varphi)^2) \quad (4.31)$$

with the so-called Placzek-Teller factor

$$b_{J''}^{(2)} = \frac{J''(J'' + 1)}{(2J'' - 1)(2J'' + 3)} \quad (4.32)$$

for rotational states J'' in the Q_v branch.

\mathcal{I} : The irradiance in the incident excitation light, which cancels out in relative Raman intensities but plays an important role for the signal-to-noise-ratio.

The intensity expression in Equation (4.22), given in terms wavenumber, can be converted to wavelengths which derives the Raman intensity for a given isotopologue x by

$$I_{\text{Raman},x}(\lambda_s, N_x) = C \cdot \lambda_0^{-1} \cdot \lambda_s^{-3} \cdot N_x \cdot \Phi_x \cdot \mathcal{I} \quad (4.33)$$

Table 4.2: Nuclear properties of hydrogen molecules and their influence on rotational Raman line intensities. For the homonuclear molecule, the spin statistics influence the spin degeneracy of the rotational energy levels and their population. In contrast, the heteronuclear isotopologues are not affected. Based on Ref. [Lon02].

	H ₂ , T ₂	D ₂	HD, HT, DT
Parity of total wave function Ψ	-1	+1	not defined
Nuclear spin of each nucleus	$1/2$	1	$(1/2, 1), (1/2, 1/2), (1, 1/2)$
Number of nuclear wave functions with			
$P = 1$	3	6	-
$P = -1$	1	3	-
Nuclear spin degeneracy g_N			
J'' odd	3	3	1
J'' even	1	6	1

with the following factors:

- Φ_x : line strength function for a fixed polarisation configuration,
- C : all remaining coefficients,
- N_x : molar number.

This equation is used in the subsequent chapters to define a response function, linking the individual line strength of an isotopologue to the corresponding molar fraction.

4.1.4 Raman spectroscopy on hydrogen isotopologues

Since the three hydrogen isotopes display a large relative mass difference, the shifts in molecular energy levels are significant and result in distinct as well as separated lines, making Raman spectroscopy suitable for quantitative composition monitoring of all six hydrogen isotopologues.

In the following section, a brief history of using LARA to monitor tritiated hydrogen molecules is presented. The first published experimental determination of the molecular constants of T₂ was accomplished by EDWARDS et al. [Edw78]. A decade later, VEIRS et al. [Vei87] studied the Raman shifts of all six hydrogen isotopologues with an accuracy better 1 cm⁻¹. At TLK, first experiments using hydrogen isotopologues and tritiated methane were performed by ENGELMANN et al. [Eng92], [Jew97]. During the 90's, a collaboration between the Tritium Engineering Laboratory in Japan and the Los Alamos National Laboratory developed and deployed a LARA-system at the Tritium Systems Test Assembly (TSTA) facility [Oku91; Ohi92; Ohi95; Ohi96].

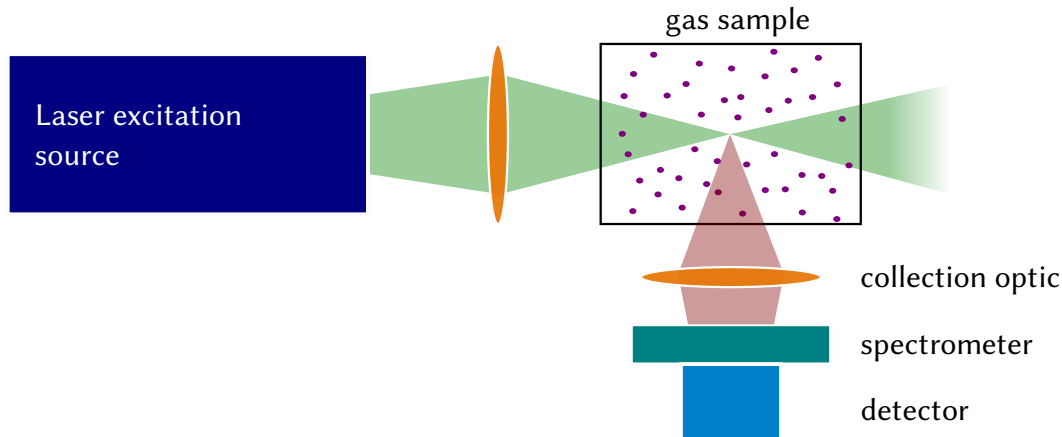


Figure 4.5: Overview of a basic Raman system. A 90°-setup has the advantage of reduced excitation light being scattered into the collection optics. All collection components have an impact on the wavelength-dependant response function of the system necessitating individual calibration.

First developments towards the KATRIN LARA system started by TAYLOR et al. [Tay01]¹ and were extended by LEWIS [Lew07], monitoring a continuous flow of stable isotopologues as proof of principle. In order to meet the design requirements, the experiments were extended to static samples and extensive investigation of systematic effects [Stu10a; Sch11; Fis14]. In 2010 the first operational test, a circulating tritiated gas sample was monitored under KATRIN-like conditions over 60 days, was done within the LOOPINO experiment [Fis11]. During this field test campaign, it was shown that the design relative precision of 0.1 % within 250 s was achieved, which was later improved to 60 s [Sch14a].

The system performed without major issues during the first tritium campaigns of KATRIN [Ake20a], meeting all operational and stability requirements [Ake20b].

Further studies for improved limit of detection and reduced measurement time, using a capillary Raman system, were carried out by RUPP et al. [Rup15a; Jam15; Rup15b; Sch15a].

In order to overcome the limitation of Raman spectroscopy to molecules because of the necessary ro-vibrational transitions, investigations to use electronic excitation of ⁴He induced by β -electrons were started in 2015 with promising results [Sch15b].

Based on these developments and achievements, one can summarise that LARA has become a valuable tool for gas composition monitoring in KATRIN, and further applications and improvements are promising.

The general schematic of a basic LARA-system is shown in Figure 4.5 and typically consists of the following components

1. Excitation laser source,
2. Sample cell,

¹In this work, a proof of principle for hydrogen monitoring using LARA in the context of nuclear fusion was performed. Subsequent sample cells were further developed from this setup.

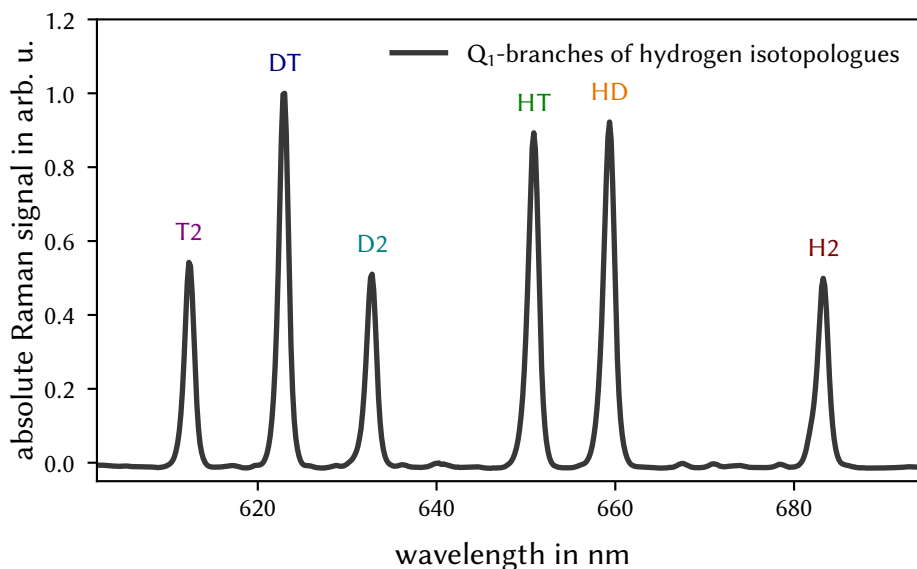


Figure 4.6: Spectrum of the Q_1 -branches in an equi-concentrated sample of all six hydrogen isotopologues. The species can be defined via the line position given by Equation (4.10). Although the sample has equal parts atomic H, D, and T the resulting mixture in chemical equilibrium is dominated by the heteronuclear isotopologues. For details see Chapter 7.

3. Collection optics,
4. Spectrometer,
5. Detector.

For composition monitoring using hydrogen isotopologues, the focus is on the Q_1 -branches with no change in rotational quantum number J , thus $J'' = J'$. These offer several advantages [Sch14a]:

1. Adequate distance between the individual isotopologues for straight forward identification and quantification.
2. Sufficient distance from the laser wavelength typically used in experimental applications of $\lambda_L = 532$ nm.
3. Although the Q_1 -branch has a substructure, this is typically not resolved by a medium resolution recording system. Using the integrated peak intensity offers a higher peak intensity and is virtually temperature independent.
4. Minimal interference from parasitic spectral features, originating from fused silica windows necessary in the setup [Fis14].

A typical spectrum of the Q_1 -branches of all six hydrogen isotopologues, as acquired and analysed within this work, is given in Figure 4.6. As described theoretically, the branches are well separated and suitable for individual peak identification. Although certain overlaps exist, e.g. the $S_1(J=2)$ -line of T_2 overlaps with the Q_1 -branch of DT, these can be corrected for composition monitoring [Stu10b].

In summary, LARA is a valuable technique for monitoring tritiated gas samples offering the following advantages:

1. Only the optical LARA-cell comes into contact with tritiated gas, all other components are outside the second containment for easy adjustment and maintenance (see Section 5.2.3);
2. Unambiguous identification and quantification of all six hydrogen isotopologues;
3. Suitable limit-of-detection and measurement time for near real-time gas sampling.

In the next section, the optimisation of the detection setup and the necessary calibration steps to derive the molar fractions from the recorded spectrum are presented.

4.2 Experimental setup of the KATRIN LARA system

4.2.1 Overview of Components

The development and general setup of the LARA3-system used at KATRIN is well described in SCHLÖSSER et al. [Sch11], SCHLÖSSER [Sch14a], FISCHER [Fis14] and AKER et al. [Ake20b] and thus are only briefly summarised here.

The beam path, shown in Figure 4.7, can be divided into three parts:

- (i) The 532 nm excitation laser beam is guided via mirrors to an optical isolator and a $\lambda/2$ plate. These are necessary to ensure the laser has a single polarisation plane vertically from the breadboard to maximise Raman light intensity. The beam is then focused into the tritium gas filled LARA-cell inside the second containment (details in Chapter 5). After passing through the cell, the beam is back-reflected to increase irradiance of the sample. In order to avoid damage of the laser from the backgoing beam, the optical isolator deflects the beam towards a beam dump as well as a laser power meter and a photo diode for beam diagnostic.
- (ii) The scattered Raman light is collected via the collection optics L3 and L4 which focus the light into a slit-to-slit fibre bundle fixed onto the breadboard. A linear polariser sheet ensures the polarisation plane of the scattered light to unambiguously determine the line strength functions necessary for calibration.
- (iii) Coming from the fibre, the light passes a long pass filter to suppress the laser and Rayleigh light before entering the spectrometer, which projects the spectrum onto the attached CCD detector.

A more in depth description of the setup used in this work and the differences to the LARA3 system is given in the next chapter (Section 5.4.2).

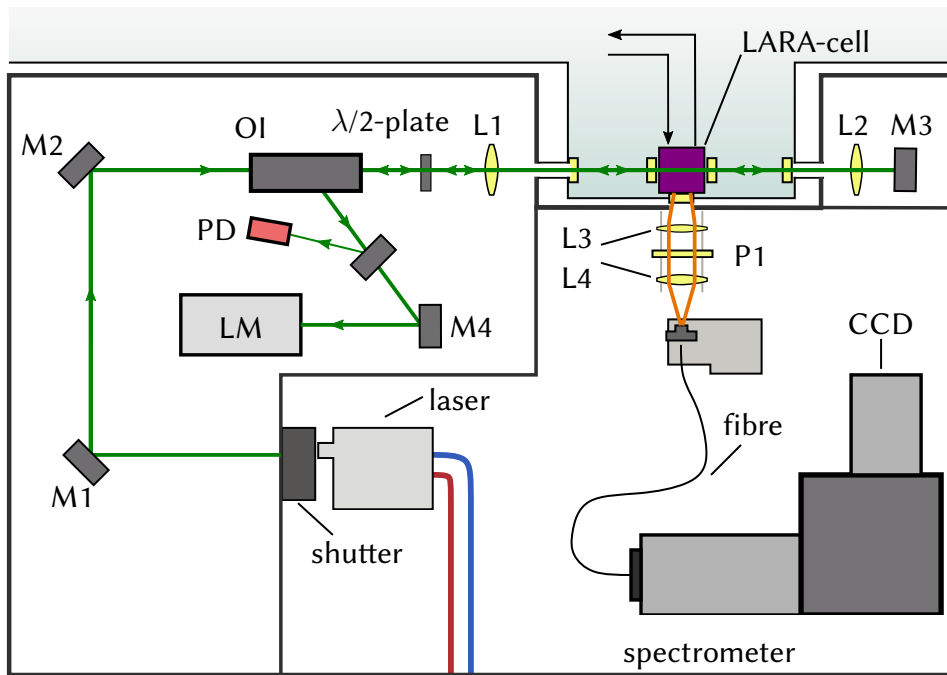


Figure 4.7: Overview of the LARA3 setup used at KATRIN. The excitation laser beam is focused through the LARA-cell before being back-reflected into the cell for increased signal strength. In order to avoid damage of the laser an optical isolator (OI) deflects the backgoing beam into a laser power monitor (LM) and photo diode (PD) for beam monitoring and safety interlocks. Additional components are: M1, M2, M3, M4 = high-reflectance laser mirrors; L1, L2 = focusing lenses; L3, L4 = collection optics and P1 = polarise sheet. Figure based on Ref. [Fis14].

4.2.2 Description of spectrum analysis

In order to convert the raw signal acquired by the CCD into a Raman spectrum suitable for quantitative analysis, several processing steps are performed. All steps are executed within the LARASOFT-software, an in-house development written in LabVIEW. Details of the individual steps and their parameters are described in detail in Ref. [Sch11; Jam13c; Fis14] and [Ake20b] and are only briefly summarised here.

(i) Dead pixel removal:

If a pixel signal constantly deviates significantly from the mean value of the surrounding pixels or demonstrates a high dark current, the pixel is removed from analysis and the mean value of the neighbouring pixels is used.

(ii) Cosmic ray removal:

A passing muon through the CCD-sensor causes a significant increase of a single pixel intensity between two measurements. These temporal changes can be detected and the signal removed [Sch13b].

(iii) Baseline subtraction:

Due to background intensity, light leaks or laser induced fluorescence in the LARA-cell the baseline of the system must be corrected. A Savitzky-Golay Coupled Advanced Rolling-Circle Filter (SCARF) is applied, as described in Ref. [Jam13c].

(iv) Response function correction:

In order to normalise the peak intensities to the corresponding molar concentration the individual sensitivity of the system for each isotopologue must be considered. Details of the response function are given in the next chapter.

For an in-depth review of the performance of the software during the KATRIN measurement campaigns see [Ake20b].

4.3 Calibration strategy for the KATRIN LARA system

Based on Equation (4.22) one can introduce the spectral sensitivity function

$$\eta(\lambda) = \frac{I(\varphi, \theta)_{p^s, p^i, \text{exp}}}{I(\varphi, \theta)_{p^s, p^i}} \quad (4.34)$$

which considers all wavelength dependent transmission and sensitivity properties of the setup. Here the numerator and denominator are associated with the measured and expected (according to Equation (4.21)/Equation (4.22)) intensities, respectively.

Combining this function with the molecular- and transition-specific constants one can define a global response function R of the Raman system

$$I(\varphi, \theta)_{p^s, p^i, \text{exp}} = \underbrace{\eta(\lambda) \cdot k_{\tilde{\nu}} \cdot \tilde{\nu}_0 \cdot \tilde{\nu}_s^3 \cdot \Phi(\varphi, \theta, \alpha, \gamma)_{p^s, p^i}}_R \cdot \mathcal{I} \cdot N_i \quad (4.35)$$

This gives the isotopologue-, transition and experiment-specific response function R_x which connects measured signal strength S_x and molar number N_x for each isotopologue via

$$S_x = R_x \cdot N_x \quad (4.36)$$

This can be simplified to the relative Raman signal intensity that corresponds to the molar fraction of the isotopologue x normalised to the integral signal intensities by:

$$S_{x,\text{rel}} = \frac{S_x}{\sum_{j=1}^n S_j} \quad (4.37)$$

$$= \frac{R_x \cdot N_x}{\sum_{j=1}^n R_j \cdot S_j} \quad (4.38)$$

This has the advantage that inevitable fluctuations in laser power \mathcal{I} and wavelength $\tilde{\nu}_0$ cancel out in the ratio.

The individual response function can be decomposed into two contributions, according to

$$R_x = R_{x,\text{spec}} \cdot R_{x,\text{theo}} \quad (4.39)$$

with

$R_{x,\text{spec}}$: spectral sensitivity of the setup,

$R_{x,\text{theo}}$: theoretical Raman intensity of the individual transition,

which will both be explained in detail in the next section.

This leads to two possible, complementary calibration strategies, which are illustrated in Figure 4.8:

- (i) Separately measuring the experiment specific spectral sensitivity and combining that with the general theoretical intensity of the isotopologues;
- (ii) Using accurate gas samples of all hydrogen isotopologues to determine the individual response function.

For method (ii), it is essential to analyse a mixed gas sample, not a single pure gas species. Although pure gases are commercially available for the homonuclear stable isotopologues H_2 and D_2 as well as potentially feasible for HD [Wen49; Mir20], an isotopically pure sample does not provide insight into the *relative* calibration factors needed, see Equation (4.38). The obtained single sensitivity factor would be sensitive to response function variations, e.g. laser power fluctuations, which cancel out in relative intensity measurements. In addition, isotopically pure samples of all tritiated isotopologues are neither available nor stable (for details see Section 7.3.1).

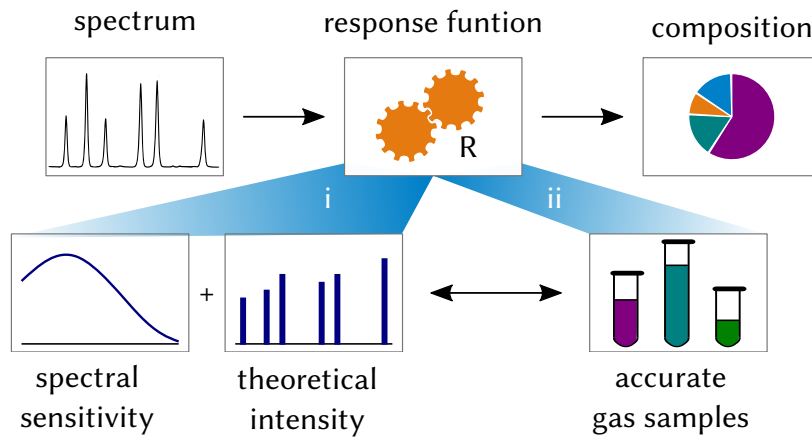
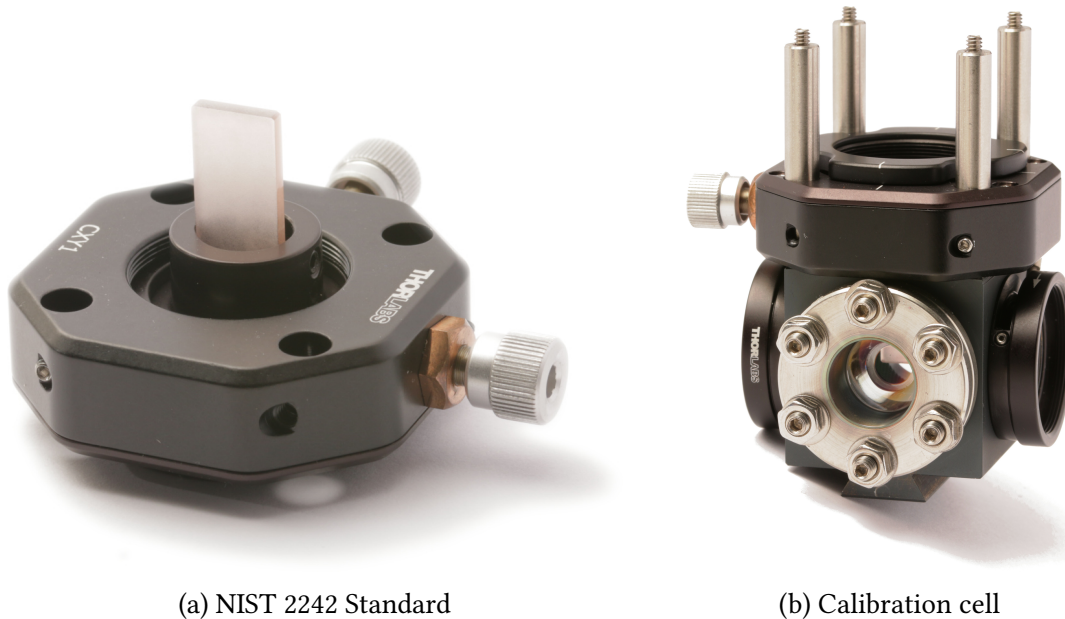


Figure 4.8: Calibration strategy for LARA-systems for KATRIN. Method (i) depends on a luminous spectral standard and known theoretical intensity factors for each isotopologue. While the calibration via (i) can be performed with the setup in place, it is based on ab-initio calculations and extrapolations [Ryc80; Sch87]. Thus, method (i) needs to be verified via method (ii) with accurate gas samples, which is the main objective of this work.



(a) NIST 2242 Standard

(b) Calibration cell

Figure 4.9: Image of NIST traceable luminous spectrum 2242 and calibration cell holder. The standard (a) generally used for system calibration [Etz05] can be mounted (b) in place of the gas sample cell to evaluate the systems spectral sensitivity. Note that the standard has been polished at KIT due to the excitation beam entering from the lateral side in contrast to the intended front illumination [Sch15c].

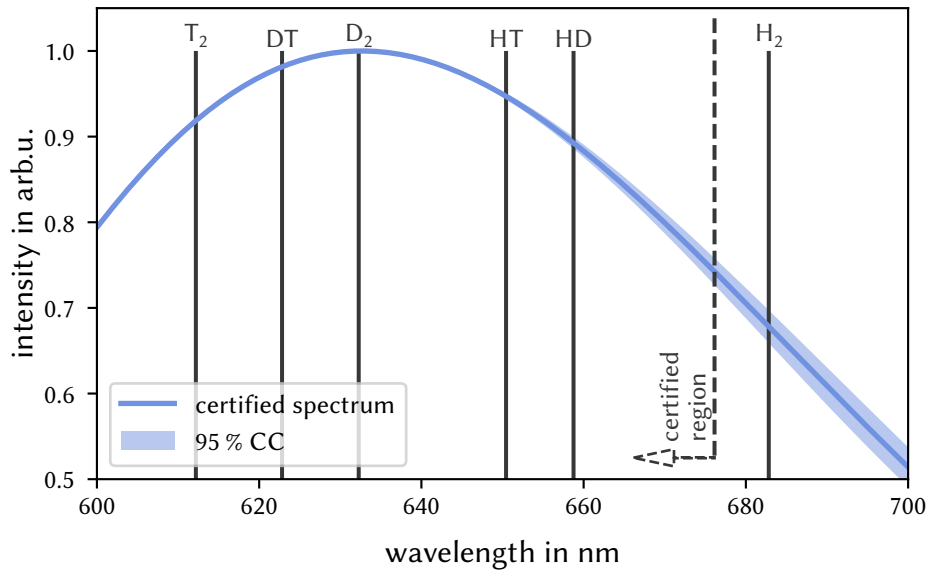


Figure 4.10: Certified spectrum of NIST SRM2242 luminous standard. Irradiated by a light source of 532 nm, the emitted spectrum can be approximated by a 5th-order polynomial, which is valid within the verified region and its related confidence interval [Nat19]. All Q₁-lines of hydrogen isotopologues are well covered by the standard except H₂ which is in the extended region with higher uncertainty.

4.3.1 Influence of spectral sensitivity

The optical transmission and detection efficiency are both wavelength dependent and are influenced by various components, including:

- Arrangement of the collection optics and focussing onto the fiber bundle,
- Mechanical stability of the fiber bundle mounts,
- 2-dimensional spectral sensitivity of the CCD detector.

In order to account for these variations, a traceable luminous standard SRM2242 provided by National Institute of Standards and Technology (NIST) is used to determine the spectral sensitivity of a given setup (see Figure 4.9) [Nat19]. The standard can be mounted inside the second containment in place of the gas cell. Irradiated by the laser, the standard emits a certified spectrum (shown in Figure 4.10) which can be used to determine the spectral response function of the setup.

Detailed investigations for adapting the standard to the 90°-scattering setup used at TLK and influence of the exposure to tritium atmosphere have been performed in Ref. [Sch14a; Sch15c]. Studies related to the uncertainty budget of the calibration procedure and components used were carried out by ZELLER².

²G. ZELLER: 'Development of a calibration procedure and calculation of the uncertainty budget for the KATRIN laser Raman system'. Master's thesis. Karlsruhe Institute of Technology, EKP, 2017, available at katrin.kit.edu.

Although the luminous standard is operated under slightly different conditions than specified, it was shown that this procedure can be performed inside a glovebox environment necessary for tritium operation and fulfils all repeatably requirements. But this method includes one caveat: As shown in Figure 4.10, the Q_1 -branch of H_2 is within the extended region of the certified spectrum, which suffers from an increased uncertainty.

4.3.2 Influence of theoretical intensity

In addition to the experiment-specific spectral sensitivity the general, isotopologue-specific theoretical intensities must be known to obtain the full response function (see Equation (4.39)).

These isotopologue-specific factors can in principle be gained via the two tensor invariants α and γ (see Equation (4.13)). Up to now, these invariants were derived by SCHWARTZ et al. [Sch87] for all six hydrogen isotopologues using quantum mechanical ab-initio calculations and extrapolations (polarisability tensors based on Ref. [Ryc80]). Although a numerical value was reported, no confidence interval and thus trueness level of the tensor invariants were stated.

This issue was addressed in depolarisation ratio measurements for all six isotopologues. the associated tensor invariants were re-calculated for 532 nm laser excitation by LEROY³ The validation showed that all calculated depolarisation ratios agreed to within 5 % of the experimental values [Sch13b; Jam13a; Sch14a]. Therefore, in this work the reported theoretical intensities for LARA-calibration were used in the application of method (i).

4.3.3 Status of the calibration for quantitative analysis and the need for a dedicated experimental calibration facility

For KATRIN to achieve the design sensitivity on neutrino mass of

$$m(\nu_e) = 0.2 \text{ eV} \quad (90 \% \text{ C. L.}) \quad (4.40)$$

several accuracy targets must be met in regards for the monitoring of the source gas [Ang04]. In the context of accuracy, one has to distinguish between

1. Precision:
The repeatability or reproducibility of the measurement. It is also a indicator sensitivity changes.
2. Trueness:
The proximity of measurement results to the true value.

³R. LEROY: 'Recalculation of Raman transition matrix elements of all hydrogen isotopologues for 532 nm laser excitation'. Personal communication. Department of Chemistry, University of Waterloo, ON, Canada, 2011.

The combination of both is considered the accuracy of the measurement (based on ISO 5725-1:1994(EN) [ISO94]).

In order to account for changes in the source gas composition throughout the measurement campaign, a precision of

$$\Delta_{\text{spec}}\epsilon_{\text{T}} \leq 0.1 \% \quad (4.41)$$

is required to detect shifts in concentration, which was already achieved in 2012 [Sch12].

The ratio κ between HT and DT as well as the overall molar fraction trueness needs to be known with a trueness of [Bod15]

$$\Delta_{\text{true}}\kappa \leq 10 \% \quad (4.42)$$

Using the calibration approach method (i), as reported in Ref. [Sch14a], it was demonstrated that a general trueness of better 3% was achieved, exceeding the broader KATRIN requirements by a factor of three. In general, method (i) has several advantages:

- The optical system can be conveniently setup where needed;
- Only a single measurement is necessary to verify and periodically check the spectral sensitivity;
- No tritiated samples need to be handled and transferred to the system.

Nonetheless, the factors derived with method (i) need to be verified using method (ii) for ascertained trueness [Nie18].

This was done for all the three stable isotopologues, achieving an accuracy for the general response function R on a sub-percent level [Sch13c], and the deviation between the methods of $(1.9 \pm 3.1) \%$ [Sch14a]. However, the verification of the theoretical intensities is aggravated due to the H_2 -line positioned in the extended region of the SRM standard with increased uncertainty.

Up to now, this verification for the radioactive isotopologues was missing. Although tritium samples are commercially available, these are usually used for calibration of tritium-in-air monitors specialised for trace amounts of T_2 [Dea15]. Hence these samples contain only minute amounts of tritium in a carrier gas, e.g. N_2 [Otl05], and are not suitable for the task of calibrating a monitoring system demanding highly tritiated samples. Therefore a new, clean-sheet experiment was called for to fill this missing link.

4.4 Objectives of this work

As mentioned in the section above, a suitable calibration strategy for the LARA system used to monitor the gas composition of the WGTs of KATRIN relies on two complimentary components:

- (i) Spectral sensitivity of the setup,
- (ii) Theoretical intensity of the specific molecular transition.

The spectral sensitivity is obtained by a certified spectrum from a luminous standard, a procedure which was successfully demonstrated [Sch15c].

The theoretical intensities, which depend on the molecule specific polarisation tensor invariants, were calculated for 532 nm laser excitation⁴, based on the original *ab initio* quantum calculations by SCHWARZ and LEROY for 488 nm laser excitation [Sch87]. These tensor values were experimentally verified using depolarisation ratios. The obtained measurement uncertainty of $\approx 5\%$ is used as an uncertainty estimate on the theoretical intensity values [Jam13b; Sch13a].

This calibration strategy was verified using accurate gas samples prepared in the HYdrogen DEuterium Equilibrium experiment (HYDE) with an accuracy of $< 3.1\%$ ⁵.

Note that this was only done for the stable isotopologues on account of the limitation of HYDE to H₂ and D₂. Due to the good agreement between both methods, the theoretical intensities for the tritiated isotopologues were assumed to be true as well [Sch13c].

In order to independently confirm these crucial yet missing calibration factors for KATRIN, accurately mixed gas samples of the radioactive isotopologues are mandatory. These should be provided by the new TRItium HYdrogen DEuterium experiment (TRIHUDE), which has the following objectives to address the remaining open issues:

1. Enable gas sample production of all six hydrogen isotopologues in chemical equilibrium;
2. Verify the theoretical intensities for tritiated hydrogen isotopologues;
3. Reduce the calibration uncertainty related to theoretical line intensities.

The addition of T₂ to the gas samples introduced significant challenges, e.g.

- Radiochemical reactions within the gas sample [Sou86; Uda92a];
- Limited initial T₂-gas purity [Dör05];
- Production of decay-³He;
- Gas-wall-interactions via both isotope exchange reactions and impurity production, e.g. methane [Pra61; Kan64; Nas65; Mor77];
- Extensive material and safety requirements due to the radiotoxic properties of tritium [Aka91; Man93].

In order to characterise the tritiated gas samples, all of these issues must be addressed and the experimental effort is described in the subsequent chapters. The general concept and design requirements of TRIHUDE are given in Chapter 5.

⁴R. LEROY: 'Recalculation of Raman transition matrix elements of all hydrogen isotopologues for 532 nm laser excitation'. Personal communication. Department of Chemistry, University of Waterloo, ON, Canada, 2011.

⁵S. RUPP: 'Proof of concept of a calibration method for the laser Raman system for KATRIN based on the determination of the system's spectral sensitivity'. Master's thesis. Karlsruhe Institut of Technology, 2012, available at katrin.kit.edu.

Details on sample production and the calibration model functions are presented in Chapter 6, together with the results for the stable isotopologues.

Chapter 7 provides an in-depth study on the radiochemical implications of tritium in calibration gas samples and the derived theoretical intensity factors of the radioactive isotopologues. All findings are then discussed within the context of KATRIN and their possible impact in $m(\nu_e)$ -measurements (Section 7.5).

5 Experimental setup of the calibration facility TRIHYDE for LARA-calibration

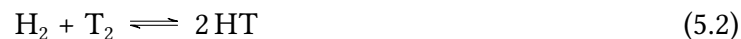
For accurate calibration of the LARA-systems used at TLK, gas samples of all six hydrogen isotopologues are indispensable. This work is based on the experience gained during operation of the predecessor HYDE using the three stable isotopologues H₂, D₂ and HD. In this chapter the basic working principle and experiment setup are described. It also covers implications and operational challenges introduced by tritium on gas sample preparation. The chapter concludes with a description of selected key components and the commissioning with respect to the experiments performed in the later Chapters 6 and 7.

5.1 Experimental goals and working principle

The main objective of TRIHYDE is the experimental cross-check of the theoretical intensity factors needed for LARA calibration. This necessitates the two basic functionalities:

1. Provide gas samples of all six hydrogen isotopologues in chemical equilibrium with relative uncertainty <1 %.
2. Provide the capability for in-situ calibration of any attached LARA system.

These samples need to be available in both *binary* forms of homonuclear mixtures H₂:D₂, H₂:T₂ and D₂:T₂ as well as *tertiary* samples including the corresponding heteronuclear isotopologue. In the tertiary sample the following equilibrium reactions for hydrogen isotopologues are encountered [Jon48; Jon49]:



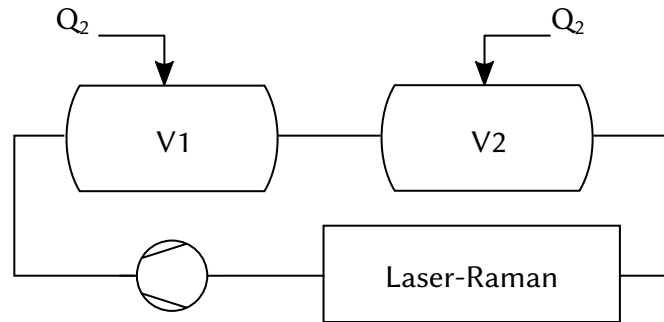


Figure 5.1: Overview of a basic manometric-volumetric mixing setup. The molar ratio of the sample is given by the pressure-volume-temperature ratio of the gas mixture(s) inside V1 and V2 before circulating via a pump.

In TRIHYDE, these samples are prepared using the manometric-volumetric method, analogous to the HYDE experiment; this method is based on DIN 6146:2018-10 [DIN18]¹.

A basic setup is given in Figure 5.1, consisting of two volume calibrated vessels, two gas inlets, a circulation pump and analytical tool. The molar ratio of the sample is given by the pressure, volume and temperature ratio before circulation using the ideal or real gas law, depending on the used conditions. After circulation is started the sample ratio will homogenise to the given ratio and in case of a stable sample the ratio is constant. For radioactive samples, at start of circulation the exchange reactions between both components will also start.

These samples can then be used to determine the absolute correction factors as well as the theoretical intensity factors necessary for calibration (see Section 4.3 and Section 6.2)

Besides the aforementioned goals, the experiment needs to address the following additional tasks:

- (i) Incorporate capabilities to guarantee the purity of gas samples, e.g. to remove decay-³He from T₂-sample and to determine gas purity before sample preparation.
- (ii) Include additional analytical methods and tools developed at TLK for in-situ benchmarking and characterisation.
- (iii) Provision of gas samples to other experiment, for either further studies like tritium loading in materials or round robin test of TLK analytics .
- (iv) Analysis of provided gas samples
Using all implemented analysis tools the system should allow for analysis of gas samples from other experiments, e.g. process gas from KATRIN loops, Catalytic Permeat Purification Experiment (CAPER) or purge gas from DPS.

¹During the conception phase DIN ISO 6146:1983-04 [DIN83] was valid, which now has been superseded by the 2018-issue [DIN18]. The major changes in the current issue are associated with the uncertainty calculation in accordance with the Guide to Uncertainty Measurement (GUM)[ISO08].

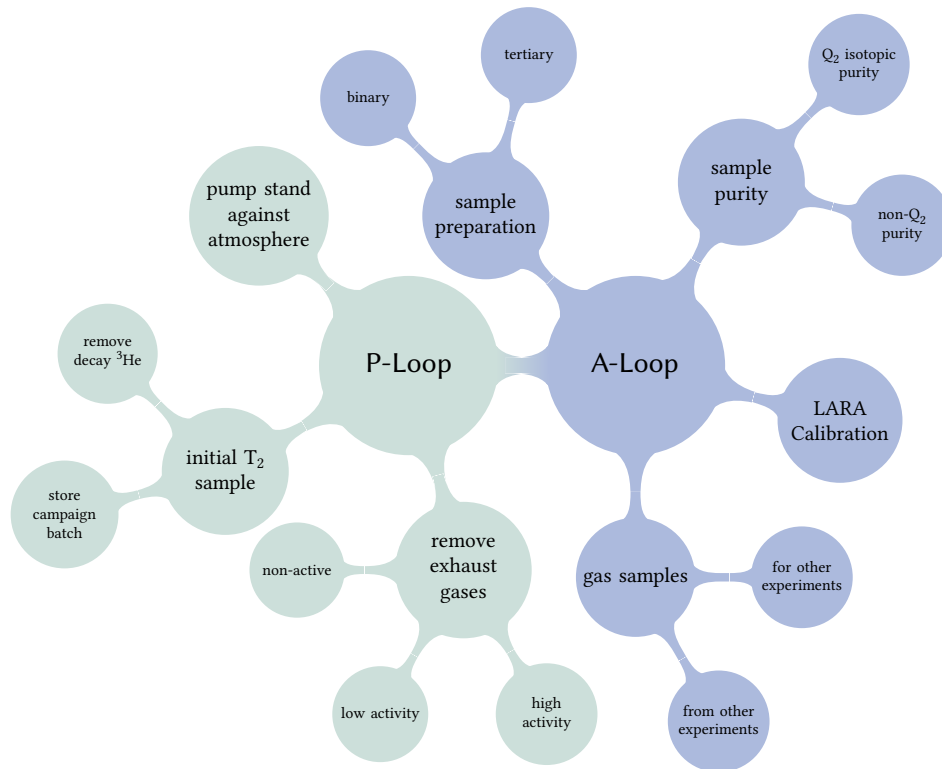


Figure 5.2: Overview of the A-Loop and the P-Loop tasks. The P-Loop provides T_2 to the A-Loop which prepares and analysis the gas sample. All exhaust gases are then transferred back to the P-Loop.

- (v) Connection to existing TLK infrastructure and providing additional processing resources. New or smaller experiments demanding tritium should be able to use TRIHYDE as an interface for a straight-forward setup. Using TRIHYDE as a backup system integrated with the TLK systems should also make the closed tritium processing loop of TLK more reliable for uninterrupted KATRIN-operation.

Providing all these capabilities makes TRIHYDE a permanent user facility at TLK. To fulfil all aforementioned requirements TRIHYDE consists of two interconnected but independently operable parts:

- Analysing-loop (A-Loop):
All tasks related to gas sample preparation, mixing and analysis are performed in the analysing loop.
- Processing-loop (P-Loop):
This part is the connection to the TLK-infrastructure [Hut95] to deal with gas inlet, exhaust gases as well as removing decay helium.

Figure 5.2 gives an overview of all the necessary capabilities while their implementation and design implications regarding tritium operation is discussed in the following sections.

5.2 Design considerations of TRIHYDE

5.2.1 General design considerations

In general, tritiated gas samples can be produced using two main methods:

- (i) Continuous mixing via flow control [Hor83],
- (ii) Pressure and volume controlled mixing (manometric and volumetric respectively) [Blo67; Jar16].

Using flow control a sample can either be mixed by simultaneous flow of both constituents or by diluting an initial sample by maintaining a controlled flow [Le 78]. While this method can provide highly-accurate sampling using e.g. heat-capacity flow controller (katharometers), it is unsuitable for LARA-calibration. Due to the continuous flow the chemical equilibration of the sample, either by a catalyst or other reaction chain, cannot be facilitated while at the same time analysing the binary sample.

In contrast, the volumetric-manometric procedure method uses a batchwise sample preparation using calibrated mixing volumes [Otl05] or e.g. a syringe pump [Bie18]. Despite being dependent on more components compared to the flow-method which all contribute to the uncertainty budget, this method is favoured for tritiated gas sample for the following reasons:

- Easy sampling of gas before circulation, enabling measurement of initial gas purity;
- Well defined time when gases mix to both analyse the binary and tertiary mixture;
- More economical because no continuous tritium flow necessary.

Conventionally, the procedure is called a purely *volumetric* method when two or more very precisely known volumes of different gases but at the same pressure are combined [Sch15d]. Otherwise, it is referred to as the *manometric* method.

The manometric method can be implemented using only a single mixing volume to cancel out uncertainties in volume and pressure sensor calibration, as described in DIN 6146:2018-10 [DIN18]. For tritiated mixtures this has the disadvantage that the mixed gases start already to interact while filling the second gas, making analysis of the binary and tertiary mixture impossible. Using more than two mixing vessels only makes the setup more complicated while bringing no advantage. For gas samples using more than two gas species the sample can be prepared step-wise using one of the vessels as a storage vessel in each step.

The system needs to operate in a pressure range of ($1 \cdot 10^{-3}$ to 900) mbar with consistent accuracy to allow for experiments with highly tritiated samples as well as samples with only trace amounts of tritium. This dictates the choice of pump and pressure sensor selection. For higher pressure the LARA-signal quality improves, in general because the SNR increases, but additional systematics might be introduced for tritiated samples due to exchange interactions.

5.2.2 Improvements over the predecessor experiment HYDE

Based on the experience gained during the LARA calibration using samples produced within the HYDE [Sch14a] the following identified improvements were implemented:

- (i) Optimised mixing vessel design for improved gas homogenisation:
The gas flow through the T-shaped mixing vessels in HYDE created a ‘dead volume’ which suppressed gas mixing. This negatively impacted sample preparation. TRIHYDE uses vessels with a straight-flow-through design to eliminate this possible influence (see Section 5.4.1 for more details).
- (ii) Reduction of inner surface:
Reducing the inner surface reduces possible gas-wall-interactions and their influence on sample composition, especially considering tritiated samples [Mor77]. This can be realised by reducing the overall piping length, which is a trade-off to usability of the loop. During construction all components were positioned to provide convenient handling while also reducing piping length to a minimum. The final inner surface area is comparable to HYDE while offering more analysis capabilities. In addition, all connections are outlaid to minimise ‘dead volumes’ during circulation.
- (iii) Improved catalyst design:
For better temperature control the new catalyst setup is equipped with accurate gas temperature sensors at inlet and outlet as well as multiple temperature sensors along the heating sleeve. For further studies the catalyst setup can be replaced with minimal effort. Compared to HYDE the maximum temperature is limited to $<200\text{ }^{\circ}\text{C}$ for components not enclosed by a dedicated insulation vacuum. This is due to the elevated tritium permeability through the vessel walls [Aus72] at higher temperatures.

In addition, the TRIHYDE design includes the following general refinements:

- Reduced mixing vessel volume by a factor of 2 for better tritium economy,
- Reduced volume uncertainty by a factor of 2,
- Addition of temperature sensors in the mixing vessels and along the circulation loop,
- Initial gas purity verification using both Quadrupole Residual Gas Analyser (RGA) and Binary Gas Analyser (BGA),
- Three pumping stages for reduced minimal residual pressure.

5.2.3 Considerations for T_2 handling

In order for TRIHYDE to process tritiated gases additional safety related design requirements² need to be addressed, namely:

²The tritium related design requirements are disclosed in TRITIUM LABORATORY KARLSRUHE: *Technical terms of delivery and acceptance of TLK*. 2016

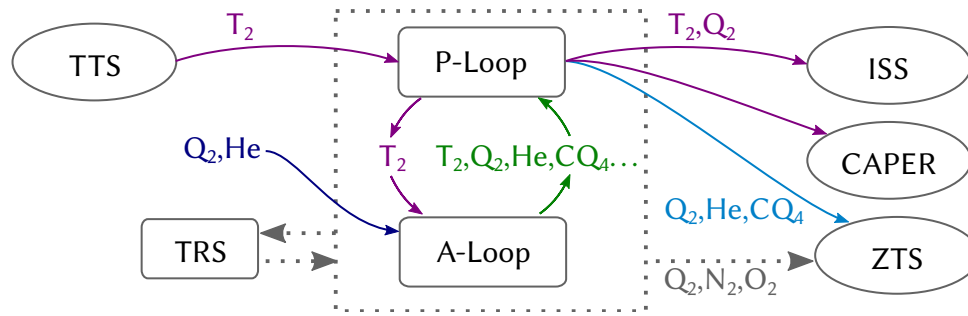


Figure 5.3: Gas handling of TRIHYDE with TLK infrastructure. Exhaust gases from the P-Loop are distributed depending on the composition: radioactive mixtures of only hydrogen isotopologues are transferred to the Iss, tritiated mixtures with impurities to CAPER and low activity mixtures to the Central Tritium Retention System (ZTS). The second containment (dotted line) activity level is controlled by cycling via the Tritium-Retention-System (Trs).

(i) Construction materials:

Due to the aggressive and corrosive properties of tritium all wetted materials must be metallic [Bel93]. In case of non-avoidable polymers only halogen-free, radiation resistant materials with low hydrogen content must be used. All materials must be referenced with a material certificate according to DIN 10204:2004 [DIN05].

(ii) Second containment:

As a consequence of the high permeation of hydrogen through stainless steel as well as containment in case of a system leak, the tritium bearing primary system must be enclosed in a glovebox. The glovebox pressure is kept below atmospheric pressure to have a positive pressure gradient in case of leakage. To ensure that no mixture of hydrogen and oxygen can occur forming an explosive atmosphere the second containment is flushed with nitrogen and the oxygen level is kept below 2%. The operation within the glovebox poses additional consideration with regards to positioning, operability, maintainability and replacement of components.

(iii) Safety interlocks:

In order guarantee safe operation, reliability and high-availability (i.e. sufficiently high uptime), an industry-grade process control system must be used. To maintain compatibility to the existing TLK process control system a *SIEMENS SIMANTIC S7-300* is used for operation and sensor readings. All safety related interlocks, e.g. pump over-pressure or temperature control were implement based on extensive HAZOP deliberation in accordance to DIN EN 61882 [DIN17].

In Figure 5.3 the basic gas flow integration of TRIHYDE with in the TLK-infrastructure is given. The initial T_2 gas originating from either the Isotope Separation System (Iss) [Nef98] or the General tritium storage facility (TLG) [Bes92] is transferred via the Tritium Transfer System (TTS) [Sch91] to a buffer vessel in the P-Loop. Within the P-Loop the gas can be processed via a permeator to remove non-tritium impurities. This T_2 gas is transferred to the A-Loop and combined with stable isotopes from an external supply to

prepare the calibration gas sample. During sample preparation possible impurities like tritiated methane can form [Kan64; Mor77]. The resulting gas mixture is pumped back to the P-Loop. Depending on the general gas composition the exhaust gas is distributed via TLK's closed tritium loop as follows:

- (i) Highly tritiated mixtures with negligible non-hydrogen components are transferred to the Iss for direct isotope separation;
- (ii) Tritiated mixtures with significant non-hydrogen components ($>1\%$) are processed in CAPER;
- (iii) All other gases with trace amounts of tritium are transferred to the ZTs. [Bes08]

The activity level of atmosphere in the second containment, enclosing both loops, is constantly monitored and controlled by cycling via the TRs [Vol95] while the glovebox pressure is maintained by venting to the ZTs.

Gas samples for and from other experiments can be transferred via three double-door transfer systems. Within both the A- and P-Loop, various buffer vessels, evacuation lines and component bypasses for maintenance purposes are built-in.

5.2.4 Evaluation of the uncertainty budget

The ultimate goal of TRIHYDE is to achieve a relative uncertainty of the sample molar ratio of 1 % or better. To quantify the uncertainty requirements of individual components an uncertainty budget based on the principles described in the GUIDE TO UNCERTAINTY MEASUREMENT (GUM) is prepared.[ISO08]. This is accomplished by the following seven steps, as described in Ref. [Kes02]:

1. Basic description of the measurement procedure to determine an arbitrary measurement entity Y .
2. Description of the model function $y = f(x)$ combining all input quantities x .
3. Collection of all available information about the input quantities x .

Within the GUM framework two types of uncertainties are distinguished:

- (i) Type A are all uncertainties originating from repeated measurements;
 - (ii) Type B uncertainties contain all other contributions, including calibration certificates, manufacturer specification and general knowledge.
4. Conversion to standard uncertainties using fixed rules.

In order to combine uncertainties σ_x of input quantities of Type A and B, all uncertainties need to be adjusted to so-called standard uncertainty $u(\bar{x})$.

- (i) Type A uncertainties from a series of n measurements follow a Gaussian distribution around the arithmetic mean \bar{x} . Here, the standard deviation of

$$\sigma_{\bar{x}} = \sqrt{\frac{1}{N} \sum_i^N (x_i - \bar{x})^2} \quad (5.7)$$

is used as standard uncertainty $u(\bar{x})$. If the sample n is small (degrees of freedom $\nu = n - 1 < 40$), then the associated correction factor $t_p(\nu)$ from the Student's distribution needs to be applied.

$$u(\bar{x}) = t_p(\nu) \cdot \sigma_x \quad (5.8)$$

- (ii) Type B uncertainties σ_x do not necessarily follow a Gaussian distribution, but can have a range of possible probability density functions. Possible functions include rectangular distributions, often used for calibration certifications, and linear distributions, for example for temperature drifts in many pressure sensors. In case of a Gaussian distribution, the uncertainty $\sigma_{x,\text{Gaussian}}$ is treated analogous to a type A uncertainty. In order to convert a non-Gaussian uncertainty $\sigma_{x,\text{non-Gaussian}}$ to a standard uncertainty $u(x)$, the underlying distribution needs to be identified. Based on the distribution, an associated weighting factor G is used to correct the coverage interval $\sigma_{x,\text{non-Gaussian}}$ to a standard uncertainty

$$u_{\text{Gaussian}} = \frac{1}{\sqrt{G}} \cdot \sigma_{y,\text{non-Gaussian}} \quad (5.9)$$

For a complete list of possible distributions and associated weighting factors, see Ref. [ISO08].

5. Propagation of input uncertainties to the relevant output quantities.

For uncorrelated uncertainties x_i , the combined uncertainty is given by

$$u_c(y) = \sqrt{\sum_i (c_i \cdot u(x_i))^2} \quad (5.10)$$

where c_i is the sensitivity coefficient given by

$$c_i = \frac{\partial f}{\partial x_i}. \quad (5.11)$$

6. The combined uncertainty $U(y)$ for the measurement result y is given by

$$U(y) = k \cdot u_c(y) \quad (5.12)$$

using the so-called coverage factor $k = 1, 2, \dots$. In order to obtain a 2- σ coverage interval, a coverage factor $k = 2$ is used. If not otherwise noted a coverage factor of $k = 1$ is used throughout this work.

7. Reporting the final result in the form

$$Y = y \pm U \quad \text{with} \quad k = 1. \quad (5.13)$$

Here Y is the measurement entity, y the best estimate given by the model function $f(x)$ and U the combined uncertainty for a coverage factor of 1.

In TRIHYDE the measurement entity is the number of molecules N inside the mixing vessels, given by the ideal gas law³. The related model function is

$$N = \frac{(p \pm \delta p) \cdot (V \pm \delta V)}{k_B \cdot (T \pm \delta T)} \quad (5.14)$$

with the associated sensitivity factors:

$$c_p = \frac{\delta N}{\delta p} = \frac{V}{k_B \cdot T} \quad (5.15)$$

$$c_V = \frac{\delta N}{\delta V} = \frac{p}{k_B \cdot T} \quad (5.16)$$

$$c_T = \frac{\delta N}{\delta T} = -\frac{p \cdot V}{k_B \cdot T^2} \quad (5.17)$$

An overview of the resulting uncertainty contributions in TRIHYDE is given in Table 5.1, which are described in detail in EBENHÖCH⁴. The main contributions are the uncertainty of the volume and pressure measurements; they need to be addressed already during the conception phase to keep them as low as possible, on principle. A description of both the volume measurement to achieve the required $u_V = 0.2\%$ and pressure instrumentation is given in Section 5.4.1

For reduced uncertainty of the particle number ratio it is beneficial to ensure all gases have identical temperature which can be verified by both absolute temperature and pressure measurements (see Chapter 6 for details.)

To achieve the relative uncertainty target of 1% based on Table 5.1 it is paramount to quantify the initial gas purity which is time-variant and not stated a priori for all tritiated mixtures. Although estimates of effects like isotope exchange reactions and gas-wall interactions were done, these must be verified experimentally within the loop. These issues are addressed in Chapter 7 by sampling the gas prior to each measurement and carry out additional estimates of gas purity evolution during circulation.

Based on the uncertainty estimations, the target accuracy of the experiment can be surpassed for stable isotope mixtures and can be achieved for tritiated gas mixtures pending experimental verification.

³The ideal gas law be assumed for all gases and pressure regimes used in this work; results using Van-der-Waals equation differ by $<0.01\%$.

⁴S. EBENHÖCH: 'Conception and test of an experiment to produce mixtures of gaseous hydrogen isotopologues with high accuracy'. Master's thesis. Karlsruhe: Karlsruher Institut of Technology, 2015.

Table 5.1: Uncertainty budget of an A-Loop gas sample in a single vessel. The individual contributions are either from datasheets entries or ‘sub-budgets’ of the individual measurement.

Standard uncertainty	Parameter	Uncertainty contribution
gas purity ^a	u_{p, H_2}	$1 \cdot 10^{-4} \% \cdot p$
	u_{p, D_2}	$2 \cdot 10^{-6} \% \cdot p$
	u_{p, T_2}	$x^b \% \cdot p$
gas-wall interactions ^b	$u_{p, desorption}$	$< 2 \% \cdot p$
pressure sensor reading ^c	$u_{p, accuracy}$	$0.12 \% \cdot p$
pressure sensor zero ^c	$u_{p, zero}$	$0.002 \% \cdot p_{FS} \cdot \Delta T^d$
pressure sensor span ^c	$u_{p, span}$	$0.015 \% \cdot p_{FS} \cdot \Delta T^d$
pressure average	$u_{p, s}$	$s(\bar{p})^f$
signal converter pressure signal ^f	$u_{p, S7}$	$0.05 \% \cdot p_{FS}$
mixing vessel volume ^h	$u_{V, k=1}$	$0.25 \% \cdot V$
temperature sensor PT100 ^h	$u_{T, PT100}$	$0.15 + 0.002 \cdot T^i$
temperature average	$u_{T, s}$	$s(\bar{T})^f$
signal converter temperature signal ^g	$u_{T, S7}$	$0.5 \% \cdot T_{FS}$

^a gas purity certificate provided by *Linde*, verified via mass spectrometer

^b see Chapter 7

^c datasheet *MKS 627D*

^d Full scale of sensor, i. e. 1000 mbar and 2.6 mbar

^e difference from zeroing temperature, usually 25 °C.

^f arithmetic average

^g datasheet *Siemens Simatic S7-300*

^h see Section 5.4.1

ⁱ $[T]$ in °C

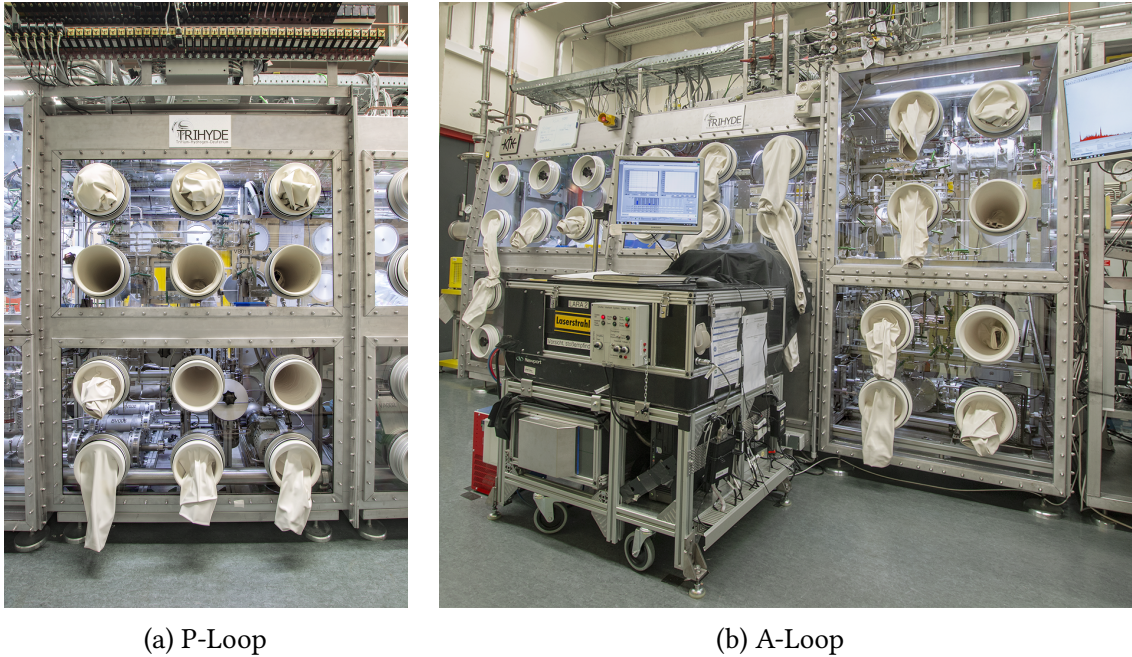


Figure 5.4: Image of the glovebox containing the P- and the A-Loop. In front of the A-Loop, the LARA2 setup is attached to the glovebox appendix.

5.3 Description of the TRIHYDE setup

This section describes the basic setup and operation of the A- and P-Loops necessary for sample preparation. A photograph of both loops within the second containment is shown in Figure 5.4.

5.3.1 The analysing loop (A-Loop) for gas sample production

For gas sample preparation and analysis the A-Loop contains the following main elements:

- two mixing vessels,
- gas inlet for stable gases,
- tritium transfer line from the P-Loop,
- LARA system,
- circulation pump.

A simplified flow diagram is given in Figure 5.5.

Before each run the loop is evacuated via the P-Loop. If necessary the catalyst and the mixing vessels can be heated up to 200 °C for improved outgassing. The stable isotopes are supplied by external gas bottles and can be extended to use additional gas species.

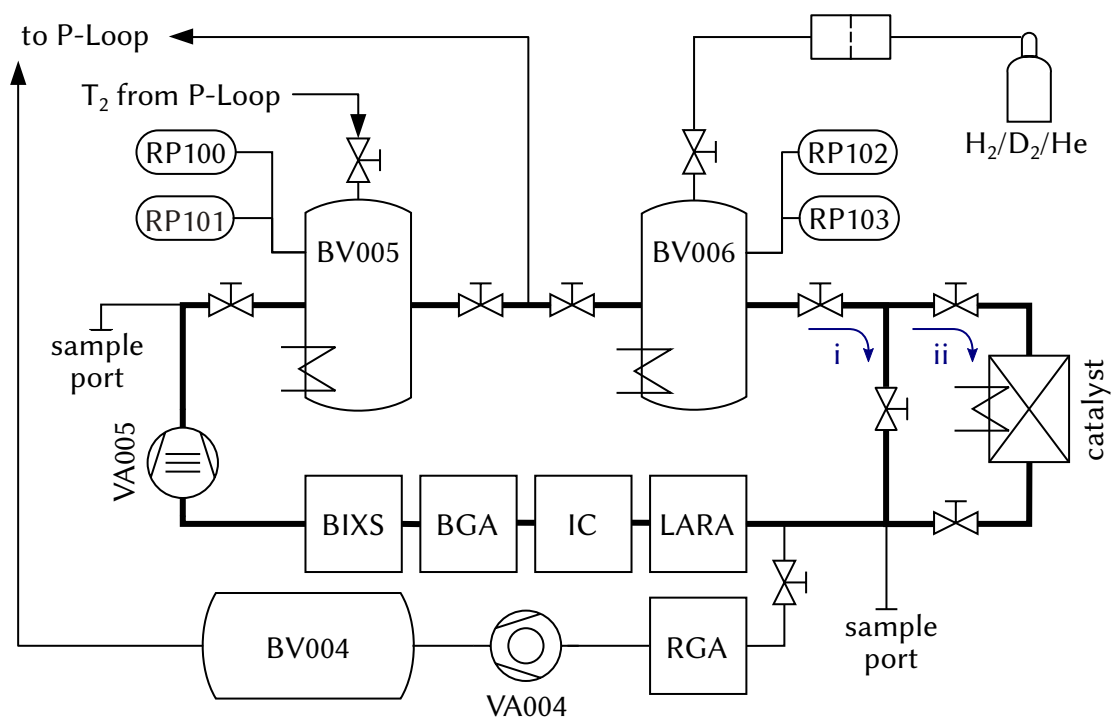


Figure 5.5: Simplified overview of the A-Loop. All external gases (H_2 , D_2 , He) are guided through a getter filter before entering the primary system. The pressure inside each mixing vessel (BV005 and BV006) is measured by two pressure gauges (RP) with overlapping measuring range. The sample can be circulated (using vacuum pump VA005) either through the catalyst or bypassing it (passes (ii) or (i), respectively). While circulating, the gas sample is in-situ analysed via LARA, Ionisation Chamber (IC), Binary Gas Analyser (BGA) and Bixs. Due to the lower operating pressure, the gas sample for the Quadrupol Residual Gas Analyser (RGA) is extracted via a dosing valve and a turbomolecular pump (VA0004) into a buffer vessel (BV004). Here, only the key components and valves for loop operation are shown. Not shown are components like additional instruments and safety devices present in the actual setup.

He-supply is provided by the central-He-distribution of TLK. To guarantee no tritium leakage from the primary system outwards a system of check valves and automatic valves maintain a positive pressure gradient towards the primary system. All gases are filtered using gas filters⁵ to ensure the certified gas purity is maintained within the loop. Installed flow controllers can be used to either flush the system or to prepare samples using the continuous flow method as described in Section 5.2.

After filling the mixing vessels BV005 and BV006 to the target molar ratio the gases can be circulated through the catalyst (pass (i)) or bypass it (pass (i)). While circulating the gas, its activity (a) and composition (c) is continuously monitored a chain of in-series tools:

- Laser Raman Spectroscopy (LARA) - composition monitor [Fis11],
- Ionisation Chamber (IC) - activity monitor [Wag11],
- Binary Gas Analyser (BGA) - composition monitor [Löf03],
- Beta Induced Xray Spectrometry (Bixs) - activity monitor [Röl13].

These tools can operate in a pressure range of (1 to 900) mbar. With the RGA system requiring a maximum operating pressure of $1 \cdot 10^{-3}$ mbar or below, this device needs to be actively pumped. The inlet pressure is controlled by an all-metal manual gas dosing valve⁶. BV004 is used as a buffer vessel to operate the turbopump VA004 independent of the vacuum pumps of the P-Loop.

The sample port for accepting gas samples and all analytical tools are on the suction side of VA005 in order to avoid unacceptable pressure peaks. Sample ports for prepared samples and BV005 are downstream of the pump to enable gas compression into sample cylinders.

Not shown in the overview are auxiliary components, i.e.

- General instrumentation for loop operation,
- Redundant safety sensors in case of over temperature and pressure,
- Bypass valves for maintenance,
- Additional piping for individual component evacuation,
- Check valves and pressure gradient monitoring at gas inlet.

5.3.2 The processing loop (P-Loop) for tritiated gas handling

The P-Loop operation can be grouped into the following tasks:

1. Vacuum pumping against atmospheric pressure,
2. Tritium supply for the A-Loop,
3. Removal of non-hydrogen impurities.

⁵SAES Group, 20045 MI, Italy. Type MC50-*FV 902 & 904

⁶Pfeiffer vacuum 420VED016, All-metal gas dosing valve, manually actuated, DN 16 CF-R

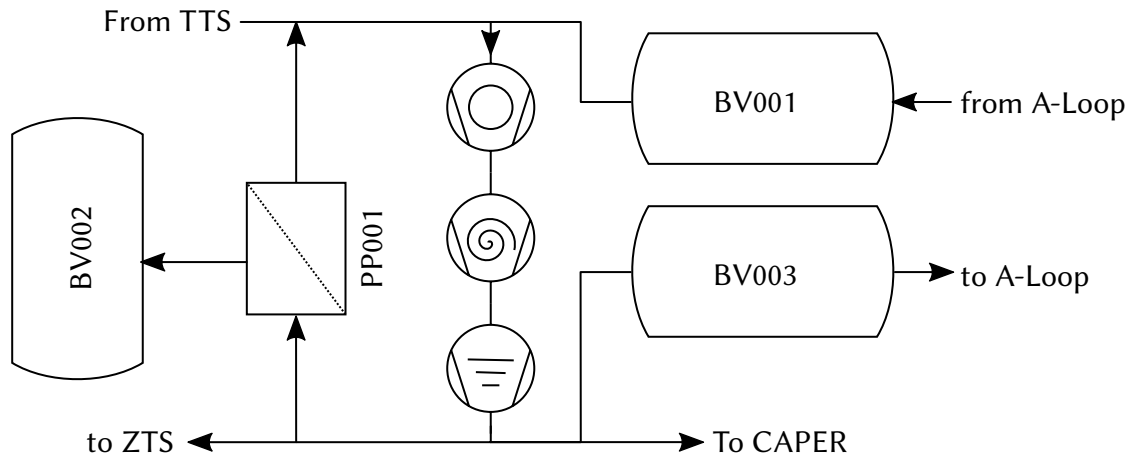


Figure 5.6: Simplified overview of the P-Loop. This view omits components like valves, instruments and safety devices present in the actual setup. Specifications of the pumps is given in Section 5.3.2.

Table 5.2: Selected specifications of used pumps.

Pump	Manufacturer	Type	Compression ratio	Min.pressure (mbar)
VA001	Siemens Interatom ^a	IAS	$1 \cdot 10^1$	<500
VA002	Normetex ^a	M15	$2 \cdot 10^4$	$5 \cdot 10^{-3}$
VA003	Pfeiffer	HiPace80 ^b	$1.4 \cdot 10^5$	$<1 \cdot 10^{-8}$
VA004	Pfeiffer	HiPace80 ^b	$0.4 \cdot 10^5$	$<1 \cdot 10^{-8}$
VA005	Senior Metal Bellows	MB601	$\approx 1 \cdot 10^1$	100

^a at present not commercially available.

^b not all-metal wetted surfaces.

Based on these tasks the main components are:

(i) Vacuum pumps:

A total of three vacuum pumps in series are used for gas transfer within the system, and for evacuation of individual parts:

- Metal bellows pump (backing pump),
- Scroll pump (roughing pump),
- Turbomolecular pump (vacuum pump).

All pumps are oil free and with the exception of the turbomolecular pumps all-metal. Using all pumps, a minimal residual pressure of well below $1 \cdot 10^{-4}$ mbar can be reached in all parts, sufficient for LARA calibration sample preparation.

(ii) Pd-Permeator:

In order to remove non-hydrogen impurities, a permeator made from eight $\varnothing 1.33$ mm \times 144 mm Pd tubes, each with 0.1 mm wall thickness, is operated, analogous to the design used in the KATRIN loops [Pen97; Wel09]. The membranes are heated to 400 °C to suppress metal hydrate formation and avoid hydrogen embrittlement. During operation the gas can either be ‘pushed’ or ‘pulled’ through the membrane, similar to the KATRIN feed loop and circulation loop. The bleed gas from the permeator is collected in BV002 and can be cycled through the permeator.

(iii) Buffer vessels:

For gas storage during measurement campaigns or operational reasons three 7 l vessels made from off-the-shelf CF-components were constructed.

In normal operation a tritium batch used in a measurement campaign is transferred from the TTs via a double-wall-pipe into BV003. Depending on gas composition the received gas can be guided through the permeator before reaching the buffer vessel BV003. This gas is then expanded into the A-Loop as needed for sample preparation. The exhaust gas from the A-Loop is collected in BV001 and then distributed to either ZTs, CAPER or ISS via TTs, depending on gas composition (see Figure 5.3).

5.4 Overview of selected components

5.4.1 Mixing vessels

Selection of Components

For the manometric mixing the two mixing vessels should ideally have identical volume, with their pressure and temperature monitoring sufficient for the uncertainty goal as described in Section 5.2.4. In order to fulfil these as well as requirements for tritium operation the mixing vessels are set up as follows:

(i) Shape and components:

Building the vessels from off-the-shelf standard components has the advantage of consistent parts dimensions and straightforward material and design certification. Therefore, both cylinders are made from standard CF63 and CF40 flanges and connectors supplied by VACOM⁷.

In contrast to HYDE the volume was reduced by 50 % to better match sample volume demand and improve tritium economy. The overall shape is cylindrical with minimal possibility for 'dead volume' with suppressed gas mixing.

At the design stage it was considered using oxygen-free copper as main material for vessels and piping⁸. This would result in much reduced impurity build-up due to suppressed interaction of tritium with copper [Nis00; Per08]. Due to limitations in certified connection techniques all piping was laid out in stainless steel VCR-fittings manufactured by Swagelok⁹. Applying a Au-coating to the mixing vessel's inner surface to reduce memory effects [Röl15a] was considered. However, this was not implemented because the relative small contribution of the coated surface and therefore limited effect.

(ii) Valves:

The main isolation valves of the mixing vessel are all-metal bellows sealed manual valves with spherical stem tip supplied by Swagelok. To enable precise pressure control each vessel's inlet valve has a SS316 cone-shaped regulation stem tip, offering a precision in pressure regulation of $\sim 1 \cdot 10^{-3}$ mbar.

(iii) Pressure sensors:

To meet the trueness requirements laid out in Section 5.2.4 each vessel is equipped with two temperature-stabilised, all-metal capacitive pressure sensors of type MKS 627D Baratron¹⁰. These sensors offer gas species independent pressure measurement with an uncertainty of 0.12 % of reading over three orders of magnitude. To cover a wide pressure range both a 1000 mbar and a 2.67 mbar (=2 Torr) full-scale are integrated to cover six pressure decades with a sensible overlap. Each can be regularly zeroed within the setup.

(iv) Temperature sensors and control:

Each vessel includes a custom-build temperature sensor constructed from a class A Pt100 probe contained in a stainless steel cylinder and placed within the gas stream. The sensor fulfils all tritium related requirements for a primary system according to [Tri15]. The sensor is read-out by a 4-wire circuit and has a specified uncertainty

⁷VACOM Vakuum Komponenten & Messtechnik GmbH, 07751 Großlöbichau, Germany

⁸A. REIN: 'Estimation and analysis of impurities in calibration gas mixtures for the Tritium-Hydrogen-Deuterium-Experiment (TRIHYDE)'. Master's thesis. Karlsruhe Institut of Technology, IEKP, 2015.

⁹Swagelok Company, Ohio 44139, USA

¹⁰MKS Instruments Inc, Massachusetts 01810, USA

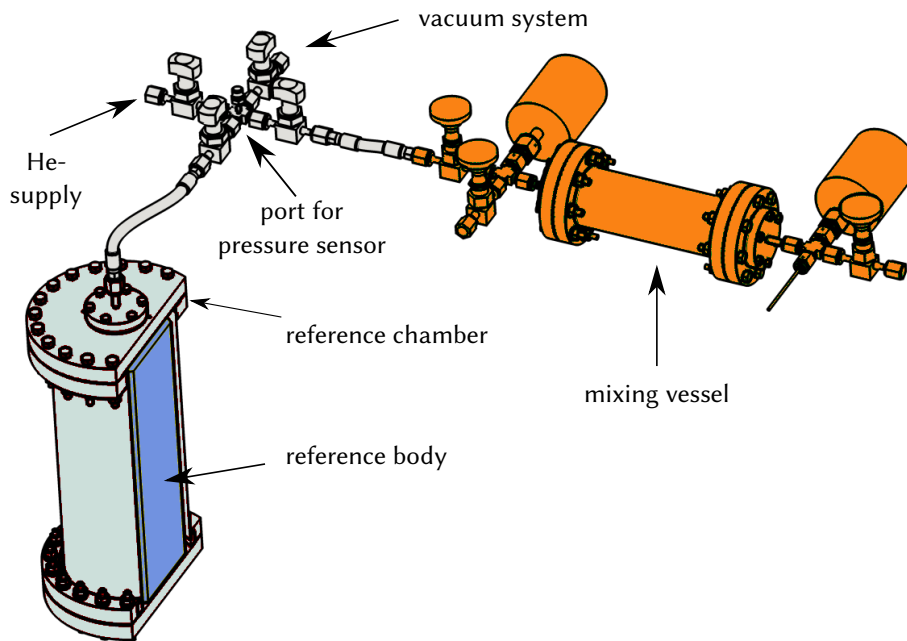


Figure 5.7: Volume determination setup of mixing vessels. In order to achieve the required volume accuracy of the mixing vessels, a dedicated measurement setup based on the method described in Ref. [Köl11] was built. After evacuating the whole system, either the mixing vessel or reference chamber was filled with helium. The subsequent gas expansion measurements were repeated with and without the reference body inside the reference chamber. Based on the reference body geometry, which was milled with high accuracy, the inner volume of the mixing vessels was derived from the gas expansion measurements.

according to DIN EN 60751:2008 [DIN08] of:

$$\sigma(T) = \pm 0.15^\circ\text{C} + 0.002 \cdot T . \quad (5.18)$$

In addition, a heating sleeve (controlled by two built-in Pt100 sensors) can be used for bake-out of the vessel to temperatures up to 200 °C. These can be used also for temperature stabilisation of the mixing vessels above glovebox temperature.

A CAD rendering of the mixing vessels is given in Figure 5.7.

Experimental determination of the inner volume

Common methods to determine the inner volume of a vessel include:

- Geometric calculation by component dimensions,
- Weighing the vessel filled with a dense medium,
- Filling the vessel with a fluid and determine the used fluid volume.

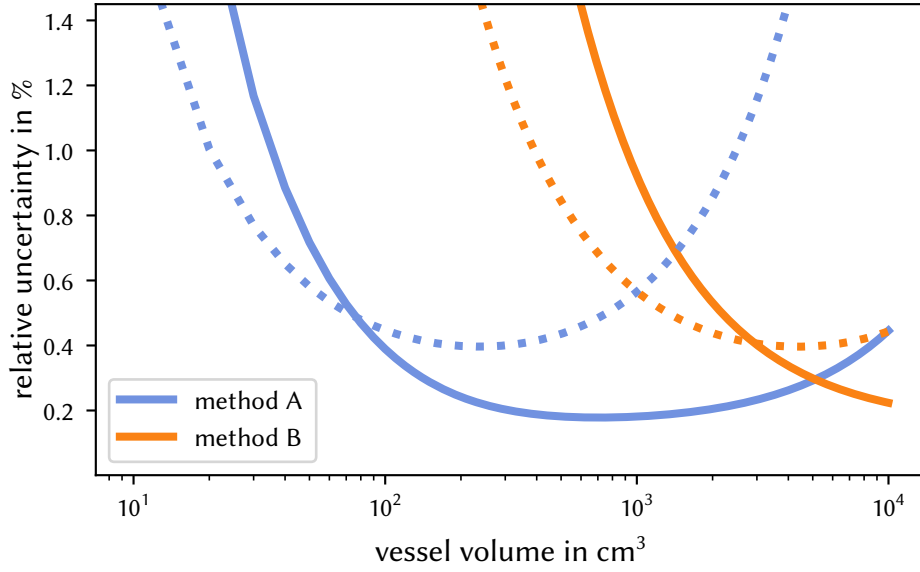


Figure 5.8: Uncertainty of volume determination depending on reference body. In contrast to the optimised setup (solid line) the uncertainty of the existing setup by [Köl11] (dotted line) does not meet the TRIHYDE requirement of 0.2 % for a volume of $\sim 800 \text{ cm}^3$. In method (A) gas is expanded from the sample volume, in method (B) from the reference volume.

The latter two methods are unsuitable due to the sensitive membranes of the pressure sensors and the non-guaranteed removal of all fluids before vacuum operation. The first option does not provide the required uncertainty level based on variety in connection dimension as well as manufacturer data.

A suitable method for vacuum systems is volume determination by gas expansion. By expanding gas into or from a known reference volume V_R the unknown volume V_v is given by:

$$V_v = V_R \cdot \frac{p_R^i - p^{eq}}{p^{eq} - p_v^i} \quad (5.19)$$

with the initial fill pressure p^i and equilibrium pressure p^{eq} .

The achievable uncertainty is limited by the pressure readout and reference volume. In Ref. [Köl11] an alternative method is described: one or two reference cylinders V_R are used which can be machined with high accuracy to reduce the reference volume uncertainty. By using an expansion measurement with and without a reference cylinder (V_i ; V_j) present in the reference chamber the inner vessel volume V_v is given by:

$$V_v = \frac{V_i - V_j}{\alpha_j - \alpha_i} \quad (5.20)$$

with

$$\alpha_i = \frac{p_i - p_{iV}}{p_{iR} - p_i} \quad (5.21)$$

$$\alpha_j = \frac{p_j - p_{jV}}{p_{jR} - p_j} \quad (5.22)$$

In Figure 5.8 the achievable uncertainty of the existing setup at TLK is given (based on Ref. [Köl11]), as a function of on the unknown volume. The uncertainty is influenced by whether gas is expanded from (method A) or into (method B) the reference chamber. In general, neither method generally offers the required uncertainty of $<0.2\%$ using the existing setup; an optimally adapted setup¹¹ is required to estimate volumes of about 800 cm^3 .

An overview of the volume measurement setup is given in Figure 5.7 and contains:

(i) A reference cylinder:

A milled aluminium cylinder with a total volume of $(4380.20 \pm 2.35)\text{ cm}^3$ including three ‘feet’ with an diameter of 2 mm to avoid gas trapping below the cylinder. The body is placed in the reference chamber using a suction knob.

(ii) A reference chamber:

Constructed from standard CF components with an empty volume of $\sim 59\,000\text{ cm}^3$. When performing multiple gas expansion measurements the volume varies as a result to opening and closing the chamber cancel themselves out.

The pressure and temperature readings are performed using the mixing vessel instrumentation as well as a dedicated pressure sensor of the same type.

Based on the uncertainty calculation according to GUM the volumes are determined to

$$V_{\text{BV}005} = (809.1 \pm 2.0)\text{ cm}^3 \quad (5.23)$$

$$V_{\text{BV}006} = (810.8 \pm 2.0)\text{ cm}^3 \quad (5.24)$$

both identical within the uncertainty margin and comparable to the value expected from geometry.

5.4.2 LARA2-Setup

Overview of components and setup

This section provides a brief overview of the setup of the LARA2-system which is described in detail by SCHLÖSSER [Sch14a] and FISCHER [Fis14]. In Figure 5.9 an image and schematic of the optical setup is given including the following main components (technical details in Table 5.3):

¹¹S. EBENHÖCH: ‘Conception and test of an experiment to produce mixtures of gaseous hydrogen isotopologues with high accuracy’. Master’s thesis. Karlsruhe: Karlsruher Institut of Technology, 2015.

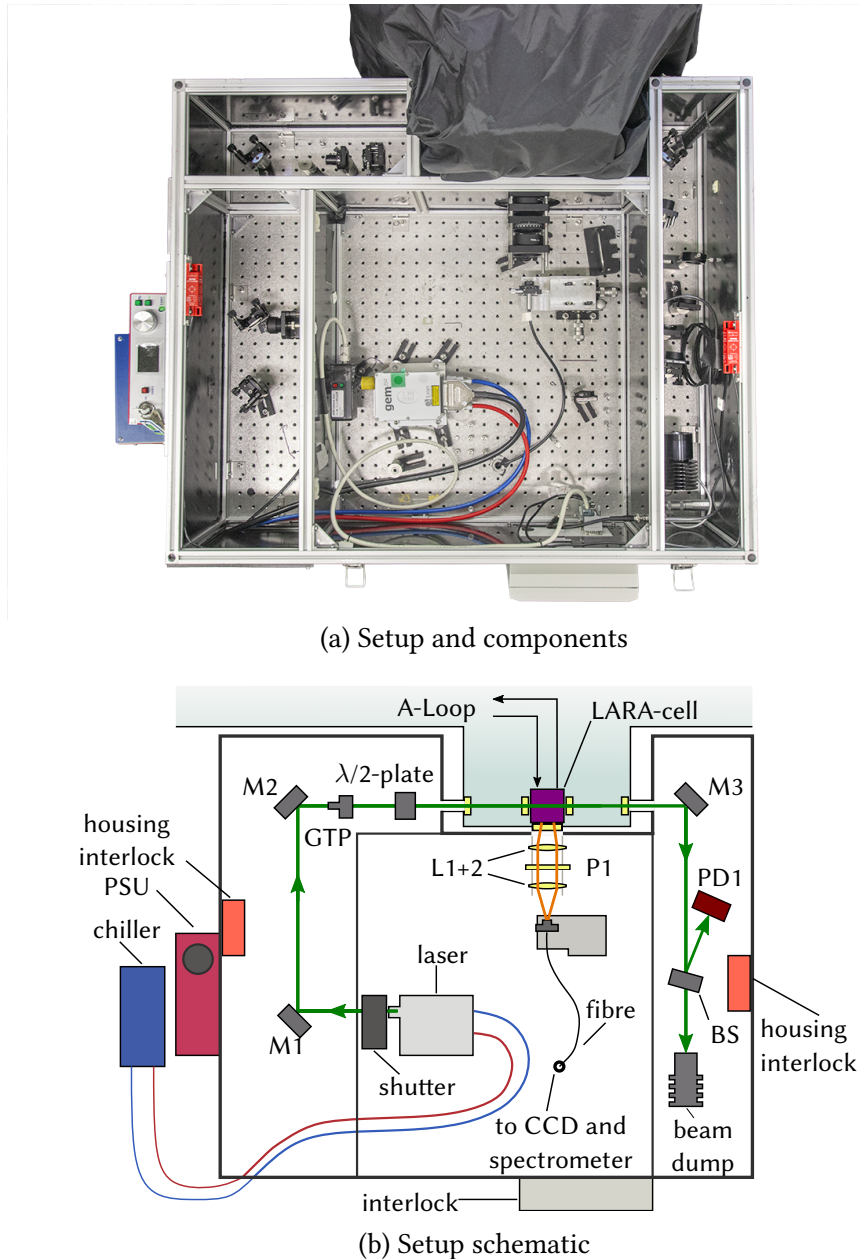


Figure 5.9: Beam path of LARA2 setup. The laser beam is guided via mirrors through a Glan-Taylor polariser (GTP), the gas-filled LARA-cell to a beam dump. A beam-splitter (BS) reflects 10% of the beam to a photo diode (PD) which controls the shutter via the interlock in case of intensity loss. The Raman-scattered light is focused by the lens pair L1+2 onto a fibre bundle and guided to the spectrometer and CCD below the optical table. The polariser P1 improves the Raman signal discrimination over ambient light. For improved ambient light suppression the appendix is covered in optical cloth, in addition to the LARA-cell enclosure made from dark anodised aluminium elements. Additional elements are M1, M2, M3 = beam steering mirrors; PSU = power supply unit; Permanent pinholes for beam alignment are not shown.

Table 5.3: Overview of LARA2 components.

Device	Model	Manufacturer	Specifications
Laser	GEM532 with MPC6000	Laser Quantum ^a	$P_L = (50 \text{ to } 2000) \text{ mW (CW)}$ ND:YVO ₄ 2 nd harmonic (TEM ₀₀)
Chiller	P103	Thermotek ^b	stability = $\pm 0.2 \text{ K}$
Glan-Taylor polariser	GT5-A	Thorlabs ^c	extinction ratio $1 \cdot 10^5:1$
LARA-cell		in-house development	$\Delta p_{\max} = 1 \text{ bar}$ broad-band AR-coating
Collection Optic	AC508-075- A-ML	Thorlabs ^c	AR Coating (400 to 700) nm
Raman filter	RazorEdge	Semrock ^d	$T > 0.97$ for $\lambda_{\text{Raman}} = 532 \text{ nm}$ $T < 10^{-6}$ for $\lambda_L = 532 \text{ nm}$
Fibre bundle	Custom	CeramOptec ^e	48 individual fibres, core = $100 \mu\text{m}$ Bundle height = 6 mm
Spectrometer	Acton SP 2150	Princeton ^f	$f = 150 \text{ mm}$ with aperture $F/4.0$ grating 600 g/mm $\lambda_{\text{range}} = (500 \text{ to } 750) \text{ nm}$
CCD-detector	PIXIS:400	Princeton ^f	back-illuminated 1340x400 pixel array pixel size $20 \mu\text{m} \times 20 \mu\text{m}$ $T_{\text{CCD}} \leq 70 \text{ }^\circ\text{C}$ Dark noise $\approx 10^{-3} \text{ e}^-/\text{s/pixel}$
Acquisition software	LARAsoft	in-house	Version 1.2 ^g written in labVIEW ^{hi}

^a Laser Quantum Ltd, Stockport, England

^b Thermotek AG, Baden-Baden, Germany

^c Thorlabs Inc., Newton, New Jersey, USA

^d IDEX Health & Science LLC, Rochester, New York, USA

^e CeramOptec GmbH, Bonn, Germany

^f Teledyne Princeton Instruments, Trenton, New Jersey, USA

^g The current version 2 was not available at the start of the measurement campaign

^h National Instruments, Austin, Texas, USA

ⁱ LARA2 driver limited to 32-bit systems

1. Laser source:

Due to the direct proportionality of laser power and scattered light intensity and the reduced Raman cross-section below ambient pressures inside the LARA cell a high-power 2 W diode pumped solid-state laser is used. The single transverse mode laser is water-cooled to a temperature stability of $\Delta T = \sim 0.1$ K for power stability during operation. In accordance with safety regulations the laser outlet is protected by a shutter connected to an interlock system. If the optical enclosure is opened or beam power at a control photo-diode is lost the shutter is locked closed.

The beam is guided via mirrors through a Glan-Taylor polariser (to improve the polarisation cleanliness) and a $\lambda/2$ -plate (to turn the polarisation plane from horizontal to vertical), before it is focused into the LARA-cell.

After traversing the cell the beam is split to the interlock photo-diode and a beam dump.

2. Raman cell:

The Raman cell consists of a metallic cube with 5 cm edge length, two manual valves for gas in- and outlet and four fused silica windows bonded into CF-16 flanges provided by CCFE¹² [Eng92]. Both laser windows are anti-reflective coated optimised for 532 nm while the perpendicular Raman light collection windows have a broadband AR coating for nearly lossless transmission of the scattered light [Tay01].

The Raman cell is the only part of the LARA-system in contact with tritium, making the setup convenient to adjust and maintain. The interface between the optical setup and the second containment is the *appendix* which includes three AR coated windows for laser and scattered light transmission as well as ambient light suppression by enclosing the cell in dark hard anodised aluminium shields. To avoid laser back reflection the windows are tilted by 1.5°. For consistent placement the cell has a dovetail joint to a clamp-like mount inside the appendix which connects to the base plate of the external optical setup.

3. Light collection optic and fibre:

Two achromatic doublets, one focused to the scattering region within the cell and one focused to the inlet of the fibre, transmit the scattered light towards the spectrometer. A long-pass filter is used to suppress light originating from Rayleigh scattering; reflections from within the cell and fluorescence in the cell windows; all can be up to three orders-of-magnitude higher intensity than the Raman light intensity.

The alignment and position of fibre, collection optics and filter are one of the primary contributors to the spectrally varying sensitivity of the setup necessitating calibration after each modification.

4. Spectrometer:

For composition monitoring it is sufficient to record and analyse the Q_1 -branches of

¹²Culham Centre for Fusion Energy, Special Techniques Group, OX14 3DB Oxfordshire, UK

all six hydrogen isotopologues, which fall within the spectral range (612 to 680) nm [Stu10a]. The setup is not optimised to single-line detection because the integral peak signal is used for higher absolute signal intensity. A wavelength calibration was performed for initial peak identification using a Ne hollow-cathode lamp.

5. CCD array detector:

The spectra is recorded using a detector with a back-illuminated CCD sensor of size 1340x440 pixel, operated at $-75\text{ }^{\circ}\text{C}$ for reduced dark noise. Using on-chip binning reduces the readout to 20 'lines' rather than the parent 400 pixel lines; this significantly cuts down on readout noise.

All subsequent data acquisition and basic processing was done in LARAsoft as described in Ref. [Jam13c]. These steps included e.g. :

- cosmic ray removal via time correlation;
- baseline subtraction via rolling circle filter;
- spectral sensitivity correction based on NIST SRM2242;

as described in Section 4.2.2.

Differences to KATRIN LARA-system

The general setup of LARA3 used for WGTS source gas monitoring is similar to the LARA2 system, but includes some iterative improvements from lessons-learned building previous systems:

1. Laser Power:

LARA3 deploys a 4 W Laser Quantum Finesse laser with identical wavelength to LARA2. The increased power yields higher Raman intensities and is especially suitable for the low pressures of ~ 150 mbar used in KATRIN [Sch11]. This is comparable to the cell pressures used during the TRIHYDE-campaigns hence the LARA2-system would benefit from a higher power laser.

2. Back-reflection of the laser beam:

In LARA3 the laser beam after passing through the cell is collimated, reflected and refocused into the cell. The beam is then deflected away from the incoming beam via an optical insulator to avoid performance instabilities and damage to the laser head[Fis14]. By double-passing the beam through the cell the scattered light intensity is doubled, increasing the SNR.

Additional minor differences in component selection and setup, e.g. database connection or beam monitoring exist but are of lesser importance. It should be notes that, while slightly different in their setup, the calibration procedures, analysis methods and basic optical setup are identical for both LARA2 and LARA3 systems.

Table 5.4: Overview of selected Loop instrumentation parameter.

Parameter	RGA	BGA	BIXS
manufacturer	MKS ^a	SRS ^b	TLK
model	HPQ3S	BGA244HP	TRACE2.0
method	mass spectrometer	speed of sound	x-ray spectrometer
type	composition	composition ^c	activity
detector	farraday cup with tungsten filament	acoustic resonator	Amptek OEM AXR SSD ^d
max. pressure	$1 \cdot 10^{-3}$ mbar	170 bar	1000 mbar ^g
min. pressure	$8 \cdot 10^{-11}$ mbar	<344 mbar ^f	-
operating temperature	(10 to 40) °C	(-20 to 70) °C ^e	-40 °C
measurement frequency	1 min ^{-1h}	4.4 Hz	1 min ^{-1h}

^a MKS Instruments Inc, Massachusetts 01810, USA

^b Stanford Research System, California 94089, USA

^c in general limited to two components

^d Amptek Inc, Massachusetts 01730, USA

^e cavity stabilised at 45 °C

^f depending on gas species

^g differential pressure at Beryllium x-ray window

^h user selectable, depending on target accuracy

5.4.3 Additional analytical methods

In this section, a brief overview of selected additional methods currently installed in TRIHYDE is given, summarising their important operating parameters in Section 5.4.3. All systems were connected to a dedicated NPT-server synchronised to the DCF77-signal¹³ to ensure time synchronicity among the various components. These methods have the common task of further improving sample composition monitoring.

Mass spectrometer

For identification of non-hydrogen components in the loop a quadrupol mass spectrometer is used as residual gas analyser (RGA). Although mass spectrometers are successfully used in tritium analytics [Ich85] they have some limitations:

1. Low maximum pressure:

Despite the ability to discriminate between all hydrogen isotopologue ions, the maximum gas pressure of usually $1 \cdot 10^{-6}$ mbar is a major disadvantage [Cal01]. Due

¹³Meinberg GmbH, Bad Pyrmont, Germany. Model DCF600

to the low pressure, a pumping or expansion arrangement must be implemented for process monitoring, which can alter gas composition.

2. Peak overlaps:

Due to several overlaps of key mass signal, e.g. ^3He , HD and T^+ at 3 u or ^4He , D_2 and HT at 4 u, a high resolution system is necessary to discriminate the individual isotopes. These systems usually use either soft ionisation [Yu16] or long quadrupol filters [Kle16]. Although commercially available, in general these systems are limited in maximum pressure and mass range (typically (1 to 20) u).

In TRIHYDE, the main purpose is identification of gas impurities above 9 u and therefore require a mass range of at least (1 to 100) u. The focus is not the quantification of hydrogen species, but qualification of heavier components, preferring a higher operating pressure to limit pressure difference between process gas and gas sample. From initial experiments the limit of detection for tritiated methane of the existing setup is $\sim 0.3\%$ ¹⁴.

The RGA is controlled via the supplied *MKS Process Eye* software in version 5.81 and initial calibration was done using a $\text{CO}_2\text{-He-N}_2$ reference sample. During the measurement campaigns the inlet pressure was kept constant at $1 \cdot 10^{-4}$ mbar using the manual inlet valve and a *MKS 627D Baratron* with $1 \cdot 10^{-1}$ mbar full scale.

Binary Gas Analyser

In general, the speed of sound c_o of a gas mixture is a function of the molar fraction x_i , molecular weight M_i and heat capacity C_{pi} at constant pressure of each component i is given by [Löf03]:

$$c_o^2 = R_0 \cdot T \frac{\sum x_i C_{pi}}{\sum x_i M_i \sum x_i (C_{pi} - R_0)} \quad (5.25)$$

with absolute temperature T and universal gas constant R_0 . In case of a binary mixture of known constituents Equation (5.25) can be solved to obtain the molar ratio. Common applications for these measurements include:

- Leak detection in cryogenic storage facility [Alh15],
- Gas quality analysis in medical or petrochemical industries [Dou16].

This approach, in general, has several advantages[Sta16]:

- + Typical accuracy of about 0.1 % (dominated by pressure reading),
- + No moving parts,
- + High time resolution,
- + High zero and drift stability of 5 ppm/yr
- + Tritium compatible material and no possible ignition sources .

¹⁴A. REIN: ‘Estimation and analysis of impurities in calibration gas mixtures for the Tritium-Hydrogen-Deuterium-Experiment (TRIHYDE)’. Master’s thesis. Karlsruhe Institut of Technology, IEKP, 2015.

But associated with the basic measurement principle the method suffers from several disadvantages.

- No gas species identification:
The gases used must be known a-priori to solve Equation (5.25) for a given ratio.
- Only binary mixtures:
Using only the speed-of-sound measurement, the molar ratio can only be determined for a binary mixture, even if further information about the gas composition is available.

In TRIHYDE, the system is predominately used to confirm the initial gas purity and verify the homogenisation time constant of the calibration gas sample. The system is especially useful to detect nitrogen contamination due to the large difference in speed-of-sound of N_2 and hydrogen isotopes (349 m s^{-1} vs. 1270 m s^{-1} [Zuc02]). Studies of speed-of-sound properties in tritiated mixtures are ongoing providing experimental verification to theoretical calculations [Ma20].

In order to measure the speed-of-sound, the gas is guided through a cylindrical cavity within the BGA. The cavity has acoustic resonances whose frequencies are proportional to the speed-of-sound in the cavity. On both opposite ends, an acoustic transducer is coupled to the cavity. At one end the transducer functions as a speaker and emits a broad-band signal from $\sim(0.5 \text{ to } 10) \text{ kHz}$. At the other end, the transducer functions as a microphone and measures the transfer function through the cavity. The resonant frequencies are determined by Lorentzian line shape fits to the spectrum and used to derive the speed-of-sound of the gas [Sta15].

In order to normalise the speed-of-sound under measurement conditions to standard conditions, the experimental pressure is measured by a *Honeywell SPT 0015P* pressure sensor directly connected to the BGA.

Beta Induced X-Ray Spectrometer

The basic principle of BETA INDUCED XRAY SPECTROMETRY (BIXS) for activity monitoring in tritiated gases was first described in Ref. [Cur72] and is based on the detection of bremsstrahlung originating from attenuated beta electrons. The spectrum intensity is depending to the tritium activity but influenced by gas pressure and setup. BIXS is a promising tritium sampling technique, which is currently in use for inline process control [Röl15a], tritium depth profiling in material [Mat02] or tritiated water [Nie15]. It is also deployed for activity monitoring of the WGTs [Bab12] and CPS purge gas at KATRIN. These examples illustrate the wide application range of BIXS, spanning high tritium content in the WGTs; tritium traces in helium in CPS; and emphasise the necessary wide concentration range of gas samples provided by TRIHYDE.

A basic setup for a gaseous BIXS cell, based on the TRitium Activity Chamber Experiment (TRACE), is shown in Figure 5.10 and is assembled containing the following components:

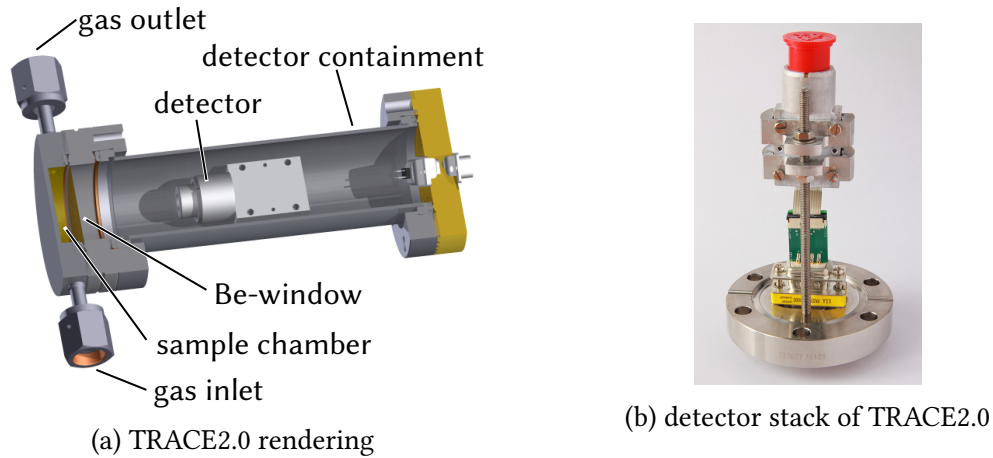


Figure 5.10: Setup of the BIXS experiment TRACE2.0. The detector is placed inside the containment for optimal x-ray detection efficiency but at a sufficient distance from the sample chamber to keep it within the temperature specification of the electronics during bakeout.

- (i) Au-coated sample chamber,
- (ii) Au-coated Be window,
- (iii) Silicon Drift Detector (SDD) for x-ray detection,
- (iv) Second containment in case of window failure and to prevent detector contamination when used inside a glove box.

Process gas flows through the sample chamber where decay beta-electrons are stopped in the chamber walls; the subsequent bremsstrahlung is transmitted via a Be-window to the detector. The acquired spectrum is affected by the spectral distribution of the tritium beta-electrons; the transport function of the setup; the detection efficiency of the detector; and the characteristic x-ray lines of exposed materials.

The cell used in TRIHYDE named TRACE2.0 is a design iteration of TRACE¹⁵¹⁶ with the following improvements:

- (i) reduced sample chamber volume,
- (ii) simplified detector containment,
- (iii) designed for bake-out of sample chamber up to 200 °C¹⁷.

¹⁵S. EBENHÖCH: 'Systematische Untersuchungen eines Röntgendetektorsystems zur Überwachung der KATRIN-Tritiumquelle'. Bachelor's thesis. Karlsruhe: Karlsruher Institut für Technologie, 2012.

¹⁶D. WALTER: 'Charakterisierung einer BIXS-Messzelle zur Bestimmung der Tritiumkonzentration in Prozessgasen mittels statischen und dynamischen Messungen'. Bachelor's thesis. Karlsruhe: Karlsruher Institut für Technologie, 2014.

¹⁷M. OEHLER: 'Construction and setup of an optimised BIXS measuring device and temperature dependent measurements of the detector performance'. Bachelor's thesis. Karlsruhe: Karlsruher Institut für Technologie, 2015.

During the measurements performed in this thesis work, the cell was used for basic activity monitoring. For a more in-depth performance characterisation of the design, further studies will need be performed in future work.

5.5 Commissioning of TRIHYDE

Before the two measurement campaigns using stable and radioactive isotopologues commenced an extensive process commissioning was performed. During this phase functionality and correct positioning of all components were verified including the following steps:

- (i) Helium leak testing to $<1 \cdot 10^{-9}$ mbar l s⁻¹ for all individual connections;
- (ii) X-ray quality testing of >50 % of all welds;
- (iii) Inspection and testing of electrical safety;
- (iv) Signal integrity check for all measurement system cabling;
- (v) Calibration and plausibility check of all sensors;
 - a) Matching of all pressure sensors by filling both loops with N₂ at various pressures,
 - b) Verification of the flow controller by filling the mixing vessels and comparing the pressure increase vs the flow rate,
- (vi) Pump direction, performance and achievable minimum pressure;
- (vii) Confirmation of all safety interlocks;
 - a) Disconnection of all possible ignition sources,
 - b) Pump shutoff in case of over pressure,
 - c) Positive pressure gradient at gas inlet.

After the successful basic commissioning the first measurement campaign using stable isotopologues was performed. These measurements were all performed without closed second containment and connection to the tritium processing part on TLK-infrastructure, using a scroll pump in place of the ZTs and guiding exhaust gases directly to a vent.

Prior to tritium operation, the integrity of the second containment leakrate of ≤ 0.1 % h⁻¹, the functionality of the TRS, and the system maintaining an inert-gas atmosphere in the glovebox were verified (details in Section 7.1.2).

Based on the design and setup of TRIHYDE the system performance exceeds the predecessor HYDE-experiment and is able to provide gas samples of all six hydrogen isotopologues with sufficient accuracy for LARA-calibration. A basic summary of the process parameters and capabilities is given in Table 5.5.

Table 5.5: Summary of general TRIHYDE components and capabilities.

(i) Experimental capabilities		(ii) Overview of components	
Parameter	Capability	Components	Quantity
gas species	H ₂ , D ₂ , T ₂ , He ^a	valves	113
pressure range	(1 · 10 ⁻³ to 900) mbar	pressure sensors	39
temperature range	(20 to 200) °C	additional sensors ^b	25
mixing volume	max. 1.6 litre	electrical heaters	5
volume uncertainty	<0.25 %	pumps	5
pressure uncertainty	<0.15 %	connections	308
temperature uncertainty	<0.2 %	welds	354

^a expandable to other gas species

^b includes e.g. temperature sensors and activity monitors

6 LARA-calibration based on the stable hydrogen isotopologues H₂, D₂, and HD

In order to process tritiated gas samples, a detailed commissioning of TRIHYDE using the stable isotopologues is required. The first part of this chapter describes the sample preparation process as well as the analysis strategy using TRIHYDE, including the signal processing of the obtained LARA spectrum. In the second part the results of the LARA-calibration for both *binary* H₂-D₂ as well as *tertiary* H₂-HD-D₂ samples are discussed and compared to the results obtained using the predecessor setup HYDE. The conclusions drawn from these TRIHYDE studies with stable isotopologues are of great relevance for the investigation of tritium-containing samples. It is paramount to evaluate the system's properties before the introduction of tritium, in order to understand the impact tritium might have on the preparation of samples and their evolution over time. All operations with tritium are more demanding, due to limited access to many of the system components and the required safety measures. Hence, it was deemed necessary to characterise full performance and handling procedures prior to T₂ measurements.

6.1 Overview of measurements with H₂ and D₂

The mandatory process commissioning of the TRIHYDE-experiment was carried out with N₂ before starting with H₂-D₂ measurements. During this phase all system components were tested whether they reached and fulfilled their specified performance. Also, all safety interlocks were checked for full functionality.

The ultimate goal of the subsequent scientific commissioning was the proof of readiness for tritium operation, and includes the following steps:

1. Characterisation of the setup systematics, e.g. homogenisation time and achievable gas purity;
2. Preparation of stable gas samples of H₂ and D₂ both for binary mixtures (containing only homonuclear molecules) and tertiary mixtures in chemical equilibrium (featuring heteronuclear HD as well);
3. Determination of the Raman calibration factors R_x .

A more detailed overview is provided in Figure 6.1.

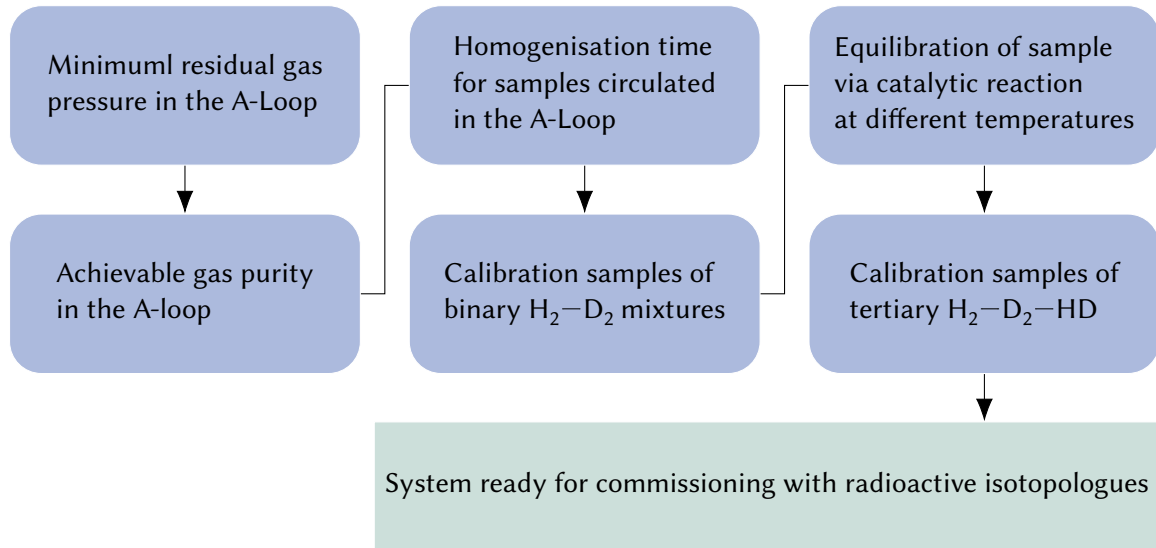


Figure 6.1: Overview of measurement steps in H_2 campaign. All steps are required to verify the general system performance and readiness for subsequent tritium operation.

For all measurements, the TRIHYDE-setup was disconnected from the tritium-processing TLK-infrastructure and exhaust gases were removed via a dedicated pumping system, which was only used during the non-radioactive campaign.

The results and experience gained can be compared to those from the predecessor experiment HYDE in order to verify the results reported in Ref. [Sch13b]. Furthermore, one can estimate the achievable accuracy of the calibration factors for the radioactive isotopologues.

6.2 Experimental determination of the calibration factors

In the first half of this section, the sample preparation procedure is described, followed by an overview of the signal analysis and determination of calibration factors.

6.2.1 Description of experimental procedure and analysis strategy

Each sample was prepared using the procedure summarised in Table 6.1. The full step-sequence was executed to ensure that

- the residual gas inside the loop and wall deposits from previous samples did not influence the molar ratio;

Table 6.1: Overview of the measurement procedure for calibration-gas samples with stable isotopologues. The components are named according to the flowchart shown in Figure 5.5.

Step	Procedure
1.1	Evacuate complete vacuum system to $<1 \cdot 10^{-3}$ mbar
1.2	Cool down all components to glovebox temperature
2.1	Flush gas filters to remove trace amounts of N_2 or other impurities in H_2
2.2	Fill BV005 to target pressure with H_2 (range (100 to 900) mbar)
2.3	RGA measurement of gas purity
3.1	Evacuate piping to $<1 \cdot 10^{-3}$ mbar
3.2	Flush gas filters to remove trace amounts of N_2 or other impurities in D_2
3.3	Fill BV006 to target pressure with D_2 (range (100 to 900) mbar)
4.1	Circulate via bypass as well as catalyst for <20 min to prime the system and catalyst
4.2	RGA measurement of gas purity
5	Repeat steps 1 to 3
6.1	Circulate via bypass for >20 min and record LARA-spectra with 60 s acquisition time
6.2	Stop circulation and perform RGA measurement
7.1	Open valves to catalyst, close inlet valve of bypass, and circulate for >20 min
7.2	Stop circulation and perform RGA measurement
8.1	Increase catalyst temperature to 50°C , and circulate for >20 min
8.2	Stop circulation and perform RGA measurement
9	Repeat steps 8.1 and 8.2 in 25°C -steps up to 150°C

- no additional impurities were present in the pure H_2 and D_2 samples;
- both binary H_2 - D_2 and tertiary H_2 - D_2 - HD samples were prepared for each initial molar ratio.

Analogously to the experiments described in Ref. [Sch14a], the loop was wetted/primed with a sample of the same isotopic ratio to mitigate a possible shift introduced while circulating gas the A-Loop.

In preliminary experiments, it was discovered that N_2 could migrate into the sample via the gas supply lines. This is likely caused by back diffusion through the safety check valves. The N_2 -level was on a sub-percent level but could be reduced below the minimum detectable partial pressure of the RGA ($1 \cdot 10^{-10}$ mbar) by flushing of the filter stage sufficiently long prior to filling the mixing vessels.

Any mixture of H_2 and D_2 will tend to its isotopologue ratio, governed by the balanced exchange reaction



for a given temperature; it depends on the equilibrium constant

$$K_{eq}(T) = \frac{[HD]^2}{[H_2] \cdot [D_2]}. \quad (6.2)$$

A more detailed description of the equilibration process and the significant role of tritium's radiochemistry is given in Section 7.3. Due to the low reaction rate of the first order equilibration reaction, an isolated mixture of H_2 and D_2 will only reach chemical equilibrium on a timescale of months/years. Therefore, one can assume that the isotopologue ratio does not change during sample circulation. Thus, the initial binary mixture was used to determine the calibration factors R_{H_2} and R_{D_2} .

Like in the HYDE setup, the mixture was circulated via an $Pd-Al_2O_3$ catalyst reactor to produce HD according to the chemical equilibrium reaction (Equation (6.2)). In order to evaluate the temperature dependence of the equilibrium constant and the catalyst reaction, the temperature of the catalyst was stepwise increased during the measurements.

After each step, a RGA-measurement was performed to verify that no impurities were introduced during sample processing. During the RGA-measurements, circulation was stopped in order to minimise pressure fluctuations at the RGA-inlet. In case the RGA spectra showed any impurity contamination, the gas was discarded and subsequently the filter-flushing was extended by at least a factor of 2.

In Figure 6.2 the pressure, temperature and concentration profiles of a typical sample production are displayed. For better clarity, the priming procedure is omitted. The individual traces display the following measurement data:

- RP100 and RP102 represent the pressure in the mixing vessels while RP106 represents the pressure in the LARA-cell. During circulation, the pressure readings diverge due to the dynamic pressure drop along the loop.

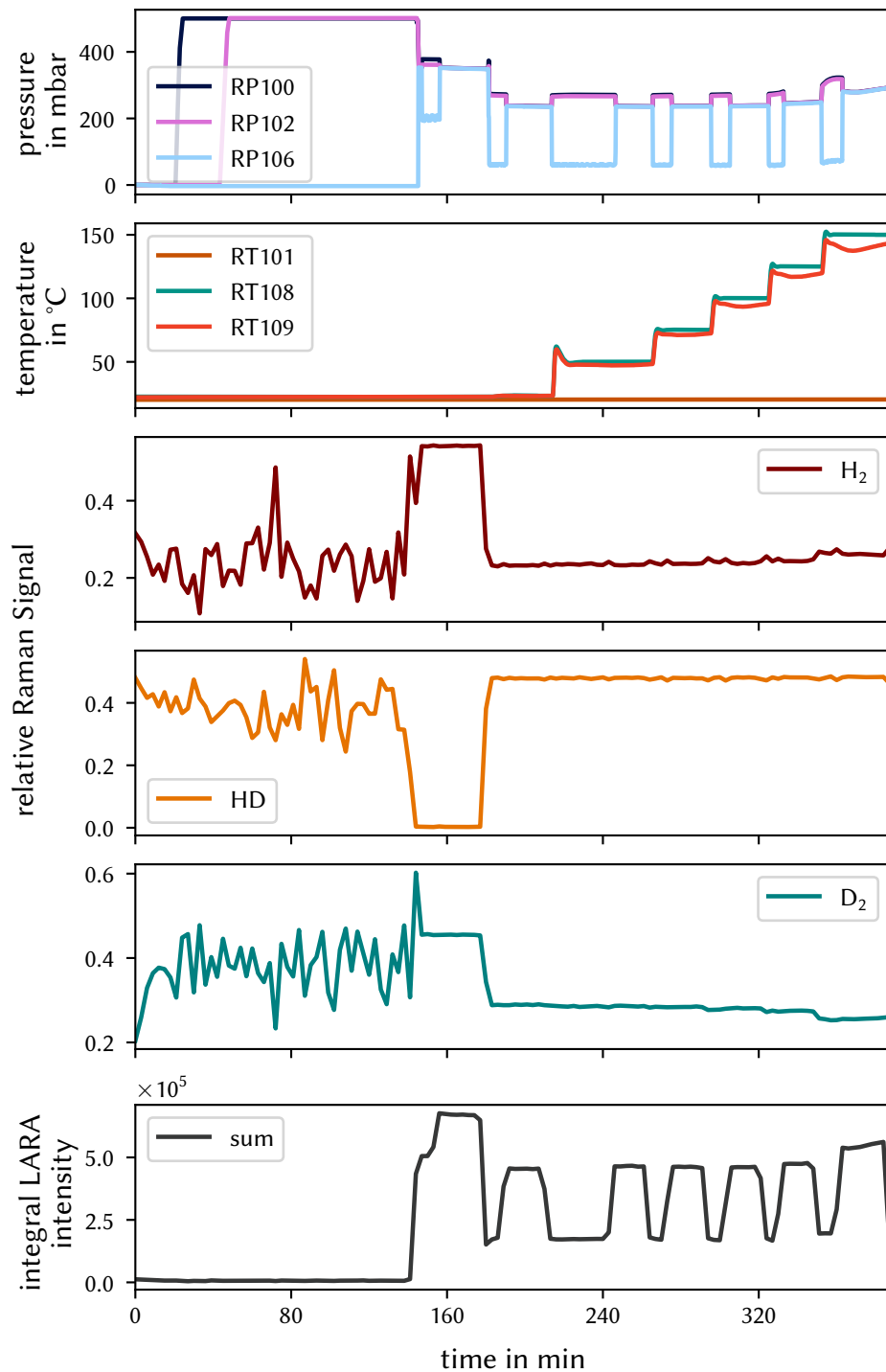


Figure 6.2: Pressure, temperature, concentration and Raman signal profile of a typical calibration run with stable isotopologues of ratio 50-50. Prior to the displayed measurement data, the loop was primed with a sample prepared with the same molar ratio, circulated via the bypass and catalyst. RT108 represents the catalyst inlet and RT109 the outlet temperature while RT101 is the temperature in one of the mixing vessels. At each temperature step, circulation was stopped while recording an RGA spectrum. No system calibration was applied.

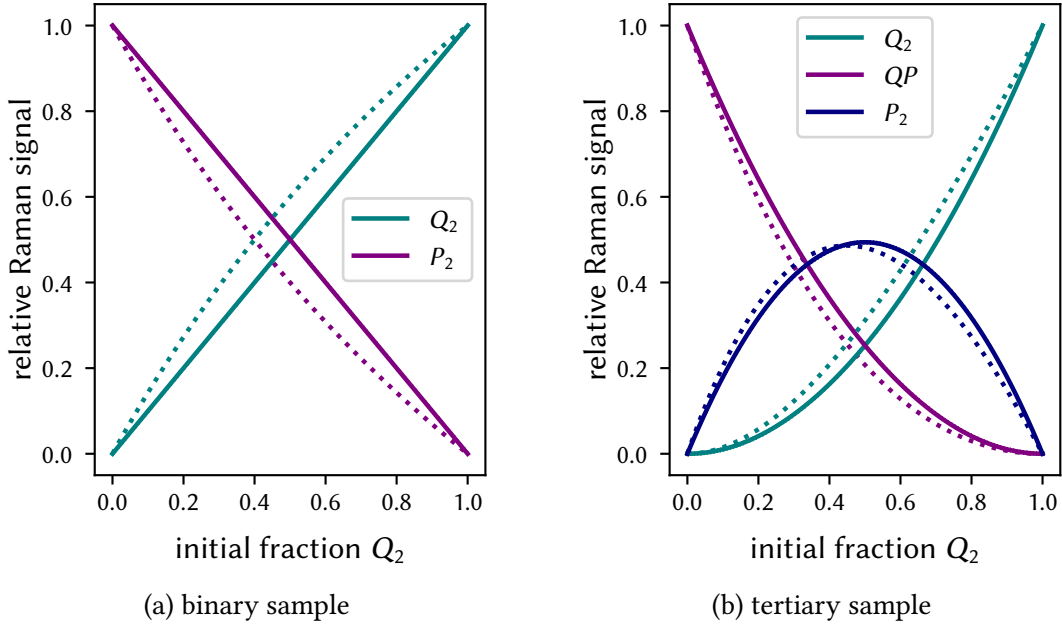


Figure 6.3: Sample calibration curves of binary and tertiary gas samples using arbitrary calibration factors and equilibrium constants. The straight lines are for an ideal calibration factor of $R_x = 1$. Applying the calibration factors introduces a shift for each isotopologue according to Equation (6.3). Note that $Q, P \in H, D, T$.

- The temperature sensors RT108 and RT109 are located at the inlet and outlet of the catalyst cylinder and RT101 reads the temperature of the mixing vessels. At temperatures above 100°C , it took longer for the outlet temperature to reach the set temperature. The temperature sensors of the mixing vessels are positioned sufficiently far away from the catalyst to be affected by the elevated catalyst temperature.
- Throughout loop evacuation the relative Raman signals fluctuated marginally around zero. After starting circulation, the sample is homogenised after ~ 5 min and nearly constant signals for H_2 and D_2 were observed, proportional to the initial pressure ratio. No significant HD signal was observed. When circulating via the catalyst, HD is produced according to Equation (6.2) with a corresponding decline in H_2 and D_2 . At temperatures $>75^\circ\text{C}$, a continuous decrease of D_2 and increase of H_2 was observed. This effect and possible causes are discussed in Section 6.2.3.
- The integral LARA-signal intensity was proportional to the gas pressure, which increased linearly with catalyst temperature.

The relative Raman signal S_x for particular molar fraction y_x and calibration factor R_x is given by [Sch14a]:

$$S_x = \frac{y_x \cdot R_x}{\sum y_Q \cdot R_Q} \quad Q = H_2, D_2, HD \quad (6.3)$$

In Figure 6.3, the effect of calibration factors on the calibration curves is illustrated for binary and tertiary mixtures of arbitrary isotopologues. For $R_x \neq 1$, isotopologue-specific factors introduce a visible shift from the ideal curves according to $R_x = 1$.

The initial molar fraction is determined by the pressure and volume ratio of the mixing vessels and the relative Raman signal is obtained by averaging the signal strength during the corresponding circulation step. Details on LARA-signal processing can be found in Section 6.2.2. By simultaneously fitting the calibration curve to the data points the respective calibration factors can be derived. For a binary sample, only the calibration factors of the homonuclear isotopes can be measured. In contrast, a tertiary sample offers access to both homonuclear and heteronuclear isotopologues. However, using distinct binary and tertiary samples has several advantages. When using the binary sample, the determination of the homonuclear calibration factors benefits from:

- (i) Increased SNR for the main sample components due to the suppression of the negligible third isotopologues,
- (ii) Lower statistical uncertainty of the calibration curve regression using fewer free parameter,
- (iii) No possible systematic effects introduced by the catalyst and equilibration reaction.

Using the tertiary sample, the calibration factor of the corresponding heteronuclear isotopologue can be obtained and the results crosscheck with the binary sample.

The calibration factors can be derived from the LARA-signals with and without spectral sensitivity correction:

- (a) Without spectral sensitivity correction:

The derived calibration factors represent the absolute calibration factors R_x for the system in its present state. These factors can be used for high accuracy composition measurements within TRIHYDE, e.g. samples from other experiments. Although these factors can be obtained with a relative lower uncertainty, they are neither transferable to other systems nor can they be mitigated in case the setup is altered.

- (b) With spectral sensitivity correction:

Applying the sensitivity correction given by the SRM-standard the derived factors are the theoretical sensitivity factors necessary for the calibration process described in Ref. [Sch13c]. These factor can be implemented in all other TLK Raman systems to improve composition measurement trueness. Since the gas sample uncertainty is combined with the spectral standard uncertainty, the resulting uncertainty is higher.

Both factors are useful for composition monitoring using LARA-systems, although the factor with incorporated spectral sensitivity correction is more important due to its general applicability and relative ease of implementation.

All analysis was performed using the software tools *pandas* [McK10], *scipy* [Vir20] and *lmfit* [New14] within the Python programming environment (here Python v3.7.6). Pressure and temperature readouts were recorded with a *Siemens Simatic PCS 7*, which was also

used for process control of the experiment. The Raman spectra were recorded using the software package *LARAsoft* version 1.2 as described in Ref. [Jam13c] and in Section 4.2.2.

6.2.2 Evaluation of the measurement uncertainty

Uncertainty associated with the properties of gas samples

The sample composition uncertainty is derived from the uncertainty budget given in Section 5.2.4. For stable gas samples it is dominated by the following factors:

- Gas purity:
The initial purity of H_2 was given as $>99.9999\%$ by the manufacturer and confirmed via RGA. For D_2 the initial purity was stated as $>99.8\%$ with the remaining 0.2% assumed to be HD . The HD content was confirmed via LARA-measurements calibrated using the existing calibration factors as well as RGA-measurements.
During long-term circulation in the commissioning phase, no change in isotopic composition was observed, hence gas-wall-interactions or leaks could be excluded. By evacuating the loop to $<1 \cdot 10^{-3}$ mbar the residual loop pressure contribution to the sample is less than 1 ppm.
- Temperature:
Both gases were fully thermalised after filling the mixing vessels as confirmed by the constant temperature and pressure readings, allowing the assumption that both gases are at the same temperature prior to mixing. As long as the gases are within $1^\circ C$, the contributing uncertainty is less than 0.3% .
- Pressure:
The stated uncertainty of the pressure sensor is $\sigma_p = 0.12\%$ of the actual reading (not for full scale, as is frequent specified) Since the pressure ratio and not the absolute reading is important for the molar fraction, all sensors were zero-adjusted prior to each individual run, as specified by the manufacturer.
- Volume:
The uncertainty of the mixing vessel volume is $\sigma_V = 0.2\%$, as derived in Section 5.2.4 with.

Using these values the estimated uncertainty for the initial molar fraction of the gas sample is of the order 0.4% , according to Section 5.2.4. This value is below the uncertainty stated in Chapter 5 due to the absence of radiochemical gas-wall reactions, as well as reactions within the gas sample.

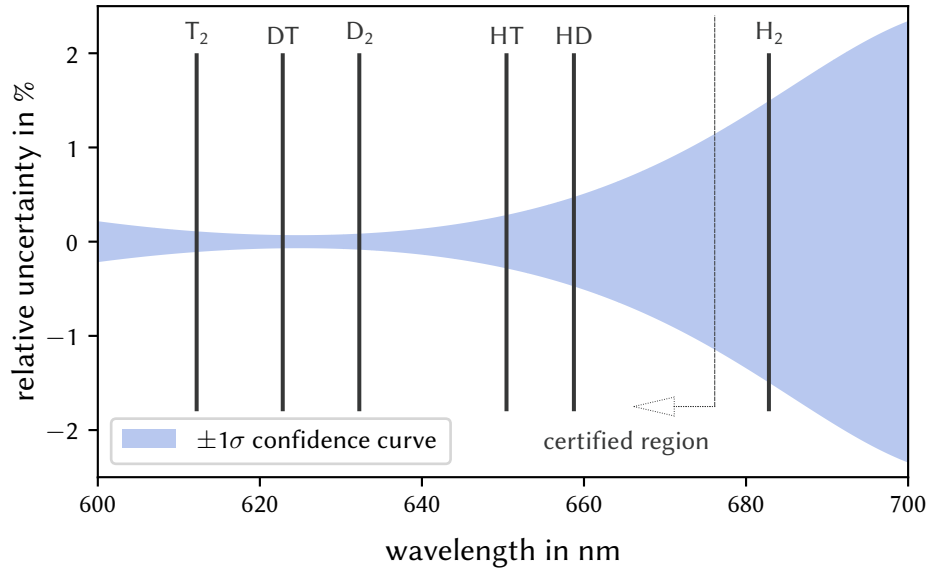


Figure 6.4: Confidence interval of the NIST luminescence standard SRM 2242. Within the certified spectrum, the 1σ uncertainty interval is given by fifth-order polynomial, while the extended region with increased uncertainty is given as a dataset. The parameters for both regions are provided by Ref. [Nat19].

Uncertainty of the relative Raman signal intensity

For each LARA spectrum the scattered light was integrated for 60 s unless otherwise noted. In order to convert the CCD signal to a Raman spectrum, the following basic processing steps, as described in Section 4.2.2, were performed using LARASOFT:

- (i) Dead pixel removal;
- (ii) Cosmic ray removal;
- (iii) Baseline subtraction;
- (iv) Spectral sensitivity correction:

Depending on whether the absolute calibration factors or the theoretical sensitivity is measured this step is optional. In order to correct for the wavelength depending efficiency of the optical setup, including the CCD detector, collection optics and the fibre bundle, the SRM standard [Nat19] as described in Section 4.3.1 is used to record a reference spectrum. The uncertainty band for the SRM2242 standard is shown in Figure 6.4. Full details on the calibration procedure can be found in Ref. ZELLER¹; a summary is given in Section 4.3.1. The combined spectral uncertainty is given by the luminescence standard and the calibration procedure [Nie18].

¹G. ZELLER: 'Development of a calibration procedure and calculation of the uncertainty budget for the KATRIN laser Raman system'. Master's thesis. Karlsruhe Institute of Technology, EKP, 2017, available online at katrin.kit.edu.

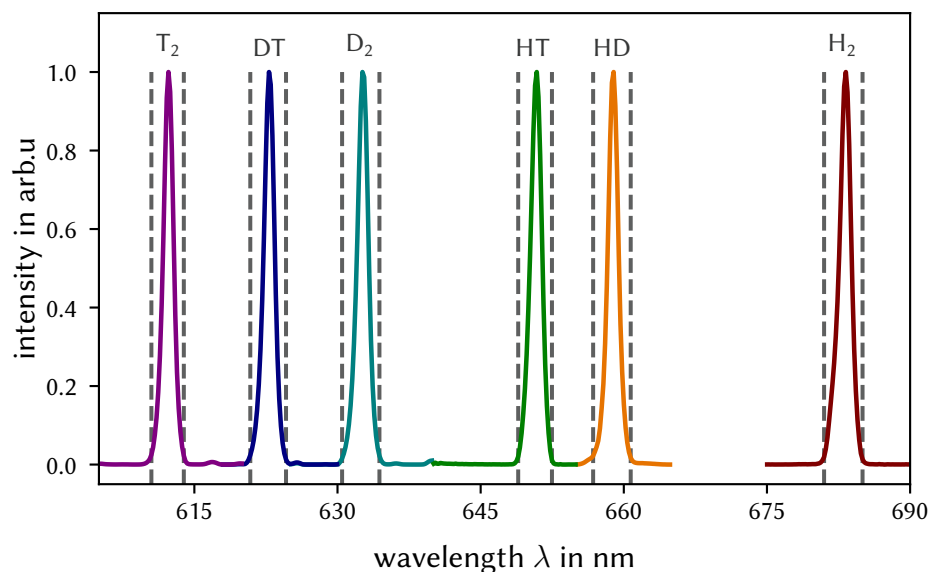


Figure 6.5: Q_1 -branch intervals for all hydrogen isotopologues used during calibration. The interval width is determined by a prominence factor of 0.98 for each isotopologue individually, see the main text for further explanation. For concentration measurements, the integral signals were used.

In order to convert the recorded spectra to peak intensity values, the Q_1 -branches for each isotopologue were integrated within a specific wavelength interval. Given the sufficient separation between the vibrational branches, these integrals can be used to quantify the individual branch intensities. However, overlaps from S_1 - and O_1 -lines are possible, e. g. S_1 - D_2 and O_1 - H_2 are within the Q_1 - HD integration interval. These overlaps can be corrected for by measuring the signal ratio between the S_1 -lines as well as the O_1 -lines and the Q_1 -branches respectively for a single isotopologue. The derived overlap intensities are subtracted from the affected Q_1 -branch.

In order to obtain reproducible and transferable intervals, the peak widths were determined by using the *peak-prominence-function* from SciPy's signal module². The *prominence* of a peak describes how much a peak stands out from the baseline within a specified interval and is defined as the vertical distance between the peak and its lowest contour line. The *prominence value* P describes the relative difference between the peak maximum and the baseline minimum³.

This procedure was selected as it results in reproducible integral intervals and is not influenced by the individual peak shape. Thus, the procedure is applicable to all LARA systems used at TLK. A value of $P = 0.98$ was chosen as a combination of maximum signal strength,

²Within this work, the function `scipy.signal.find_peaks()` as implemented in the package v1.5.2 was used.

³Further details of the function and implementation can be found in the SciPy documentation (see <https://docs.scipy.org/doc/>).

robustness against baseline noise and independence of search interval. The resulting peak intervals are shown in Figure 6.5.

In contrast the analysis performed at KATRIN uses individual shape-fits to each Q_1 -branch, which has the advantage of being less susceptible to beam walk or drift of the system. This is important for the long-term stability needed in KATRIN operation; on the other hand, this methodology may add fit uncertainties. During the relative short sample preparation and analysis times in TRIHYDE, which are on a scale of hours to a few days, the integration of the peak intensity is preferred method. Without the shape-fits, only the shot-noise of the intensity signals needs to be considered.

The wavelength calibration of the spectrometer was done using a Ne-calibration light source, in order to enable the unambiguous identification of the individual branches (see reference [Lai20] for line positions of tritiated isotopologues). However, the wavelength calibration accuracy has no influence on the sensitivity calibration, as the integration intervals are derived from the prominence values and not from user-selected wavelength intervals.

For the calibration data points, the weighted relative Raman signal was averaged during each of the individual measurement steps summarised in Table 6.1.

Uncertainty of the calibration curve determination

In order to retrieve the calibration factors, the model function as described in Equation (6.3) is fitted to the calibration data points given by the relative Raman signals and initial molar fractions. This was done by simultaneously minimising the residuals for all isotopologues using the Python package *lmfit*⁴ [New14].

Due to the correlation of the calibration factors and the small sample size, a bootstrap resampling method was used to estimate the statistical uncertainty of the regression [Efr83; Efr93]. This approach is analogous to the data analysis applied in reference [Sch14a].

For the bootstrap sampling the data points were independently and randomly resampled with replacement, meaning the same datapoints can appear multiple times in the new bootstrap sample. For each calibration dataset, at least 10^4 data sets were resampled with uniform probability distribution. The calibration curve, as described in Equation (6.3), is refitted to the bootstrap sample and the resulting distribution is used as an estimate for the mean value and uncertainty width of the LARA calibration factors.

In order to also consider the uncertainties of the initial molar fractions, the complete dataset is shifted by the composition uncertainty, as derived in Section 6.2.2, in both direction on the x-axis and resampled respectively. From the resulting new mean values, the larger difference between the new and the unshifted value is used as an estimate of the

⁴Within this work, the function *lmfit.minimizer()* based on the Levenberg-Marquardt algorithm as implemented in the package v0.9.13 was used.

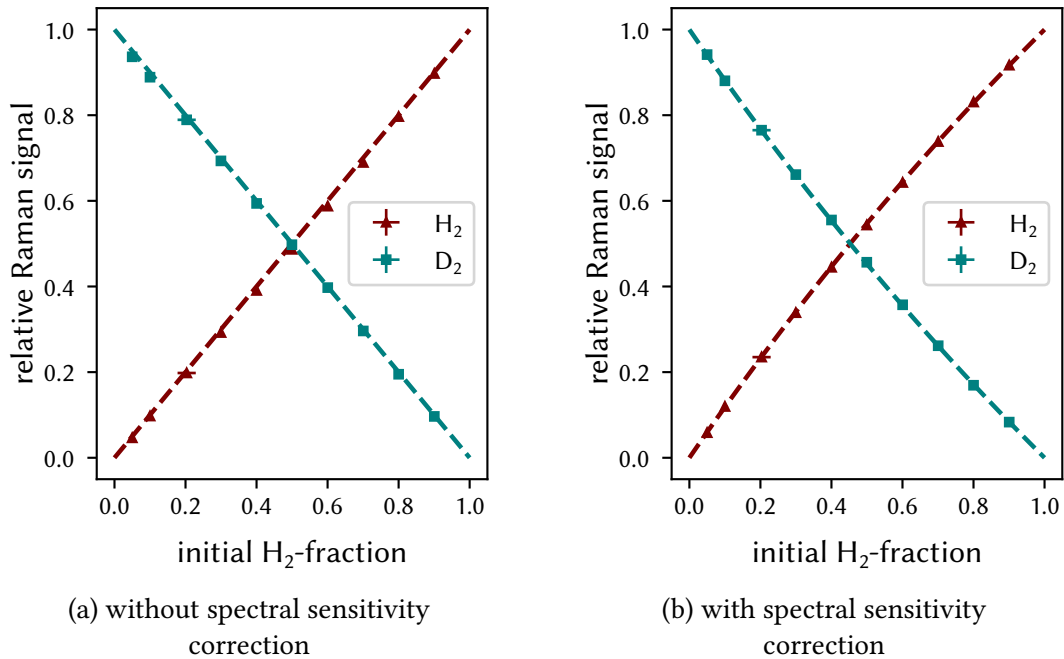


Figure 6.6: Calibration curve for H_2 – D_2 binary mixtures. The initial molar fraction are determined by the pressure ratio in the mixing vessels. The Raman signal are derived by averaging the individual Q_1 -branch intensities after the gas sample was homogenised and the intensity remained constant. After applying the spectral sensitivity correction, the shift introduced by the theoretical intensity is clearly visible. The model function is given in Equation (4.38).

systematic influence on the sample composition. Given a similar Gaussian-like distribution of the shifted bootstrap resample, the shift does not change the statistic uncertainty and is therefore a usable estimate of the largest possible uncertainty of the gas sample composition. This approach can be further refined in the future to consider the individual uncertainty contributions, which will in all likelihood lower the stated uncertainty.

6.2.3 Experimental results of the LARA calibration factors

Calibration factors for binary mixtures of $H_2 + D_2$

In Figure 6.6 the calibration curve for the binary mixture of H_2 and D_2 is shown, with and without spectral sensitivity correction. It can be seen that the model function Equation (6.3) describes the dataset quite well. While the non-corrected curve appear resembles a linear function, the spectral sensitivity correction introduces a distinct bend. This suggests that the correction factors for spectral sensitivity and theoretical transition strength are comparable in size, but of opposite signs.

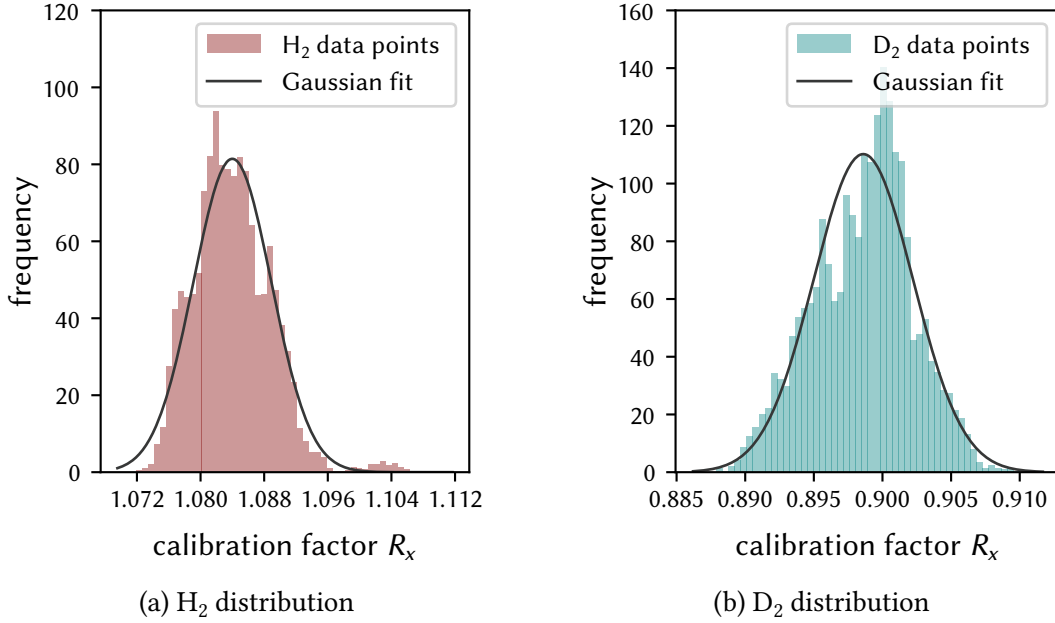


Figure 6.7: Bootstrapping distribution for H_2 – D_2 binary calibration data. In order to evaluate the statistical uncertainty of the calibration factors each calibration curve is resampled and refitted. The width of the resulting distribution gives an estimate of the statistical uncertainty of the fit parameter. Note that the data sets include spectral sensitivity correction.

The resulting absolute calibration factors derived without correction are

$$R_{H_2} = 1.0065 \pm 0.0016 \quad (6.4)$$

$$R_{D_2} = 0.9935 \pm 0.0017 \quad (6.5)$$

The absolute value of an individual calibration factor is not of physical importance for relative quantification, but the ratio between to calibration factors is. The particular ratio here is found to be

$$R_{H_2/D_2} = 1.0130 \pm 0.0024. \quad (6.6)$$

This means that without applying any sensitivity correction the H_2 -concentration is over-estimated by 1.3 % compared to the D_2 values. These particular results are only applicable for the setup in the state that was used during the measurements, but the low uncertainty value of 0.24 % demonstrates the achievable composition accuracy with TRIHYDE.

For illustration, the distributions for the bootstrap resampling results are shown in Figure 6.7. To a good approximation, the observed distributions are Gaussian; their width can be used as an estimator for the statistical uncertainty of the calibration factors.

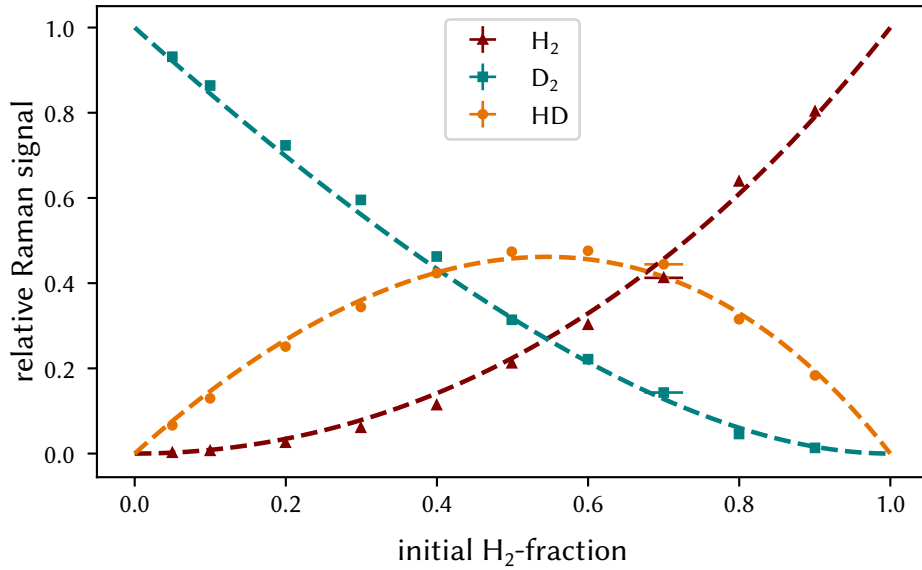


Figure 6.8: Calibration curve for H_2 – D_2 – DT -tertiary mixtures. Note that no spectral sensitivity correction is applied. Due to the atomic ratio shifts detected in each run, introduced by the Pd – Al_2O_3 -catalyst, the model function (dashed line) does not match with the calibration data points.

Using the same analysis approach for the spectrally-corrected datapoints, the resulting factors are

$$R_{H_2} = 1.0840 \pm 0.0057 \quad (6.7)$$

$$R_{D_2} = 0.8986 \pm 0.0036 \quad (6.8)$$

$$R_{H_2/D_2} = 1.2063 \pm 0.0080 \quad (6.9)$$

As expected, the application of spectral intensity correction using the SRM standard results in a higher uncertainty of the resulting calibration factors. The value reported in Ref. [Sch14a] is $R_{H_2/D_2} = 1.151 \pm 0.051$, which is about 5 % larger than the TRIHYDE value derived here, but within the uncertainty band. These factors can be crosschecked with the additional factors obtained during the measurement campaign including the radioactive isotopologues (see Chapter 7).

Calibration factors for tertiary mixtures of $H_2 + D_2 + HD$

Performing the same analysis steps for the equilibrated, tertiary gas sample results in the calibration curve shown in Figure 6.8. Note that only the calibration curve without spectral sensitivity correction is displayed.

Despite describing the general shape of the calibration curve, the data points do not match the model functions. The resulting calibration factors $R_{H_2} = 0.877$ and $R_{D_2} = 1.307$ differ from the values obtained from the binary mixture by more than 40 %.

This deviation is likely caused by chemical diffusion processes in the catalyst⁵. In this context, several observations can be made:

- (i) The relative atomic fractions of H and D, which are derived from the relative signals S_x of the individual isotopologues, defined as:

$$S_H = S_{H_2} + 1/2 \cdot S_{HD} \quad (6.10)$$

$$S_D = S_{D_2} + 1/2 \cdot S_{HD}, \quad (6.11)$$

showed a sharp drop of S_H by up to 30 % in each run, when starting to circulate the mixture via the bypass. In case of a non-accumulating catalyst, which only reacts the gas sample into chemical equilibrium, the S_H and S_D should remain constant. If there is some gas exchange with the catalyst the atomic ratio could change. The priming step during sample preparation (see Section 6.2.1) was implemented to minimise effects introduced by such behaviour, which proved to be not effective. This effect may be caused by

- (a) Outgassing of D_2 stored in the catalyst material originating from the priming step:

This is unlikely since no observed increase of D_2 or HD concentration is observed when circulating a pure H_2 sample. It is also unlikely to be gas trapped between the catalyst pebbles due to evacuating the complete loop to $<1 \cdot 10^{-3}$ mbar; therefore, residual gas are only at the ppm-level.

- (b) Stronger adsorption of H to Pd:

The dissociation energy of $E_{H_2} = 4.362 \text{ kJ mol}^{-1}$ at 25 °C is about 2 % smaller compared to $E_{D_2} = 4.4436 \text{ kJ mol}^{-1}$ [Hol17].

Hence the dissociation pressure, which describes the pressure of gas in equilibrium with the solid at a given temperature, is smaller for PdH compared to PdD [Bes03]. Therefore, it is more likely for Pd to adsorb H instead of D.

- (ii) As shown in Figure 6.2, at temperatures >75 °C a continuous, diametrical trend for the H_2 and D_2 data was observed while the HD -concentration was constant. This suggests a thermally activated diffusion process of either D_2 into the bulk, or H_2 outgassing from the catalyst. In different experimental runs, priming the catalyst material at different temperatures before sample preparation, no change in behaviour observed any longer. This behaviour was also not observed by heating a non-equilibrated binary mixture via the mixing vessels heating system while circulating the gas in the loop. All this makes it rather difficult to study the thermal dependence of the chemical equilibrium constant K_{eq} .

In order to produce well defined tertiary gas sample in chemical equilibrium, the relative atomic signals must not change during the equilibration process. Therefore, the values

⁵L. FASSELLT: 'Calibration of a Laser-Raman-System with accurate gas samples of inactive hydrogenisotopologues'. Bachelor's Thesis. Karlsruhe Institut für Technologie, ETP/TLK, 2019.

Table 6.2: Comparison of the H_2 – D_2 factors derived in HYDE and TRIHYDE.

	HYDE		TRIHYDE	
	value	σ (%)	value	σ (%)
R_{H_2}	1.013	0.4	1.006	0.16
R_{D_2}	0.969	0.3	0.994	0.17
R_{H_2/D_2}	1.045	0.7	1.013	0.23

derived during this campaign cannot be used for LARA calibration. In reference [Sch13c], no relative atomic signal shifts on that scale were not reported during experiments at HYDE, which also used a catalyst moderated equilibration process.

A likely cause of these shifts is the choice of catalyst material. In HYDE a 0.5 wt.-% Pt– Al_2O_3 catalyst was used instead of a 20 wt.-% Pd– Al_2O_3 catalyst. Due to the unfavourable isotope dependent properties of Pd compared to Pt, the catalyst initially used in the TRIHYDE setup was not suitable to produce calibration sample in chemical equilibrium. Note that the adverse effect was even amplified by using a relative higher amount of catalyst material, which was larger in relation to the processed gas volume. Changing an appropriately scaled amount of Pt– Al_2O_3 catalyst material showed a strong decrease in the atomic ratio shift, but did not completely suppress it.

In order of the general objective, the determination of the calibration factor of the radioactive isotopologues, and the already performed verification of the non-radioactive factors in HYDE (including HD) to an adequate level, no further studies in regards to stable tertiary mixtures were carried out during this work. In consequence, a different, non-catalyst approach to prepare the tertiary samples of radioactive isotopologues had to be investigated, as described in Chapter 7. A more detailed study of the influence of catalyst material and geometry on sample preparation could be undertaken at a later stage, as the design and instrumentation of TRIHYDE allows a straightforward change of the catalyst assembly.

6.2.4 Comparison of TRIHYDE results with predecessor experiment HYDE

For comparison, all calibration factors from the HYDE⁶ and TRIHYDE campaigns for the stable isotopologues are collated in Table 6.2. Note, however, that the absolute values of the calibration factors are not transferable between systems due to their setup dependant nature. But note, too, that the uncertainties in TRIHYDE are reduced by a factor of three.

⁶S. RUPP: ‘Proof of concept of a calibration method for the laser Raman system for KATRIN based on the determination of the system’s spectral sensitivity’. Master’s thesis. Karlsruhe Institut of Technology, 2012, available online at katrin.kit.edu

This can be attributed to the following main improvements of the setup:

- Streamlined mixing vessel geometry:
In HYDE the mixing vessels are constructed in an inverted T-shape while the TRIHYDE vessels are of single-cylinder flow-through design. This avoids non-flow pockets in which gas may not mix and can contribute to an unwanted discrepancy in molar concentration. Due to the more effective mixing during circulation, the homogenisation time in TRIHYDE is about 5 min while in HYDE it takes about five times longer. HYDE also required regular changes in valve configuration to push gas through the cylinders [Sch13b].
- Reduced volume uncertainty:
Using a dedicated volume determination setup, optimised for the mixing vessel volume, reduced the volume uncertainty from 0.5 % to less than 0.25 % [Köl11].
- Reduced pressure reading uncertainty:
In TRIHYDE, the pressure in each mixing vessels is measured by two temperature stabilised sensors with overlapping measurement range of (1000 to $\sim 10^{-2}$) mbar. All used sensors have a relative uncertainty of 0.12 % of reading (compare Section 5.4.1). This is an improvement over the HYDE setup, in which the pressure was measured using a single sensor with an absolute uncertainty of 0.3 mbar, regardless of the pressure reading.
- Additional gas purity measurements:
During the HYDE campaign only the initial gas purities provided by the supplier were carried forward into the uncertainty estimates; in TRIHYDE the initial gas purities are actually verified by RGA measurements in each run. Furthermore, in TRIHYDE the gas filter stage (see Section 5.3) ensures the highest available purity, which may otherwise be diluted before reaching the mixing vessels. This was not implemented at HYDE, thus the actual composition of the initial gas was only assumed.

6.3 Evaluation of the results with reference to the experimental procedures using tritiated gas mixtures

For a successful operation of the Loop with tritiated gases, the observations and lessons-learned during the H_2 - D_2 campaign need to be assessed. In general, the procedures and operation of the loop used here are also applicable to tritium operation; key are the following points:

- (i) The observed homogenisation time of (5 to 10) min of a sample during circulation is assumed to be independent on the isotopic composition. Hence, the time interval pre-

sumed to be the same for tritiated mixtures and the homogenisation be differentiated from chemical reactions within the tritiated gas sample.

- (ii) A sufficient flushing of the filters needs to be performed to ensure no impurities in stable gases, which also needs to be verified for each prepared sample by RGA measurements.
- (iii) For binary mixtures, the lower systematic uncertainties relative to the HYDE setup allow for the higher margins of uncertainty associated with tritiated mixtures.

However, due to the observed shifts in relative atomic ratios introduced by the catalyst material, the existing setup and procedures are unsuitable for tertiary gas samples (simply, the calibration is not sufficiently accurate). In order to find a suitable method of preparing tertiary mixtures of tritiated isotopologues in chemical equilibrium, two options can be considered:

- (i) Perform an in-depth study to find and characterise a suitable catalyst material and procedure that ensures a stable relative atomic composition and consistent equilibration;
- (ii) Appraise the equilibrium reactions of all hydrogen isotopes, as discussed in the literature, in order to ascertain whether the proposed process(es) produce accurate and predictable molar ratios [Uda92b].

In both cases, the general systematics and kinematics of processing tritium need to be characterised before calibration sample preparation can commence (see Section 7.1.2).

6.4 Conclusions

With determination of the H_2 - D_2 calibration factors, the commissioning of TRIHYDE using stable gases is complete. The overall outcome of this commissioning phase is that general sample preparation procedure, as well as the analysis strategy are deemed to be suitable and applicable to tritiated samples.

Using a similar procedure as in HYDE, the absolute calibration factors R_{H_2} and R_{D_2} were determined with a relative uncertainty level of $<0.2\%$, which equates to a threefold reduction in uncertainty compared to HYDE. However, note that the tabulated numerical factors are only valid for the actual TRIHYDE system and may differ for setup alterations. This improvement is primarily a result of the reduction in pressure reading uncertainty and the mixing volume uncertainty. This demonstrates TRIHYDE's capability to analyse as well as to provide stable gas samples from or for other experiments within the TLK.

The low uncertainties levels achieved thus far may serve as an excellent baseline for analysing tritiated samples, which will inevitably introduce further uncertainties from:

- Initial sample composition,
- Isotope exchange reactions and impurity production,

- Multiple possible reaction chains,
- Gas-wall interactions.

Comparing the obtained theoretical sensitivity factors to the values derived in Ref. [Sch14a], both values agree to within 5 % to each other, and within their respective uncertainty intervals. The observed deviation can be attributed to the uncertainties in the SRM calibration procedure as well as assuming the largest possible uncertainty during analysis. Using the results from the remaining isotopologues, it can be verified whether this deviation is significant or is an artefact associated with the listed factors.

The Pd–Al₂O₃-catalyst material introduced serious shifts in the atomic ratio of the sample; therefore it is deemed unsuitable to provide accurate samples in chemical equilibrium. A change to the same catalyst material used in HYDE showed improvements, but still exhibited noticeable deviation from the initial molar ratio. As a consequence, the sensitivity factor for R_{HD} could not be verified. Notwithstanding, the general trueness of the current factor used for the theoretical sensitivity correction was already sufficiently verified by SCHLÖSSER [Sch14a]. Since HD is not a major constituent of the WGTS-gas column, and the current values already fulfil the KATRIN-requirements, no further investigations regarding the stable isotopologues were carried out in the scope of this work.

Based on the experience gained in the H₂–D₂ campaign, the following modifications for tritium operation were identified:

- (i) During this campaign, a sample with the target molar ratio was prepared before the actual calibration sample in order to ‘prime’ the system. However, this procedure showed to detectable improvement in the system’s accuracy and can thus be omitted. As a consequence, a more economic use of tritium gas is anticipated.
- (ii) Initial gas purity must be verified using both RGA and LARA in each run due to possible changes in composition introduced by isotope exchange reactions as well as impurity buildup.
- (iii) Sample preparation in chemical equilibrium and given molar concentration needs to use a non-catalyst process without shifting the atomic ratio of the sample. Deviations in the atomic ratio can be detected *in situ* and allow for characterisation of the self-equilibration process.

In conclusion, the TRIHYDE setup surpasses its predecessor HYDE in accuracy, as well as in capabilities, and can be used to improve the LARA calibration trueness necessary for composition monitoring at TLK. Besides improved systematics and instrumentation, the system is well equipped to tackle the issues posed by tritiated mixtures.

7 LARA-calibration including the radioactive hydrogen isotopologues T₂, HT and DT

Following the studies for the stable hydrogen isotopologues discussed in the previous chapter, the novel possibility to determine the theoretical sensitivity factors for the radioactive isotopologues are described. The chapter is divided into two main parts: First, the necessary experiments to characterise the use of T₂ in calibration samples. Subsequently, the calibration measurements for the LARA system are presented. The chapter concludes with a discussion of the calibration results within the framework of the KATRIN experiment and an outlook on possible future studies with the TRIHYDE-facility.

7.1 General overview

7.1.1 Summary of procedures using tritiated gases

In general, the procedures are based on the results from the measurements utilising the stable isotopologues H₂ and D₂; however, additional effects associated with tritium need to be taken into account. All measurements performed in the T₂-campaign shared the ultimate objective to determine the theoretical spectral sensitivity correction R_{theo} of the tritiated isotopologues. In order to achieve this goal three main aspects have to be addressed:

1. Process commissioning of the primary system and the secondary containment,
2. Evaluation of systematic effects introduced by tritiated gases in the primary system,
3. Production, measurement and analysis of calibration gas samples for all tritiated isotopologues.

The sequence of individual steps on the road from commissioning to final LARA-system calibration and verification is summarised in Figure 7.1. These steps were implemented to address the additional challenges introduced by tritiated calibration gas samples, as identified in Ref. [Sch14a], including:

- (i) Fulfill all technical and process requirements for tritium handling,
- (ii) Evaluate achievable isotopic purity and Helium content in any initial T₂-sample,

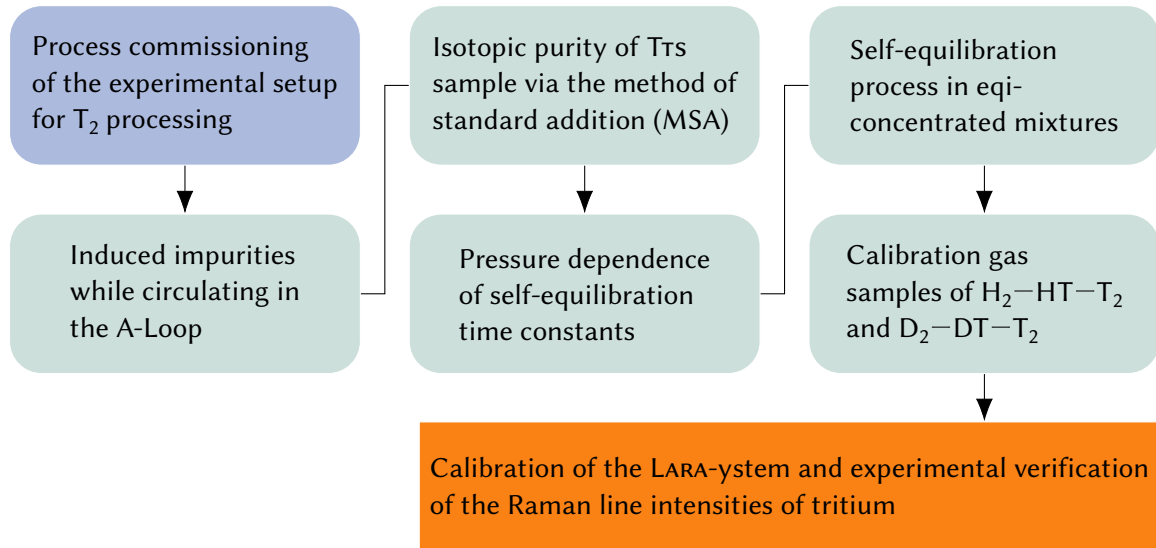


Figure 7.1: Overview of the measurement goals in the T_2 campaign. The item in blue is executed without tritium, the green items all include tritium measurements.

- (iii) Study the self-equilibration of pure-gas mixture, induced by radiochemistry, and adjust sample preparation,
- (iv) Evaluate impurity formation due to gas-wall interactions in the system.

In order to address these four challenges, the following measurements were performed:

After successful integration of TRIHYDE within the tritium-processing TLK infrastructure (see Section 7.1.2), preliminary measurements were performed with increasing T_2 partial pressure. Initial measurements started with less than 1 mbar while circulating the gas sample in the mixing loop. These long-term measurements helped to estimate the achievable T_2 -purity after gas transfer from TTs to TRIHYDE and from the P-Loop to the A-Loop. The contribution of both impurity buildup, e.g. formation tritiated methane, CO and CO_2 from interactions with the stainless steel [Kan64; Mor77], as well as isotope exchange reactions in gas-wall interactions [Aka08] were studied using the LARA2 and RGA systems.

When producing tritiated gas samples, in contrast to the non-radioactive gas samples, the major difference is the process of self-equilibration ([Uda92a; Gan99; Saz11]; also see Section 7.3). This process is vital for producing mixtures in chemical equilibrium for two or more isotopologues on a reasonable time scale; during this time it has to be guaranteed that the stability of the gas sample is not affected. The dynamics of this process may also depend on experimental properties like wall surface quality, turbulent flow through the circulation pump and excitation from the LARA laser; how all these contribute to measurement results in the actual system setup needs to be investigated. Measurements with H_2-T_2 as well as $H_2-D_2-T_2$ have been performed at different pressure levels to find a suitable parameter set for producing the calibration gas within reasonable equilibration time constant τ_x .

Table 7.1: Overview of the measurements performed with the tritiated isotopologues. The isotopologues given are the initial, non-equilibrated isotopes. The stated maximum fill pressure in the loop can be higher than the mean pressure in the mixing loop while circulating the gas. For this general overview, all numerical entries represent approximate values only.

Run	Goal	Initial isotopologues	Duration (h)	Maximum pressure (mbar)
35 to 43	Change of initial T_2 sample concentration while circulating with increasing partial pressure	T_2	1500	5 to 30
52	Self-equilibration in the equiconcentrated sample of all three isotopes	T_2, H_2, D_2	100	100
53 to 66	binary calibration points H_2-T_2	T_2, H_2	1000	100
63	Self-equilibration in the equiconcentrated sample of all three isotopes	T_2, H_2, D_2	1000	300
68	Estimation of the initial DT concentration by adding D_2	T_2, D_2	400	75
71 to 82	D_2-T_2 -DT calibration factors	T_2, D_2	550	500
86 to 98	H_2-T_2 -HT calibration factors	T_2, H_2	900	500

In order to evaluate the initial T_2 gas sample composition independent of the LARA calibration factors, a modified method of standard addition (MSA) based on Ref. [DIN13] was developed and tested (see Section 7.2.2). This was performed for DT only, since due to gas purification via gas chromatographic isotope separation, this isotopologue initially dominates [Nef98]. In this measurement, an initial T_2 sample was iteratively diluted with D_2 to increase the DT signal in a controlled manner. Using a linear regression, the initial concentration was estimated without relying on calibration factors of the system. In combination with RGA-measurements, the T_2 -sample composition estimate and its uncertainty were utilised in the calibration measurement.

For LARA calibration, two datasets for each combination of H_2-T_2 and D_2-T_2 were required:

- (i) a *binary* dataset with only the initial isotopologues not in chemical equilibrium,
- (ii) a *tertiary* dataset with all three corresponding isotopologues in chemical equilibrium.

Each datapoint was generated following the procedure described in Chapter 6, where the two gas species are individually analysed prior to mixing and then circulated sufficiently long to achieve a homogenised and equilibrated gas sample. The H_2-T_2 -campaign was performed twice at different pressures to evaluate the influence of pressure on the equilibration constant τ_x . An overview of the general measurement runs and allocated time is given in Table 7.1.

7.1.2 Commissioning of TRIHYDE using tritiated gases

The commissioning of the TRIHYDE-experiment incorporated two steps:

1. Technical commissioning phase,
2. Scientific commissioning phase.

In the technical commissioning, all connections to the TLK infrastructure were established. This included the T_2 -transfer-line from the TTs [Dör05], the exhaust-gas-transfer-line to CAPER [Bor05] for high impurity level gases, and a connection of the primary and secondary containment to the ZTs [Bes08]. All of these connections were tested to the required maximum acceptable integral leakrate of less than $1 \cdot 10^{-8}$ mbar l s⁻¹ by either helium leak test or pressure test [Bes08]. The secondary containment was tested by a pressure test to a leakrate less than 0.1 Vol.-% h⁻¹ starting at a pressure difference of 10 mbar. These tests were performed before operating the connection valves to any of the tritium processing facilities. After successfully establishing all connections, the second containment environment (pure N₂, with O₂ levels limited to (1.5 to 2) %) and the TRs for controlling the glove box activity level were commissioned.

Following the technical commissioning, in the scientific commissioning phase key questions regarding LARA calibration were investigated, with the emphasis on initial gas composition and effects of self-equilibration inside the mixing loop.

7.2 Experimental determination of the initial tritium purity

For each campaign a single batch of T_2 was transferred from the TTS to TRIHYDE and stored in the buffer vessel BV003. Due to interactions with the stainless steel walls containing H₂ and C as well as tritium decay, the gas composition will change over time [Mor77; Gil80; Dic90]. In order to reach the necessary uncertainty level, these changes must be investigated before LARA-calibration samples could be prepared.

A gas sample for calibration measurement does not need to be 100 % pure, but its impurities need to be known at the level of 1 % or better. These measurements focused on the initial sample composition transferred from the TTs and composition change during the mixing process. In order to achieve this, both LARA and RGA-measurements were used.

7.2.1 Impurity build-up during sample preparation and measurements

In first experiments after commissioning of all infrastructure necessary for tritium processing, the change in gas composition was monitored over a period of approximately

1500 hours (62 days). The mixing loop was initially filled with 1 mbar T_2 to perform a basic functional test of all devices measuring radioactivity, i. e. Bixs and ionization chamber (IC). The pressure was then progressively increased up to 30 mbar in order to study the formation of impurities and evolution of sample composition.

In order to evaluate the subsequent impurity formation has on sample composition, the relative Raman signals of tritiated hydrogen isotopologues and tritiated methane as well as the pressure reading at BV005 (RP100) and the LARA-cell (RP106) are shown in Section 7.2.1. During normal operation the gas was continuously circulated via VA005, hence the different pressure levels at different A-Loop locations. To increase the loop pressure during gas injection, VA005 was stopped and both sensors read a similar pressure, although RP106 shows a systematic offset of about -6 mbar.

Initial isotope exchange reactions from gas-wall interactions Due to the low gas pressure inside the sample-cell, the LARA signals show a poor signal to noise ratio. Thus, the relative signals likely underestimate the T_2 fraction and overestimate the other fractions, e.g. HT and tritiated methane. However, the relative signals can be used as an estimate of the sample composition change while circulating in the A-Loop.

Over the period of the complete run, a constant decrease in T_2 - and increase in HT-concentration was observed. This is mainly attributed to exchange reactions with the available H_2 reservoir in the stainless steel walls. The HT content only increased at a rate of less than $0.1\% h^{-1}$; but this is still large enough to impact on the calibration runs (run time normally longer than 50 h). No increase in DT levels is observed due to the low concentration of D_2 in the stainless steel walls despite the preceding experiments using H_2 and D_2 . Combined with observations from long-time circulations of >600 h (see Section 7.3.4), the isotopic exchange reaction due to gas-wall interactions had no significant effect on gas sample quality.

In order to estimate memory effects, after about 200 h the LARA cell was evacuated, which showed no significant residual T_2 signal. During maintenance work on the system, the optical cover of the LARA appendix was removed for about 1 day after 240 h. This led to a perceived increase in the T_2 -signal due to the detection of room light within the LARA cell. The spectrum of the installed lighting features a fluorescence line close to the Q_1 -branch of T_2 ; this leads to a perceived tritium signal.

Characterisation of the influence of tritiated methane formation Another possible impact on gas purity is the formation of tritiated methane, which needs to be characterised. On account of the low SNR and insufficient spectrometer resolution, two broad wavelength intervals were integrated to give an estimate on methane production:

- CXT_3 (X = H, D): (585.7 to 589.9) nm,
- CT_4 : (583.2 to 585.2) nm.

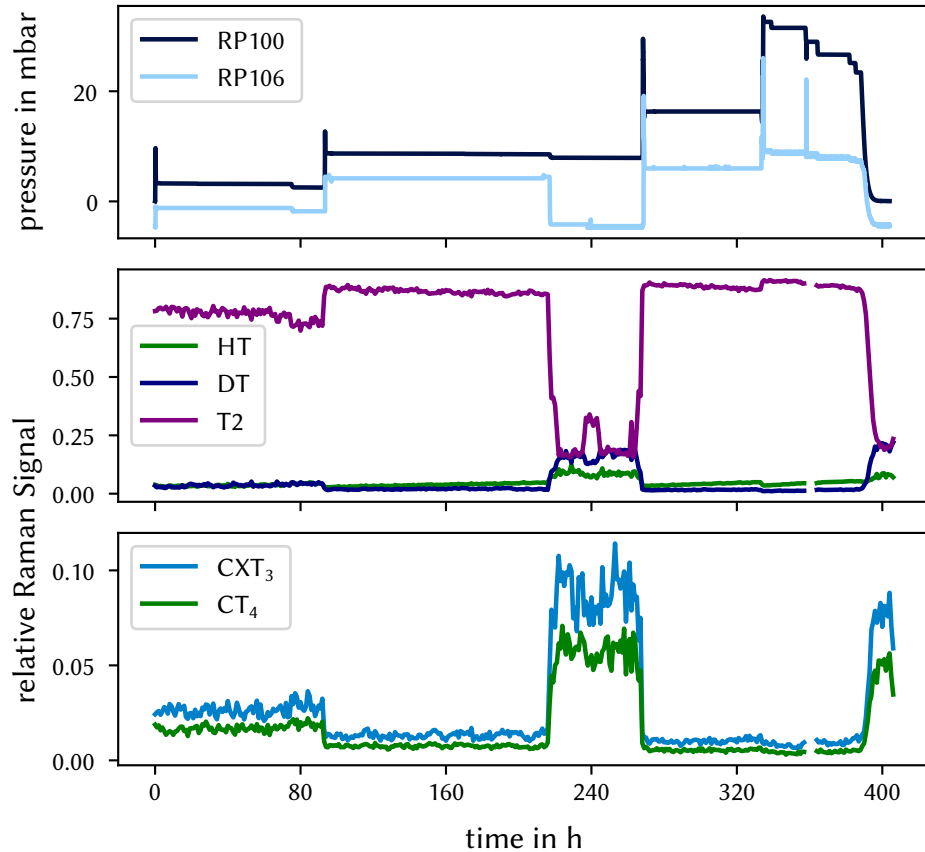


Figure 7.2: Pressure and concentration profiles during initial tritium circulation. RP100 represents the pressure in BV005 and RP106 measures the pressure inside the LARA cell. RP106, in addition to a general offset of about -6 mbar, measures a smaller pressure compared to RP100 when circulating the gas due to position close the inlet of VA005 (compare to Figure 5.5). When the pressure in the Loop was increased by only filling BV005, the circulation pump was turned off. This leads to the ‘spikes’ at the beginning of each pressure step. The LARA signals for methane are integrated wavelength intervals, as given in the text. No distinction for different methane isotopologues (e.g. CHT_3 , CH_2T_2 , CDT_3 ...) was possible because of insufficient spectral resolution. Note that when the LARA cell was evacuated for background measurements (around the 240 h mark), the signals fluctuate around zero and the relative signals do not represent the molar fractions of the gas sample.

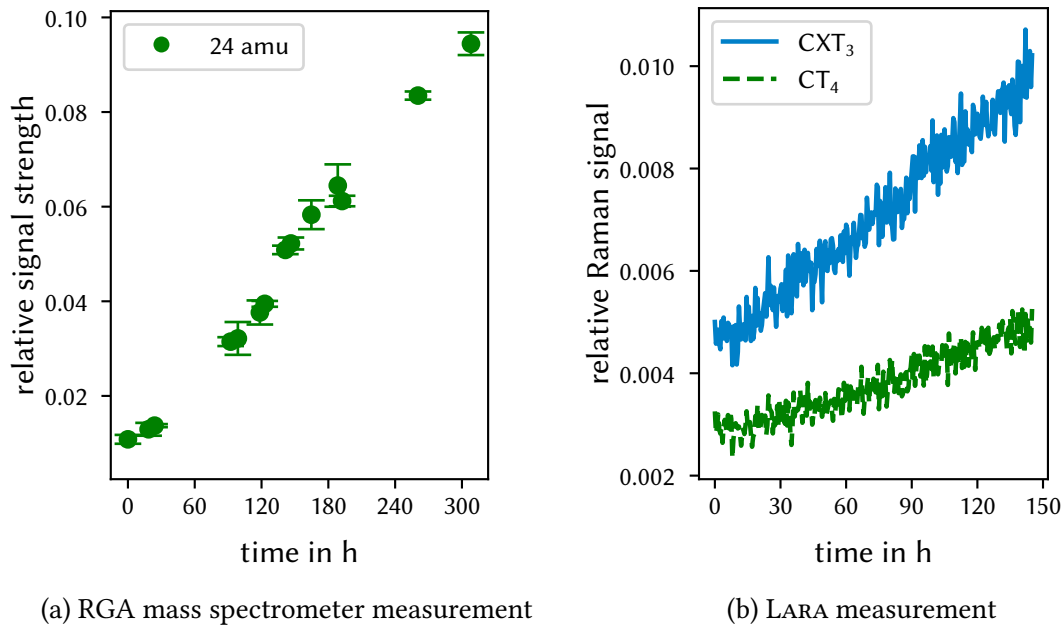


Figure 7.3: Methane production during initial T_2 circulation. For the RGA-measurements (a), the ratio between the 6 u and 24 u signal is used as an indicator for tritiated methane CT_4 . The linear regression slope is $(2.843 \pm 0.065) \cdot 10^{-4} \text{ h}^{-1}$. The methane LARA signal (b) is derived by integrating over a broad wavelength interval containing several tritiated methane lines. In both diagrams, no correction for instrument sensitivity was applied. Due to a lack of calibration factors, the signal strengths can only be used as a qualitative indicator, but not for composition quantification.

Since no sensitivity correction nor isotope signal separation was applied, these values were only used as an indicator for methane production, but not for quantification.

In order to crosscheck the chosen wavelength intervals and signal trends, the LARA signals were compared to the mass spectrometer measurements during the phases with gas pressures $> 10 \text{ mbar}$ (see Figure 7.3). Due to the associated gas loss of the RGA measurement inside the loop, RGA measurements were performed periodically for $\sim 10 \text{ min}$ at an inlet pressure of $1 \cdot 10^{-4} \text{ mbar}$. As an indicator for methane production, the signal ratio between 6 u (T_2) and 24 u (CT_4) was used, but no ionisation intensity correction was applied. The signals at 20 u and 22 u (CHT_3 , CH_2T_2) show an analogous trend; however, these signals should be treated with caution since they could result from a superposition of the equi-mass species CH_2T_2/HTO and of CHT_3/T_2O , respectively.

Both devices show a similar trend and can thus be used to crudely estimate the rate of production; accurate quantification was not possible.

A linear fit to the relative RGA signal at 24 u shows a slope of $(2.843 \pm 0.065) \cdot 10^{-4} \text{ h}^{-1}$. Assuming a pure T_2 sample and a circulation time of about 3 days, this would result in a relative methane production of about 0.015.

This notable initial methane formation is likely due to:

(i) Low T_2 pressure in the Loop:

When forming tritiated methane in gas-wall interactions, a lower pressure results in a lower ratio between gas volume and reaction surface. Thus, the relative methane formation is higher for lower gas pressures compared to higher pressures. During the preparation of the calibration samples, the gas pressure was at least tenfold higher ((250 to 500) mbar), which reduces the relative impact of methane formation on the sample composition.

(ii) Pure T_2 sample:

Using pure T_2 will have a higher formation rate compared to mixtures with lower tritium partial pressure due to the higher ratio between T_2 molecules and wall surface. Thus, formation rates are likely to be lower during calibration sample preparation.

(iii) No prior exposure to T_2 :

Based on the reaction between the tritium molecules and the available carbon reservoir in the stainless steel wall, this reservoir depletes with each methane formation. Therefore, it is likely to observe lower formation rates in subsequent measurement campaigns after tritium exposure.

In conclusion, an initial increase in methane levels was detectable, but is not likely to impact calibration measurements. This was confirmed during the D_2 -DT- T_2 campaign, see Section 7.4.3 for details.

No trace signals of CO or CO₂ were observed during all measurement runs, neither in initial gases nor during sample preparation.

7.2.2 Evaluation of the initial sample purity using the method of standard addition

The sample production for TRIHYDE relies on high purity initial gases or well defined initial gas compositions. These are easy to provide for the non-radioactive isotopes, but become a challenge for gases with tritium content:

- The P-Loop is able to separate decay-helium from the initial T_2 -sample, but cannot change the isotopic compositions for hydrogen isotopes. The initial T_2 -sample composition is therefore that provided by the TLK-infrastructure. Utilising a gaschromatographic process, the Isotope Separation System (Iss) separates the individual isotopologues by retention time via a capillary [Nef98]. Due to rather similar retention times, the gas column pushed through the capillary has an overlap between the T_2 and DT fraction. Depending on the process parameter(s), a small but non-negligible fraction of DT will be present in all samples and must be considered for sample preparation in TRIHYDE.
- As shown in the previous section, the initial gas composition changes over time and is influenced by storage time and circulation time. Therefore, the gas composition

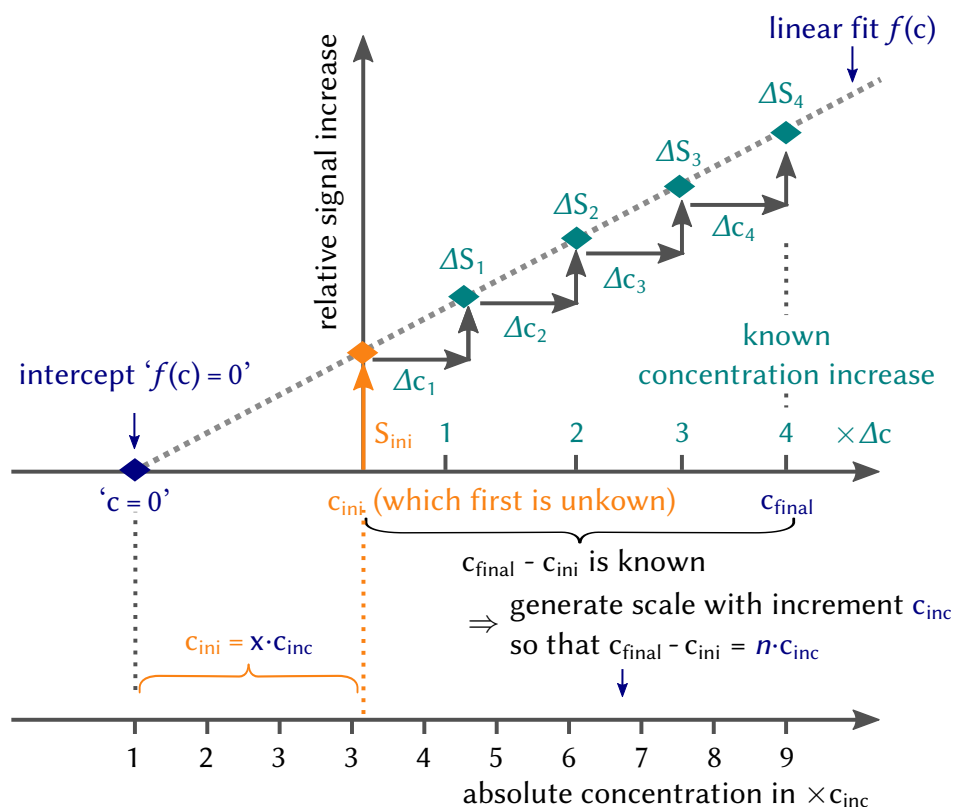


Figure 7.4: Schematic overview of the method of standard addition. Procedure: Starting with an 'unknown' relative concentration c_{ini} , known amounts Δc of a standard are added, resulting in relative signal increases ΔS ; the axis intercept of the data fit yields the numerical value for the initial impurity as $c_{ini} = x \cdot \Delta c$. The requirements for the applicability of this procedure are given in the text.

of both radioactive and stable reagents was measured before every calibration run. Although the LARA system is suitable to quantify the initial isotopic composition, solely relying on the LARA system to determine gas composition for the calibration of the LARA system would lead to circular reasoning. Thus, the initial gas composition must be estimated by addition methods. The RGA gives a good estimate of non-hydrogen impurities and is capable of identifying individual hydrogen isotopologues, but is not able to reliably quantify molar fractions to meet TRIHYDE requirements.

A possible solution to obtain an initial estimate and confirmation for LARA measurements is the method of standard addition (MSA).

This method is commonly used in impurity analysis and uses the signal increase due to controlled concentration increase. An overview of the principle is shown in Figure 7.4, based on the standardised procedure defined in Ref. [DIN13].

A *standard* of the minute amount of an initial impurity is added step-wise and its molar fraction thus increases by a known amount. Using the difference in signal strength associated with each addition step, a linear calibration function can be derived in units of

the added standard. The absolute value of the initial impurity is then determined on the derived calibration scale.

Amongst others, for the applicability of the method the following requirements must be met:

- the standard is available with high purity,
- a linear correlation between standard added and concentration increase,
- precise addition of the standard is possible,
- a linear correlation between standard concentration and measurement signal strength.

Applying this method for DT is challenging, since DT is not available as a single isotopologue in high purity and the added amount of DT is not constant due to the self-equilibration process in tritiated gases. However, the absolute LARA-signal strength is proportional to the molar DT fraction, which is one of the basic requirements for this method.

In order to address these shortcomings, a modified method of standard addition (MSA) was developed to make it applicable for DT measurements¹:

- Instead of DT, a well defined amount of D_2 was added,
- DT is auto-generated within the sample itself via self-equilibration and can be estimated using Equation (7.15) as well as K_{eq} given in Figure 7.8.

The pressure in the loop and the relative Raman signals are given in Figure 7.5. First, the buffer vessel BV005 and the LARA-cell were filled to 600 mbar of the gas sample used in the D_2 -DT- T_2 -campaign and analysed via LARA and RGA. Subsequently, the buffer vessel VA006 was filled with 10 mbar D_2 and the two components circulated for at least 12 h.

The mixed gas was then compressed into BV005 and the remaining loop is evacuated to $<1 \cdot 10^{-3}$ mbar. The signal ‘spikes’ visible in the relative Raman signals at the beginning of each step are due to this evacuation step. In this period, only the baseline noise was detected and the relative signals do not represent a molar fraction. After each step the procedure is repeated, each time adding 10 mbar of D_2 . Due to the limited compression factor of VA005, not all gas was transferred into BV005 and the overall gas pressure drops in each subsequent step, as shown in the first row in Figure 7.5.

As expected, the isotopologues D_2 and T_2 react to DT while the other isotopologues only show a baseline signal. The maximum DT-concentration in chemical equilibrium is reached for an initial D_2 concentration of $c_{DT} = 0.5$. If the D_2 concentration is increased above 0.5, the associated equilibrium concentration of DT decreases, as shown in Figure 6.3. As a result, the equilibration reaction slope is reversed in the last reaction step shown in Figure 7.5. Due to the decreasing gas pressure and thus decreasing absolute Raman signal intensity, the baseline noise for the H_2 , HD and HT signals increase with each step.

¹J. BRAUN: ‘Development of a modified standard addition method for determining the isotope ratio of a tritiated gas sample by Laser-Raman spectroscopy’. Bachelor’s thesis. Karlsruhe Institut of Technology, 2020.

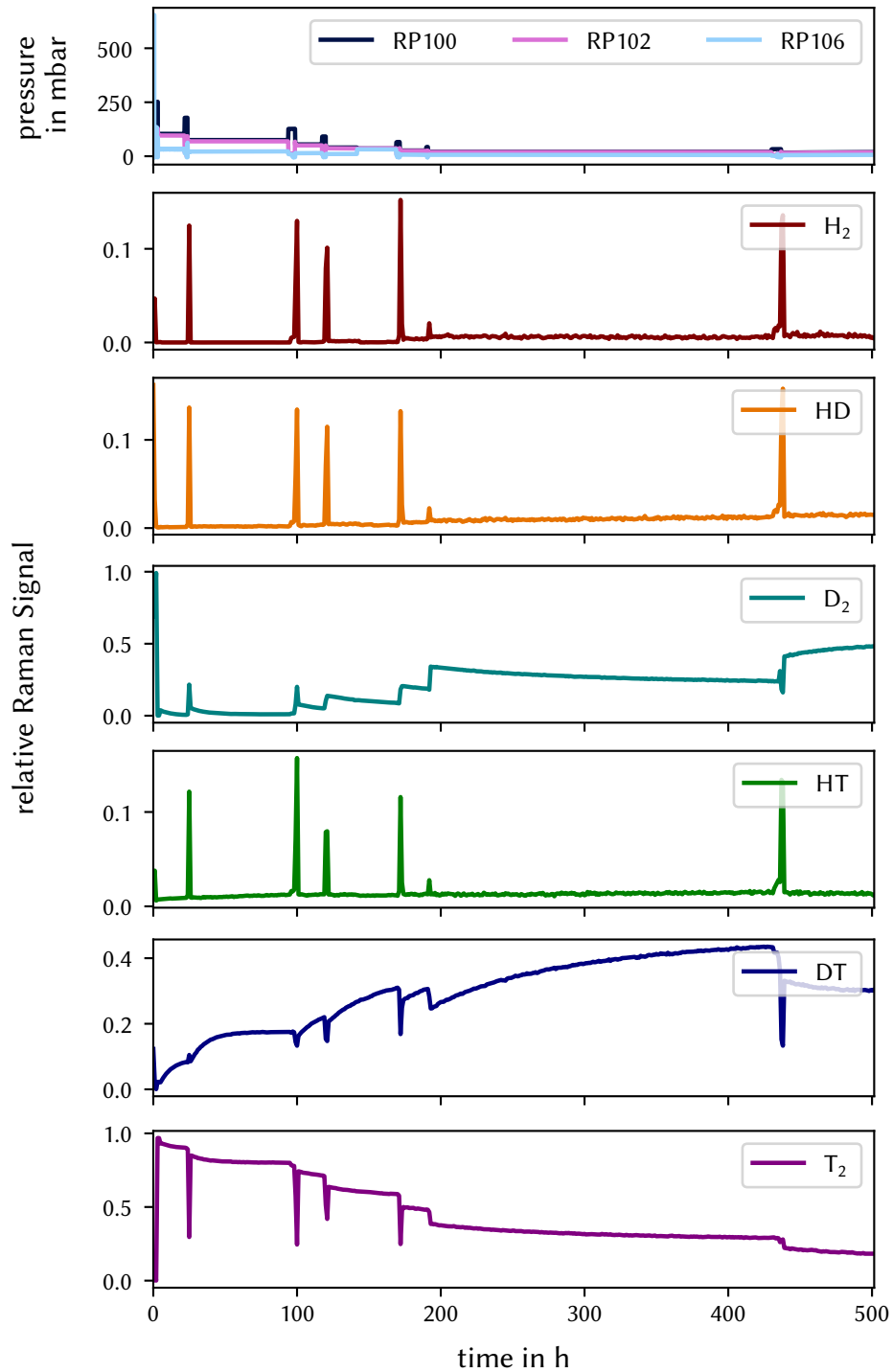


Figure 7.5: Pressure and concentration profiles during MSA procedure. After the initial sample of 600 mbar T_2 from the P-Loop is measured, incremental amounts of 10 mbar of D_2 are added and the mixture is circulated to achieve a reasonable equilibrium. The loop was evacuated to $<10^{-3}$ mbar after each step, noticeable by the ‘spikes’ in the LARA plots when only baseline noise was detected. Due to process-related gas loss, the signal-to-noise ratio decreased after each D_2 -addition. Note, that a maximum concentration of DT is reached for a 50:50 ratio of D and T and subsequent addition of D_2 will reduce the DT concentration (as illustrated in Figure 6.3).

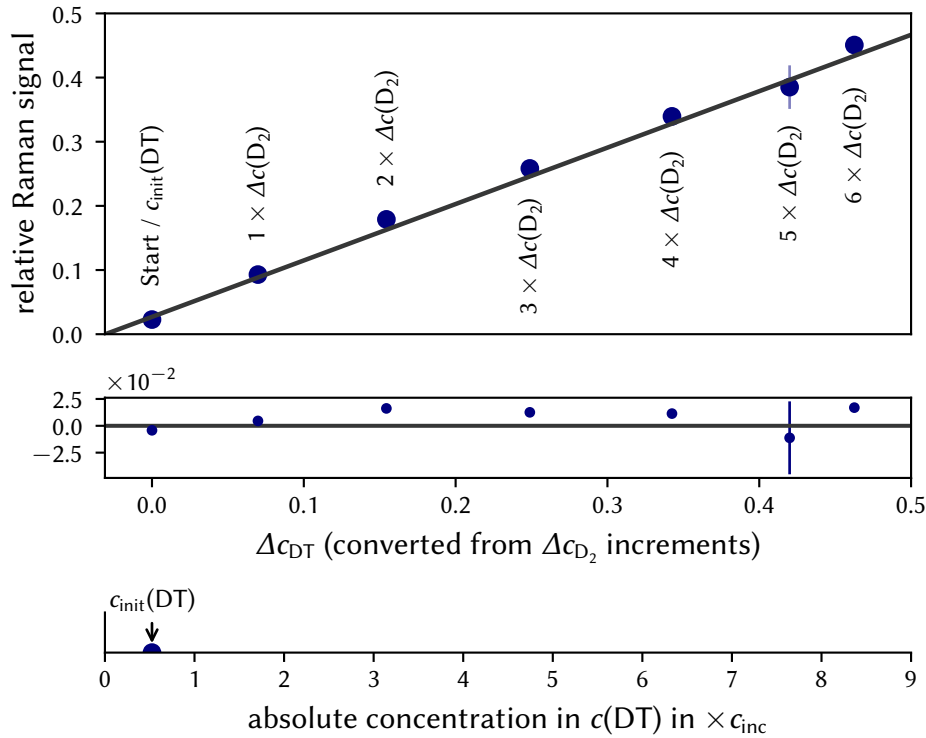


Figure 7.6: Standard addition method for estimating the initial DT-concentration before mixing. The relative DT signal after each D_2 -addition is estimated from an exponential curve of the self-equilibration. The change in c_{DT} is given from the pressure ratio of the mixing vessels, the composition of the previous gas mixture and the Equation (7.15). The large uncertainty for $5 \times \Delta c(D_2)$ is due to the short measurement interval available for extrapolating the Raman signal in chemical equilibrium.

For all steps, no constant relative Raman signals and thus chemical equilibrium was reached. This is due to the low gas pressure and associated long equilibration time constants. Thus, the relative Raman signals in equilibrium were extrapolated by a weighted exponential fit to each step. A detailed description of the equilibration reaction and the justification for an exponential fit model are given in Section 7.3.

In order to estimate the change in DT concentration Δc_{DT} , an initial value for DT is necessary. Assuming a D_2 -level below the detection limit of the LARA2-system, this gives an initial molar fraction of 0.0002. Based on the chemical equilibrium ratios, the resulting fraction of 0.97 T_2 and 0.0278 DT were derived. All other isotopologues were not considered during this measurement. For each addition step, the resulting equilibrium and the derived change in DT concentration Δc_{DT} were calculated. It was shown in a numerical analysis that a reasonable assumed initial molar composition can improve the result, but is not essential. When assuming an initial theoretical absolute pure T_2 sample, the MSA procedure is still able to experimentally determine the correct concentration in the actual sample to within a molar fraction of 0.0025.

In Figure 7.6 the uncalibrated, relative Raman signals in dependence of Δc_{DT} are shown. In order to use only addition steps with increasing Δc_{DT} , only the data points up to $c_{D_2} = 0.5$ are considered. All data points follow a linear trend, as required for a successful MSA procedure. However, the relative Raman signal around $\Delta c_{DT} = 0.42$ shows a significant higher uncertainty compared to the other data points. This is due to the short circulation time from which the equilibrium concentration is extrapolated; nonetheless the data point is compatible with the general linear trend.

In order to consider both uncertainties due the extrapolated relative Raman signal in chemical equilibrium in y-direction and the estimation of Δc_{DT} , a linear fit using an orthogonal distance regression algorithm (ODR), as described in Ref. [Aig73], was applied. The resulting fit parameters are

$$R_{DT} = (0.8793 \pm 0.0044) \cdot \Delta c_{DT} + (0.027 \pm 0.013). \quad (7.1)$$

This gives an estimate for the initial DT concentration independent of the LARA-calibration factors of

$$c_{DT} = 0.031 \pm 0.015. \quad (7.2)$$

This value is comparable to estimates and empirical values of $c_{T_2} \sim 0.98$ encountered in other experiments [Dör05]. Considering the modifications to the general MSA, a stated uncertainty of 50 % is acceptable. This uncertainty value is used as an estimator of the initial gas purity uncertainty used in gas sample preparation and is therefore an conservative value (see Section 7.4.1).

In summary, the method of standard addition is applicable for tritiated gas mixtures, but can be further improved using the following procedure:

- (i) Reduction of pressure loss in each addition step:

In each step the gas was compressed into BV005, but due to the compression factor of ~ 10 of VA005, about 70 % of gas was not transferred and thus lost during loop evacuation. This could be improved by using a vacuum pump with higher compression factor and shorter piping: however, at present neither of the options can be incorporated into the existing setup. A higher gas pressure would be beneficial for several reasons, like e.g.

- Increased SNR for the lower concentration values,
- Shorter self-equilibration time constants τ_x and thus reduced uncertainty associated with the exponential fit.

- (ii) Reduced amount of D_2 in each step:

Using smaller changes in Δc_{DT} results in a shorter equilibration time. This is due to the smaller relative concentration change, thus reducing or avoiding uncertainties associated with the extrapolation of the equilibrium concentrations.

(iii) Higher initial T_2 -pressure:

Using an starting T_2 -pressure in BV005 of >800 mbar gives a better SNR and faster equilibration times, thus lowering statistical uncertainties.

(iv) Longer equilibration times:

By circulating the gas sample for longer, a better estimate on the relative signal strength in chemical equilibrium can be obtained. At lower pressures, this may lead to impracticably long measurement times.

7.2.3 Implications of the initial T_2 gas purity for LARA-calibration measurements

Combing the results of the previous two sections, it becomes inescapable that in each measurement run one always needs to determine the initial T_2 -purity. The composition change of undesired isotopologues (e.g. H_2 in a D_2 - T_2 -mixture) was detectable, but had no impact on the TRIHYDE goal of a sample uncertainty of 1 %. This is mainly due to the relatively shorter sample preparation times of <72 h.

When comparing the H_2 - D_2 -measurements in HYDE and TRIHYDE, the initial gas purity is the main uncertainty contribution of the gas samples.

It is advantageous to use a single batch of T_2 prepared and transferred from the TTs and stored in the P-Loop for all calibration samples of a single campaign. The initial gas composition of the T_2 sample for each calibration sample is shown in Figure 7.7. The overall change in composition of the tritiated isotopologues is below 0.2 %, with the major concentration shift happening in the first 80 h; thereafter, the concentrations remain virtually unchanged. This is likely due to an equilibration process with the available H_2 and D_2 within the stainless steel wall of the storage vessel of the P-Loop. The absolute gas storage pressure was about 800 mbar, at least twofold the tritium partial pressure used in sample preparation. In case of pure self-equilibration process within the gas, the equilibration time constants could be shorter than the 6 h observed during sample preparation (see Section 7.3.2). However, the equilibration reaction is likely to be attenuated when happening in gas-wall interactions. Thus, an equilibration curve with a conservative time constant of 22 h is used to describe the gas composition in Figure 7.7.

Due to the processes of Iss, TTs and tritium storage in the P-Loop, the gas purity itself cannot be increased beyond the system-inherent limits. In general, this does not pose a problem for sample preparation as long as the following implications are considered:

- (i) The tritium gas composition is measured for each sample preparation.
- (ii) Only a single batch of tritium from the TTs is used since the gas composition is reasonably constant after an initial change.
- (iii) Any initial helium concentration can be removed by processing the gas via the Pd-permeator in the P-Loop or Iss [Pen97]. The subsequent, relative ^3He formation

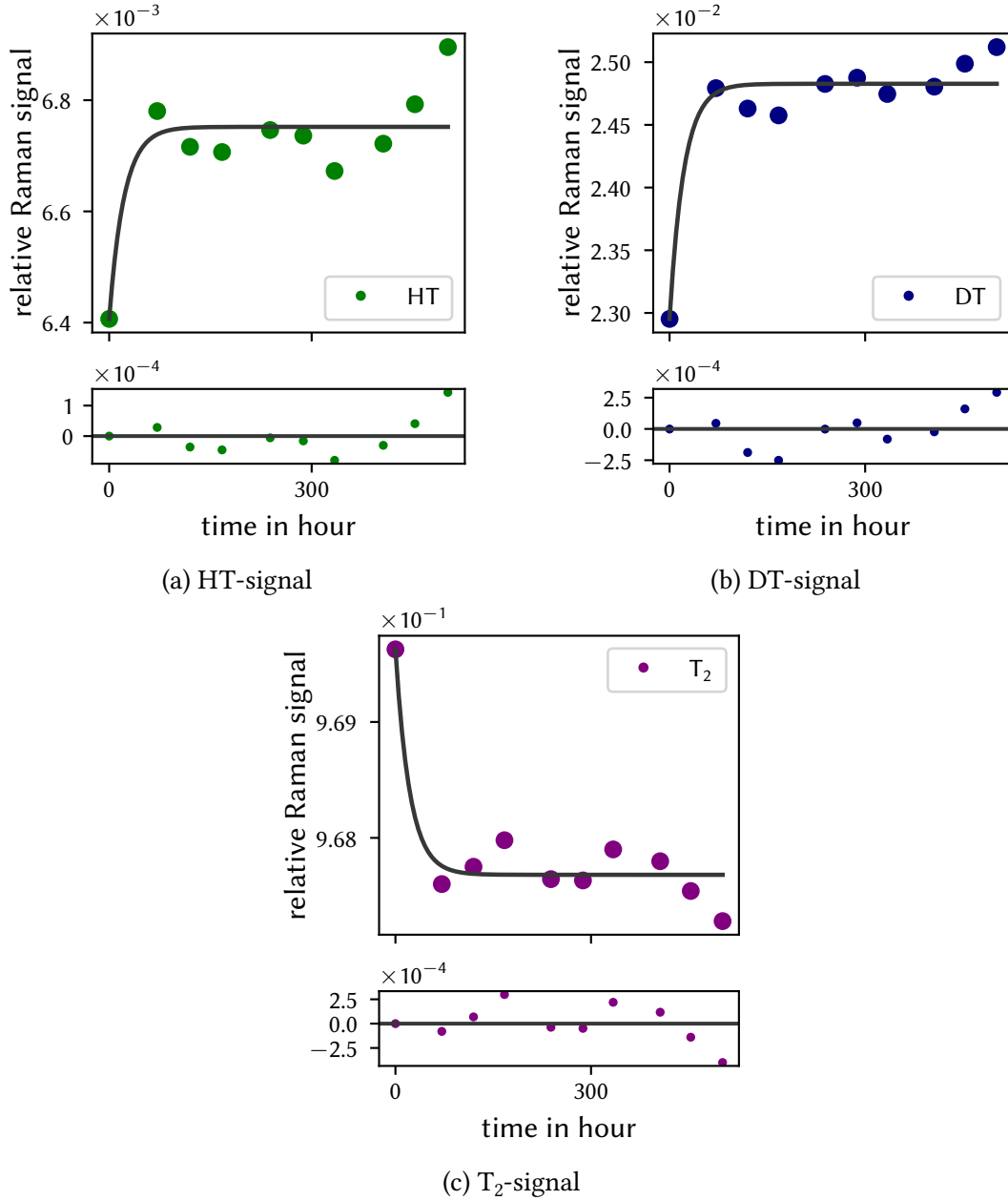


Figure 7.7: Initial T_2 -sample composition during the D_2 - T_2 campaign. The gases used in each calibration run are individually sampled and averaged for at least 60 min before mixing. Assuming an equilibration process as observed during sample preparation, an exponential curve with a time constant $\tau_x \sim 22$ h fits the data reasonably well. Note that the actual τ_x may be smaller.

due to tritium decay within TRIHYDE is about $1.5 \cdot 10^{-4} \text{ d}^{-1}$. This is insignificant for a single preparation of about three days. Based on a calibration campaign of ten samples, this results in an relative formation of $c_{\text{He}^3} \sim 0.003$, which is well within the general measurement uncertainty. Thus, a single batch with no subsequent gas processing was used in the calibration runs.

In order to estimate the uncertainty of the initial gas samples for calibration, the dominating value of 50 % of DT was used in Section 7.4.1 and impurity formation like methane or undesired isotopologues were not included due to their low impact on sample composition.

7.3 Influence of self-equilibration in tritiated gas mixtures

In order to analyse both *binary* and *tertiary* (e.g. H_2-T_2 and H_2-HT-T_2) mixtures, the calibration sample needs to proceed towards chemical equilibrium concentrations for the reaction



These isotope exchange reactions in the gas phase have been extensively studied for the stable hydrogen isotopologues; however, for the case of radioactive isotopologues being involved only a small number experimental results have been published (see [Jon48]; [Mat52]; [Ter69]; and [Sou86]). According to Ref. [Gan99], the exchange reactions in the gas phase are organised in several groups.

The first group of reactions is the direct interaction of saturated-molecule interactions. Due to the high activation energy and low probability of such a direct reaction, relying on this process alone would result in intractable long sample preparation time [Bau66]. For a mixture of stable isotopologues, this is the only possible exchange reaction. The associated very long equilibration time makes the use of a catalyst necessary, which introduces further uncertainties and undesired effects on sample composition (see Chapter 6).

In tritiated mixtures, the tritium decay enables additional radiochemical reactions, which enhance the self-equilibration process. In principle, it is possible to use only these reactions to bring the gas sample into chemical equilibrium within a practical timescale. As a consequence, this procedure avoids any uncertainties associated with reactions with the catalyst material. The following sections give an overview of the radiochemical processes initiated by the tritium decay.

7.3.1 Introduction to self-equilibration processes

Further (secondary) processes besides direct interactions between the diatomic isotopologues are ion-molecule and atom-molecule reaction chains. For ion production, both

daughter products from tritium decay, i.e. ${}^3\text{He}^+$ and the β -electron, can start the reaction chain with $Q = \text{H}, \text{D}, \text{T}$ [Gan99]:

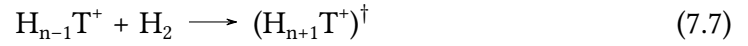


According to [Tho58], these ions trigger the initiation reaction

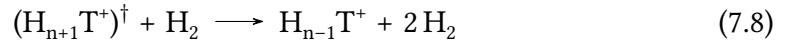


Here, these and all following reactions are exemplified for hydrogen and tritium, but can occur for all six isotope combinations. The subsequent chain propagation is described in detail in Ref. [Saz11] for odd-numbered ion clusters with $n = 3, 5, 7, \dots$:

1. Addition of a molecule to an ion-cluster with vibrational excitation (denoted by (\dagger)):



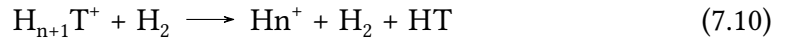
2. Dissociation of the excited cluster after collision with an hydrogen molecule



3. Intramolecular isotopic exchange



4. Dissociation of the excited changed cluster



These reaction chains are terminated via



where $(-)$ denotes either an electron, negative ion or wall interaction [Pyp78]. The reaction rates of the single chains all depend on temperature, concentration gradient and pressure of the gas mixture and determine the effective equilibration time τ_x .

Additional impurities 'R' can further inhibit or enhance the reaction, as studied in Ref. [Aqu65; Uda92a]:



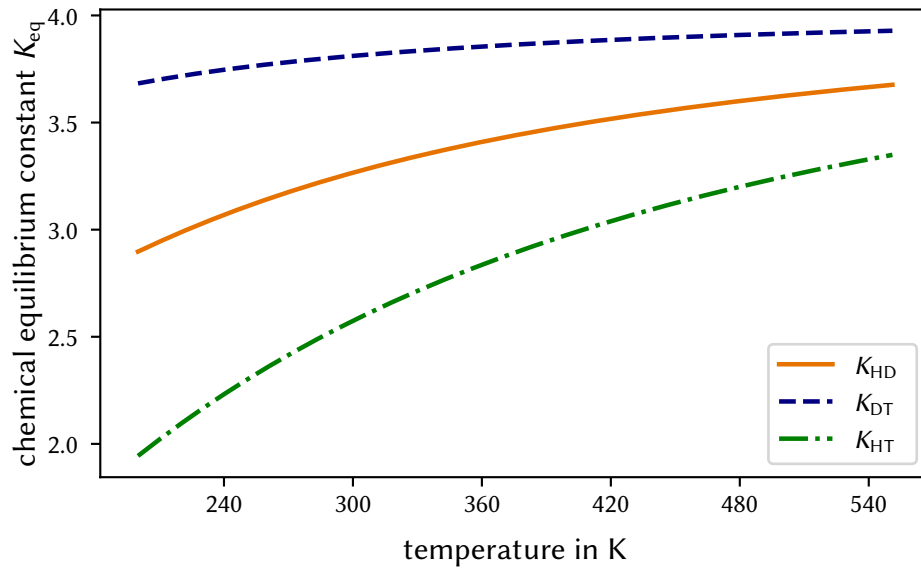


Figure 7.8: Temperature dependence of the chemical equilibrium constant K_{eq} . The constants are calculated based on the spectroscopic data reported in Ref. [Pac14] using the method described in Ref. [McQ00]. In this temperature interval the values agree with the numbers given in Ref. [Jon48] within 1 %. At higher temperatures, deviations of up to 5 % were observed.

In TRIHYDE, likely occurring impurities are tritiated water species from residual moisture and tritiated methane as discussed in Section 7.2.1. In reference [McC83], it is reported that HTO has no effect on equilibration time, while the presence of CT_4 as low as (50 to 150) ppm can significantly slow down the process of equilibration. This is comparable to the estimated CT_4 -levels during TRIHYDE measurements and may prolong sample preparation, although one has to remember that the reaction rate has no impact on the resulting sample accuracy.

Under the influence of the aforementioned reaction rates, the mixtures tend to an equilibrium state - provided sufficient time has passed- given by

$$K_{eq} = \frac{[AB]^2}{[A] \cdot [B]} \quad (7.15)$$

with [A] and [B] denoting the concentration or molar fractions of the reagents. These constants K_{eq} can be derived via the molecular properties of the isotopologues. First, the translational, rotational and vibrational contributions to the partition function Q_x at a given temperature for each isotopologue x are calculated. The chemical equilibrium constant in Equation (7.15) is given by the expression

$$K_{eq} = \frac{Q_{AB}^2}{Q_A \cdot Q_B} \cdot e^{-\Delta_r E_0/RT} \quad (7.16)$$

where $\Delta_r E_0$ is the difference in energies of the ground states of the product and the reactants, which is calculated from the bond dissociation energies of the species, and the universal gas constant R . For details, see Ref. [McQ00, Chapter 9], [Atk06, Chapter 17] and [Bar16].

Figure 7.8 shows the temperature dependence of the equilibrium constants used within this work. The values were derived using the spectral data published in Ref. [Pac14], which agree with the values reported in Ref. [Jon48] within 0.1 %, up to 500 K. A possible explanation for deviation at higher temperatures between the values of reference [Jon48] and the calculations used within this work is the different number of energy levels considered. When only considering energy states up to $v = 0$, $j = 10$, the calculated and published values are identical. Including vibrational energy states up to $v = 20$ allows a more accurate calculation of the equilibrium constants at higher temperatures, but ultimately, these differences have no impact in the temperature range of TRIHYDE.

7.3.2 Determination of the pressure dependence

The calibration sample preparation process has to fulfil two diametrical requirements:

1. High pressure for optimal SNR in LARA signal,
2. Unambiguous distinction between the binary and tertiary composition of the calibration mixtures.

Since the reaction rates outlined in Section 7.3.1 can vary over several orders of magnitude, depending on pressure, a sufficiently low pressure had to be found as process parameter [Saz11].

In order to find a suitable measurement pressure, two equi-concentrated mixtures at 70 mbar and 300 mbar were prepared and circulated in the loop for up to 600 h. In Figure 7.9, the first 80 h are presented. The chemical equilibrium ratio is calculated for each equilibration reaction according to Equation (7.15). For the higher pressure, the reaction ratios reach their respective equilibrium constants K_{eq} of 2.5 to 3.6 in less than 48 h (see Figure 7.8). The lower pressure sample exhibits a similar trend but is several orders of magnitude lower than the equilibrium value. In order to reliably determine the associated equilibration time constants τ_x , the mixture would have to be circulated for an unacceptable long time. Nevertheless, one can estimate that the time constants are at least in the order of days to weeks. Eventually, the sample will also tend to the same equilibrium state and the curves of both samples will terminate at the same equilibrium constants for each respective isotopologue.

In order to further investigate the effect of pressure on equilibration time, the time constants observed from H_2 - T_2 at four different pressures are shown in Figure 7.10 and the data points collated in Table 7.2. The stated pressure is the combined pressure from both mixing vessels; it does not represent the circulation pressure in the loop, which is much lower at the level of only about 30 %. For each isotopologue, the equilibration time is derived from an individual exponential fit according to Equation (7.17).

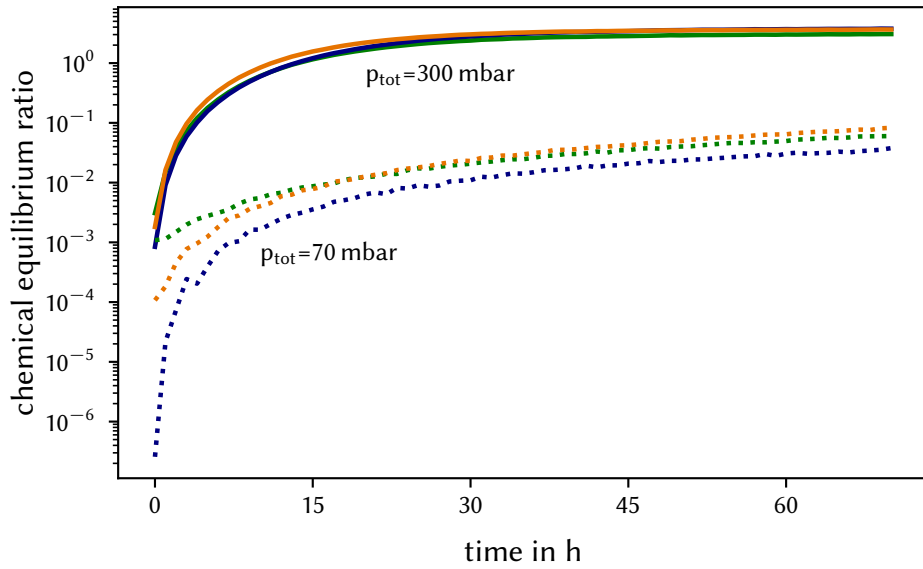


Figure 7.9: Equilibration process in equiconcentrated gas samples at 300 mbar (continuous) and 70 mbar (dotted). The ratio is an indicator for the equilibration process status and is equal to the equilibrium constant K_{eq} after a sufficiently long time has elapsed (see Equation (7.15)). The value is calculated for each mixed isotopologue from the relative Raman signal intensity. Each equilibration reaction has its individual but similar characteristic time τ_x which is strongly influenced by pressure. After sufficient time, all curves will terminate in the respective equilibrium value of 2.5 to 3.6.

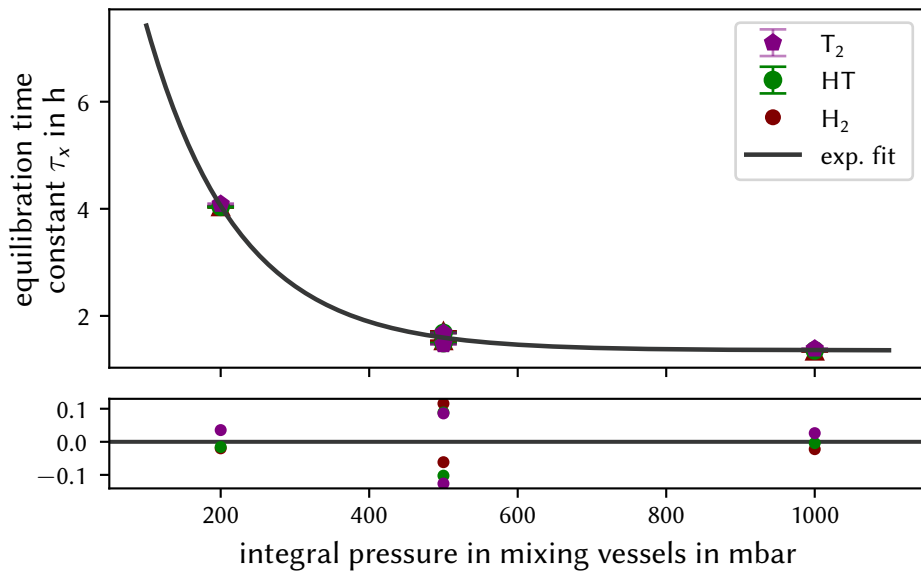


Figure 7.10: Pressure dependence of the self-equilibration time constants τ_x for 50:50 $H_2:T_2$ calibration samples. The time constants were derived from individual fits to each isotopologue. Based on Ref. [Saz11], the equilibration time constant is an exponential function of the system pressure. For better clarity, the data points are collated in Table 7.2.

Table 7.2: Equilibration time constants of T_2 – H_2 mixtures in the range from (200 to 1000) mbar. The total pressure is the combined pressure of both mixing vessels before the gases are mixed. The system pressure during the subsequent circulation is lower by $\sim 30\%$.

System pressure (mbar)	Equilibration time constant		
	τ_{T_2}	τ_{HT}	τ_{H_2}
200	4.034 ± 0.010	4.038 ± 0.009	4.089 ± 0.011
500	1.532 ± 0.003	1.491 ± 0.002	1.467 ± 0.002
500	1.709 ± 0.002	1.683 ± 0.002	1.680 ± 0.002
1000	1.338 ± 0.002	1.357 ± 0.002	1.387 ± 0.002

According to Ref.[Saz11], the equilibration time constants have an exponential dependence on the system pressure, which agrees with the observations within this work. When increasing the system pressure, the equilibration time decreases. However, the observed time constants are roughly two orders of magnitude higher than the published values, which are in the order of seconds.

This deviation can have a multitude of reasons:

- systematic effects associated with system setup;
- influence of the gas circulation in the loop in contrast to a static sample;
- impact of impurities on reaction chains;
- incorrect reaction chain models.

These influences can be further studied with the setup.

Based on this experience, a sample preparation pressure of ~ 500 mbar was chosen as a trade-off between measurement time and the availability of binary and tertiary samples.

7.3.3 Determination of the time constants

For the hydrogen isotopologues the kinematics of self-equilibration can be described by a first order reaction equation and therefore the concentrations of reagent molecules should follow an exponential curve [Gan99]. Consequently, the mole fraction development y_x for each isotopologue in a mixture of only two hydrogen isotopes is given by

$$y_x(t) = A_x \cdot e^{-t/\tau_x} + C_x \quad (7.17)$$

with τ_x the characteristic time constant and C_x the equilibrium concentration ratio.

This function is individually fitted to each isotopologue in every calibration sample, with an example curve of 60:40 T_2 : D_2 shown in Figure 7.11. In all sample preparation runs using D_2 and T_2 , the following was observed:

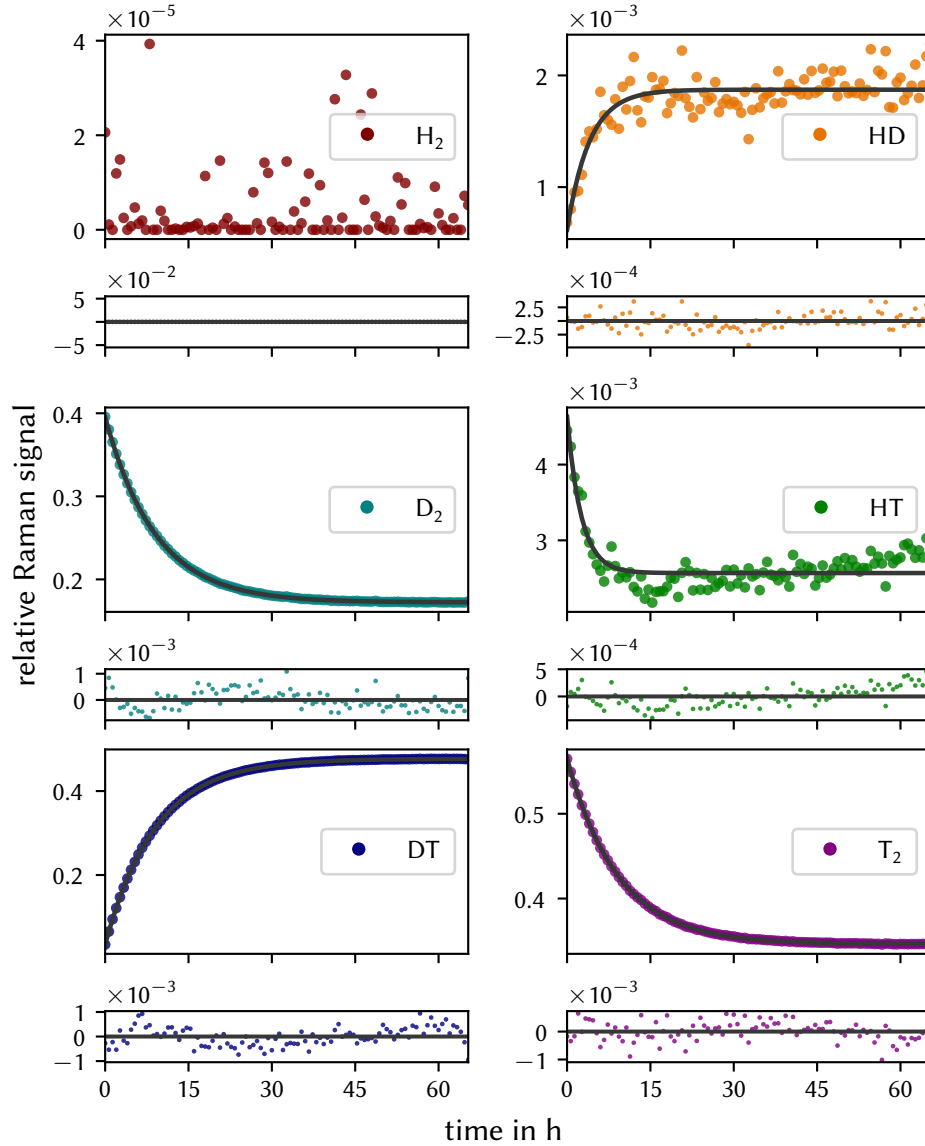


Figure 7.11: Self-equilibration process of a 60:40 D_2 – T_2 gas sample in a typical calibration run. For each point the relative LARA signal is integrated over 60 min. The solid curves represent fits with a single exponential function with a similar time constant τ_x for each isotopologue, in the range (6 to 14) h. For HT, the data deviates from a single exponential function and suggest a secondary exponential distribution, see text for details. Note that no fit was performed to H_2 because the signal is at the noise level and no meaningful trend can be extracted.

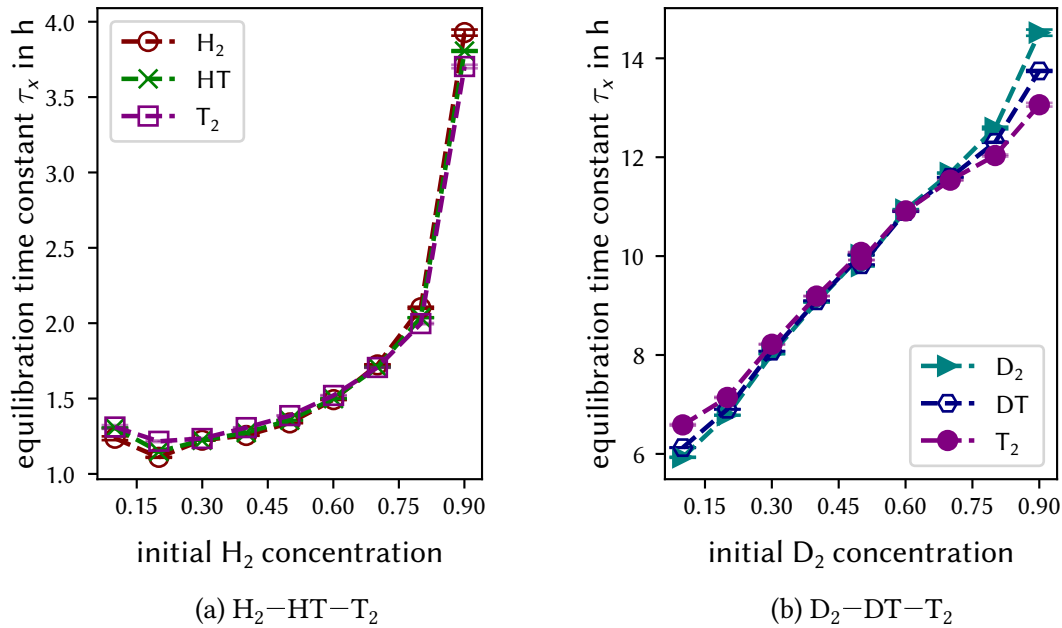


Figure 7.12: Influence of the concentration gradient on the equilibration time constant τ_x . Each isotopologue concentration is fitted individually by an exponential function after mixing; the initial D_2 -concentration is given by the pressure-volume-ratio before mixing. The divergence at the higher initial D_2 concentration can be explained with higher fitting uncertainty (the equilibration time is longer than the effective measurement time).

- (i) No additional H_2 formation was observed and the relative Raman signal remained at the noise level, which is equivalent to a relative concentration of ~ 10 ppm. As a consequence, no meaningful trend can be extracted.
- (ii) Due to the presence of HT in the initial tritium gas, the formation of HD and associated decrease of HT was observed. On account of the large concentration difference between $c_T \gg c_H$ and $c_D \gg c_H$, only HD and no H_2 were formed.
- (iii) The progression of the main components D_2 , DT and T_2 is well described by the respective exponential function and the equilibrium concentration ratio.
- (iv) For HT, an additional slope was identified which was also confirmed in long-term-experiments (see Section 7.2.1 and reference [Fis11]). It is interpreted as being due to second-order gas-wall interactions with the hydrogen reservoir given by the stainless steel walls. However, this has no impact on the LARA calibration samples due to the comparatively slow time constant and amplitude.

In order to shed light into the kinematics of the equilibration process, in Figure 7.12 the time constants τ_x are plotted as a function of the concentration gradient. The time constants are derived from a single exponential fit to each isotopologue.

At the time of writing, there was no experimentally validated description of reaction rates in dependence of temperature, pressure and concentration; only few theoretical calculations

are available [Gan99; Saz11]. These state that the reaction order with respect to the molar tritium fraction is 0.5, which would result in a root-shaped dependence. However, the data shown in Figure 7.12 suggest a more complex dependence:

- (i) In the H_2 - T_2 -campaign, the overall time constants are about a factor of five shorter than those observed in the D_2 - T_2 campaign. For all samples, the results of the individual fits agree within 2.5 %, suggesting that no other equilibration reactions contribute significantly. The deviation of the time constants for a tritium content of 10 %, which results in a slower reaction, might be caused by unidentified impurity residues, which may adversely affect the equilibration reaction [Uda92a].
- (ii) During the D_2 - T_2 -campaign the dependence can be approximated by a linear function which would correspond to an reaction order of 1. The deviation from the expected behaviour may be due to various effects:
 - Fitting inaccuracies associated with long equilibration time constants:
For low T_2 -concentrations the equilibration time is longer compared to higher concentrations and the measurement time was not sufficient to record the end of the process. This can also explain the parameter deviation for all three isotopologues which is not present in the reaction amplitude parameter.
 - Reaction inhibition by CT_4 :
As observed by McCONVILLE et al., minute impurities of CT_4 can slow down the reaction rates by up to an factor of 10 [McC83]. The T_2 -gas used to prepare the 90:10 D_2 - T_2 -sample was stored in the P-Loop buffer vessel the longest and therefore is likely to have the highest CT_4 -level in all samples. These impurities did not significantly impact the sample composition, but could have altered the equilibration time constant τ_x .

In conclusion, the observed unexpected concentration-dependence of the reaction rates show that the reaction kinematics are more complex than expected. The exact reaction orders and impurities influences are not consequential for LARA calibration, but might be further studied with the TRIHYDE experiment at a later stage.

7.3.4 Experimental study of self-equilibration of all six isotopologues

In order to verify the exponential reaction order of the equilibrium exchange between two isotopes, an equiconcentrated mixture of $H_2:D_2:T_2$ was prepared and circulated at an combined pressure of 300 mbar for 800 h. The first 100 h of the concentration development are displayed in Figure 7.13.

These reactions cannot solely be described by a single exponential function (see Equation (7.17)), since every isotope participates in two reaction channels simultaneously. For illustration, the relative Raman signals of T_2 during the equilibration process are shown in

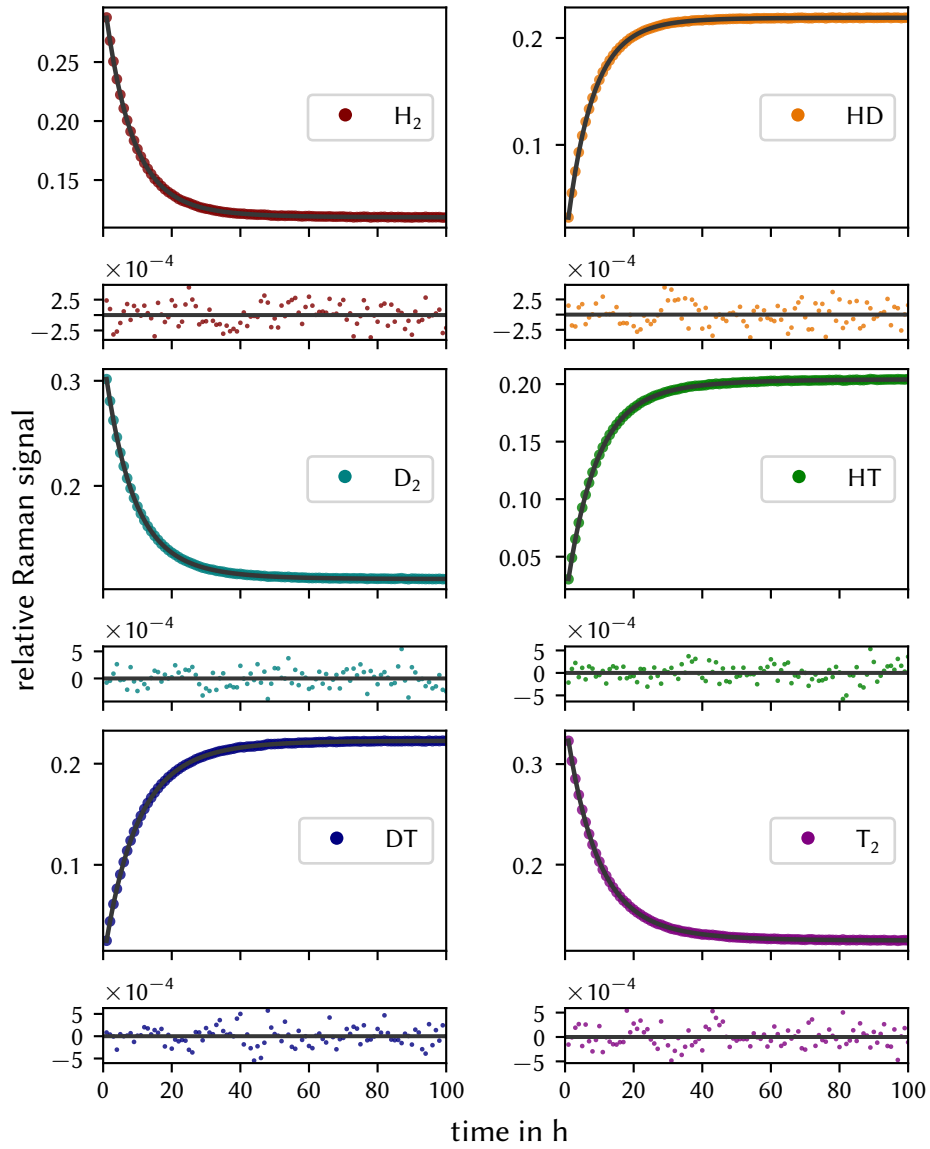


Figure 7.13: Equilibration process in the equiconcentrated gas sample at 300 mbar. For each point the relative LARA signal is integrated over 60 min. The solid lines represent fitted with an double exponential functions, as described in Equation (7.18) with time constants in the range (2 to 27) h. For illustration, the relative Raman signal for T_2 on a logarithmic scale is shown in Figure 7.14.

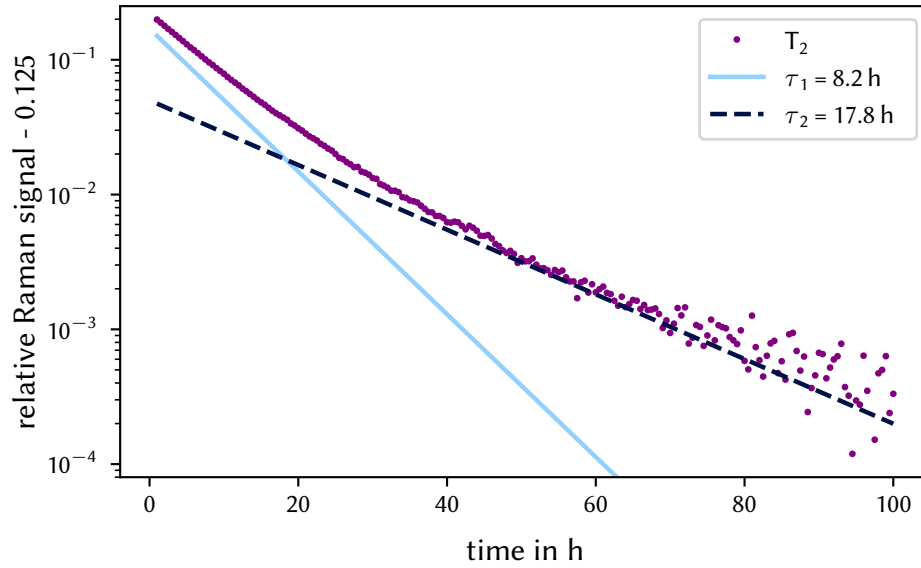


Figure 7.14: Equilibration process of T_2 in an equiconcentrated gas sample at 300 mbar on a logarithmic scale. The concentration in chemical equilibrium of $c_{T_2} = 0.125$ was subtracted in order to illustrate the different time constants. If the equilibration process could be described using a single exponential function, one would expect a single linear slope.

Figure 7.14. One can easily identify the two independent slopes of the respective reaction channel.

In the case of first-order reactions, both channels can be described represented by dual-exponential functions of the form

$$y_x(t) = A_{1,x} \cdot e^{-t/\tau_{1,x}} + C_{1,x} + A_{2,x} \cdot e^{-t/\tau_{2,x}} + C_{2,x} \quad (7.18)$$

as described in Ref. [Uda92a]. The resulting concentration ratio of the sample can be calculated using Equation (7.15) and the so-called ‘reactor series method’ described in Ref. [Mei69], which assumes a series of dedicated hypothetical catalysts for each reaction. Similar to the curves in Figure 7.11, the model function matches the concentration evolution rather well and supports an reaction order of one.

Table 7.3 gives the decay fit parameters for all six individual fits. These can be grouped in fast and slow reactions, with time constants of ~ 8 h and (20 to 30) h time constant, respectively; this is in line with the results from the equilibration using only two isotopes. As a result, one can assume that the individual equilibration processes can be described as 1st order process. Thus, for gas mixtures that have not yet reached the equilibrated state, the molar fractions in chemical equilibrium can be extrapolated using exponential fits.

Once equilibrium is reached after about 100 h, a quasi-linear slow increase in HT, HD as well as corresponding decrease in T_2 , DT is observed in the remaining 700 h of the measurement run; this is in line with the results reported in Ref. [Fis11]. The atomic ratio

Table 7.3: Equilibration time constants of the equiconcentrated gas sample at 300 mbar. The equilibration time constants are derived from dual exponential fits to each isotopologues, as described in Equation (7.18).

Isotopologue	τ_1	τ_1
H ₂	7.70 ± 0.11	19.6 ± 1.6
HD	7.44 ± 0.03	27.1 ± 5.8
D ₂	7.64 ± 0.15	16.41 ± 0.79
HT	7.66 ± 0.10	16.45 ± 0.81
DT	8.16 ± 0.11	15.53 ± 0.51
T ₂	8.25 ± 0.18	17.80 ± 0.97

during these processes changed by a factor of ~ 10 faster than the estimated ratio change from tritium decay, further suggesting that these reactions are not equilibration reaction but diffusion processes. Again, these processes were neither significant nor were they considered during LARA calibration sample preparation because their contributions were small and the associated time constants were very large.

7.4 Experimental determination of the calibration factors for T₂, DT and HT

The goal of this section is to both determine the absolute calibration factors for the LARA2 system as well as the theoretical sensitivity factors R_{theo} for tritiated isotopologues. After describing of the experimental and analysis procedure, the results are discussed in the context of the KATRIN experiment.

7.4.1 Description of the experimental procedure and the analysis strategy

The measurement procedure was similar to that used in the preparation of the stable-isotopologue sample, as described in Chapter 6. However, it differed in three important aspects:

- Based on the findings in Section 7.2.3, the composition of each individual gas was measured using LARA and RGA. In all measurements, the non-hydrogen components were below the RGA detection limits of $\sim 0.01\%$.
- No priming / wetting of the loop was performed since no catalyst was used and no atomic ratio change during sample production was observed ($< 1 \cdot 10^{-4} \text{ h}^{-1}$).
- Only the process of self-equilibration was used to accomplish chemical equilibrium.

Table 7.4: Overview of sample preparation procedure for tritiated isotopologues. The steps are similar to the procedure outlined in Table 6.1, but omitting the priming and catalysing steps.

Step	Procedure
1	Evacuate complete vacuum system to $<1 \cdot 10^{-3}$ mbar
1.2	Record LARA dark spectrum with shutter closed
2.1	Flush gas filters to remove trace amounts of N_2 or other impurities in H_2 and D_2 gas
2.2	Fill BV006 to target pressure with H_2 or D_2 ((50 to 450) mbar)
2.3	Fill LARA-cell and BGA to >400 mbar
2.4	Subsequent gas purity measurement with LARA, RGA, and BGA for >60 min
3.1	Evacuate LARA-system and piping to $<1 \cdot 10^{-3}$ mbar
3.2	Fill BV005 to target pressure with T_2 ((50 to 450) mbar)
3.3	Fill LARA-cell and BGA to >400 mbar
3.4	Subsequent gas purity measurement with LARA, RGA, and BGA for >60 min
4.1	Evacuate all piping to $<1 \cdot 10^{-3}$ mbar
4.2	Open valves between BV005 and BV006 to check for pressure reading offset
4.3	Circulate gas via pump until gas sample is homogenised and in thermal equilibrium ((24 to 72) h)
4.4	RGA measurement after completion of the equilibration process
4.5	Evacuate complete vacuum system to $<1 \cdot 10^{-3}$ mbar

A detailed overview of the measurement procedure is given in Table 7.4. The most defining measurement parameter is the selection of the target pressure during circulation. A higher pressure improves the SNR and the quality of the LARA signal, but also leads to significant shorter equilibration time constants, which may impact calibration-analysis for the non-equilibrated mixtures. Lower pressures enable good separation of the non-equilibrated phase but result in unacceptable long self-equilibration times which introduce additional fitting uncertainty and increase uncertainties due to impurity formation (e.g. ^3He). A combined target pressure of 500 mbar was chosen as a trade-off between equilibration time and signal strength.

An overview of a typical calibration sample production is shown in Figure 7.15. Similar to measurements of the stable isotopologues described in Chapter 6, the homogenisation time was about 5 min, marked by the maximum concentration of T_2 . The self-equilibration process started instantly after all valves were opened, but did not change the isotopic composition by more than 0.1 % during the homogenisation phase.

During the self-equilibration phase, the LARA-spectra were integrated over a 20 min interval to smooth the curve and reduce the noise level. For each isotopologue, an exponential function, given in Equation (7.17), was fitted. Based on the obtained equilibration parameter, the initial binary and the final tertiary relative signal strengths were derived.

Depending on which data set is used, the uncertainty of the Raman signal includes

- Poisson-noise for event count rate,
- statistical uncertainty from the fit parameter,
- uncertainty of the spectral sensitivity correction from the NIST-standard.

The fractions of the gas sample were determined using the pressure ratio of the mixing vessels and chemical equilibrium constants, given in Figure 7.8.

In order to obtain the resulting equilibration isotopologue concentration, the function as shown in Equation (7.17) was fitted to the calibration data.

Based on the description in Equation (6.3), the calibration factors R_x for a binary T_2 - Q_2 mixture were derived by the model function for the relative Raman signal S_x and initial molar fraction N^i :

$$S_{T_2} = \frac{R_{T_2} \cdot N_{T_2}^i}{R_{T_2} \cdot N_{T_2}^i + R_{Q_2} \cdot N_{Q_2}^i} \quad , \quad (7.19)$$

$$S_{Q_2} = \frac{R_{Q_2} \cdot N_{Q_2}^i}{R_{T_2} \cdot N_{T_2}^i + R_{Q_2} \cdot N_{Q_2}^i} \quad . \quad (7.20)$$

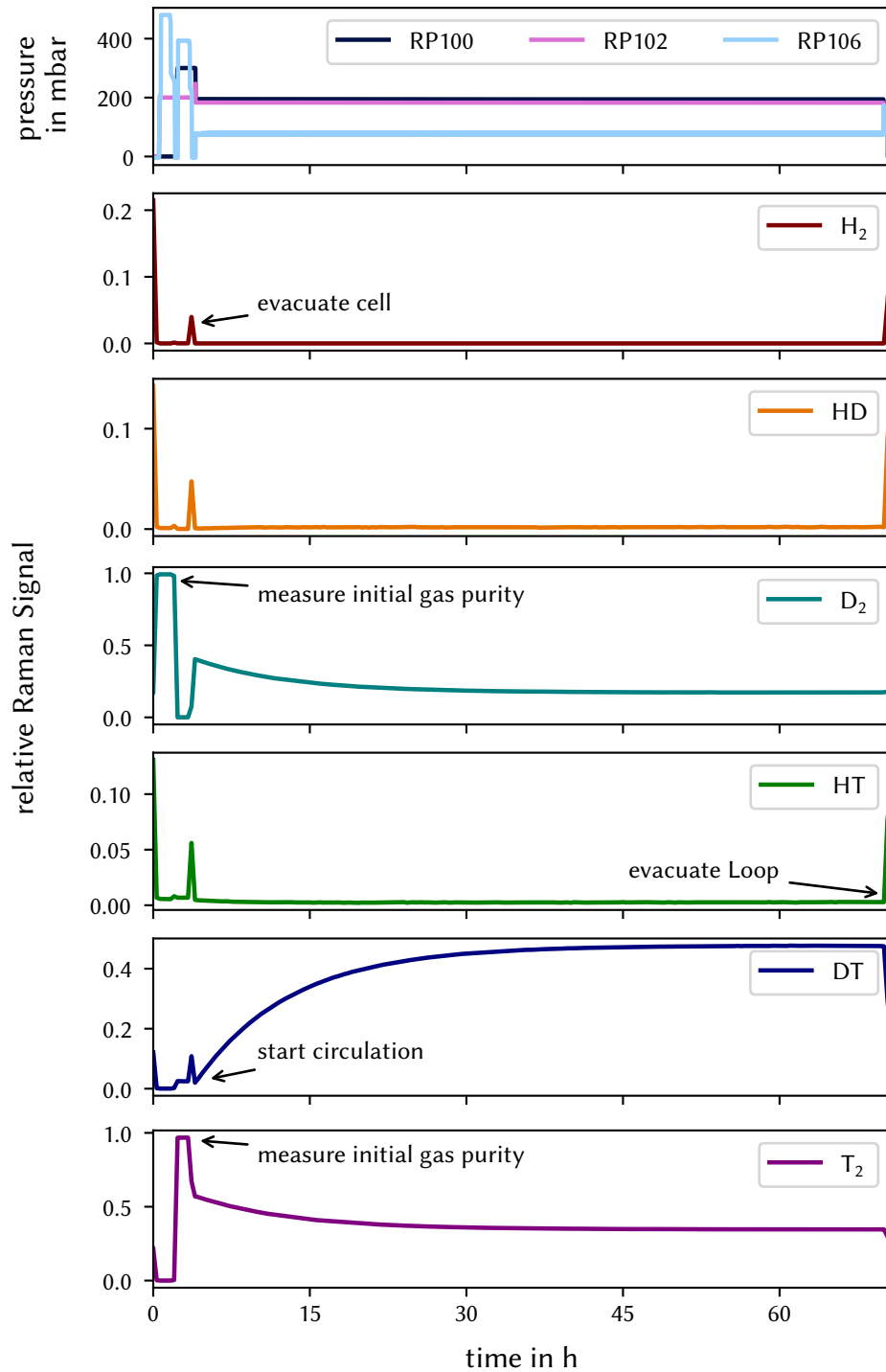


Figure 7.15: Pressure and Raman signal profiles of a typical calibration run for a 60:40 T_2 : D_2 mixture. In each run, gases were analysed using LARA, RGA and BGA to verify the initial gas purity. Subsequently both mixing vessels were filled to the desired target pressure which sum up to 500 mbar. Afterwards, the gases were circulated continuously until the end of the run to homogenise and equilibrate the mixture. A detailed description of the measurement schedule is given in Table 7.4.

In case of an equilibrated, tertiary mixture the relative signal for T₂ is given by

$$S_{T_2} = \frac{R_{T_2} \cdot N_{T_2}^{eq}}{R_{T_2} \cdot N_{T_2}^{eq} + R_{Q_2} \cdot N_{Q_2}^{eq} + R_{QT} \cdot N_{QT}^{eq}} \quad (7.21)$$

$$= \frac{R_{T_2} \cdot (N_{T_2}^i - \xi)}{R_{T_2} \cdot (N_{T_2}^i - \xi) + R_{Q_2} \cdot (N_{Q_2}^i - \xi) + R_{QT} \cdot (N_{QT}^i + 2\xi)}. \quad (7.22)$$

Here the reaction extend ξ describes the amount of heteronuclear molecules that have formed during the equilibration process. This amount depends on the equilibrium constant K_{eq} described in Equation (7.15) and is given by

$$\xi(K_{eq}) = \frac{b - \sqrt{b^2 - 4(K_{eq} - 4)(K_{eq} \cdot N_{T_2}^i \cdot N_{Q_2}^i - (N_{QT}^i)^2)}}{2(K_{eq} - 4)} \quad (7.23)$$

with

$$b = K_{eq}(N_{T_2}^i + N_{Q_2}^i) + 4N_{QT}^i \quad (7.24)$$

for $K \neq 4$ [Sch14a].

The calibration curves for binary and tertiary mixtures were derived by the same procedure as the stable calibration samples (see Section 6.2.1). In addition to the general gas sample uncertainties given by the TRIHYDE setup (see Section 6.2.1), the uncertainty of the T₂-sample composition was considered. All data points were shifted by the combined uncertainty in composition (x-axis) in both directions and the same regression and bootstrap resampling was performed. The larger difference from the non-shifted results was used as an estimate for the systematic uncertainty of the prepared gas sample composition.

The uncertainties in y- and x-direction are not correlated and thus can be combined using classic error propagation to give the full calibration factor uncertainty.

7.4.2 Calibration factors for mixtures of T₂ + H₂ + HT

In order to determine the calibration factors, two measurement campaigns were performed at different pressures levels:

- (i) 100 mbar,
- (ii) 500 mbar.

These pressures denote the combined pressure in both mixing vessels before mixing, hence the resulting circulation pressure was lower. Besides a higher pressure, the second campaign also used a single tritium gas batch transferred from the TTs. All samples were prepared following the step sequence summarised in Table 7.4. In order to evaluate the reproducibility of the procedure, the 50:50 sample was prepared twice.

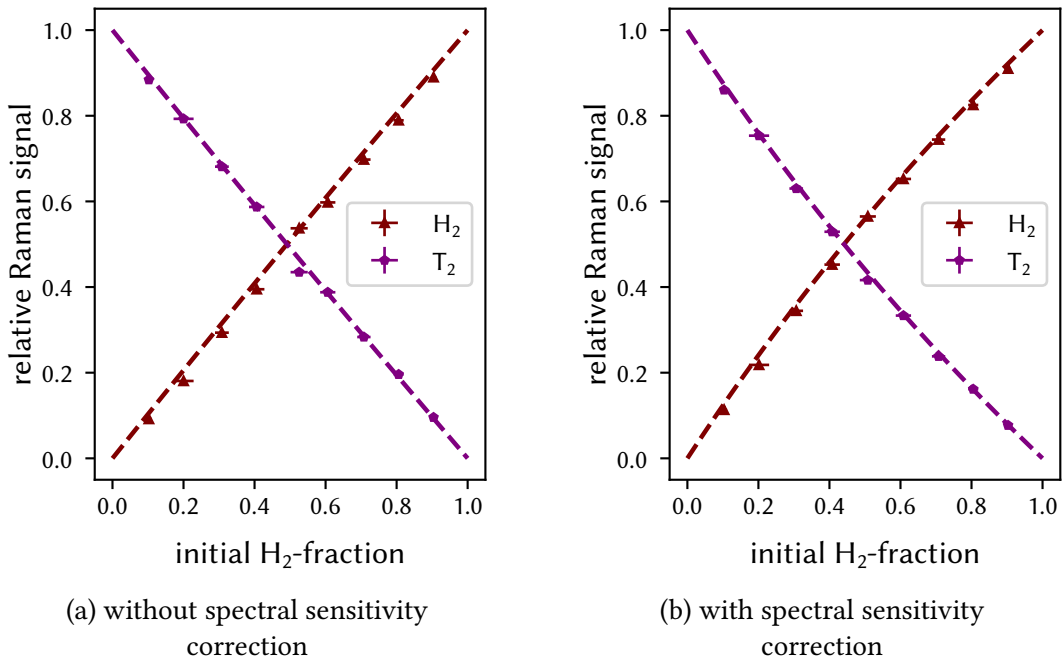


Figure 7.16: Calibration curve for H_2 – T_2 binary mixtures. Each point is measured according to the procedure outlined in Section 7.4.1. The relative Raman signal is determined by averaging the LARA signal during the first 60 minutes after sample homogenisation. The initial combined pressure in the mixing vessels was 100 mbar. The model functions for each isotopologue are described in Equation (7.20) and were fitted simultaneously in order to derive the calibration factors.

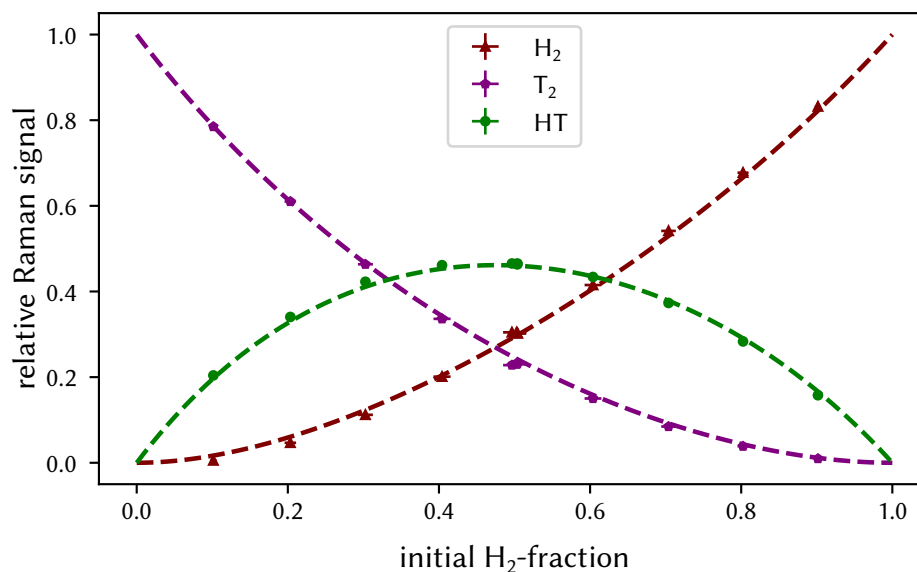


Figure 7.17: Calibration curve for H_2 - T_2 -HT tertiary mixtures with applied spectral sensitivity correction. The calibration curves were determined by the initial molar fractions and derived from Equation (7.22). The relative Raman signals associated with chemical equilibrium of the mixture are derived values, deduced from the asymptotes to the exponential data fits for the individual isotopologues.

Binary H_2 - T_2 samples In Figure 7.16, the resulting calibration curves from campaign (ii) are shown, with and without spectral sensitivity correction. As expected, due to the largest shift of theoretical intensities between H_2 and T_2 , the effect of the spectral sensitivity is rather prominent.

In order to determine the initial signal ratio, the relative signals after the homogenisation phase, i.e. maximum T_2 -signal within 5 min of mixing, were used. Due to the strong pressure dependence of the self-equilibration process (see Figure 7.10), the transition to chemical equilibrium is slow enough to assume a constant gas composition during the averaging time interval of 10 min.

This results in lower uncertainties compared to the sample from campaign (ii). Although the higher pressure allows for a higher signal-to-noise-ratio, the progressing self-equilibration and the need to describe the process via a model-function offsets this advantage. However, the calibration factors from both campaigns differ by less than 3.5 % and agree within their uncertainty. Based on the fact that the values from campaign (i) are less likely to be affected by the equilibration process, these should be used for system calibration.

Tertiary H_2 -HT- T_2 samples During the first campaign, due to lower loop pressure and associated longer equilibration time, the sample was circulated via the same catalyst-material used in HYDE (see Section 6.2.3) in order to achieve chemical equilibrium. Similar

Table 7.5: LARA calibration factors R_x for H_2 –HT– T_2 . Of physical importance is not the numerical value, but the ratio between the factors. Due to the higher number of free parameters, the uncertainties derived from the tertiary mixtures are higher. Note that the factors are derived from different sample pressures for the binary ($p_{\text{tot}}=100$ mbar) and tertiary ($p_{\text{tot}}=100$ mbar) measurements.

Isotope	without spectral correction				with spectral correction			
	R_x	σ_{tot}	Δ_{sys}	σ_{stat}	R_x	σ_{tot}	Δ_{sys}	σ_{stat}
H_2	1.027	0.024	0.021	0.012	1.118	0.015	0.011	0.011
T_2	1.004	0.017	0.014	0.009	0.887	0.015	0.010	0.012
H_2	1.010	0.003	0.002	0.001	1.000	0.002	0.002	0.001
HT	1.058	0.025	0.014	0.020	0.969	0.011	0.023	0.016
T_2	1.079	0.017	0.013	0.012	0.832	0.014	0.029	0.020

to measurements with the stable isotopologues, this introduced substantial shifts in the atomic ratio of up to 50 %, varying in each sample preparation. Thus, these values were useless for system calibration.

In the second campaign, the signal ratios for the equilibrium concentrations were determined by fitting an exponential function, as given by Equation (7.17), to the individual relative signals. During the sample preparation time of 48 h, neither significant additional reactions nor shifts in atomic ratios were observed.

In order to obtain the calibration factors, the three functions given in Equation (7.22) were simultaneously fitted using a chemical equilibrium reaction constant $K_{\text{eq}} = 2.574$. This value was derived in Section 7.3 which agrees with the value reported in Ref. [Jon48]. During the regression, this value was kept fixed.

All calibration factors for both mixtures are summarised in Table 7.5. The uncertainties of the calibration factors derived from tritiated mixtures are about a factor of three higher than those using only stable isotopologues (see Section 6.2). This is the result of the higher initial gas composition uncertainty as well as the introduction of the self-equilibration model.

In order to validate the absolute theoretical intensity, the ratio between the calibration factors R_{H_2} and R_{T_2} can be calculated, analogous to the approach described in Section 6.2. This gives a value of

$$R_{H_2/T_2} = 1.261 \pm 0.021, \quad (7.25)$$

which is slightly lower than the value obtained from theory and depolarisation measurements of $R_{H_2/T_2} = 1.285 \pm 0.050$ [Sch14a], although within the uncertainty. Using the measured value for R_{T_2} , the ratio for R_{HT} is found to be

$$R_{H_2/HT} = 1.083 \pm 0.035, \quad (7.26)$$

which agrees with the theoretically derived value of $R_{H_2/HT} = 1.078 \pm 0.033$.

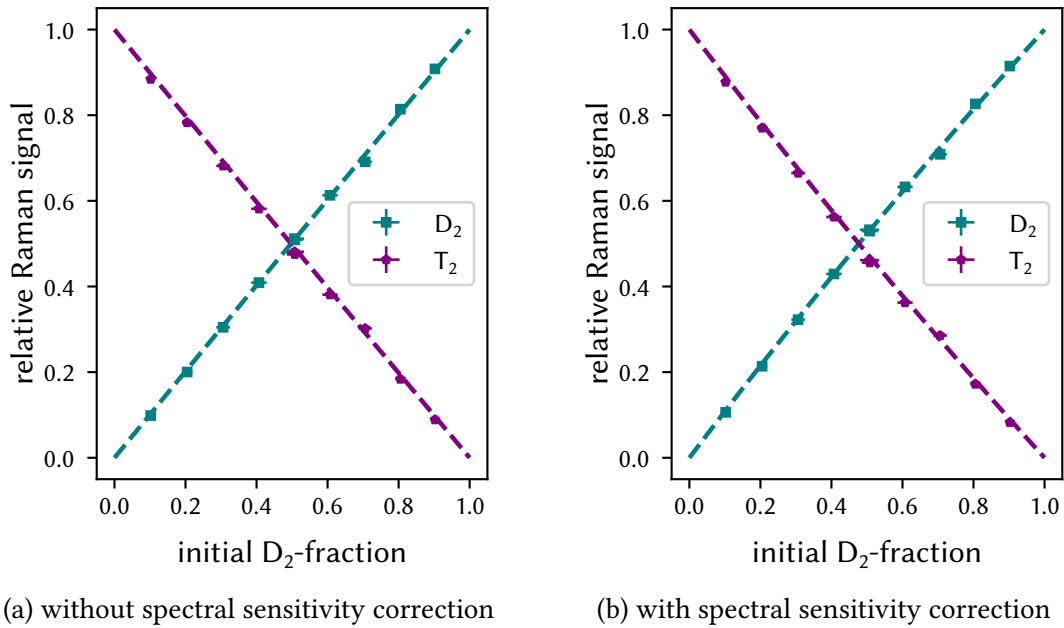


Figure 7.18: Calibration curve for D_2 – T_2 binary mixtures. Each point is measured according to the procedure outlined in Section 7.4.1. The relative Raman signal is derived from the y-intercept of the exponential fit to each equilibration reaction. Both curves given by Equation (7.20) are fitted simultaneously to quantify the calibration factors.

Based on the agreement between the experimentally and theoretically derived calibration factors, one may conclude that the currently used calibration approach should also be valid for the radioactive isotopologues T_2 and HT. The impact of these values will be discussed in Section 7.5.

7.4.3 Calibration factors for mixtures of $T_2 + D_2 + DT$

The samples for the D_2 – DT – T_2 -campaign were all prepared and analysed using the procedure described in Section 7.4.1. No significant deviations in purity level or parameter changes were observed, besides the already described higher self-equilibration time constant compared to H_2 – T_2 (see Figure 7.10).

Binary D_2 - T_2 samples In Figure 7.18, the calibration curves of the binary mixture in dependence of the initial D_2 -fraction are given, with and without spectral sensitivity correction. The relative Raman signals were derived from the exponential fits, for the point in time in which the homogenisation phase was complete, corresponding to the maximum in T_2 and D_2 relative signals. In order to evaluate the reproducibility, a 50:50 sample was prepared again after all other ratios were measured. Despite the higher systematic uncertainty contributions in the equi-concentrated sample, no deviation was observed.

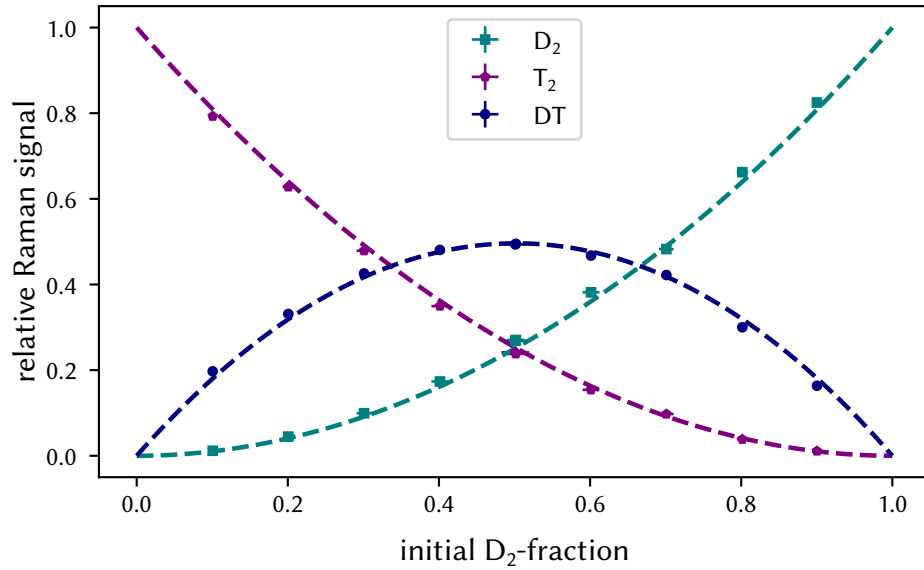


Figure 7.19: Calibration curve for D_2 – T_2 – DT tertiary mixtures with applied spectral sensitivity correction. The data points are given by the exponential fit to the self-equilibration curve of each isotopologue. For the fitting of the calibration curve, the chemical equilibrium constant at the given temperature was fixed and the individual calibration factors were free parameters (Equation (7.22)).

In contrast to the H_2 – T_2 calibration curves shown in Figure 7.16, the difference in shape between corrected and non-corrected data is less pronounced. This is due to the fact that the relative difference between the sensitivity correction for D_2 and T_2 is lower by factor of ~ 2 .

Tertiary D_2 - DT - T_2 samples For the tertiary mixtures, the equilibrium ratios of all three isotopologues were calculated for their given initial values according to Equation (7.15) and Equation (7.22). The chemical equilibrium constant value of $K_{eq} = 3.811$, as given by [Jon48] and calculated in Section 7.3, was used and not varied during the regression calculation.

The resulting calibration factors are collated in Table 7.6. As mentioned in Section 7.4.2, only the ratio between two factors is of physical importance, not the single numerical value. Similar to the observations from the H_2 - T_2 -campaign, all non-corrected calibration factors are compatible with a numerical value of $R_x = 1$. Since the lines of the deuterium isotopologues are between the other branches, this was expected. The total calibration uncertainties of about 1 % give an estimate with which precision the calibration samples in TRIHYDE can be prepared.

In case of tertiary mixtures, the uncertainty is about three times higher than for binary mixtures. This comprises the additional uncertainties of initial values, chemical equilibrium constant and other free parameters for the regression calculation. The difference in

Table 7.6: LARA calibration factors R_x for D_2 – DT – T_2 . Of physical importance is not the numerical value but ratio between the factors. Due to the higher number of free parameters the uncertainties for the equilibrated ratio is higher.

Isotope	without spectral correction				with spectral correction			
	R_x	σ_{tot}	Δ_{sys}	σ_{stat}	R_x	σ_{tot}	Δ_{sys}	σ_{stat}
D_2	1.016	0.013	0.0089	0.0093	1.058	0.01	0.008	0.006
T_2	1.001	0.011	0.0060	0.0095	0.962	0.015	0.009	0.012
D_2	1.004	0.003	0.0026	0.001	1.001	0.002	0.001	0.001
DT	1.007	0.029	0.027	0.011	0.963	0.026	0.023	0.010
T_2	1.004	0.039	0.0333	0.021	0.925	0.034	0.029	0.020

uncertainties of one order of magnitude for D_2 and the tritiated isotopologues is associated with the uncertainty of the initial DT -content, as determined by the LARA-system itself and the uncertainties given in Section 7.2.2. This initial DT -content is due to the gas chromatographic process in the Iss, which separates the isotopologues based on their respective retention time in a capillary. As a consequence, a spillover of the DT fraction into the T_2 sample is unavoidable.

The derived ratios of the calibration factor R_{H_2/T_2} for the binary and tertiary sample agree within 1 %; however, due to the lower uncertainty of the results using only two isotopologues, the values from the binary sample should be used for LARA calibration.

The difference in uncertainty level before and after spectral correction is less pronounced than encountered in the H_2 – T_2 -measurements. Note that all Q_1 -branch positions in this campaign lie within the certified region of the NIST SRM standard and have an average uncertainty below 0.2 %, hence the spectral sensitivity correction uncertainty is dominated by the calibration process of the CCD-bins and not the standard [Nie18; Ake20b].

Up to now, all calibration factors have been established except the one for DT . As already mentioned, the experimental calibration factor for a single isotopologue has no physical meaning; the ratio between two factors are necessary for LARA calibration. In order to derive the ratio $R_{H_2/DT}$, the ratio $R_{T_2/DT}$ must be calculated first. This ratio is then normalised to the calibration factor of H_2 using the R_{H_2/T_2} obtained from the binary H_2 - T_2 measurements. The derived calibration factor is found to be

$$R_{H_2/DT} = 1.200 \pm 0.038 \quad (7.27)$$

which is in very good agreement with the theoretical value of 1.203 ± 0.044 . Compared to the calibration factors derived for the other isotopologues, the uncertainty is higher due to the uncertainty of the initial DT concentration and the applied normalisation to R_{H_2} .

Methane formation during sample preparation Prior to the sample preparations for this measurement campaign, it was shown that the formation of tritiated methane is detectable, but does not noticeably affect the sample composition (see Section 7.2.1). In order to confirm these finding, the trend of the relative LARA signals for methane is analysed and compared to the expected formation rates. Using the total inner surface of the setup and the outgassing rates reported in Ref. [Fis11], a relative methane production rate of $\sim 4.9 \cdot 10^{-6} \text{ h}^{-1}$ was expected².

For each sample prepared during the D_2 – DT – T_2 -campaign, a linear fit was applied to the relative LARA signals S_{CXT_3} . The derived mean fitting parameters are

$$S_{\text{CXT}_3}(t) = (3.1 \pm 2.6) \cdot 10^{-6} \text{ h}^{-1} \cdot t + (4.16 \pm 0.45) \cdot 10^{-4} . \quad (7.28)$$

This formation rate agrees with the expected values derived from Ref. [Fis11]. The low formation rate and low initial relative signal strength show that the formation of tritiated methane have no noticeable impact on sample composition.

If methane formation was significant, one would observe a change in the atomic ratios T, H and D during the equilibration phase. In all sample preparation runs, which lasted up to 5 days, no shift in the atomic ratios was observed; thus confirming that methane formation had no significant impact on sample composition.

7.5 Comparison to literature values and implications for KATRIN

While the calibration factors R_x without spectral correction can only be used for the LARA2-system at TRIHYDE as is, the values obtained after spectral correction are deemed universal for all tritium monitoring LARA-systems, including the system deployed at the KATRIN experiment. The theoretical sensitivity factors currently used at the KATRIN experiment are those listed in Ref. [Sch14a] and are based on theoretical calculations with the uncertainties estimated from depolarisation measurements. For the stable isotopologues, the theoretical sensitivities were confirmed in the HYDE-experiment.

Due to the good agreement between depolarisation and calibration gas sample measurements, the calculated theoretical sensitivities for the radioactive isotopologues were used to measure the source gas composition in the WGTS for the neutrino mass analysis during the first measurement campaign, see Ref. [Ake19]. As a consequence, the dominating uncertainty for composition monitoring is the uncertainty derived from the depolarisation measurements.

In Figure 7.20 the currently used LARA-calibration factors and the values obtained in TRIHYDE are displayed together with their uncertainty bands. For all six isotopologues,

²A. REIN: ‘Estimation and analysis of impurities in calibration gas mixtures for the Tritium-Hydrogen-Deuterium-Experiment (TRIHYDE)’. Master’s thesis. Karlsruhe Institut of Technology, IEKP, 2015.

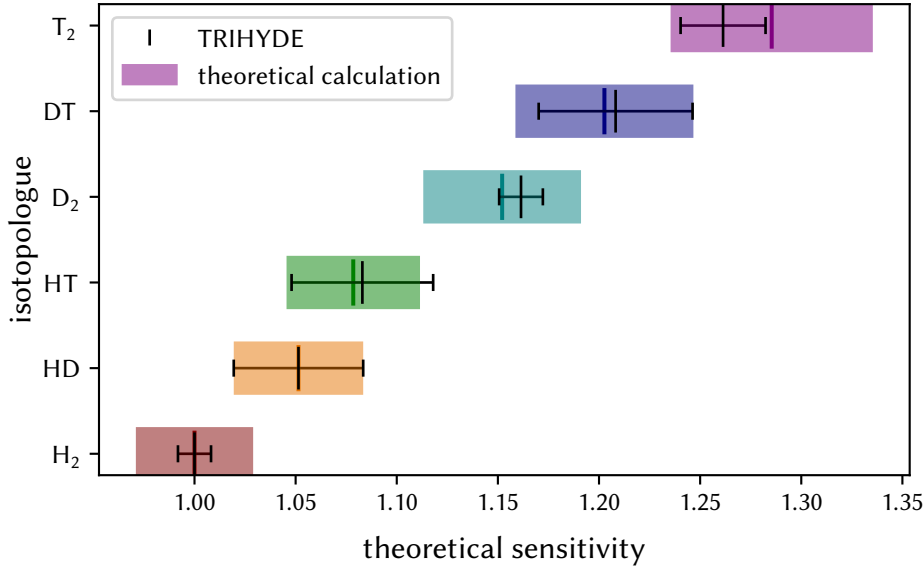


Figure 7.20: Comparison of TRIHYDE and literature values for the theoretical sensitivities of all hydrogen isotopologues. The literature values and symmetrical uncertainties (colored bars) are described in Ref. [Sch13b]. The TRIHYDE values are displayed as black bars denoting the combined experimental uncertainty. Since no experimental values for HD were established within this work, the R_{HD} -values from [Sch13b] are shown.

both values agree within the uncertainty margins, validating that the currently used calibration factors are indeed applicable in the composition monitoring of KATRIN, and thus can be used for $m(\nu_e)$ -mass measurements.

The accuracy achieved in TRIHYDE lowers the uncertainty for T_2 by a factor of 2.5, further improving the trueness of the LARA monitoring capabilities for KATRIN. Despite exceeding the KATRIN requirements of 10 % trueness [Sch11] already with the values reported in Ref. [Sch14a], the experimental validation was still missing.

Comparing the values for T_2 , the sensitivity value obtained in this measurement is about 2 % lower than the current value, indicating that the current measurements overestimate the T_2 content in the WGTS-gas. However, for a nominal gas composition with $c_{T_2} = 95\%$ and $c_{DT} = 5\%$, the relative difference in measurement composition between theoretical intensity values from calculations and experimental values, is less than 0.1 %. This change in measured composition is well within the uncertainty of the gas composition monitoring in the WGTS. As a consequence, this shift has no negative effect of the already performed neutrino mass analysis and published value in Ref. [Ake19]. However, the updated calibration factor and uncertainty should be used in future analysis.

Using gas mixtures with a lower T_2 -content, the effect would be more pronounced but still rather small. In an hypothetical equi-concentrated T_2 -DT mixture the relative difference in composition measurement is about 1 %. Nonetheless, the reduced uncertainty is beneficial

not only in KATRIN measurements but also for activity monitoring and accountancy at TLK, or other tritium processing facilities.

7.6 Conclusions

Respective the open issues identified in Section 4.3.3, the TRIHYDE experiment was primarily designed to provide the experimental determination of theoretical Raman sensitivity for tritiated hydrogen isotopologues. In order to achieve this goal, several preliminary studies were carried out in order to evaluate and account for the additional systematic effects introduced by the radiochemistry of tritium, i.e.

- Production of tritiated methane due to gas-wall interactions,
- Gas purity of the initial T_2 -gas sample,
- Self-equilibration reaction of the prepared sample.

All of these questions were addressed during the H_2-T_2 and D_2-T_2 campaigns, and the findings can be summarised as following:

- (i) Using a modified method of standard addition, the initial DT content for the actual T_2 -sample was estimated to be 0.030 ± 0.015 . This demonstrates the general applicability of using TRIHYDE to perform a MSA with tritiated isotopologues and the value obtained is comparable to other estimates [Dör05].
- (ii) Based on mass spectrometer and LARA measurements, the formation of tritiated methane was observed, at the expected low levels. However, these had no significant impact on the calibration samples due to the pressures and timescales used.
- (iii) A systematic study of self-equilibration reaction for tritiated gas mixtures was carried out, confirming that the production of chemical equilibrated samples within an acceptable time frame and without the use of a catalyst or other means, which can potentially change the atomic ratio of the sample.
- (iv) The calibration factors for all tritiated hydrogen isotopologues have been experimentally measured with an uncertainty of about (1 to 3) %. Due to the increased systematics of the sample preparation and analysis, the uncertainties for the heteronuclear isotopologues exhibit threefold higher values, in comparison to the homonuclear species.
- (v) All experimental values are compatible with the currently used values derived from ab-initio calculations reported in Ref. [Sch13b] within the uncertainty intervals. Despite the measured values for T_2 being about 2 % lower than currently used, the impact on composition for mixtures of $>95\%$ T_2 is negligible.

Based on these results, the calibration approach for source gas monitoring at KATRIN, which relies on an optical standard and theoretical intensities, is finally fully validated.

All currently used values have been crosschecked and confirmed, using by accurate gas samples of all six hydrogen isotopologues.

Thanks to the low uncertainty in the calibration factors derived for the current LARA2-system, it henceforth can be used as an high-accuracy analysis tool for other experiments at TLK. This includes gas samples from KATRIN loops and components, Iss and TTS samples, as well as ongoing T_2 -loading experiments in various materials.

Using the experimental calibration factors, the calibration trueness of all currently deployed LARA-systems at TLK benefits from the uncertainty reduction which improves composition monitoring accuracy at each experiment, especially for lower T_2 content.

With reference to the results presented here, the following improvements and additional measurements are proposed:

- (i) Estimate of the initial HT content via the method of standard addition.

As seen in the TRIHYDE campaigns as well as observed by KATRIN loops operation, a considerable amount of HT is produced during operation [Fis11; Ake20b]. In order to obtain an additional estimate of HT-impurities and uncertainty besides sole LARA measurements, the modified MSA can be performed in TRIHYDE with the following improvements:

- smaller addition steps,
- higher pressures,
- longer measurement times.

- (ii) Detailed study of self-equilibration rates.

Several studies on reaction rates have been reported which can be grouped into three categories:

- (a) Experimental studies; see [Dor54; Gen70; Uda92b],
- (b) Theoretical studies or calculations; see [Mor67; Gan99; Saz11],
- (c) Studies of the influence of impurities; see [Tho58; Aqu65; Uda92a].

Using TRIHYDE, well-defined samples in regard to pressure and mole fraction can be produced. Using such samples, *in-situ* and real-time studies can be carried out, which can elucidate the influence of the various reaction chains, and thus will aid in the understanding of the general kinematics of the equilibration process.

- (iii) Use TRIHYDE samples for round robin tests at TLK.

Using the samples prepared for LARA-calibration, the recorded data can be used to cross-calibrate and characterise other built-in analytical tools, like Bixs [Ake20c] and BGA, to further expand TRIHYDE capabilities to analyse provided gas samples. These samples can be distributed to other experiments at TLK for a round robin test, bench-marking all deployed analytical methods, especially chromatography and ionisation chambers.

- (iv) Perform characterisation measurements with hydrogen and non-hydrogen mixtures. Up to now, only samples prepared of hydrogen isotopes were used, despite the general ability to use additional gases. Using a similar preparation procedure, samples of e.g. T₂ in He can be produced and used to characterise the performance of suitable analytical methods, either for KATRIN or possible future fusion reactors [Nis06].

In conclusion, the TRIHYDE-experiment is a valuable addition to the analytical tool set at TLK and can be used to further develop various tools and methods used for tritium sample analysis, process control, and accountancy.

8 Summary and Outlook

Summary The observation of neutrino flavour oscillations has shown that neutrinos must have a finite, non-zero mass. This was the first confirmed proof for physics beyond the Standard Model of elementary particle physics, which in its basic form assumes neutrinos to be massless. Although many experimental efforts have expanded our knowledge of the oscillation parameters, no experimental approach has yet reached sufficient sensitivity to provide a definitive value of the neutrino mass. The absolute value of the neutrino mass scale remains one of the fundamental questions. The answer thereof is required to improve cosmological models as well as to help scrutinise theoretical extensions of the Standard Model to account for neutrino mass generation. Different approaches can access the neutrino mass scale, e.g. indirect methods like cosmological observation, searches for the neutrinoless double-beta-decay or direct searches.

The most stringent direct experimental limit of $m(\nu_e) < 1.1$ eV (90 % C. L.) for the effective electron neutrino mass up-to-date was reported by the KATRIN [Ake19]. The limit is derived from high resolution spectroscopy of the kinematic endpoint of the tritium β -decay, which is affected by the neutrino mass.

In order for KATRIN to achieve the design sensitivity of $m(\nu_e) < 0.2$ eV (90 % C. L.), it is essential to minimise and account for systematic effects. One set of systematic effects is associated with the gas composition inside the WGTS, which provides the β -electrons for KATRIN. Due to technical reasons, the molecular T_2 inside the WGTS will always contain residues of other hydrogen isotopologues (H_2 , HD, D_2 , HT and DT). As the gas composition influences the shape of the β -spectrum, it must be considered in the neutrino mass analysis and hence continuously monitored.

At the TLK, tritium-compatible LARA-systems were developed and constructed in order to meet the performance requirements of KATRIN. In order to achieve the KATRIN design sensitivity, namely a precision of ≤ 0.1 % and a calibration trueness ≤ 10 % for source gas monitoring is necessary. For quantitative gas composition analysis, a system- and isotopologue-specific response function must be obtained.

The required calibration factors are a combination of (i) the wavelength-dependant spectral sensitivity of the optical setup; and (ii) the isotopologue-specific theoretical intensity. In the current calibration strategy, the spectral sensitivity is measured via a traceable optical standard SRM2242 provided by NIST. The theoretical intensities used are derived from molecular polarisability tensors based on theoretical calculations by SCHWARTZ et al.

[Sch87] and LEROY¹, although without a stated uncertainty. These calculations have been experimentally verified in depolarisation measurements by JAMES et al. [Jam13a] for all six hydrogen isotopologues. In a complementary calibration approach using accurate gas samples, the calibration factors for the stable isotopologues H₂, D₂ and HD have been verified in the HYDE, agreeing to within 2 % with the values reported by SCHLÖSSER et al. [Sch13b].

In order to validate the pending, KATRIN-relevant calibration factors of the radioactive isotopologues T₂, HT and DT, the new TRIHYDE was designed, constructed and commissioned at TLK, capable of providing accurate gas samples of all six hydrogen isotopologues in chemical equilibrium via the manometric method. The design includes (i) all recommendations based on experiences gained with HYDE; (ii) fulfills the safety requirements for tritium operation; and (iii) was successfully integrated in the TLK-T₂-infrastructure.

In measurements using H₂-D₂-samples, the results of HYDE were confirmed, while simultaneously reducing the absolute calibration systematics by a factor of three. This is due to combination of improved pressure diagnostics, reduced volume uncertainty, and a streamlined mixing vessel design. In addition, a mass-spectrometer (MS) and a binary-gas-analyser to verify the initial gas purity are integrated in TRIHYDE.

Based on the successful commissioning using stable isotopologues, all challenges related to tritiated gas samples were addressed within this thesis:

- (i) It was shown that the anticipated formation of methane residues due to gas-wall interactions was at an expected ppm/h-level, which is detectable but negligible for the calibration gas sample preparation.
- (ii) The initial tritium gas purity, which inevitably contains traces of at least HT and DT, was estimated using a modified standard-addition-method, independent of LARA and MS calibration. The results agreed with other estimates, thus they were carried forward in determining the uncertainty budget of the gas sample.
- (iii) Detailed studies of the self-equilibration process in tritiated mixtures showed that the process is of first order for each equilibrium reaction, e.g. T₂ + HD \rightleftharpoons HT + DT, with a strong pressure dependence on reaction speed. The resulting equilibrium-concentration agrees with the calculated values, although the concentration dependence of reaction speed showed an unexpected behaviour which, however, did not impact on sample quality. The self-equilibration process was successfully used to produce accurate tritiated gas samples including the heteronuclear isotopologues in chemical equilibrium by selecting a suitable process pressure, offering reasonable reaction rates.

¹R. LEROY: 'Recalculation of Raman transition matrix elements of all hydrogen isotopologues for 532 nm laser excitation'. Personal communication. Department of Chemistry, University of Waterloo, ON, Canada, 2011.

- (iv) Sample composition changes due to isotope exchange in gas-wall-interaction were observed, similar to those reported in Ref. [Fis11], but were on a time-scale of >600 h and therefore negligible for sample production in TRIHYDE.

These samples allowed for the first direct experimental determination of the LARA-calibration factors for the three tritiated hydrogen isotopologues, using both homonuclear samples as well as heteronuclear samples in chemical equilibrium. All measured calibration factors agreed with the theoretical predictions within the respective uncertainty intervals, validating the currently deployed calibration strategy used at KATRIN. For the homonuclear species, an uncertainty reduction of up to a factor of two was achieved, while the resulting uncertainties for the heteronuclear isotopologues were unchanged. The observed difference of the theoretical intensity of T_2 of 2 % leads to a relative concentration shift of 0.1 % for a KATRIN-like gas sample (>95 % T_2), which therefore constitutes a negligible effect. Using the experimentally determined values, the calibration trueness of all currently deployed LARA-systems at TLK can be improved.

By experimentally confirming the theoretical intensities used for source gas monitoring at KATRIN, these results provide the essential cross-check and confidence level to ensure the validity of the measured values utilised in neutrino mass analysis.

Outlook TRIHYDE is an important step to further refine the potential of Raman spectroscopic system for tritium related applications, not only limited to KATRIN. One possible refinement is the unambiguous identification of tritiated methane, which up to now shows discrepancies in predicted and measured LARA spectra [Eng92; Stu10a; Fis11].

Because of the ability to both produce and analyse *in-situ* gas samples, TRIHYDE can be used in material studies, e.g. tritium-implantation in various getter materials. Supplied gas samples, e.g. process gases from KATRIN or experimental facilities at TLK, can also be characterised with complementary analytical methods.

With the option to include multiple analytical devices and provide samples in a wide pressure and concentration range, TRIHYDE may evolve into an indispensable tool in the development of new methods for tritium monitoring. Such samples can also be used to benchmark different methods and perform a cross-calibration of the devices deployed at TLK, especially gas chromatography (GC) and Bixs. This would improve the accuracy of tritium accountancy for the various sub-systems in the closed tritium cycle at TLK. Experiences gained could thus be transferred to other tritium processing facilities, e.g. those needed for future fusion reactors.

Until now, only gas samples of hydrogen isotopologues have been studied. TRIHYDE can easily be expanded to include additional gases in order to address other user cases. These include tritium in helium, which is of particular interest in breeding blanket design for fusion research [Bor13] and tritium in argon, similar to the purge gas of the Cps of KATRIN.

In conclusion, using the TRIHYDE facility it was possible, for the first time, to prepare accurate gas samples of all six hydrogen isotopologues with tritium content on a technical scale, thus giving a valuable tool to further expand tritium analytics to *in-situ* calibration, characterisation and development of existing and forthcoming methods.

Bibliography

- [Aar17] M. G. AARTSEN, K. ABRAHAM, M. ACKERMANN, J. ADAMS, J. A. AGUILAR et al.: ‘PINGU: a vision for neutrino and particle physics at the South Pole’. In *Journal of Physics G: Nuclear and Particle Physics* (2017), volume 44(5): page 054006. DOI: 10.1088/1361-6471/44/5/054006.
- [Abb88] L. ABBOTT, A. D. RÚJULA and T. WALKER: ‘Constraints on the electron-neutrino mass from the supernova data A systematic analysis’. In *Nuclear Physics B* (1988), volume 299(4): pages 734–756. DOI: 10.1016/0550-3213(88)90371-9.
- [Abe16] K. ABE, Y. HAGA, Y. HAYATO, M. IKEDA, K. IYOGI et al.: ‘Real-time supernova neutrino burst monitor at Super-Kamiokande’. In *Astroparticle Physics* (2016), volume 81: pages 39–48. DOI: 10.1016/j.astropartphys.2016.04.003.
- [Acc16] R. ACCIARRI, M. A. ACERO, M. ADAMOWSKI, C. ADAMS, P. ADAMSON et al.: *Long-Baseline Neutrino Facility (LBNF) and Deep Underground Neutrino Experiment (DUNE) Conceptual Design Report Volume 1: The LBNF and DUNE Projects*. Technical report FERMILAB-DESIGN-2016-01. Fermilab, USA, 2016. arXiv: 1601.05471 [physics.ins-det].
- [Ago19] M. AGOSTINI, K. ALTENMÜLLER, S. APPEL, V. ATROSHCHENKO, Z. BAGDASARIAN et al.: ‘Simultaneous precision spectroscopy of pp, Be7, and pep solar neutrinos with Borexino Phase-II’. In *Physical Review D* (2019), volume 100(8). DOI: 10.1103/PhysRevD.100.082004.
- [Ago20] M. AGOSTINI, K. ALTENMÜLLER, S. APPEL, V. ATROSHCHENKO, Z. BAGDASARIAN et al.: ‘Experimental evidence of neutrinos produced in the CNO fusion cycle in the Sun’. In *Nature* (2020), volume 587(7835): pages 577–582. DOI: 10.1038/s41586-020-2934-0.
- [Agu10] A. A. AGUILAR-AREVALO, C. E. ANDERSON, S. J. BRICE, B. C. BROWN, L. BUGEL et al.: ‘Event Excess in the MiniBooNE Search for $\bar{\nu}_\mu \rightarrow \bar{\nu}_e$ Oscillations’. In *Physical Review Letters* (2010), volume 105(18). DOI: 10.1103/PhysRevLett.105.181801.
- [Ahn06] M. H. AHN, E. ALIU, S. ANDRINGA, S. AOKI, Y. AOYAMA et al.: ‘Measurement of neutrino oscillation by the K2K experiment’. In *Physical Review D* (2006), volume 74(7). DOI: 10.1103/PhysRevD.74.072003.

- [Ahn12] J. K. AHN, S. CHEBOTARYOV, J. H. CHOI, S. CHOI, W. CHOI et al.: ‘Observation of Reactor Electron Antineutrinos Disappearance in the RENO Experiment’. In *Physical Review Letters* (2012), volume 108(19): pages 24–29. DOI: 10.1103/physrevlett.108.191802.
- [Aig73] D. J. AIGNER: ‘Regression with a binary independent variable subject to errors of observation’. In *Journal of Econometrics* (1973), volume 1(1): pages 49–59. DOI: 10.1016/0304-4076(73)90005-5.
- [Aka08] K. AKAISHI, Y. TORIKAI, D. MURATA, R.-D. PENZHORN, K. WATANABE et al.: ‘On the mechanism of tritium desorption from stainless steel’. In *Journal of Vacuum Science & Technology A* (2008), volume 26(3): pages 321–327. DOI: 10.1116/1.2889391.
- [Aka91] J. and AKAISHI, G. BONIZZONI, J. CORTELLA, H. DWORSCHAK, V. FRIEDMAN et al.: *Safe handling of tritium. Review of Data and Experience. Technical report 324.* International Atomic Energy Agency, 1991.
- [Ake19] M. AKER, K. ALTENMÜLLER, M. ARENZ, M. BABUTZKA, J. BARRETT et al.: ‘Improved Upper Limit on the Neutrino Mass from a Direct Kinematic Method by KATRIN’. In *Physical Review Letters* (2019), volume 123(22). DOI: 10.1103/PhysRevLett.123.221802.
- [Ake20a] M. AKER, K. ALTENMÜLLER, M. ARENZ, W.-J. BAEK, J. BARRETT et al.: ‘First operation of the KATRIN experiment with tritium’. In *The European Physical Journal C* (2020), volume 80(3). DOI: 10.1140/epjc/s10052-020-7718-z.
- [Ake20b] M. AKER, K. ALTENMÜLLER, A. BEGLARIAN, J. BEHRENS, A. BERLEV et al.: ‘Quantitative Long-Term Monitoring of the Circulating Gases in the KATRIN Experiment Using Raman Spectroscopy’. In *Sensors* (2020), volume 20(17): page 4827. DOI: 10.3390/s20174827.
- [Ake20c] M. AKER and M. RÖLLIG: ‘Material Studies to Reduce the Tritium Memory Effect in BIXS Analytic Systems’. In *Fusion Science and Technology* (2020), volume 76(3): pages 373–378. DOI: 10.1080/15361055.2020.1712989.
- [ALE06] ALEPH, DELPHI, L3, OPAL, SLD COLLABORATIONS, THE LEP ELECTROWEAK WORKING GROUP, THE SLD ELECTROWEAK AND HEAVY FLAVOUR GROUPS: ‘Precision electroweak measurements on the Z resonance’. In *Physics Reports* (2006), volume 427(5-6): pages 257–454. DOI: 10.1016/j.physrep.2005.12.006.
- [Alh15] M. ALHROOB, R. BATES, M. BATTISTIN, S. BERRY, A. BITADZE et al.: ‘Development of a custom on-line ultrasonic vapour analyzer and flow meter for the ATLAS inner detector, with application to Cherenkov and gaseous charged particle detectors’. In *Journal of Instrumentation* (2015), volume 10(03): page C03045. DOI: <https://doi.org/10.1088/1748-0221/10/03/C03045>.

- [Alt20] K. ALTENMÜLLER, M. ARENZ, W. J. BAEK, M. BECK, A. BEGLARIAN et al.: ‘High-resolution spectroscopy of gaseous $^{83\text{m}}\text{Kr}$ conversion electrons with the KATRIN experiment’. In *Journal of Physics G: Nuclear and Particle Physics* (2020), volume 47(6): page 065002. DOI: 10.1088/1361-6471/ab8480.
- [Ams15] J. AMSBAUGH, J. BARRETT, A. BEGLARIAN, T. BERGMANN, H. BICHSEL et al.: ‘Focal-plane detector system for the KATRIN experiment’. In *Nuclear Instruments and Methods in Physics Research Section A: Accelerators, Spectrometers, Detectors and Associated Equipment* (2015), volume 778: pages 40–60. DOI: 10.1016/j.nima.2014.12.116.
- [An16a] F. AN, J. BAI, A. BALANTEKIN, H. BAND, D. BEAVIS et al.: ‘The detector system of the Daya Bay reactor neutrino experiment’. In *Nuclear Instruments and Methods in Physics Research Section A: Accelerators, Spectrometers, Detectors and Associated Equipment* (2016), volume 811: pages 133–161. DOI: 10.1016/j.nima.2015.11.144.
- [An16b] F. AN, G. AN, Q. AN, V. ANTONELLI, E. BAUSSAN et al.: ‘Neutrino physics with JUNO’. In *Journal of Physics G: Nuclear and Particle Physics* (2016), volume 43(3): page 030401. DOI: 10.1088/0954-3899/43/3/030401.
- [Ang04] J. ANGRİK, T. ARMBRUST, A. BEGLARIAN, U. BESSERER, J. BLUMER et al.: *KATRIN design report 2004*. Technical report FZKA-7090. Forschungszentrum, Karlsruhe, 2004.
- [Ant02] S. ANTUSCH, M. DREES, J. KERSTEN, M. LINDNER and M. RATZ: ‘Neutrino mass operator renormalization in two Higgs doublet models and the MSSM’. In *Physics Letters B* (2002), volume 525(1-2): pages 130–134. DOI: 10.1016/S0370-2693(01)01414-9.
- [Aqu65] V. AQUILANTI, A. GALLI, A. GIARDINI-GUIDONI and G. G. VOLPI: ‘Ion–Molecule Reactions in Hydrogen–Rare-Gas Mixtures’. In *The Journal of Chemical Physics* (1965), volume 43(6): pages 1969–1973. DOI: 10.1063/1.1697061.
- [Are16] M. ARENZ, M. BABUTZKA, M. BAHR, J. BARRETT, S. BAUER et al.: ‘Commissioning of the vacuum system of the KATRIN Main Spectrometer’. In *Journal of Instrumentation* (2016), volume 11(04): P04011–P04011. DOI: 10.1088/1748-0221/11/04/P04011.
- [Are18a] M. ARENZ, W. J. BAEK, M. BECK, A. BEGLARIAN, J. BEHRENS et al.: ‘Calibration of high voltages at the ppm level by the difference of $^{83\text{m}}\text{Kr}$ conversion electron lines at the KATRIN experiment’. In *Eur. Phys. J. C* (2018) 78:368 (2018), volume. DOI: 10.1140/epjc/s10052-018-5832-y.
- [Are18b] M. ARENZ, W.-J. BAEK, M. BECK, A. BEGLARIAN, J. BEHRENS et al.: ‘The KATRIN superconducting magnets: overview and first performance results’. In *Journal of Instrumentation* (2018), volume 13(08): T08005–T08005. DOI: 10.1088/1748-0221/13/08/T08005.

- [Are18c] M. ARENZ, W. BAEK, M. BECK, A. BEGLARIAN, J. BEHRENS et al.: ‘First transmission of electrons and ions through the KATRIN beamline’. In *Journal of Instrumentation* (2018), volume 13(04): P04020–P04020. DOI: 10.1088/1748-0221/13/04/P04020.
- [Ari85] K. ARISAKA, T. KAJITA, M. KOSHIBA, M. NAKAHATA, Y. OYAMA et al.: ‘Search for Nucleon Decay into Charged Lepton+Mesons’. In *Journal of the Physical Society of Japan* (1985), volume 54(9): pages 3213–3216. DOI: <https://doi.org/10.1143/JPSJ.54.3213>.
- [Ase11] V. N. ASEEV, A. I. BELESEV, A. I. BERLEV, E. V. GERASKIN, A. A. GOLUBEV et al.: ‘Upper limit on the electron antineutrino mass from the Troitsk experiment’. In *Physical Review D* (2011), volume 84(11). DOI: 10.1103/physrevd.84.112003.
- [Atk06] P. ATKINS and J. de PAULA: *Physical Chemistry, 8th edition*. New York: Oxford University Press, 2006.
- [Aus72] J. H. AUSTIN and T. S. ELLEMAN: ‘Tritium diffusion in 304- and 316-stainless steels in the temperature range 25 to 222 °C’. In *Journal of Nuclear Materials* (1972), volume 43: pages 119–125. DOI: 10.1016/0022-3115(72)90145-6.
- [Ayr07] D. AYRES, G. DRAKE, M. GOODMAN, J. GRUDZINSKI, V. GUARINO et al.: *The NOvA Technical Design Report*. Technical report. Office of Scientific and Technical Information (OSTI), 2007. DOI: 10.2172/935497.
- [Bab12] M. BABUTZKA, M. BAHR, J. BONN, B. BORNSCHEIN, A. DIETER et al.: ‘Monitoring of the operating parameters of the KATRIN windowless gaseous tritium source’. In *New Journal of Physics* (2012), volume 14(10): page 103046. DOI: 10.1088/1367-2630/14/10/103046.
- [Bab14] M. BABUTZKA: ‘Design and development for the Rearsection of the KATRIN experiment’. PhD thesis. Karlsruhe Institut of Technology, 2014. DOI: 10.5445/IR/1000045598.
- [Bah01] J. N. BAHCALL, M. H. PINSONNEAULT and S. BASU: ‘Solar Models: Current Epoch and Time Dependences, Neutrinos, and Helioseismological Properties’. In *The Astrophysical Journal* (2001), volume 555(2): pages 990–1012. DOI: 10.1086/321493.
- [Bah05] J. N. BAHCALL, A. M. SERENELLI and S. BASU: ‘New Solar Opacities, Abundances, Helioseismology, and Neutrino Fluxes’. In *The Astrophysical Journal* (2005), volume 621(1): pages L85–L88. DOI: 10.1086/428929.
- [Bah90] J. N. BAHCALL and H. A. BETHE: ‘Solution of the solar-neutrino problem’. In *Physical Review Letters* (1990), volume 65(18): pages 2233–2235. DOI: 10.1103/PhysRevLett.65.2233.

- [Bar16] P. S. BARKLEM and R. COLLET: ‘Partition functions and equilibrium constants for diatomic molecules and atoms of astrophysical interest’. In *Astronomy & Astrophysics* (2016), volume 588: A96. DOI: 10.1051/0004-6361/201526961.
- [Bau14] S. BAUER: ‘Energy calibration and stability monitoring of the KATRIN experiment’. PhD thesis. Muenster Univ. (Germany). Mathematisch–Naturwissenschaftliche Fakultät, 2014.
- [Bau66] S. BAUER and E. OSSA: ‘Isotope Exchange Rates. III. The Homogeneous Four-Center Reaction $H_2 + D_2$ ’. In *The Journal of Chemical Physics* (1966), volume 45(2): pages 434–443. DOI: 10.1063/1.1727585.
- [Bea80] G. BEAMSON, H. Q. PORTER and D. W. TURNER: ‘The collimating and magnifying properties of a superconducting field photoelectron spectrometer’. In *Journal of Physics E: Scientific Instruments* (1980), volume 1313(1): pages 64–66. DOI: 10.1088/0022-3735/13/1/018.
- [Bea95] D. BEAVIS, A. CARROLL and I. CHIANG: *Long baseline neutrino oscillation experiment at the AGS. Physics design report*. Technical report. Brookhaven National Laboratory, New York, USA, 1995. DOI: 10.2172/52878.
- [Bel13a] G. BELLINI et al.: ‘Final results of Borexino Phase-I on low energy solar neutrino spectroscopy’. In *Phys. Rev. D* (2013), volume 89(11): page 112007. DOI: 10.1103/PhysRevD.89.112007.
- [Bel13b] G. BELLINI, D. BICK, G. BONFINI, D. BRAVO, B. CACCIANIGA et al.: ‘SOX: Short distance neutrino Oscillations with BoreXino’. In *Journal of High Energy Physics* (2013), volume 2013(8). DOI: 10.1007/JHEP08(2013)038.
- [Bel93] G. BELLANGER and J. J. RAMEAU: ‘Influence of the Tritium in Type 316L Stainless Steel on Corrosion’. In *Fusion Technology* (1993), volume 24(2): pages 145–149. DOI: 10.13182/FST93-A30220.
- [Bes03] U. A. BESSERER: ‘Tritiumspeicherung in ZrCo’. PhD thesis. Marburg: Philipps-Universität, 2003. DOI: 10.17192/z2003.0108.
- [Bes08] U. BESSERER, L. DÖRR and M. GLUGLA: ‘Tritium Confinement, Retention, and Releases at the Tritium Laboratory Karlsruhe’. In *Fusion Science and Technology* (2008), volume 54(1): pages 160–163. DOI: 10.13182/fst08-a1786.
- [Bes92] U. BESSERER, K. HEISS and G. JOURDAN: ‘Tritium inventory evaluation program for the Tritium Laboratory Karlsruhe (TLK)’. In *Fusion Technology* (1992), volume 21(2P2): pages 419–424. DOI: <https://doi.org/10.13182/FST92-A29781>.
- [Bet34] H. BETHE and R. PEIERLS: ‘The "Neutrino"’. In *Nature* (1934), volume 133(3362): pages 532–532. DOI: 10.1038/133532a0.
- [Bie18] J. A. BIERNER, R. L. JAREK, L. K. TAKAHASHI and R. M. GARCIA: *Tritiated Gas Mixing for Z-GTS Fills & Gas Analysis Round Robin*. Technical report. Sandia National Lab.(SNL-NM), Albuquerque, NM (United States), 2018.

- [Blo67] M. BLONDEL and X. D. PHAN: *Preparation of radioactive gaseous standard*. Technical report. Commissariat a l'Énergie Atomique, Saclay (France), 1967.
- [Bod15] L. I. BODINE, D. S. PARNO and R. G. H. ROBERTSON: 'Assessment of molecular effects on neutrino mass measurements from tritium β decay'. In *Phys. Rev. C* (3 2015), volume 91: page 035505. DOI: 10.1103/PhysRevC.91.035505.
- [Bor05] B. BORNSCHEIN, M. GLUGLA, K. GÜNTHER, T. LE, K. SIMON et al.: 'Successful experimental verification of the tokamak exhaust processing concept of ITER with the CAPER facility'. In *Fusion Science and Technology* (2005), volume 48(1): pages 11–16. DOI: 10.13182/FST05-A870.
- [Bor08] B. BORNSCHEIN: 'Determination of Neutrino Mass from Tritium Beta Decay'. In *Fusion Science and Technology* (2008), volume 54: pages 59–66. DOI: 10.13182/FST54-59.
- [Bor13] B. BORNSCHEIN, C. DAY, D. DEMANGE and T. PINNA: 'Tritium management and safety issues in ITER and DEMO breeding blankets'. In *Fusion Engineering and Design* (2013), volume 88(6-8): pages 466–471. DOI: 10.1016/j.fusengdes.2013.03.032.
- [Cal01] C. CALDWELL-NICHOLS, R.-D. PENZHORN, S. GRÜNHAGEN, M. SIRCH and J. GEORGE: 'Evaluation of an Omegatron mass spectrometer for use in the plasma exhaust processing of a fusion reactor'. In *Fusion Engineering and design* (2001), volume 58: pages 395–399. DOI: [https://doi.org/10.1016/S0920-3796\(01\)00359-3](https://doi.org/10.1016/S0920-3796(01)00359-3).
- [Cha14] J. CHADWICK: 'The intensity distribution in the magnetic spectrum of beta particles from radium (B + C)'. In *Verh. Phys. Gesell.* (1914), volume 16: pages 383–391.
- [Chi10] S. CHILINGARYAN, A. BEGLARIAN, A. KOPMANN and S. VÖCKING: 'Advanced data extraction infrastructure: Web based system for management of time series data'. In *Journal of Physics: Conference Series* (2010), volume 219(4): page 042034. DOI: 10.1088/1742-6596/219/4/042034.
- [Cle98] B. T. CLEVELAND, T. DAILY, J. RAYMOND DAVIS, J. R. DISTEL, K. LANDE et al.: 'Measurement of the Solar Electron Neutrino Flux with the Homestake Chlorine Detector'. In *The Astrophysical Journal* (1998), volume 496(1): pages 505–526. DOI: 10.1086/305343.
- [Coo97] N. G. COOPER: *Los Alamos Science, Number 25 – 1997: Celebrating the neutrino*. Technical report LA-UR-97-2534. Los Alamos National Lab., New Michigan, USA, 1997. DOI: 10.2172/569122.
- [Cow56] C. L. COWAN, F. REINES, F. B. HARRISON, H. W. KRUSE and A. D. MCGUIRE: 'Detection of the Free Neutrino: a Confirmation'. In *Science* (1956), volume 124(3212): pages 103–104. DOI: 10.1126/science.124.3212.103.

- [CUO20] CUORE COLLABORATION, D. Q. ADAMS, C. ALDUINO, K. ALFONSO, F. T. AVIGNONE et al.: 'Improved Limit on Neutrinoless Double-Beta Decay in ^{130}Te with CUORE'. In *Physical Review Letters* (2020), volume 124(12): page 122501. DOI: 10.1103/PhysRevLett.124.122501.
- [Cur72] M. L. CURTIS: 'Detection and measurement of tritium by bremsstrahlung counting'. In *The International Journal of Applied Radiation and Isotopes* (1972), volume 23(1): pages 17–23. DOI: 10.1016/0020-708X(72)90097-X.
- [Dan62] G. DANBY, J.-M. GAILLARD, K. GOULIANOS, L. M. LEDERMAN, N. MISTRY et al.: 'Observation of High-Energy Neutrino Reactions and the Existence of Two Kinds of Neutrinos'. In *Physical Review Letters* (1962), volume 9(1): pages 36–44. DOI: 10.1103/physrevlett.9.36.
- [Dav64] R. DAVIS: 'Solar Neutrinos. II. Experimental'. In *Physical Review Letters* (1964), volume 12(11): pages 303–305. DOI: 10.1103/PhysRevLett.12.303.
- [Dav68] R. DAVIS, D. S. HARMER and K. C. HOFFMAN: 'Search for Neutrinos from the Sun'. In *Physical Review Letters* (1968), volume 20(21): pages 1205–1209. DOI: 10.1103/PhysRevLett.20.1205.
- [Dav94] R. DAVIS: 'A review of the homestake solar neutrino experiment'. In *Progress in Particle and Nuclear Physics* (1994), volume 32: pages 13–32. DOI: 10.1016/0146-6410(94)90004-3.
- [Dea15] J. DEAN, H. PHILLIPS, P. BURGESS, P. DOYLE and J. SIMPSON: *The examination, testing and calibration of tritium-in-air monitors for radiation protection*. Technical report. Teddington, UK: National Physical Laboratory (NPL), 2015.
- [Dem10] W. DEMTRÖDER: *Atoms, Molecules and Photons*. Berlin Heidelberg: Springer, 2010. DOI: 10.1007/978-3-642-10298-1.
- [Den17] M. DENTLER, Á. HERNÁNDEZ-CABEZUDO, J. KOPP, M. MALTONI and T. SCHWETZ: 'Sterile neutrinos or flux uncertainties? – Status of the reactor anti-neutrino anomaly'. In *Journal of High Energy Physics* (2017), volume 2017(11). DOI: 10.1007/JHEP11(2017)099.
- [Dic90] R. DICKSON: *Tritium interactions with steel and construction materials in fusion devices*. Report. CFFTP GENERAL, Ontario, Canada, 1990.
- [DIN05] DIN 10204:2004: *Metallische Erzeugnisse – Arten von Prüfbescheinigungen*. 2005.
- [DIN08] DIN EN 60751:2008: *Industrielle Platin-Widerstandsthermometer und PlatinTemperatursensoren*. 2008.
- [DIN13] DIN 32633:2013-05: *Chemische Analytik- Verfahren der Standardaddition- Verfahren, Auswertung*. 2013.
- [DIN17] DIN EN 61882: *Hazard and operability studies (HAZOP studies) - Application guide (IEC 61882:2016)*; 2017.

- [DIN18] DIN 6146:2018-10: *Gas analysis – Preparation of calibration gas mixtures – Manometric method*. 2018.
- [DIN83] DIN ISO 6146:1983-04: *Gas analysis – Preparation of calibration gas mixtures – Manometric method*. 1983.
- [Dol19] M. J. DOLINSKI, A. W. POON and W. RODEJOHANN: ‘Neutrinoless Double-Beta Decay: Status and Prospects’. In *Annual Review of Nuclear and Particle Science* (2019), volume 69(1): pages 219–251. DOI: 10.1146/annurev-nucl-101918-023407.
- [Dör05] L. DÖRR, U. BESSERER, M. GLUGLA, G. HELLRIEGEL, W. HELLRIEGEL et al.: ‘The Closed Tritium Cycle of the Tritium Laboratory Karlsruhe’. In *Fusion Science and Technology* (2005), volume 48(1): pages 262–267. DOI: 10.13182/FST05-A924.
- [Dör08] L. DÖRR, U. BESSERER, N. BEKRIS, B. BORNSCHEIN, C. CALDWELL-NICHOLS et al.: ‘A Decade of Tritium Technology Development and Operation at the Tritium Laboratory Karlsruhe’. In *Fusion Science and Technology* (2008), volume 54(1): pages 143–148. DOI: 10.13182/FST54-143.
- [Dor54] L. M. DORFMAN: ‘Absorption of tritium beta particles in hydrogen and other gases’. In *Physical Review* (1954), volume 95(2): page 393. DOI: 10.1103/physrev.95.393.
- [Dos06] N. DOSS, J. TENNYSON, A. SAENZ and S. JONSELL: ‘Molecular effects in investigations of tritium molecule β decay endpoint experiments’. In *Physical Review C* (2006), volume 73(2). DOI: 10.1103/physrevc.73.025502.
- [Dos08] N. DOSS and J. TENNYSON: ‘Excitations to the electronic continuum of $^3\text{HeT}^+$ in investigations of T_2 β -decay experiments’. In *Journal of Physics B: Atomic, Molecular and Optical Physics* (2008), volume 4411(12): page 125701. DOI: 10.1088/0953-4075/41/12/125701.
- [Dou12] DOUBLE CHOOZ COLLABORATION, Y. ABE, C. ABERLE, T. AKIRI, J. C. dos ANJOS et al.: ‘Indication of Reactor $\bar{\nu}_e$ Disappearance in the Double Chooz Experiment’. In *Physical Review Letters* (2012), volume 108(13): page 131801. DOI: 10.1103/PhysRevLett.108.131801.
- [Dou16] M. DOUBEK, V. VACEK, G. HALLEWELL and B. PEARSON: ‘Speed-of-sound based sensors for environmental monitoring’. In *2016 IEEE SENSORS*. IEEE. 2016: pages 1–3. DOI: 10.1109/ICSENS.2016.7808873.
- [Dre13] G. DREXLIN, V. HANNEN, S. MERTENS and C. WEINHEIMER: ‘Current Direct Neutrino Mass Experiments’. In *Advances in High Energy Physics* (2013), volume 2013: pages 1–39. DOI: 10.1155/2013/293986.
- [Dun08] J. A. DUNMORE, M. L. LEBER and T. K. COLLABORATION: ‘KATRIN focal plane detector’. In *Journal of Physics: Conference Series* (2008), volume 136(4): page 042056. DOI: 10.1088/1742-6596/136/4/042056.

- [Dvo19] C. DVORKIN, M. GERBINO, D. ALONSO, N. BATTAGLIA, S. BIRD et al.: ‘Neutrino Mass from Cosmology: Probing Physics Beyond the Standard Model’. In *Bulletin of the American Astronomical society: Astro2020 APC white paper collection* (2019), volume 51(7). arXiv: 1903.03689 [astro-ph.CO].
- [Edw78] H. EDWARDS, D. LONG and H. MANSOUR: ‘Pure rotational and vibration–rotational Raman spectra of tritium, $^3\text{H}_2$ ’. In *Journal of the Chemical Society, Faraday Transactions 2: Molecular and Chemical Physics* (1978), volume 74: pages 1203–1207. DOI: <https://doi.org/10.1039/F29767200865>.
- [Efr83] B. EFRON and G. GONG: ‘A Leisurely Look at the Bootstrap, the Jackknife, and Cross-Validation’. In *The American Statistician* (1983), volume 37(1): page 36. DOI: 10.2307/2685844.
- [Efr93] B. EFRON and R. J. TIBSHIRANI: *An Introduction to the Bootstrap*. Boca Raton, London, New York, Washington, D.C: Chapman & Hall, Inc, 1993.
- [Eli15] S. ELISEEV, K. BLAUM, M. BLOCK, S. CHENMAREV, H. DORRER et al.: ‘Direct Measurement of the Mass Difference of Ho-163 and Dy-163 Solves the Q-Value Puzzle for the Neutrino Mass Determination’. In *Physical Review Letters* (2015), volume 115(6). DOI: 10.1103/PhysRevLett.115.062501.
- [Ell27] C. D. ELLIS and W. A. WOOSTER: ‘The average energy of disintegration of radium E’. In *Proceedings of the Royal Society of London. Series A, Containing Papers of a Mathematical and Physical Character* (1927), volume 117(776): pages 109–123. DOI: 10.1098/rspa.1927.0168.
- [Eng17] J. ENGEL and J. MENÉNDEZ: ‘Status and future of nuclear matrix elements for neutrinoless double-beta decay: a review’. In *Reports on Progress in Physics* (2017), volume 80(4): page 046301. DOI: 10.1088/1361-6633/aa5bc5.
- [Eng92] U. ENGELMANN, M. GLUGLA, R.-D. PENZHOM and H. J. ACHE: ‘Laser Raman Spectroscopy and Omegatron Mass Spectrometry Applied to Investigations of the Radiochemical Reactions between Methane and Tritium’. In *Fusion Technology* (1992), volume 21(2P2): pages 430–435. DOI: 10.13182/fst92-a29783.
- [Erh14] M. ERHARD, S. BAUER, A. BEGLARIAN, T. BERGMANN, J. BONN et al.: ‘High-voltage monitoring with a solenoid retarding spectrometer at the KATRIN experiment’. In *Journal of Instrumentation* (2014), volume 9(06): P06022–P06022. DOI: 10.1088/1748-0221/9/06/P06022.
- [Erh18] M. ERHARD, J. BEHRENS, S. BAUER, A. BEGLARIAN, R. BERENDES et al.: ‘Technical design and commissioning of the KATRIN large-volume air coil system’. In *Journal of Instrumentation* (2018), volume 13(02): P02003–P02003. DOI: 10.1088/1748-0221/13/02/p02003.

- [Etz05] E. S. ETZ, S. J. CHOQUETTE and W. S. HURST: ‘Development and Certification of NIST Standard Reference Materials for Relative Raman Intensity Calibration’. In *Microchimica Acta* (2005), volume 149(3-4): pages 175–184. DOI: 10.1007/s00604-004-0315-2.
- [Fae20] A. FAESSLER: ‘Status of the determination of the electron–neutrino mass’. In *Progress in Particle and Nuclear Physics* (2020), volume 113: page 103789. DOI: 10.1016/j.ppnp.2020.103789.
- [Fel13] G. J. FELDMAN, J. HARTNELL and T. KOBAYASHI: ‘Long-Baseline Neutrino Oscillation Experiments’. In *Advances in High Energy Physics* (2013), volume 2013: pages 1–30. DOI: 10.1155/2013/475749.
- [Fer15] E. FERRI, D. BAGLIANI, M. BIASOTTI, G. CERUTI, D. CORSINI et al.: ‘The Status of the MARE Experiment with 187Re and 163Ho Isotopes’. In *Physics Procedia* (2015), volume 61: pages 227–231. DOI: 10.1016/j.phpro.2014.12.037.
- [Fer34] E. FERMI: ‘Versuch einer Theorie der Beta-Strahlen. I’. In *Zeitschrift für Physik* (1934), volume 88(3-4): pages 161–177. DOI: 10.1007/BF01351864.
- [Fis11] S. FISCHER, M. STURM, M. SCHLÖSSER, B. BORNSCHEIN, G. DREXLIN et al.: ‘Monitoring of Tritium Purity During Long-Term Circulation in the KATRIN Test Experiment LOOPINO Using Laser Raman Spectroscopy’. In *Fusion Science and Technology* (2011), volume 60(3): pages 925–930. DOI: 10.13182/FST11-A12567.
- [Fis12] S. FISCHER, M. STURM, M. SCHLÖSSER, R. J. LEWIS, B. BORNSCHEIN et al.: ‘Laser Raman Spectroscopy for KATRIN’. In *Nuclear Physics B - Proceedings Supplements* (2012), volume 229-232: page 492. DOI: 10.1016/j.nuclphysbps.2012.09.129.
- [Fis14] S. FISCHER: ‘Commissioning of the KATRIN Raman system and durability studies of optical coatings in glove box and tritium atmospheres’. PhD thesis. Karlsruhe: Karlsruhe Institut für Technologie, 2014. DOI: 10.5445/IR/1000043697.
- [Fog03] G. L. FOGLI, E. LISI, A. MARRONE, D. MONTANINO, A. PALAZZO et al.: ‘Solar neutrino oscillation parameters after first KamLAND results’. In *Physical Review D* (2003), volume 67(7). DOI: 10.1103/PhysRevD.67.073002.
- [For12] J. FORMAGGIO: ‘Project 8: Using Radio-Frequency Techniques to Measure Neutrino Mass’. In *Nuclear Physics B - Proceedings Supplements* (2012), volume 229-232: pages 371–375. DOI: 10.1016/j.nuclphysbps.2012.09.058.
- [Frä10] F. M. FRÄNKLE: ‘Background Investigations of the KATRIN Pre-Spectrometer’. PhD thesis. Karlsruhe Institut of Technology, 2010. DOI: 10.5445/IR/1000019392.
- [Frä11] F. M. FRÄNKLE, L. BORNSCHEIN, G. DREXLIN, F. GLÜCK, S. GÖRHARDT et al.: ‘Radon induced background processes in the KATRIN pre-spectrometer’. In *Astroparticle Physics* (2011), volume 35(3): pages 128–134. DOI: 10.1016/j.astropartphys.2011.06.009.

- [Fuk03] S. FUKUDA, Y. FUKUDA, T. HAYAKAWA, E. ICHIHARA, M. ISHITSUKA et al.: ‘The Super-Kamiokande detector’. In *Nuclear Instruments and Methods in Physics Research Section A: Accelerators, Spectrometers, Detectors and Associated Equipment* (2003), volume 501(2-3): pages 418–462. DOI: 10.1016/S0168-9002(03)00425-X.
- [Fuk98a] Y. FUKUDA, T. HAYAKAWA, E. ICHIHARA, K. INOUE, K. ISHIHARA et al.: ‘Evidence for Oscillation of Atmospheric Neutrinos’. In *Physical Review Letters* (1998), volume 81(8): pages 1562–1567. DOI: 10.1103/PhysRevLett.81.1562.
- [Fuk98b] Y. FUKUDA, T. HAYAKAWA, E. ICHIHARA, K. INOUE, K. ISHIHARA et al.: ‘Measurements of the Solar Neutrino Flux from Super-Kamiokande’s First 300 Days’. In *Physical Review Letters* (1998), volume 81(6): pages 1158–1162. DOI: 10.1103/PhysRevLett.81.1158.
- [GAL99a] GALLEX COLLABORATION: ‘GALLEX solar neutrino observations: results for GALLEX IV’. In *Physics Letters B* (1999), volume 447(1-2): pages 127–133. DOI: 10.1016/S0370-2693(98)01579-2.
- [GAL99b] GALLEX COLLABORATION: ‘GALLEX solar neutrino results and status of GNO’. In *Nuclear Physics B - Proceedings Supplements* (1999), volume 77(1-3): pages 26–34. DOI: 10.1016/S0920-5632(99)00389-8.
- [Gan99] N. GANCHUK, A. GOLUBKOV, D. KREKNIN, L. PONOMAREV, A. SELEZENEV et al.: ‘Calculation of equilibrium composition and establishing time in a mixture of three hydrogen isotopes’. In *Hyperfine interactions* (1999), volume 119(1-4): pages 357–360. DOI: 10.1023/A:1012693021607.
- [Gas17] L. GASTALDO, K. BLAUM, K. CHRYSALIDIS, T. D. GOODACRE, A. DOMULA et al.: ‘The electron capture in ^{163}Ho experiment – ECHO’. In *The European Physical Journal Special Topics* (2017), volume 226(8): pages 1623–1694. DOI: 10.1140/epjst/e2017-70071-y.
- [Gen70] C. GENTY and R. SCHOTT: ‘Quantitative analysis for the isotopes of hydrogen- H_2 , HD, HT, D $_2$, DT, and T $_2$ -by gas chromatography’. In *Analytical Chemistry* (1970), volume 42(1): pages 7–11. DOI: 10.1021/ac60283a039.
- [Gia17] A. GIACHERO, B. ALPERT, D. BECKER, D. BENNETT, M. BIASOTTI et al.: ‘Measuring the electron neutrino mass with improved sensitivity: the HOLMES experiment’. In *Journal of Instrumentation* (2017), volume 12(02): pages C02046–C02046. DOI: 10.1088/1748-0221/12/02/C02046.
- [Gil10] W. GIL, J. BONN, B. BORNSCHEIN, R. GEHRING, O. KAZACHENKO et al.: ‘The Cryogenic Pumping Section of the KATRIN Experiment’. In *IEEE Transactions on Applied Superconductivity* (2010), volume 20(3): pages 316–319. DOI: 10.1109/TASC.2009.2038581.
- [Gil80] J. T. GILL: ‘Effect of container preparation on the growth of protium and methane impurities into tritium gas’. In *Journal of Vacuum Science and Technology* (1980), volume 17(2): pages 645–654. DOI: 10.1116/1.570532.

- [GNO05] GNO COLLABORATION: ‘Complete results for five years of GNO solar neutrino observations’. In *Physics Letters B* (2005), volume 616(3-4): pages 174–190. DOI: 10.1016/j.physletb.2005.04.068.
- [Goe35] M. GOEPPERT-MAYER: ‘Double Beta-Disintegration’. In *Physical Review* (1935), volume 48(6): pages 512–516. DOI: 10.1103/PhysRev.48.512.
- [Gol58] M. GOLDHABER, L. GRODZINS and A. W. SUNYAR: ‘Helicity of Neutrinos’. In *Physical Review* (1958), volume 109(3): pages 1015–1017. DOI: 10.1103/PhysRev.109.1015.
- [Gri69] V. GRIBOV and B. PONTECORVO: ‘Neutrino astronomy and lepton charge’. In *Physics Letters B* (1969), volume 28(7): pages 493–496. DOI: 10.1016/0370-2693(69)90525-5.
- [Gro08] S. GROHMANN, J. BONN, B. BORNSCHEIN, R. GEHRING, W. GIL et al.: ‘Cryogenic design of the KATRIN source cryostat’. In *AIP Conference Proceedings* (2008), volume 985(1277). DOI: 10.1063/1.2908483.
- [Gro09] S. GROHMANN: ‘Stability analyses of the beam tube cooling system in the KATRIN source cryostat’. In *Cryogenics* (2009), volume 49(8): pages 413–420. DOI: 10.1016/j.cryogenics.2009.06.001.
- [Gro15] S. GROH: ‘Modeling of the response function and measurement of transmission properties of the KATRIN experiment’. PhD thesis. Karlsruhe Institute of Technology, 2015. DOI: 10.5445/IR/1000046546.
- [Gui20] M. GUIGUE and PROJECT 8 COLLABORATION: ‘Status of the Project 8 Phase II’. In *Journal of Physics: Conference Series* (2020), volume 1342: page 012025. DOI: 10.1088/1742-6596/1342/1/012025.
- [Hac17] M. T. HACKENJOS: ‘KATRIN "First Light" - Commissioning and Modelling of the Beamline’. PhD thesis. Karlsruhe Institute of Technology, 2017. DOI: 10.5445/IR/1000078933.
- [Hak04] H. HAKEN and H. C. WOLF: *Atom- und Quantenphysik*. Berlin, Heidelberg: Springer, 2004. DOI: 10.1007/978-3-642-18519-9.
- [Hak13] H. HAKEN and H. C. WOLF: *Molecular physics and elements of quantum chemistry: introduction to experiments and theory*. Berlin Heidelberg: Springer Science & Business Media, 2013. DOI: 10.1007/978-3-662-08820-3.
- [Har15] F. T. HARMS: ‘Characterization and Minimization of Background Processes in the KATRIN Main Spectrometer’. PhD thesis. Karlsruhe Institut of Technologie, 2015. DOI: 10.5445/IR/1000050027.
- [Her06] H. C. W. HERMANN HAKEN: *Molekülphysik und Quantenchemie: Einführung in die experimentellen und theoretischen Grundlagen*. Berlin, Heidelberg: Springer, 2006. DOI: <https://doi.org/10.1007/3-540-30315-4>.

- [Her89] G. HERZBERG: *Molecular spectra and molecular structure*. New York: Springer Science+Business Media, 1989.
- [Hig64] P. W. HIGGS: ‘Broken Symmetries and the Masses of Gauge Bosons’. In *Physical Review Letters* (1964), volume 13(16): pages 508–509. DOI: 10.1103/PhysRevLett.13.508.
- [Hir87] K. HIRATA, T. KAJITA, M. KOSHIBA, M. NAKAHATA, Y. OYAMA et al.: ‘Observation of a neutrino burst from the supernova SN1987A’. In *Physical Review Letter* (14 1987), volume 58: pages 1490–1493. DOI: 10.1103/PhysRevLett.58.1490.
- [Hir88] K. HIRATA, T. KAJITA, M. KOSHIBA, M. NAKAHATA, S. OHARA et al.: ‘Experimental study of the atmospheric neutrino flux’. In *Physics Letters B* (1988), volume 205(2-3): pages 416–420. DOI: 10.1016/0370-2693(88)91690-5.
- [Hol17] A. HOLLEMAN, E. WIBERG and N. WIBERG: *Anorganische Chemie, 103. Auflage*. Berlin: De Gruyter, 2017. DOI: <https://doi.org/10.1515/9783110495850>.
- [Hor83] N. HORIUTI: ‘System for Preparation of Standard Tritium Gas Sample for Calibration of Monitoring System’. In *Journal of the Atomic Energy Society of Japan / Atomic Energy Society of Japan* (1983), volume 25(3): pages 201–206. DOI: 10.3327/jaesj.25.201.
- [Höt12] M. HÖTZEL: ‘Simulation and analysis of source-related effects for KATRIN’. PhD thesis. Karlsruhe Institute of Technology, 2012. DOI: 10.5445/IR/1000031259.
- [Hub03] P. HUBER and W. WINTER: ‘Neutrino factories and the “magic” baseline’. In *Physical Review D* (2003), volume 68(3). DOI: 10.1103/PhysRevD.68.037301.
- [Hub79] K. P. HUBER and G. HERZBERG: ‘Constants of diatomic molecules’. In *Molecular Spectra and Molecular Structure*. Boston, MA: Springer, 1979: pages 8–689. DOI: 10.1007/978-1-4757-0961-2_2.
- [Hut95] E. HUTTER, U. BESSERER and G. JACQMIN: *Treatment of tritiated exhaust gases at the Tritium Laboratory Karlsruhe*. 1995. DOI: 10.2172/95666.
- [Ich12] A. ICHIKAWA: ‘Design concept of the magnetic horn system for the T2K neutrino beam’. In *Nuclear Instruments and Methods in Physics Research Section A: Accelerators, Spectrometers, Detectors and Associated Equipment* (2012), volume 690: pages 27–33. DOI: 10.1016/j.nima.2012.06.045.
- [Ich85] K. ICHIMURA, N. INOUE, K. ASHIDA, M. MATSUYAMA, H. MIYAKE et al.: ‘Pressure measurement in tritium atmospheres by mass spectrometer and tritium effect.’ In *Radioisotopes* (1985), volume 34(2): pages 83–86. DOI: 10.3769/radioisotopes.34.2_83.
- [Irv83] J. M. IRVINE and R. HUMPHREYS: ‘Neutrino masses and the cosmic-neutrino background’. In *Journal of Physics G: Nuclear Physics* (1983), volume 9(7): pages 847–852. DOI: 10.1088/0305-4616/9/7/017.

- [ISO08] ISO/IEC GUIDE 98-3:2008-09: *Uncertainty of measurement - Part 3: Guide to the expression of uncertainty in measurement (GUM:1995)*. Bureau International Genève, Switzerland, 2008.
- [ISO94] ISO 5725-1:1994(EN): *Accuracy (trueness and precision) of measurement methods and results — Part 1: General principles and definitions*. 1994.
- [Jam13a] T. M. JAMES, M. SCHLÖSSER, S. FISCHER, M. STURM, B. BORNSCHEIN et al.: ‘Accurate depolarization ratio measurements for all diatomic hydrogen isotopologues. Depolarization ratios for all diatomic hydrogen isotopologues’. In *Journal of Raman Spectroscopy* (2013), volume 44: pages 857–865. DOI: 10.1002/jrs.4283.
- [Jam13b] T. M. JAMES: ‘Quantitative Raman spectroscopy of gases related to KATRIN’. PhD thesis. Swansea University (United Kingdom), 2013.
- [Jam13c] T. M. JAMES, M. SCHLÖSSER, R. J. LEWIS, S. FISCHER, B. BORNSCHEIN et al.: ‘Automated Quantitative Spectroscopic Analysis Combining Background Subtraction, Cosmic Ray Removal, and Peak Fitting’. In *Applied Spectroscopy* (2013), volume 67(8): pages 949–959. DOI: 10.1366/12-06766.
- [Jam15] T. M. JAMES, S. RUPP and H. H. TELLE: ‘Trace gas and dynamic process monitoring by Raman spectroscopy in metal-coated hollow glass fibres’. In *Analytical Methods* (2015), volume 7(6): pages 2568–2576. DOI: 10.1039/c4ay02597k.
- [Jan15] A. JANSEN: ‘The Cryogenic Pumping Section of the KATRIN Experiment - Design Studies and Experiments for the Commissioning’. PhD thesis. Karlsruhe Institut of Technology, 2015. DOI: 10.5445/IR/1000047146.
- [Jan17] H.-T. JANKA: ‘Neutrino Emission from Supernovae’. In *Handbook of Supernovae*. Edited by A. W. ALSABTI and P. MURDIN. Cham: Springer International Publishing, 2017: pages 1575–1604. DOI: 10.1007/978-3-319-21846-5_4.
- [Jar16] R. L. JAREK, H. C. PEEBLES and J. A. BIERNER: *Tritium Gas Analysis Capabilities and Results from Sandia National Laboratories*. Technical report. Sandia National Lab.(SNL-NM), Albuquerque, New Mexico, USA, 2016.
- [Jew97] J. JEWETT: *Raman spectroscopic and mass spectrometric investigations of the hydrogen isotopes and isotopically labelled methane*. Technical report. Fluor Daniel Hanford, Inc., Richland, Washington, USA, 1997.
- [Jon19] R. R. JONES, D. C. HOOPER, L. ZHANG, D. WOLVERSON and V. K. VALEV: ‘Raman techniques: fundamentals and frontiers’. In *Nanoscale research letters* (2019), volume 14(1): pages 1–34. DOI: <https://doi.org/10.1186/s11671-019-3039-2>.
- [Jon48] W. M. JONES: ‘Thermodynamic functions for tritium and tritium hydride. The equilibrium of tritium and hydrogen with tritium hydride. The dissociation of tritium and tritium hydride’. In *The Journal of Chemical Physics* (1948), volume 16(11): pages 1077–1081. DOI: 10.1063/1.1746727.

- [Jon49] W. JONES: ‘Thermodynamic functions for tritium deuteride. The dissociation of tritium deuteride. Equilibria among the isotopic hydrogen molecules’. In *The Journal of Chemical Physics* (1949), volume 17(11): pages 1062–1064. DOI: 10.1063/1.1747113.
- [Käf12] W. KÄFER: ‘Sensitivity Studies for the KATRIN experiment’. PhD thesis. Karlsruhe Institut of Technology, 2012. DOI: 10.5445/IR/1000026021.
- [Kam08] KAMLAND COLLABORATION: ‘Precision Measurement of Neutrino Oscillation Parameters with KamLAND’. In *Physical Review Letter* (2008), volume. DOI: 10.1103/PhysRevLett.100.221803.
- [Kan64] R. J. KANDEL: ‘Methane–Tritium System. II. Kinetics of the Exchange Reaction’. In *The Journal of Chemical Physics* (1964), volume 41(8): pages 2435–2442. DOI: 10.1063/1.1726283.
- [KAT01] KATRIN COLLABORATION: *KATRIN: A next generation tritium beta decay experiment with sub-eV sensitivity for the electron neutrino mass*. 2001. arXiv: hep-ex/0109033 [hep-ex].
- [Kaz08a] O. KAZACHENKO, B. BORNSCHEIN, L. BORNSCHEIN, F. EICHELHARDT, N. KERNERT et al.: ‘TRAP—a cryopump for pumping tritium on pre-condensed argon’. In *Nuclear Instruments and Methods in Physics Research Section A-accelerators Spectrometers Detectors and Associated Equipment* (2008), volume 587: pages 136–144. DOI: 10.1016/j.nima.2007.12.024.
- [Kaz08b] O. KAZACHENKO, B. BORNSCHEIN, N. KERNERT, L. DOERR, M. GLUGLA et al.: ‘Tritium Processing Loop for KATRIN Experiment’. In *Fusion Science and Technology* (2008), volume 54(1): pages 67–70. DOI: 10.13182/FST08-A1766.
- [Kes02] W. KESSEL: ‘Measurement uncertainty according to ISO/BIPM-GUM’. In *Thermochimica Acta* (2002), volume 382(1-2): pages 1–16. DOI: [https://doi.org/10.1016/S0040-6031\(01\)00729-8](https://doi.org/10.1016/S0040-6031(01)00729-8).
- [Kim13] S.-B. KIM, T. LASSERRE and Y. WANG: ‘Reactor Neutrinos’. In *Advances in High Energy Physics* (2013), volume 2013: pages 1–34. DOI: 10.1155/2013/453816.
- [Kin08] S. F. KING: ‘Neutrino mass models: A road map’. In *Journal of Physics: Conference Series* (2008), volume 136(2): page 022038. DOI: 10.1088/1742-6596/136/2/022038.
- [Kle16] C. C. KLEPPER, T. M. BIEWER, U. KRUEZI, S. VARTANIAN, D. DOUAI et al.: ‘Extending helium partial pressure measurement technology to JET DTE2 and ITER’. In *Review of Scientific Instruments* (2016), volume 87(11): page 11D442. DOI: 10.1063/1.4963713.

- [Kle19a] M. KLEESIEK, J. BEHRENS, G. DREXLIN, K. EITEL, M. ERHARD et al.: ‘Beta-Decay spectrum, response function and statistical model for neutrino mass measurements with the KATRIN experiment’. In *The European Physical Journal C* (2019), volume 79(3): pages 1–24. DOI: 10.1140/epjc/s10052-019-6686-7.
- [Kle19b] M. KLEIN: ‘Tritium ions in KATRIN: blocking, removal and detection’. PhD thesis. Karlsruhe Institut of Technology, 2019. DOI: 10.5445/IR/1000093526.
- [Kob73] M. KOBAYASHI and T. MASKAWA: ‘CP-Violation in the Renormalizable Theory of Weak Interaction’. In *Progress of Theoretical Physics* (1973), volume 49(2): pages 652–657. DOI: 10.1143/PTP.49.652.
- [Kod01] K. KODAMA, N. USHIDA, C. ANDREOPOULOS, N. SAOULIDOU, G. TZANAKOS et al.: ‘Observation of tau neutrino interactions’. In *Physics Letters B* (2001), volume 504(3): pages 218–224. DOI: 10.1016/S0370-2693(01)00307-0.
- [Kod98] K. KODAMA, M. GÜLER, E. PESEN, M. SERIN-ZEYREK, R. SEVER et al.: *The OPERA ν_τ appearance experiment in the CERN-Gran Sasso neutrino beam*. Technical report CERN-SPSC-98-25 ; LNGS-LOI-97-8-add-1 ; SPSC-M-612. Geneva: CERN, Geneva, Switzerland, 1998.
- [Köl11] Z. KÖLLÖ, C. G. ALECU and H. MOOSMANN: ‘A New Method to Measure Small Volumes in Tritium Handling Facilities, Using p-V Measurements’. In *Fusion Science and Technology* (2011), volume 60(3): pages 972–975. DOI: 10.13182/fst11-a12578.
- [Kon47] E. J. KONOPINSKI: ‘ H^3 and the Mass of the Neutrino’. In *Physical Review* (1947), volume 72(6): pages 518–519. DOI: 10.1103/PhysRev.72.518.2.
- [Kra05] C. KRAUS, B. BORNSCHEIN, L. BORNSCHEIN, J. BONN, B. FLATT et al.: ‘Final results from phase II of the Mainz neutrino mass search in tritium β decay’. In *The European Physical Journal C* (2005), volume 40(4): pages 447–468. DOI: 10.1140/epjc/s2005-02139-7.
- [Kra16] M. KRAUS: ‘Energy-Scale Systematics at the KATRIN Main Spectrometer’. PhD thesis. Karlsruhe Institute of Technology, 2016. DOI: 10.5445/IR/1000054447.
- [Kuc18] L. KUCKERT, F. HEIZMANN, G. DREXLIN, F. GLÜCK, M. HÖTZEL et al.: ‘Modelling of gas dynamical properties of the Katrin tritium source and implications for the neutrino mass measurement’. In *Vacuum* (2018), volume 158: pages 195–205. DOI: 10.1016/j.vacuum.2018.09.036.
- [Lai20] K.-F. LAI, V. HERMANN, T. M. TRIVIKRAM, M. DIOUF, M. SCHLÖSSER et al.: ‘Precision measurement of the fundamental vibrational frequencies of tritium-bearing hydrogen molecules: T₂, DT, HT’. In *Physical Chemistry Chemical Physics* (2020), volume 22(16): pages 8973–8987. DOI: <https://doi.org/10.1039/D0CP00596G>.

- [Le 78] Y. LE GALLIC and H. GOENVEC: ‘Gaseous standards: Tritium gas flow’. In *Environment International* (1978), volume 1(1): pages 31–34. DOI: 10.1016/S0160-4120(78)80073-7.
- [Lee57] T. D. LEE and C. N. YANG: ‘Parity Nonconservation and a Two-Component Theory of the Neutrino’. In *Physical Review* (1957), volume 105(5): pages 1671–1675. DOI: 10.1103/PhysRev.105.1671.
- [Les06] J. LESGOURGUES, L. PEROTTO, S. PASTOR and M. PIAT: ‘Probing neutrino masses with CMB lensing extraction’. In *Physical Review D* (2006), volume 73(4). DOI: 10.1103/PhysRevD.73.045021.
- [Lew07] R. J. LEWIS: ‘Development of a Raman system for in-line monitoring of tritium at the Karlsruhe Tritium Neutrino (KATRIN) experiment’. PhD thesis. Swansea University (United Kingdom), 2007.
- [Löf03] T. LÖFQVIST, J. DELSING and K. SOKAS: ‘Speed of sound measurements in gas-mixtures at varying composition using an ultrasonic gas flow meter with silicon based transducers’. In *International Conference on Flow Measurement: 12/05/2003-14/05/2003*. 2003.
- [Lon02] D. A. LONG: *The Raman Effect*. Chichester, West Sussex, England: John Wiley & Sons, Ltd, 2002. DOI: 10.1002/0470845767.
- [Lor02] T. J. LOREDO and D. Q. LAMB: ‘Bayesian analysis of neutrinos observed from supernova SN 1987A’. In *Physical Review D* (2002), volume 65(6). DOI: 10.1103/PhysRevD.65.063002.
- [Luk12] S. LUKIC, B. BORNSCHEIN, L. BORNSCHEIN, G. DREXLIN, A. KOSMIDER et al.: ‘Measurement of the gas-flow reduction factor of the KATRIN DPS2-F differential pumping section’. In *Vacuum* (2012), volume 86(8): pages 1126–1133. DOI: 10.1016/j.vacuum.2011.10.017.
- [M G79] P. R. M. GELL-MANN and R. SLANSKY: *Supergravity*. Edited by P. van NIEUWENHUIZEN et al. North Holland, Amsterdam, North Holland Publishing, 1979: pages 315–321.
- [Ma20] X. MA, X. TANG, Z. WANG, Q. WANG and D. GAO: ‘Speed of sound in hydrogen isotopes derived from the experimental pvt data and an improved quantum law of corresponding state’. In *Scientific Reports* (2020), volume 10(1): pages 1–9. DOI: <https://doi.org/10.1038/s41598-020-58011-9>.
- [Mak62] Z. MAKI, M. NAKAGAWA and S. SAKATA: ‘Remarks on the Unified Model of Elementary Particles’. In *Progress of Theoretical Physics* (1962), volume 28(5): pages 870–880. DOI: 10.1143/PTP.28.870.
- [Man93] F. MANNONE: *Safety in Tritium Handling Technology*. Netherlands: Springer, 1993. DOI: 10.1007/978-94-011-1910-8.

- [Mat02] M. MATSUYAMA, T. MURAI and K. WATANABE: ‘Quantitative measurement of surface tritium by β -ray-induced X-ray spectrometry (BIXS)’. In *Fusion science and technology* (2002), volume 41(3P2): pages 505–509. DOI: 10.13182/FST02-A22640.
- [Mat52] H. MATTRAW, C. PACHUCKI and L. M. DORFMAN: ‘Mass Spectrometric Determination of the Hydrogen-Tritium Equilibrium’. In *The Journal of Chemical Physics* (1952), volume 20(5): pages 926–926. DOI: 10.1063/1.1700612.
- [McC06] R. L. MCCREERY: ‘Photometric Standards for Raman Spectroscopy’. In *Handbook of Vibrational Spectroscopy*. Edited by J. CHALMERS and P. GRIFFITHS. New York: J. Wiley, 2006. DOI: 10.1002/0470027320.s0706.
- [McC83] G. McCONVILLE, D. MENKE and R. ELLEFSON: ‘Reaction rates of D₂+ T₂ mixtures at 295 K’. In *Journal of Vacuum Science & Technology A: Vacuum, Surfaces, and Films* (1983), volume 1(3): pages 1441–1446. DOI: <https://doi.org/10.1116/1.572037>.
- [McD02] A. B. McDONALD: *Direct Evidence for Neutrino Flavor Transformation from Neutral-Current Interactions in SNO*. 2002. DOI: 10.1063/1.1524553.
- [McD03] A. B. McDONALD, J. R. KLEIN and D. L. WARK: ‘Solving the Solar Neutrino Problem’. In *Scientific American* (2003), volume 288(4): pages 40–49. DOI: 10.1038/scientificamerican0403-40.
- [McK10] W. MCKINNEY: ‘Data Structures for Statistical Computing in Python’. In *Proceedings of the 9th Python in Science Conference (SciPy 2010)*. SciPy, 2010. DOI: 10.25080/majora-92bf1922-00a.
- [McQ00] D. McQUARRIE: *Statistical Mechanics*. Sausalito, Calif: University Science Books, 2000.
- [Mei30] L. MEITNER and W. ORTHMANN: ‘Über eine absolute Bestimmung der Energie der primären Beta-Strahlen von Radium’. In *Zeitschrift für Physik* (1930), volume 60(3-4): pages 143–155. DOI: 10.1007/BF01339819.
- [Mei69] H. MEISSNER, C. KUSIK and W. DALZELL: ‘Equilibrium compositions with multiple reactions’. In *Industrial & Engineering Chemistry Fundamentals* (1969), volume 8(4): pages 659–665. DOI: <https://doi.org/10.1021/i160032a010>.
- [Mer15] S. MERTENS: ‘Status of the KATRIN Experiment and Prospects to Search for keV-mass Sterile Neutrinos in Tritium β -decay’. In *Physics Procedia* (2015), volume 61: pages 267–273. DOI: 10.1016/j.phpro.2014.12.043.
- [Mik86] S. P. MIKHEYEV and A. Y. SMIRNOV: ‘Resonant amplification of ν oscillations in matter and solar-neutrino spectroscopy’. In *Il Nuovo Cimento C* (1986), volume 9(1): pages 17–26. DOI: 10.1007/BF02508049.

- [MIN06] MINOS COLLABORATION: ‘Observation of muon neutrino disappearance with the MINOS detectors and the NuMI neutrino beam’. In *Physical Review Letters* (2006), volume. DOI: 10.1103/PhysRevLett.97.191801.
- [Mir20] S. MIRZ, T. BRUNST, R. GRÖSSLE and B. KRASCH: ‘Concentrated Nonequilibrium HD for the Cross Calibration of Hydrogen Isotopologue Analytics’. In *Fusion Science and Technology* (2020), volume 76(3): pages 284–290. DOI: 10.1080/15361055.2020.1711688.
- [Moh02] R. N. MOHAPATRA: ‘ICTP Lectures on Theoretical Aspects of Neutrino Masses and Mixings’. In *Beyond the desert: Accelerator, non-accelerator and space approaches into the next millennium. Proceedings, 3rd International Conference on particle physics beyond the standard model, Oulu, Finland, June 2-7, 2002*. 2002. arXiv: hep-ph/0211252 [hep-ph].
- [Mor67] K. MOROKUMA, L. PEDERSEN and M. KARPLUS: ‘Vibrational vs. translational activation in the H₂, H₂ and H₂, D₂ exchange reactions’. In *Journal of the American Chemical Society* (1967), volume 89(19): pages 5064–5065. DOI: <https://doi.org/10.1021/ja00995a055>.
- [Mor77] MORRIS G. A.: *Methane Formation in Tritium Gas exposed to Stainless Steel*. Technical report. Lawrence Livermore Laboratory, University of California, Livermore, California, USA, 1977.
- [Nak08] T. NAKADAIRA, T. HARUYAMA, K. KASAMI, S. KOIKE, A. ICHIKAWA et al.: ‘T2K Target’. In *AIP Conference Proceedings* (2008), volume 981(290). DOI: 10.1063/1.2898964.
- [Nas65] J. B. NASH: *The production of tritium labeled methane and ethane in the ch₄-t₂ system*. Technical report UCRL-16009. Lawrence Livermore Laboratory, University of California, Livermore, California, USA, 1965.
- [Nat18] NATIONAL INSTITUTE FOR NUCLEAR PHYSICS: *The sox project is cancelled due to the impossibility of realizing the source with the required characteristics*. 2018. URL: <https://web.archive.org/web/20180309012856/http://home.infn.it/en/media-outreach/press-releases/2789-infn-e-cea-annullano-il-progetto-sox-per-l-impossibilita-di-realizzare-la-sorgente-con-le-caratteristiche-necessarie-all-esperimento-2> (visited on 15th Sept. 2020).
- [Nat19] NATIONAL INSTITUTE OF STANDARDS & TECHNOLOGY: *Standard Reference Material 2242: Relative Intensity Correction Standard for Raman Spectroscopy: 532 nm Excitation*. Edited by C. A. GONZALEZ and S. J. CHOQUETTE. 2019.
- [Nef98] G. NEFFE, U. BESSERER, J. DEHNE, E. HUTTER, H. KISSEL et al.: ‘Routine operation of the gas chromatographic isotope separation system of the Tritium Laboratory Karlsruhe’. In *Fusion Engineering and Design* (1998), volume 39-40: pages 987–993. DOI: 10.1016/S0920-3796(97)00163-4.

- [New14] M. NEWVILLE, T. STENSITZKI, D. B. ALLEN and A. INGARGIOLA: *LMFIT: Non-Linear Least-Square Minimization and Curve-Fitting for Python*. Version 0.8.0. 2014. DOI: 10.5281/zenodo.11813.
- [Nie15] S. NIEMES, M. STURM, R. MICHLING and B. BORNSCHEIN: ‘High level tritiated water monitoring by Bremsstrahlung counting using a silicon drift detector’. In *Fusion Science and Technology* (2015), volume 67(3): pages 507–510. DOI: <https://doi.org/10.13182/FST14-T66>.
- [Nie18] S. NIEMES and G. ZELLER: ‘Calibration strategy and status of tritium purity monitoring for KATRIN’. In *28th International Conference on Neutrino Physics and Astrophysics (NEUTRINO 2018)*. Heidelberg, 2018. DOI: 10.5281/zenodo.1302940.
- [Nis00] M. NISHIKAWA, N. NAKASHIO, T. SHIRAIISHI, S. ODOI, T. TAKEISHI et al.: ‘Tritium trapping capacity on metal surface’. In *Journal of Nuclear Materials* (2000), volume 277(1): pages 99–105. DOI: 10.1016/S0022-3115(99)00133-6.
- [Nis06] M. NISHI, T. YAMANISHI and T. HAYASHI: ‘Study on tritium accountancy in fusion DEMO plant at JAERI’. In *Fusion Engineering and Design* (2006), volume 81(1-7): pages 745–751. DOI: 10.1016/j.fusengdes.2005.08.052.
- [Nob20a] NOBEL MEDIA AB: *The Nobel Prize in Physics 1930*. 2020. URL: <https://www.nobelprize.org/prizes/physics/1930/summary/> (visited on 28th Aug. 2020).
- [Nob20b] NOBEL MEDIA AB: *The Nobel Prize in Physics 1957*. 2020. URL: <https://www.nobelprize.org/prizes/physics/1957/summary/> (visited on 22nd Sept. 2020).
- [Nob20c] NOBEL MEDIA AB: *The Nobel Prize in Physics 1994*. 2020. URL: <https://www.nobelprize.org/prizes/physics/1995/summary/> (visited on 22nd Sept. 2020).
- [Ohi92] S. OHIRA: ‘On-line Tritium Process Gas Analysis by Laser Raman Spectroscopy at TSTA’. In *Fusion Science & Technology* (1992), volume. DOI: 10.13182/fst92-2.
- [Ohi95] S. O’HIRA, H. NAKAMURA, K. OKUNO, D. J. TAYLOR and R. H. SHERMAN: ‘Beta-Decay Induced Reaction Studies of Tritium by Laser Raman Spectroscopy – T2-CO system –’. In *Fusion Technology* (1995), volume 28(3P2): pages 1239–1243. DOI: 10.13182/FST95-A30579.
- [Ohi96] S. O’HIRA and K. OKUNO: ‘Development of Real-Time and Remote Fuel Process Gas Analysis System Using Laser Raman Spectroscopy’. In *Fusion Technology* (1996), volume 3300: pages 869–873. DOI: 10.13182/fst96-a11963046.
- [Oku91] K. OKUNO, T. UDA, S. O’HIRA and Y. NARUSE: ‘Development of In-Situ Gas Analyzer for Hydrogen Isotopes in Fusion Fuel Gas Processing’. In *Journal of Nuclear Science and Technology* (1991), volume 28(6): pages 509–516. DOI: 10.1080/18811248.1991.9731390.

- [OPE14] OPERA COLLABROATION, N. AGAFONOVA, A. ALEKSANDROV, A. ANOKHINA, S. AOKI et al.: ‘Observation of tau neutrino appearance in the CNGS beam with the OPERA experiment’. In *Progress of Theoretical and Experimental Physics* (2014), volume 2014(10): pages 101C01–101C01. DOI: 10.1093/ptep/ptu132.
- [Otl05] R. L. OTLET, I. D. MATHER and M. POTTINGER: ‘Apparatus for the Calibration/Certification of Direct Reading Tritium in Air Monitors’. In *Fusion Science and Technology* (2005), volume 48(1): pages 362–365. DOI: 10.13182/FST05-A943.
- [Ott08] E. W. OTTEN and C. WEINHEIMER: ‘Neutrino mass limit from tritium β decay’. In *Reports on Progress in Physics* (2008), volume 71(8): page 086201. DOI: 10.1088/0034-4885/71/8/086201.
- [Pac14] K. PACHUCKI and J. KOMASA: ‘Accurate adiabatic correction in the hydrogen molecule’. In *The Journal of chemical physics* (2014), volume 141(22): page 224103. DOI: 10.1063/1.4902981.
- [Pal15] N. PALANQUE-DELABROUILLE, C. YÈCHE, J. BAUR, C. MAGNEVILLE, G. ROSSI et al.: ‘Neutrino masses and cosmology with Lyman-alpha forest power spectrum’. In *Journal of Cosmology and Astroparticle Physics* (2015), volume 2015(11): pages 011–011. DOI: 10.1088/1475-7516/2015/11/011.
- [Pan05] N. PANAGIA: ‘A Geometric Determination of the Distance to SN 1987A and the LMC’. In *Springer Proceedings in Physics* (99 2005), volume: pages 585–592. DOI: 10.1007/3-540-26633-X_78.
- [Par20] PARTICLE DATA GROUP: ‘Review of Particle Physics’. In *Progress of Theoretical and Experimental Physics* (2020), volume 2020(8). DOI: 10.1093/ptep/ptaa104.
- [Päs15] H. PÄS and W. RODEJOHANN: ‘Neutrinoless double beta decay’. In *New Journal of Physics* (2015), volume 17(11): page 115010. DOI: 10.1088/1367-2630/17/11/115010.
- [Pau30] W. PAULI: *Wissenschaftlicher Briefwechsel mit Bohr, Einstein, Heisenberg u.a. Band II: 1930–1939 / Scientific Correspondence with Bohr, Einstein, Heisenberg a.o. Volume II: 1930–1939*. Edited by K. v. MEYENN. Berlin Heidelberg: Springer, 1930. 832 pages. DOI: 10.1007/978-3-540-78801-0.
- [Pen97] R.-D. PENZHORN, U. BERNDT, E. KIRSTE and J. CHABOT: ‘Performance Tests of Palladium/Silver Permeators with Tritium at the Tritium Laboratory Karlsruhe’. In *Fusion Technology* (1997), volume 32(2): pages 232–245. DOI: 10.13182/fst97-a19893.
- [Per08] A. N. PEREVEZENTSEV, A. C. BELL, L. A. RIVKIS, V. M. FILIN, V. V. GUSHIN et al.: ‘Comparative study of the tritium distribution in metals’. In *Journal of Nuclear Materials* (2008), volume 372(2-3): pages 263–276. DOI: 10.1016/j.jnucmat.2007.03.215.

- [Pla18] PLANCK COLLABORATION, N. AGHANIM, Y. AKRAMI, M. ASHDOWN, J. AUMONT et al.: ‘Planck 2018 results. VI. Cosmological parameters’. In *A&A* 641, A6 (2020) (2018), volume. DOI: 10.1051/0004-6361/201833910.
- [Pon68] B. PONTECORVO: ‘Neutrino Experiments and the Problem of Conservation of Leptonic Charge’. In *Sov. Phys. JETP* (1968), volume 26: pages 984–988.
- [Pra11] M. PRALL: ‘Transmission Function of the Pre-Spectrometer and Systematic Tests of the Main-Spectrometer Wire Electrode’. PhD thesis. Universität Münster, 2011.
- [Pra12] M. PRALL, P. RENSCHLER, F. GLÜCK, A. BEGLARIAN, H. BICHSEL et al.: ‘The KATRIN pre-spectrometer at reduced filter energy’. In *New Journal of Physics* (2012), volume 14(7): page 073054. DOI: 10.1088/1367-2630/14/7/073054.
- [Pra61] T. H. PRATT and R. WOLFGANG: ‘The Self-induced Exchange of Tritium Gas with Methane’. In *Journal of the American Chemical Society* (1961), volume 83(1): pages 10–17. DOI: 10.1021/ja01462a002.
- [Pri15] F. PRIESTER, M. STURM and B. BORNSCHEIN: ‘Commissioning and detailed results of KATRIN inner loop tritium processing system at Tritium Laboratory Karlsruhe’. In *Vacuum* (2015), volume 116: pages 42–47. DOI: 10.1016/j.vacuum.2015.02.030.
- [Pri20] F. PRIESTER, D. HILLESHEIMER, A. MARSTELLER, M. RÖLLIG and M. STURM: ‘Tritium Processing Systems and First Tritium Operation of the KATRIN Experiment’. In *Fusion Science and Technology* (2020), volume 76(4): pages 600–604. DOI: 10.1080/15361055.2020.1730118.
- [Pyp78] J. PYPYER and C. BRIGGS: *Kinetics of the radiation-induced exchange reactions of H₂, D₂, and T₂: a review*. Technical report. Lawrence Livermore Laboratory, University of California, Livermore, California, USA, 1978.
- [Ram28] C. V. RAMAN and K. S. KRISHNAN: ‘A New Type of Secondary Radiation’. In *Nature* (1928), volume 121: pages 501–502. DOI: 10.1038/121501c0.
- [Rei59] F. REINES and C. L. COWAN: ‘Free Antineutrino Absorption Cross Section. I. Measurement of the Free Antineutrino Absorption Cross Section by Protons’. In *Physical Review* (1959), volume 113(1): pages 273–279. DOI: 10.1103/PhysRev.113.273.
- [Röl13] M. RÖLLIG, F. PRIESTER, M. BABUTZKA, J. BONN, B. BORNSCHEIN et al.: ‘Activity monitoring of a gaseous tritium source by beta induced X-ray spectrometry’. In *Fusion Engineering and Design* (2013), volume 88(6-8): pages 1263–1266. DOI: 10.1016/j.fusengdes.2012.11.001.

- [Röl15a] M. RÖLLIG, S. EBENHÖCH, S. NIEMES, F. PRIESTER and M. STURM: ‘Development of a compact tritium activity monitor and first tritium measurements’. In *Fusion Engineering and Design* (2015), volume 100: pages 177–180. DOI: 10.1016/j.fusengdes.2015.05.056.
- [Röl15b] M. RÖLLIG: ‘Tritium analytics by beta induced X-ray spectrometry’. PhD thesis. Karlsruhe Institut of Technology, 2015. DOI: 10.5445/IR/1000054050.
- [Röt19] C. RÖTTELE: ‘Tritium suppression factor of the KATRIN transport section’. PhD thesis. Karlsruhe Institut of Technology, 2019. DOI: 10.5445/IR/1000096733.
- [Rup15a] S. RUPP, T. M. JAMES, H. H. TELLE, M. SCHLÖSSER and B. BORNSCHEIN: ‘Enhanced Sensitivity of Raman Spectroscopy for Tritium Gas Analysis Using a Metal-Lined Hollow Glass Fiber’. In *Fusion Science and Technology* (2015), volume 67(3): pages 547–550. DOI: 10.13182/fst14-t76.
- [Rup15b] S. RUPP, A. OFF, H. SEITZ-MOSKALIUK, T. JAMES and H. TELLE: ‘Improving the Detection Limit in a Capillary Raman System for In Situ Gas Analysis by Means of Fluorescence Reduction’. In *Sensors* (2015), volume 15(9): pages 23110–23125. DOI: 10.3390/s150923110.
- [Ryc80] J. RYCHLEWSKI: ‘An accurate calculation of the polarizability of the hydrogen molecule and its dependence on rotation, vibration and isotopic substitution’. In *Molecular Physics* (1980), volume 41(4): pages 833–842. DOI: 10.1080/00268978000103191.
- [SAG02] SAGE COLLABORATION: ‘Solar neutrino flux measurements by the Soviet-American gallium experiment (SAGE) for half the 22-year solar cycle’. In *Journal of Experimental and Theoretical Physics* (2002), volume 95(2): pages 181–193. DOI: 10.1134/1.1506424.
- [SAG99] SAGE COLLABORATION: ‘Measurement of the Solar Neutrino Capture Rate by SAGE and Implications for Neutrino Oscillations in Vacuum’. In *Physical Review Letters* (1999), volume 83(23): pages 4686–4689. DOI: 10.1103/PhysRevLett.83.4686.
- [Sak91] A. D. SAKHAROV: ‘Violation of CP invariance, C asymmetry, and baryon asymmetry of the universe’. In *Soviet Physics Uspekhi* (1991), volume 34(5): pages 392–393. DOI: 10.1070/PU1991v034n05ABEH002497.
- [Sal18] P. F. de SALAS, S. GARIAZZO, O. MENA, C. A. TERNES and M. TÓRTOLA: ‘Neutrino Mass Ordering from Oscillations and Beyond: 2018 Status and Future Prospects’. In *Frontiers in Astronomy and Space Sciences* (2018), volume 5(36). DOI: 10.3389/fspas.2018.00036.
- [San11] M. C. SANCHEZ: ‘Muon Neutrino Disappearance and Tau Neutrino Appearance’. In *XXXI Conference on Physics in Collision, Vancouver, Canada, August 28 to September 1, 2011. Proceedings*. 2011. arXiv: 1112.0618 [hep-ex].

- [Saz11] A. SAZONOV and E. MAGOMEDBEKOV: ‘Hydrogen Isotope Equilibration Induced by Tritium Radiation-Ab Initio Approach to Reaction Kinetics’. In *Fusion Science and Technology* (2011), volume 60(4): pages 1383–1386. DOI: <https://doi.org/10.13182/FST11-A12688>.
- [Sch11] M. SCHLÖSSER, S. FISCHER, M. STURM, B. BORNSCHEIN, R. J. LEWIS et al.: ‘Design Implications for Laser Raman Measurement Systems for Tritium Sample-Analysis, Accountancy or Process-Control Applications’. In *Fusion Science and Technology* (2011), volume 60: pages 976–981. DOI: [10.13182/fst11-a12579](https://doi.org/10.13182/fst11-a12579).
- [Sch12] M. SCHLÖSSER, S. FISCHER, M. HÖTZEL and W. KÄFER: ‘Accuracy of the Laser Raman system for KATRIN’. In *Proceedings of the International School of Physics "Enrico Fermi", Course CLXXXII "NeutrinoPhysics and Astrophysics"*. Edited by G. BELLINI. 2012: pages 333–336. DOI: [10.3254/978-1-61499-173-1-333](https://doi.org/10.3254/978-1-61499-173-1-333).
- [Sch13a] M. SCHLÖSSER, T. M. JAMES, S. FISCHER, R. J. LEWIS, B. BORNSCHEIN et al.: ‘Evaluation method for Raman depolarization measurements including geometrical effects and polarization aberrations. Evaluation method for Raman depolarization measurements’. In *Journal of Raman Spectroscopy* (2013), volume 44: pages 453–462. DOI: [10.1002/jrs.4201](https://doi.org/10.1002/jrs.4201).
- [Sch13b] M. SCHLÖSSER, S. RUPP, H. SEITZ, S. FISCHER, B. BORNSCHEIN et al.: ‘Accurate calibration of the laser Raman system for the Karlsruhe Tritium Neutrino Experiment’. In *Journal of Molecular Structure* (2013), volume 1044: pages 61–66. DOI: [10.1016/j.molstruc.2012.11.022](https://doi.org/10.1016/j.molstruc.2012.11.022).
- [Sch13c] M. SCHLÖSSER, H. SEITZ, S. RUPP, P. HERWIG, C. G. ALECU et al.: ‘In-Line Calibration of Raman Systems for Analysis of Gas Mixtures of Hydrogen Isotopologues with Sub-Percent Accuracy’. In *Analytical Chemistry* (2013), volume 85(5): pages 2739–2745. DOI: [10.1021/ac3032433](https://doi.org/10.1021/ac3032433).
- [Sch14a] M. SCHLÖSSER: *Accurate Calibration of Raman Systems: At the Karlsruhe Tritium Neutrino Experiment*. Switzerland: Springer International Publishing, 2014. DOI: [10.1007/978-3-319-06221-1](https://doi.org/10.1007/978-3-319-06221-1).
- [Sch14b] J. S. SCHWARZ: ‘The Detector System of the KATRIN Experiment - Implementation and First Measurements with the Spectrometer’. PhD thesis. Karlsruhe Institut of Technology, 2014. DOI: [10.5445/IR/1000042772](https://doi.org/10.5445/IR/1000042772).
- [Sch15a] M. SCHLÖSSER, B. BORNSCHEIN, S. FISCHER, T. M. JAMES, F. KASSEL et al.: ‘Raman spectroscopy at the tritium laboratory Karlsruhe’. In *Fusion Science and Technology* (2015), volume 67(3): pages 555–558. DOI: <https://doi.org/10.13182/FST14-T78>.
- [Sch15b] M. SCHLÖSSER, O. PAKARI, S. RUPP, S. MIRZ and S. FISCHER: ‘How to Make Raman-Inactive Helium Visible in Raman Spectra of Tritium-Helium Gas Mixtures’. In *Fusion Science and Technology* (2015), volume 67: pages 559–562. DOI: [10.13182/fst14-t79](https://doi.org/10.13182/fst14-t79).

- [Sch15c] M. SCHLÖSSER, S. RUPP, T. BRUNST and T. M. JAMES: ‘Relative Intensity Correction of Raman Systems with National Institute of Standards and Technology Standard Reference Material 2242 in 90°-Scattering Geometry’. In *Applied Spectroscopy* (2015), volume 69: pages 597–607. DOI: 10.1366/14-07748.
- [Sch15d] H. SCHOEN: *Handbook of Purified Gases*. Berlin, Heidelberg: Springer, 2015. 532 pages. DOI: 10.1007/978-3-540-32599-4.
- [Sch16] K. SCHÖNUNG: ‘Development of a Rear Wall for the KATRIN Rear Section and investigation of tritium compatibility of Rear Section components’. PhD thesis. Karlsruhe Institute of Technology, 2016. DOI: 10.5445/IR/1000056077.
- [Sch87] C. SCHWARTZ and R. J. L. ROY: ‘Nonadiabatic eigenvalues and adiabatic matrix elements for all isotopes of diatomic hydrogen’. In *Journal of Molecular Spectroscopy* (1987), volume 121: pages 420–439. DOI: 10.1016/0022-2852(87)90059-2.
- [Sch91] P. SCHIRA, E. HUTTER, G. JOURDAN and R.-D. PENZHORN: ‘The Tritium Laboratory Karlsruhe: Laboratory design and equipment’. In *Fusion Engineering and Design* (1991), volume 18: pages 19–26. DOI: 10.1016/0920-3796(91)90101-U.
- [Sei19] H. SEITZ-MOSKALIUK: ‘Characterisation of the KATRIN tritium source and evaluation of systematic effects’. PhD thesis. Karlsruhe Institut for Technology, 2019. DOI: 10.5445/IR/1000090748.
- [Sig16] G. SIGL: *Astroparticle Physics: Theory and Phenomenology*. Paris: Atlantis Press, 2016. 861 pages. DOI: 10.2991/978-94-6239-243-4.
- [Sin88] D. SINCLAIR: *The Sudbury Neutrino Observatory*. 1988. DOI: 10.1007/978-3-642-73679-7_24.
- [Sis04] M. SISTI, C. ARNABOLDI, C. BROFFERIO, G. CERUTI, O. CREMONESI et al.: ‘New limits from the Milano neutrino mass experiment with thermal microcalorimeters’. In *Nuclear Instruments and Methods in Physics Research Section A: Accelerators, Spectrometers, Detectors and Associated Equipment* (2004), volume 520(1-3): pages 125–131. DOI: 10.1016/j.nima.2003.11.273.
- [Sme23] A. SMEKAL: ‘Zur Quantentheorie der Dispersion’. In *Naturwissenschaften* (1923), volume 11: pages 873–875. DOI: 10.1007/bf01576902.
- [SNO01] SNO COLLABORATION, Q. R. AHMAD, R. C. ALLEN, T. C. ANDERSEN, J. D. ANGLIN et al.: ‘Measurement of the Rate of $\nu_e + d \rightarrow p + p + e^-$ Interactions Produced by ^8B Solar Neutrinos at the Sudbury Neutrino Observatory’. In *Physical Review Letters* (2001), volume 87(7): page 071301. DOI: 10.1103/PhysRevLett.87.071301.
- [Sou86] P. C. SOUERS: *Hydrogen Properties for Fusion Energy*. Berkeley, Los Angeles, London: University of California Press, 1986. DOI: <https://doi.org/10.1525/9780520338401>.
- [Sta15] STANFORD RESEARCH SYSTEMS: *BGA244 Physics Overview*. Technical report. SRS, Sunnyvale, California, USA, 2015.

- [Sta16] STANFORD RESEARCH SYSTEMS: *Comparing thermal conductivity gas analyzers with the BGA244*. Technical report. SRS, Sunnyvale, California, USA, 2016.
- [Ste13] N. STEINBRINK, V. HANNEN, E. L. MARTIN, R. G. H. ROBERTSON, M. ZACHER et al.: *Neutrino mass sensitivity by MAC-E-Filter based time-of-flight spectroscopy with the example of KATRIN*. 2013. DOI: 10.1088/1367-2630/15/11/113020.
- [Stu10a] M. STURM: ‘Aufbau und Test des Inner-Loop-Systems der Tritiumquelle von KATRIN’. PhD thesis. Karlsruhe: Karlsruher Institut für Technologie, 2010. DOI: 10.5445/IR/1000019355.
- [Stu10b] M. STURM, M. SCHLÖSSER, R. J. LEWIS, B. BORNSCHEIN, G. DREXLIN et al.: ‘Monitoring of all hydrogen isotopologues at tritium laboratory Karlsruhe using Raman spectroscopy’. In *Laser Physics* (2010), volume 20: pages 493–507. DOI: 10.1134/s1054660x10030163.
- [Suz10] A. SUZUKI: ‘KamLAND and T2K’. In *Progress in Particle and Nuclear Physics* (2010), volume 65(1): pages 1–8. DOI: 10.1016/j.ppnp.2010.02.001.
- [Tay01] D. J. TAYLOR, M. GLUGLA and R.-D. PENZHORN: ‘Enhanced Raman sensitivity using an actively stabilized external resonator’. In *Review of Scientific Instruments* (2001), volume 72(4): pages 1970–1976. DOI: <https://doi.org/10.1063/1.1353190>.
- [Teg04] M. TEGMARK, M. A. STRAUSS, M. R. BLANTON, K. ABAZAJIAN, S. DODELSON et al.: ‘Cosmological parameters from SDSS and WMAP’. In *Physical Review D* (2004), volume 69(10). DOI: 10.1103/PhysRevD.69.103501.
- [Tel07] H. H. TELLE, A. G. URENA and R. J. DONOVAN: *Laser chemistry: spectroscopy, dynamics and applications*. Chichester, West Sussex, England: John Wiley & Sons, 2007.
- [Ter69] T. TERAOKA and R. S. BACK: ‘Radiation-induced isotopic exchange in gaseous hydrogen-deuterium mixtures’. In *The Journal of Physical Chemistry* (1969), volume 73(11): pages 3884–3890. DOI: <https://doi.org/10.1021/j100845a053>.
- [Tho58] S. O. THOMPSON and O. A. SCHAEFFER: ‘The Role of Ions in the Radiation Induced Exchange of Hydrogen and Deuterium’. In *Journal of the American Chemical Society* (1958), volume 80(3): pages 553–558. DOI: <https://doi.org/10.1021/ja01536a012>.
- [Tri15] TRITIUM LABORATORY KARLSRUHE: *Technical terms of delivery and acceptance*. Edited by TLK. 2015.
- [Tri16] TRITIUM LABORATORY KARLSRUHE: *Technical terms of delivery and acceptance of TLK*. 2016.
- [Ubi09] M. UBIETO-DÍAZ, D. RODRÍGUEZ, S. LUKIC, S. NAGY, S. STAHL et al.: ‘A broadband FT-ICR Penning trap system for KATRIN’. In *International Journal of Mass Spectrometry* (2009), volume 288(1): pages 1–5. DOI: 10.1016/j.ijms.2009.07.003.

- [Uda92a] T. UDA, K. OKUNO and Y. NARUSE: ‘Hydrogen isotope exchange reaction rate in tritium and methane mixed gas’. In *Journal of Radioanalytical and Nuclear Chemistry* (1992), volume 159(1): pages 145–154. DOI: 10.1007/bf02041027.
- [Uda92b] T. UDA, K. OKUNO and Y. NARUSE: ‘Hydrogen Isotope Exchange Reaction Rates in Tritium, Hydrogen and Deuterium Mixed Gases’. In *Radiochimica Acta* (1992), volume 56(4). DOI: 10.1524/ract.1992.56.4.209.
- [Val06] K. VALERIUS: ‘Electromagnetic design and inner electrode for the KATRIN main spectrometer’. In *Progress in Particle and Nuclear Physics* (2006), volume 57(1): pages 58–60. DOI: 10.1016/j.pnnp.2005.11.011.
- [Val09] K. VALERIUS: ‘Spectrometer-related background processes and their suppression in the KATRIN experiment’. PhD thesis. Muenster Univ. (Germany). Mathematisch-Naturwissenschaftliche Fakultät, 2009.
- [Val10] K. VALERIUS: ‘The wire electrode system for the KATRIN main spectrometer’. In *Progress in Particle and Nuclear Physics*. Neutrinos in Cosmology, in Astro, Particle and Nuclear Physics (2010), volume 64(2): pages 291–293. DOI: 10.1016/j.pnnp.2009.12.032.
- [Val11] K. VALERIUS, H. HEIN, H. BAUMEISTER, M. BECK, K. BOKELOH et al.: ‘Prototype of an angular-selective photoelectron calibration source for the KATRIN experiment’. In *Journal of Instrumentation* (2011), volume 6(01): P01002–P01002. DOI: 10.1088/1748-0221/6/01/P01002.
- [Vei87] D. K. VEIRS and G. M. ROSENBLATT: ‘Raman line positions in molecular hydrogen: H₂, HD, HT, D₂, DT, and T₂’. In *Journal of molecular spectroscopy* (1987), volume 121(2): pages 401–419. DOI: [https://doi.org/10.1016/0022-2852\(87\)90058-0](https://doi.org/10.1016/0022-2852(87)90058-0).
- [Vir20] P. VIRTANEN, R. GOMMERS, T. E. OLIPHANT, M. HABERLAND, T. REDDY et al.: ‘SciPy 1.0: fundamental algorithms for scientific computing in Python’. In *Nature Methods* (2020), volume 17(3): pages 261–272. DOI: 10.1038/s41592-019-0686-2.
- [Vol95] T. VOLLMER, U. BESSERER, K. BORCHERDING, J. DEHNE, H. DILGER et al.: ‘Safety Concept for the Tritium Laboratory Karlsruhe (TLK)’. In *Fusion Technology* (1995), volume 28(3P1): pages 988–994. DOI: 10.13182/fst95-a30534.
- [Wag11] R. WAGNER, U. BESSERER, D. DEMANGE, H. DITTRICH, T. L. LE et al.: ‘Improvement and Characterization of Small Cross-Piece Ionization Chambers at the Tritium Laboratory Karlsruhe’. In *Fusion Science and Technology* (2011), volume 60(3): pages 968–971. DOI: <https://doi.org/10.13182/FST11-A12577>.
- [Wei35] C. F. v. WEIZSÄCKER: ‘Zur Theorie der Kernmassen’. In *Zeitschrift für Physik* (1935), volume 96(7-8): pages 431–458. DOI: 10.1007/BF01337700.

- [Wel09] S. WELTE, G. ANA, I. CRISTESCU, L. DÖRR, B. KUNTZ et al.: ‘Construction and commissioning of an ITER sized Pd/Ag permeator for a water detritiation experiment’. In *Fusion engineering and design* (2009), volume 84(7-11): pages 1969–1972. DOI: <https://doi.org/10.1016/j.fusengdes.2009.02.027>.
- [Wel17] S. WELTE, E. FANGHÄNEL, S. FISCHER, F. KRAMER, T. L. LE et al.: ‘Experimental Performance Test of Key Components of the KATRIN Outer Tritium Loop’. In *Fusion Science and Technology* (2017), volume 71(3): pages 316–320. DOI: [10.1080/15361055.2017.1291233](https://doi.org/10.1080/15361055.2017.1291233).
- [Wel20] S. WELTE, M. STURM, D. HILLESHEIMER, L. LE, S. SCHÄFER et al.: ‘Tritium Supply and Processing for the First KATRIN Tritium Operation’. In *Fusion Science and Technology* (2020), volume 76(3): pages 227–231. DOI: [10.1080/15361055.2019.1705681](https://doi.org/10.1080/15361055.2019.1705681).
- [Wen49] I. WENDER, R. A. FRIEDEL and M. ORCHIN: ‘Preparation of high-purity hydrogen deuteride from lithium aluminum hydride’. In *Journal of the American Chemical Society* (1949), volume 71(3): pages 1140–1140. DOI: [10.1021/ja01171a536](https://doi.org/10.1021/ja01171a536).
- [Wil91] J. F. WILKERSON, T. J. BOWLES, J. L. FRIAR, R. G. H. ROBERTSON, G. J. STEPHENSON et al.: ‘Limit on m_e mass from observation of the beta decay of molecular tritium’. In *Nuclear Physics B - Proceedings Supplement* (1991), volume 19: pages 215–224. DOI: [10.1016/0920-5632\(91\)90202-p](https://doi.org/10.1016/0920-5632(91)90202-p).
- [Wol78] L. WOLFENSTEIN: ‘Neutrino oscillations in matter’. In *Physical Review D* (1978), volume 17(9): pages 2369–2374. DOI: [10.1103/PhysRevD.17.2369](https://doi.org/10.1103/PhysRevD.17.2369).
- [Wu57] C. S. WU, E. AMBLER, R. W. HAYWARD, D. D. HOPPES and R. P. HUDSON: ‘Experimental Test of Parity Conservation in Beta Decay’. In *Physical Review* (1957), volume 105(4): pages 1413–1415. DOI: [10.1103/PhysRev.105.1413](https://doi.org/10.1103/PhysRev.105.1413).
- [Wur17] M. WURM: ‘Solar neutrino spectroscopy’. In *Physics Reports* (2017), volume 685: pages 1–52. DOI: [10.1016/j.physrep.2017.04.002](https://doi.org/10.1016/j.physrep.2017.04.002).
- [Yan80] T. YANAGIDA: ‘Horizontal Symmetry and Masses of Neutrinos’. In *Progress of Theoretical Physics* (1980), volume 64(3): pages 1103–1105. DOI: [10.1143/PTP.64.1103](https://doi.org/10.1143/PTP.64.1103).
- [Yu16] Y. YU, J. HU, Z. WAN, J. WU, H. WANG et al.: ‘Mass separation of deuterium and helium with conventional quadrupole mass spectrometer by using varied ionization energy’. In *Review of Scientific Instruments* (2016), volume 87(3): page 035120. DOI: [10.1063/1.4944560](https://doi.org/10.1063/1.4944560).
- [Zub11] K. ZUBER: *Neutrino Physics*. Boca Raton, FL: Taylor & Francis Group, 2011. DOI: [10.1201/b11065](https://doi.org/10.1201/b11065).
- [Zuc02] A. J. ZUCKERWAR: *Handbook of the speed of sound in real gases*. Amsterdam Boston: Elsevier, 2002.

Danksagung

Diese Arbeit wäre ohne die Hilfe und Unterstützung vieler Menschen nicht möglich gewesen, denen ich hier den gebührenden Dank aussprechen möchte.

Ein großes Dankeschön gilt all meinen Betreuern, die mir mit großem Vertrauen, viel Freiraum und stetiger Unterstützung diese Arbeit ermöglicht haben. Ich danke Prof. Dr. Guido Drexlin für seine Förderung, seinen Einsatz und seinen Fokus, das Optimum für KATRIN herauszuholen. Prof. Dr. Helmut Telle danke ich für die Beratung entlang der experimentellen Phasen, der Diskussionen während der Kollaborationstreffen und der unermüdlichen Korrektur dieser Arbeit. Ganz herzlich bedanken möchte ich mich bei Dr. Beate Bornschein, die mit ihrem Vertrauen und ihrer Unterstützung dieses Projekt erst ermöglicht hat. Neben der Zusammenarbeit am Tritiumlabor möchte ich mich bei ihr auch für unsere gemeinsamen Schreibkurse bedanken, die durch ihre respektvolle und ehrliche Art den Teilnehmern und mir immer viel Spaß gemacht haben. Bei Dr. Michael Sturm möchte ich mich bedanken, dass er immer ein offenes Ohr für mich hatte und neben seiner Arbeit für KATRIN die Zeit fand, mir zu helfen.

TRIHYDE hätte nicht ohne die Unterstützung vieler Personen am TLK aufgebaut werden können, denen ich allen für ihren Einsatz und ihre Geduld danken möchte. Bei Stefan Welte und seinem Team möchte ich mich für die Hilfe bei der Planung, und der Bewältigung aller Probleme, die beim Aufbau und Betrieb aufgetreten sind, bedanken. Tobias Falke und Albert Braun möchte ich für ihren unermüdlichen Einsatz am Schweißgerät und Lecktester meinen Dank aussprechen. Für die Unterstützung, Beratung und Inbetriebnahme von Seiten der Automatisierungstechnik möchte ich mich bei Peter Schäfer, Christin Melzer, Manuel Mungenast und der restlichen MAT-Gruppe bedanken.

Ein großes Dankeschön geht an „meine“ Studierenden und HiWis Sylvia Ebenhöch, Alexander Rein, David Walter, Mark Weyrauch, Marie Oehler, Lucian Fasselt, Immanuel Müller, Christian Goffing und James Braun; die mit ihrem Einsatz und Engagement maßgeblich zum Erfolg dieser Arbeit beigetragen haben. Ich habe viel von und mit euch gelernt. Hoffentlich konntet ihr ebenfalls etwas für euren Weg mitnehmen.

Bei meinen Kollegen aus dem zweiten Stock möchte ich mich für die vielen sinnvollen und sinnlosen Diskussionen über die Jahre bedanken; es hat immer Spaß gemacht: Dr. Marco Röllig, Dr. Alexander Marsteller, Dr. Florian Priester, Dr. Robin Größle, Dr. Carsten Röttele, Bennet Krasch, Max Aker, Genrich Zeller, ... Eure Hilfsbereitschaft und euer Humor sind außergewöhnlich.

Für ihre Arbeiten an LARA und für ihre fortlaufende fachliche und moralische Unterstützung möchte ich mich herzlich bei Dr. Magnus Schlösser und Dr. Sebastian Fischer bedanken.

Danksagung

Ohne die Mitglieder der Tritiuminfrastruktur-Gruppe (Nancy Tuchscherer, David Hillesheimer, Tobias Falke, Tobias Weber, Albert Braun, Frank Kramer, Dr. Uwe Besserer, Stefan Welte und Dieter Adami) sowie der Mess- und Regelungsgruppe (Marc Lautenschläger, Christin Melzer, Manuel Mungenast und Peter Schäfer) wäre kein Experimentierbetrieb im Labor möglich. Vielen Dank an euch für die technische Unterstützung.

Ich danke Eva Porter und Sylvia Krieger für ihre unkomplizierte und prompte Hilfe bei allen administrativen Arbeiten.

Vielen Dank an die wachsamen Augen von SUM (Bernhard Heinle und Susanne Gomez), die mich bei meinen Experimenten nicht nur kontrolliert, sondern mit ihren Tipps und Ideen auch weitergebracht haben.

Herzlich möchte ich mich bei den Mitgliedern des Betriebsbüros bedanken (Dr. Jürgen Wendel, Dirk Osenberg, Sylvia Krieger, Manfred Göckel), die mich stets freundlich und geduldig bei meiner Arbeit unterstützt haben.

Für die vielen schönen Momente, die angenehme und hilfsbereite Atmosphäre und den gemeinsamen Einsatz möchte ich mich bei allen aktuellen und ehemaligen Kollegen und Kolleginnen des Tritiumlabors bedanken.

Bei Andreas Hirsch-Weber möchte ich mich stellvertretend für das „Schreibkurs-Team“ für die Zusammenarbeit am HoC bedanken. Es hat mir Spaß gemacht in diesem motivierten und diskussionsfreudigen Team über den Physik-Tellerrand hinauszublicken.

Ich danke der Graduiertenschule KSETA für die Möglichkeiten des fachlichen Austauschs und der Weiterbildungen.

Ein besonderes Dankeschön möchte ich meinen Eltern, meiner Familie und Warja aussprechen, die mich stets unterstützt haben und mir immer wieder gezeigt haben, dass es ein Leben außerhalb des Labors gibt.

Diese Liste ist sicherlich unvollständig, daher möchte ich mich auch bei allen nichtgenannten Beteiligten herzlich bedanken.